AN ABSTRACT OF THE DISSERTATION OF

Matthew A. Hertel for the degree of Doctor of Philosophy in Nuclear Engineering presented on November 6, 2020.

Title: Development of a Novel MEMS Thermal Sensor Array for Pebble Bed HTGRs

Abstract approved: _____

Brian G. Woods

A novel high temperature thermal instrument is proposed, which utilizes a dual-sensing platinum resistor encased in a mono-crystalline alpha-alumina (sapphire) substrate. The instrument is comprised of four platinum trace elements, oriented with 90° rotational symmetry atop a 1120 oriented crystal lattice substrate. All four of these sensors measure temperature directly via 4-wire ohm measurement of the absolute resistance, while two sets of orthogonal sensors measure the differential strain created by the axially dependent thermal expansion coefficient of a sapphire substrate via a WSB measurement. The RTD temperature measurement calibration is then monitored for drift and corrected by comparing the differential strain-derived measurement of temperature to the temperature derived from the RTD measurement. This allows the instrument to self-calibrate via comparison of two functionally independent measures of electron mobility and operate in extreme environments which have previously caused RTD sensors to drift from their initial calibration and introduce an undefined measurement error. The intended deployment configuration and instrument construction is defined in terms of MEMS fabrication processes and performance of the sensor is simulated to evaluate and confirm the functional applicability of the instrument for operation in pebble bed HTGR thermal environments.

Development of a Novel MEMS Thermal Sensor Array for Pebble Bed HTGRs

by

Matthew A. Hertel

A DISSERTATION

submitted to

Oregon State University

in partial fulfillment of
the requirements for the
degree of

Doctor of Philosophy

Presented November 6, 2020
Commencement June 2021

Doctor of Philosophy dissertation of Matthew A. Hertel presented on November 6th, 2020.

APPROVED:

Major Professor, representing Nuclear Engineering

Head of the School of Nuclear Science and Engineering

Dean of the Graduate School

I understand that my dissertation will become part of the permanent collection of Oregon State University libraries. My signature below authorizes release of my dissertation to any reader upon request.

Matthew A. Hertel, Author

ACKNOWLEDGEMENTS

I want to expresses sincere appreciation to a number of individuals who had a significant contribution to the creation of the body of research which comprises this doctoral dissertation. Primarily this group includes faculty, staff, and students of the Oregon State University School of Nuclear Science and Engineering. I'd specifically like to thank the members of my doctoral committee, Dr. Brian G. Woods, Dr. Andrew C. Klein, Dr. Qiao Wu, Dr. Richard Schultz and Dr. Leah Minc, for their valuable input and feedback.

The most significant contribution was provided Dr. Brian G. Woods. I have sincere and overwhelming gratitude for his willingness to provide space and resources to learn, grow, and make many mistakes along the path to assuming the role of nuclear engineer and thermal hydraulics experimentalist. For his guidance and unwavering trust, he has proven to be a valuable professional mentor and a resourceful academic pathfinder.

I also have sincere appreciation for my family, immediate and extended, for their interest and practical advice. For a lifetime of love and guidance; parents Jacqueline, Bruce, and Karen Hertel, brothers Fredrick, Patrick, and Steven, have my unending gratitude. Much is owed to Patrick specifically, for many years of invaluable companionship, advice, and unwavering support. He is the rock that provides sure footing. He is my lifelong hero and role model, a true brother and a dear friend.

To spouse Jacqueline, for many years of encouragement, love, and perfect companionship, I owe a lifetime of gratitude. No difficult task is accomplished alone, no man is an island, and this achievement would not have been possible without her support. She is the unending motivation to be the best version of myself, if only to better accompany her.

Finally, there is no comparison for the unique, delicate friendship shared between a man and his cat. Mucha is perhaps the most precious and loving companion that can be imagined, and for that she will forever be a source of perpetual happiness and a shelter for restoration of the human spirit. Her support was vital to the continued progress of the research presented. She will always be a joyful reminder of this formative time.

TABLE OF CONTENTS

TABLE OF CONTENTS (Continued)

Page

TABLE OF CONTENTS (Continued)

Page

TABLE OF CONTENTS (Continued)

Page

TABLE OF CONTENTS (Continued)

Page

LIST OF FIGURES

Figure Page

LIST OF FIGURES (Continued)

Figure Page

LIST OF FIGURES (Continued)

Figure Page

LIST OF FIGURES (Continued)

Figure Page

LIST OF FIGURES (Continued)

Figure Page

LIST OF FIGURES (Continued)

Figure Page

LIST OF TABLES

Figure Page

LIST OF APPENDIX FIGURES

Figure Page

For Jackie, with love.

Development of a Novel MEMS Thermal Sensor Array for Pebble Bed HTGRs

1 Introduction

Widespread access to a stable and economical power source has supported the most rapid period of technological development in human history. This period began with the widespread adoption and exploitation of steam power cycles during the Industrial Revolution starting in the middle of the 18th century. The late 19th century saw rapid development of electrical applications and distribution, which is associated with the Second Industrial Revolution, sometimes called the Technological Revolution, and established the de facto standard for modern access to clean, efficient energy. Modern society has become dependent upon economical access to electricity and has used the convenience of readily accessible and mobile electricity to provide everything from light and heat, to instant access to vast informational resources on virtually any subject. Practical electricity generation is perhaps the most utilitarian human technical achievement and is a worthy subject of constant development interest.

The discovery of nuclear interactions and development of subatomic physics in the late 20th century has enabled the use of nuclear chain reactions to produce the heat required to generate electrical energy. This form of thermal production has shown significant benefits when compared to combustion driven generation, and is capable of production on the scale required by society's ever-expanding energy needs without vast resource requirements or large volumes of waste generation [1]. A defining characteristic of the nuclear energy industry is the highly integrated safety culture concerned with preventing the accidental exposure of the public to nuclear materials. The unique focus on safety is in response to the relatively high potential for degradation of societal wellbeing and extensive capital damages associated with widespread radiological contamination. One method of reducing the risk of radiological release is to reduce the probability associated with severe accidents.

This focus on reducing accident probability has resulted in reactor safety being a primary design consideration for new nuclear installations, in addition to the usual economic motivations and physical design requirements. Thus, the advanced development of electricity generation via nuclear reactor technology strives to provide very large amounts of generation capacity with extremely low accident probability and economic operation. These objectives create the environment for the development of the Next Generation Nuclear Plant (NGNP) initiative, which appointed the high-temperature, single-phase gas coolant reactor as the ideal design for the next generation of nuclear reactor technology [2]. To characterize the performance and risk of severe accidents for these advanced reactors, regulators have a need for appropriate tools to characterize the physical processes associated with high temperature gas reactor operations.

The primary product of a nuclear reactor is heat. To generate the largest amount of heat that is economically feasible requires a thorough understanding of the processes by which that heat is produced in the reactor core and the method by which it is transported and converted into other forms of energy. Thermal hydraulic simulations of heat transport mechanisms occurring in the reactor core help to develop this understanding and can be used to reduce the number of physical experiments required to demonstrate that a given reactor design is adequately safe to operate [3]. The measure of safety for any given reactor can be defined as the ability of the given reactor design to mitigate the initiation of a specified accident scenario with a level of probability and predicted capital loss above an established threshold [4]. These simulations rely on experimental data for validation of their results. This validation ensures that the results produced by the numerical calculations accurately reflect the true physical system.

In the case of safety analysis for advanced reactor designs, the most applicable experimental validation data must be collected from an environment similar to that which is expected in the worst-case accident scenarios. For the high-temperature gas-cooled reactor (HTGR) family of designs, this means collecting data in an environment that presents considerable engineering challenges. The high-temperature and complex core

geometry utilized by HTGRs poses challenges for the modern measurement techniques typically used to gather data used for simulation validation [5]. Thus, the task of developing new methods of data collection from these environments is the opportunity this research endeavor seeks to address.

1.1 The High Temperature Gas Reactor (HTGR)

Nuclear reactors in operation today are predominantly light-water reactor (LWR) based designs. These fall into two general categories, the pressurized-water reactor (PWR) and the boiling water reactor (BWR). Reactor development categorizes reactor designs in terms of generation to designate the primary design motivation, and to describe the significant gaps in safety features and efficiency seen between different groups of reactor designs. To understand how HTGR designs compare to modern operating reactors, note that most HTGR designs are classified as Generation IV and are a topic of ongoing design research; whereas currently operating reactors are mostly of the Generation II designation and are relatively mature designs in the sense of technical development.

Early reactor design prototypes are classified as Generation I, and include initial design efforts from a period when nuclear engineering was still attempting to establish the best practices for reactor and safety system design. Generation II reactor designs are generally considered to be the first commercially viable plants, and are the common classification for existing nuclear power installations. Generation III designs are considered to be evolutionary in nature, in that they generally improve on the core concepts of the Generation II designs and add safety measures which are not as vulnerable to failure for common accident scenarios. This is mostly due to passive core cooling systems which can continue to operate with little or no operator action, and do not rely on pumps or powered circulation systems following an accident event. Reactors currently under construction in the United States are classified as Generation III+ designs, as they incorporate passive safety systems as a core design principle and have significantly advanced beyond the first Generation III designs; but share the same design basis and physical processes.

The most advanced reactor designs which have surpassed theoretical development and are a subject of technical development efforts, but thus far have not yet been constructed for commercial use, are mostly labeled as Generation IV designs. This category includes a number of variations of the high temperature gas reactor with unique configurations of a range of key hardware systems primarily defined by their function in terms of plant operation and accident mitigation [6]. In terms of American-based HTGR technical development, most modern designs are based on experience from predecessor plants, including the only two commercially operated, gas-cooled plants ever built in the United States; Peach Bottom, which began construction in 1962 and operated until 1974, and Fort St. Vrain, which started construction in 1968 and operated until 1989. These early plants were relatively successful demonstrations of gas-cooled reactor technology; however, a number of technical challenges increased the cost of operation and decreased the capacity factor for these early plants significantly [7] [8].

Following a general reduction in nuclear technology development interest due to the Three Mile Island and Chernobyl incidents, modern American HTGR development strategy was re-directed toward modular gas reactor design concepts with varying applications outside of power production. The increased applicability and reduced capital cost of this approach made development efforts more attractive to a wide range of potential investors and leveraged a unique feature of the HTGR; the high outlet temperature of the coolant [9].

Two core geometry variations were selected for further development; the prismatic block and pebble bed configurations, both of which utilize a similar plant structure but propose unique challenges to their implementation. Both of these designs have a number of advantages and disadvantages that would become key features of a mature plant, thus both of these designs were considered feasible deployment routes and are the topic of modern development efforts [9]. Figure 1-1 depicts the fuel geometry for both configurations. It should be noted that both fuel geometries described are formed with the same TRISO fuel particles suspended in a graphite matrix. For the pebble bed design, spherical fuel elements or ‘pebbles’ are utilized as a dynamic volume of fuel in the core region with unrestrained

movement, whereas the prismatic block design utilizes a stacked volume of static fuel in the core region. The difference in these geometries creates both opportunities and challenges for development. For example; the possibility for implementation of an on-line refueling scheme for the pebble bed configuration, at the cost of the more difficult characterization of thermal-fluid behavior and fuel migration due to the uncontrolled movement of the pebbles within the core region.

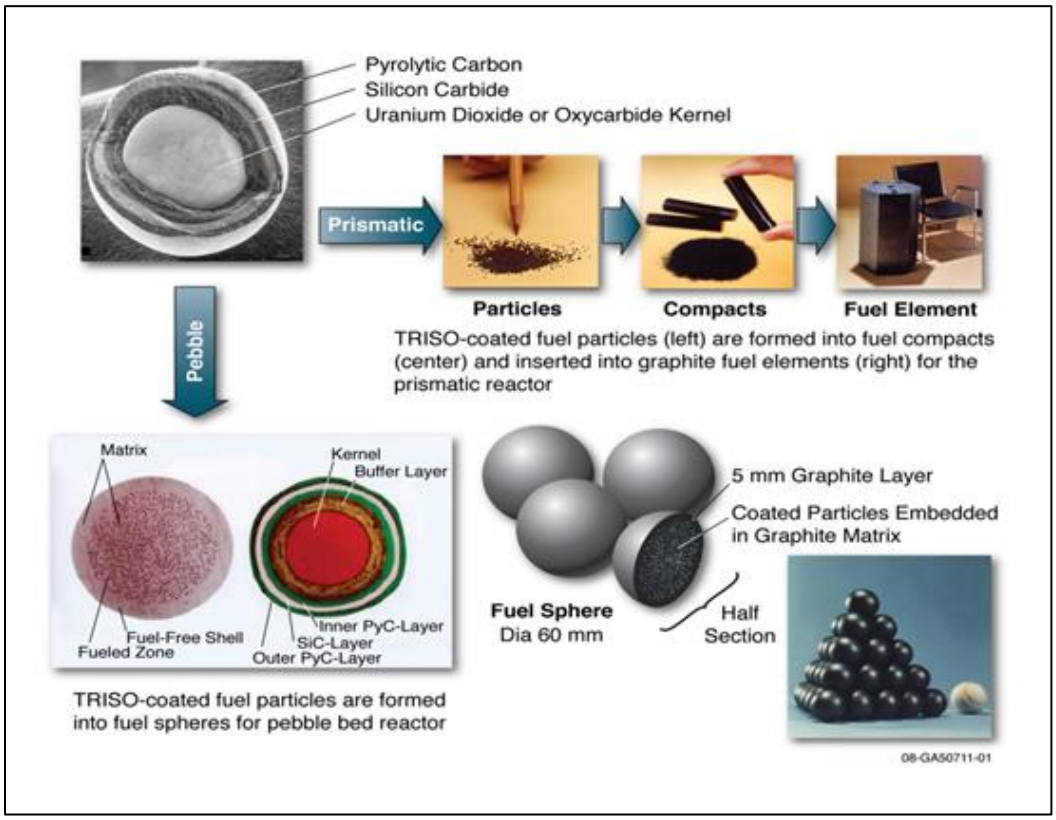

Figure 1-1: Pebble bed and prismatic block fuel geometries [10]

Outside of the core geometry, a modular design for the primary containment structure is common among most HTGR designs. Particularly, the German side-by-side, primary and secondary vessel approach is often utilized due to its demonstrated performance as a safe and efficient deployment configuration. A large number of modern non-HTGR reactor designs utilize this approach of isolating the reactor core from the secondary heat removal

system as well, as it provides a flexible and efficient method of implementing varied co-generation heat transport systems with a given primary reactor design [11].

A pair of particularly well developed and relatively modern reactor designs are depicted in Figure 1-2. The design on the right is referred to as the Modular High Temperature Gas Reactor (MHTGR). The MHTGR utilizes prismatic block fuel assemblies and is an advanced iteration of the traditional gas-cooled reactor design philosophy with a modular plant design in mind. The design on the left is referred to as the Pebble Bed Modular Reactor (PBMR-CG). The PBMR-CG utilizes pebble bed fuel geometry and is configured for co-generation in a modular plant setting. Both of these designs share many similar features outside of the core; the vessel layout is identical and operation is very similar [12].

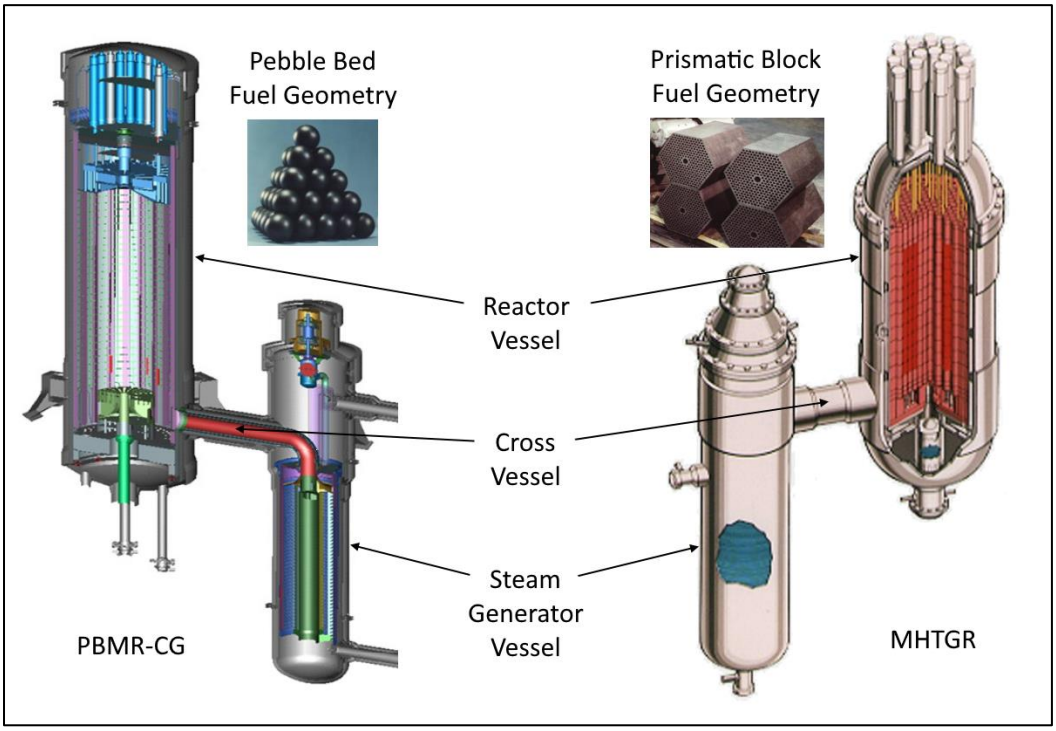

Figure 1-2: Components of the PBMR-CG and MHTGR designs [13] [14] [15] [16]

The American energy market and regulatory agencies have historically favored commercial deployment of water-cooled reactor technology as a conservative and efficient

development route for American nuclear power. This is, in part, due to the selection of the water-cooled reactor as the design-basis of choice for the U.S. Navy submarine program at the early stages of nuclear technology development. This choice motivated a large amount of research that established a body of knowledge surrounding design and operation of water-cooled reactors. This knowledge was useful to companies and regulators during the initial commercialization of grid-based nuclear power installations, creating a fast route to regulatory approval for water-cooled reactor designs [17].

Although water-cooled reactor designs do have many features which are favorable for commercial deployment, the future of nuclear power must leverage the advantages of advanced reactor designs which utilize other coolant types if further utility and efficiency is sought from new installations. Future deployment of the PBMR-CG or MHTGR; or a similar HTGR design, is primarily challenged by a current lack of regulatory knowledge and a significant lack of analytical tools when compared to water-cooled reactor systems. This provides further motivation for characterization of HTGR thermal hydraulics through development of advanced instrumentation.

1.2 Thermal Hydraulic Safety Analysis

As previously mentioned, the nuclear industry has developed a culture of safety surrounding reactor design principles which is rooted in predictive analysis for a number of transient conditions. Key parameters and operating limits are identified which indicate the onset of a transient event which could ultimately lead to the release of radioactive material. Surpassing these parameters and limits is typically the result of the failure of a specific component or group of components related to the operation of the reactor thermal transport cycle. Thus, accident scenarios are typically defined by the failure of a specific heat transport system and are grouped and labeled according to these system failures.

Thermal hydraulic safety analysis follows a tiered approach to accident mitigation. Accidents which have a relatively high probability of occurrence and have large

consequences, such as high capital cost of damages or ecological impact, are considered to have the highest risk and are given preference for safety analysis and design considerations [18]. Accidents in this category which pose fundamental challenges to mitigate, and thus must have dedicated safety features incorporated into the design of the plant, are classified as design basis accidents. Conditions associated with progression of these accidents determine upper limits for a number of key physical parameters. These critical parameters are then used as benchmarks for design of core components associated with the proposed design basis accident.

To determine what sequence of events or operating conditions could produce effects that would cause the critical parameters to exceed established limits, numerical simulations are often used to model core heat transfer phenomena and study their impact. Thus, simulation efforts have a critical relationship with reactor design and furthermore, with thermal hydraulic safety analysis. This approach reduces the cost and safety risk of analysis by minimizing the number of high-fidelity tests which must be performed to ensure mitigation strategies are based upon reliable predictions of transient behavior. A key observation is that the accuracy of the simulation results defines the limit of accuracy for the predictive analysis [19].

Numerical simulations are often based on a number of physical models which represent the most accurate, or most efficient, understanding of the physical processes involved. Some complex processes are approximated using empirical correlations between physical parameters if a more refined analytical model is not adequate for the application. These models and correlations are a subject of constant development and continuously increase in complexity as methods are improved. This increase in complexity is driven by highly refined boundary conditions to provide more similarity to the physical system. To determine the validity of these simulations, and affirm that their results are applicable to physical design specifications for the reactor type in question, the predicted parameters must be compared to measurements of a similar resolution [20]. This can be in the form

of operation data from existing installations or from dedicated testing facilities meant to recreate the effect in question with the highest level of fidelity that is economically feasible.

Testing facilities and measurement systems are often purpose-built to address a specific accident scenario or to characterize the performance and response of a specific system due to this increased demand for highly discretized, highly accurate measurements. In the case of HTGR thermal hydraulic analysis, high temperature testing facilities are utilized to gather high-fidelity safety analysis simulation validation data. Given the considerable challenges for deployment of instrumentation in the core of an operating reactor, a more practical target for instrumentation development is initial deployment in a thermal hydraulic testing facility.

1.2.1 Motivation for Development of Advanced Reactor Instrumentation

Simulation capability for HTGR heat transfer within the core structure is currently relatively limited, and thus the ability to conduct safety analysis on these systems is also impaired when compared to the safety analysis used for water-cooled reactor designs. This is, in part, due to the relative lack of experience within the nuclear industry as well as the unique challenges of gas-cooled reactor core geometry and materials. The ability to simulate the heat transfer within HTGR cores will improve over time, but is dependent on the availability of validation data to verify the accuracy of new simulation methods developed for the task. Modern simulation methods trend toward highly discretized spatial dimensions to evaluate the effects of ever-smaller flow structures and nuanced flow effects which are not obvious with bulk flow parameters. As the spatial discretization of simulations becomes smaller, the data used to validate these methods must also increase in spatial resolution [21].

Most analytical methods currently in use for HTGR systems employ bulk flow or volume averaged techniques and lack the refinement to evaluate transient flow structures at a spatial scale useful for mesoscale core design purposes. To improve the ability to collect validation data for emerging analytical techniques, it is vital that methods for collection of

local-scale heat transfer data are developed. An instrument with a very small footprint, a rugged construction, and a means for flexible data transmission would be ideal. As described in the next section, the need for high spatial resolution measurements in other industries has created a demand for this type of device as well [22]. Application to HTGR thermal hydraulics is a matter of increasing the durability of the instrument to survive and maintain measurement accuracy in the harsh core environment and tailoring the specific sensor design to the heat transfer phenomena being targeted for investigation.

1.3 Micro-Electro-Mechanical Systems (MEMS) Instrumentation

A number of instrumentation strategies have been developed for collection of data in high temperature reactor environments. Many of these methods are based upon deployment of single-point sensors placed in a relatively cool area around the active core periphery to measure flow characteristics at the inlet and outlet of the core coolant flow, or at the core boundary [23]. This is suitable for collection of operational, bulk flow data, but lacks the information density required for collection of simulation validation data, which has the additional requirements of possessing both high spatial density and high local precision to accurately characterize mesoscale energy transport within the core geometry.

Single point measurements could provide the required data resolution, but they must be deployed in an array formation or translated across a measurement volume to produce spatially dense data [24]. Another option exists in the form of optical measurements, which collect data from images of an illuminated two-dimensional plane. These are typically classified as field-of-view measurements and require line-of-sight access to the measurement volume to capture data. This is very difficult for measurements of core heat transfer phenomena due to the difficulty in obtaining line-of-sight access to the core region while ensuring the sensitive optical instruments are insulated from the harsh thermal conditions [25]. Small scale, single point instruments deployed in an array is the most straightforward method for collection of spatially dense, accurate, and dynamic data using non-optical methods and is the assumed deployment configuration for this investigation.

Micro-Electro-Mechanical-System or MEMS devices are identified as having a characteristic length of less than a millimeter, but more than a micrometer, and utilizing highly scalable and efficient fabrication methods derived from silicon processing advancements related to integrated circuit development and production [26]. These devices have demonstrated usefulness in a number of varied metrology applications, but are primarily defined by use as mechanical actuators and small-scale sensor assemblies. These assemblies, specifically consisting of multiple sensor types in an array formation, are often referred to as 'lab-on-a-chip' sensors as they are capable of integrating many different types of measurement hardware into a single instrumentation package.

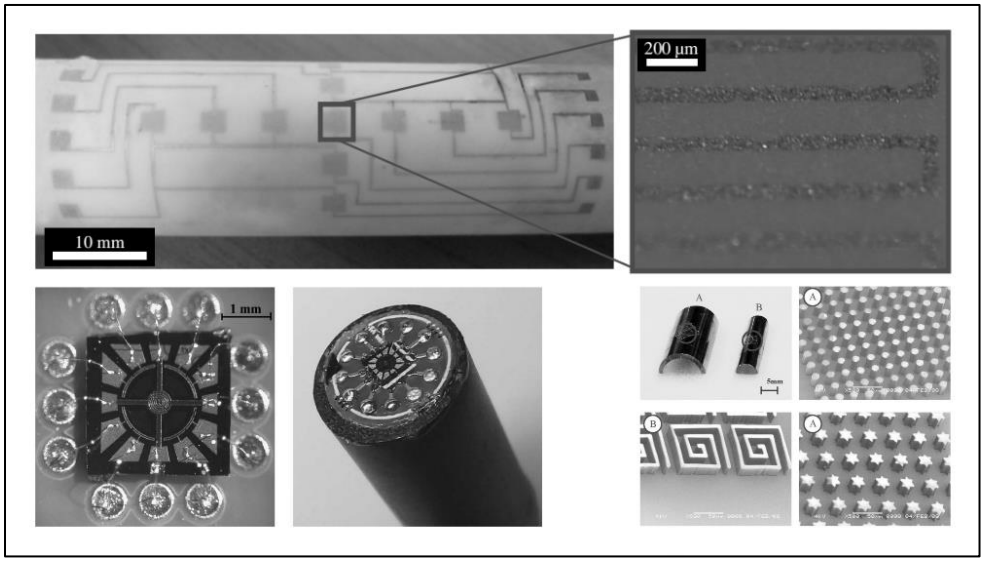

Figure 1-3: Examples of MEMS-based instrumentation [27] [28]

Relevant applications of MEMS technology as heat transfer metrology have been demonstrated for the aerospace, automotive, and industrial power production industries; however, applications for nuclear thermal hydraulic instrumentation have yet to be demonstrated, despite a number of key opportunities [29] [30]. A number of MEMS-based instruments are depicted in Figure 1-3, including thin-film RTDs and a thermal anemometer assembly, to illustrate the scale and versatility of the MEMS instrument class.

These devices are typically minimally invasive with very small power requirements, meaning they are ideal for instrument array applications. This is meaningful for thermal hydraulic experimentation applications because it means that single point instruments can be deployed in a field dense enough to validate high resolution numerical results common for modern thermal hydraulic simulation efforts. Thus, MEMS fabrication techniques are particularly suitable for the intended application and are selected as the design basis for development of a specialized instrument for use in HTGR core thermal environments.

1.3.1 Specialized Deployment Strategy Leveraging Capability of MEMS

A number of strategies exist for MEMS temperature measurement with varying strengths and shortcomings related to high temperature operation. Among the possible hardware configurations are thermocouples, resistance temperature detectors (RTDs), and CMOS semiconductor temperature detectors. Variable resistance class instruments have very simple geometry and are among the most well-characterized and accurate instrument types conducive to MEMS fabrication techniques [31]. The function of a variable resistance thermal sensor is not reliant on semiconductor physics, and thus can avoid a considerable difficulty presented by thermal noise in low bandgap materials [32], which limits the high-temperature applicability of semiconductor based MEMS instruments. Variable resistance thermal sensors instead rely on measuring electrical resistance which varies predominantly as a function of temperature. Thus, the development effort presented here-in will utilize a thin-film RTD class of sensor due to these favorable characteristics for the intended application.

Concerning the deployment configuration of the instrument, the developed device should ideally be a surface mounted instrument package. Sensors utilizing an array formation to measure heat transfer parameters in the core of an HTGR implies that the form of the sensor be such that it can be mounted directly to the surface of a coolant interface, such as the outside surface of a pebble bed fuel element. The form factor should be as minimally invasive as possible. If deployed in a pebble bed HTGR, the instrument would ideally utilize some form of wireless signal transmission so that the dynamic motion of pebble bed

fuel elements is not impeded by the presence of instrumentation hardware or signal transmission wires. Although wireless signal transmission is an extremely difficult design criteria to implement for the targeted HTGR thermal hydraulic test facility environment, it would fundamentally improve the applicability of the instrument for pebble bed HTGR configurations. In addition, the low power requirements and sensor density are both favorable characteristics for implementation of wireless signal transmission. In recognition that wireless communication is well outside the scope of this development project, a compromise is found in selecting a form factor that could be appropriate for coupling with a wireless signal transmission system at a later time.

Utilizing the favorable economics of mass production for MEMS fabrication, instrumentation packages could be fabricated into a surface mounted package that could be widely deployed during fuel assembly manufacturing. If multiple uniform thin-film RTDs can be integrated into a single instrument package, interdependent functional parameters can be utilized which could help to mitigate the effects of harsh environment calibration drift and other adverse signal distortion effects.

With all of these considerations in mind, it is obvious that the MEMS class of instrument hardware presents a number of favorable characteristics which are well aligned with the deployment and operation targets for development of a specialized thermal instrumentation package for HTGR core environments. Additional considerations regarding MEMS fabrication and instrument development are explored in later chapters of this investigation.

1.4 Research Program Purpose and Applicability

The purpose of this work is to present a proof-of-concept design and theoretical confirmation of applicability for a novel micro-electro-mechanical-system (MEMS) based instrument system capable of capturing local scale thermal parameters useful for simulation validation of HTGR heat transfer phenomena. The development of the presented design addresses noted data gaps for validation of modern simulation codes by determining the most applicable measurement technique and required sensitivity to capture specific heat

transfer phenomena in HTGR core environments. Examination of numerical simulation results in literature for the phenomena in question determines optimized design parameters for the proposed device. The device performance and durability will be simulated in an environment similar to expected HTGR core thermal conditions to demonstrate the measurement technique, and characterize limitations and deterioration mechanisms. Final results will determine the applicability of the device for collection of experimental data in specialized HTGR thermal hydraulic test facility environments.

This research is applicable because it addresses high probability accident scenarios which have little validation data using a novel instrument design specifically developed for the high temperature environment found in a HTGR core. This research identifies an approach to high temperature metrology that enables expanded applicability of resistive temperature sensors to high temperature environments. Commercial facilities outside of the nuclear sector would also benefit from the development of high-temperature sensor arrays and additional applications for the techniques developed as a part of this research initiative are identified in the final chapter of this report.

HTGR core geometry is primarily defined by the choice of prismatic block or pebble bed configurations. It is assumed that a focus on only one of the two options would be suitable for the scope of the research. The pebble bed core geometry presents a significant number of challenges in addition to those presented by the prismatic block core geometry; thus, developing an instrument that is suitable for pebble bed geometry would likely also be suitable for prismatic block geometry. The purpose indicates a motivation to develop instruments for collection of validation data, requiring that the pebble bed geometry be chosen as a design basis so that the results may be widely applicable to all HTGR designs and thermal environments.

Design targets and environmental analysis will assume a deployment form which utilizes a surface mounted thin film RTD array on an unfueled graphite fuel pebble which utilizes wireless signal transfer in an operational HTGR environment. Although the practical

deployment is likely to be as a wired instrument in a thermal hydraulic testing facility. By targeting the expanded functional capability when possible, the extension of the presented instrumentation toward that expanded use case should be relatively straightforward. To support this approach, operational data from a selected HTGR environment is utilized to develop target operational parameters for the proposed instrumentation.

1.5 Objectives of the Research Program

The objectives of this research proposal are derived from the overarching goal of developing a novel instrument capable of operation in HTGR core thermal environments. Objectives are listed here as discrete benchmarks for progress toward the development and simulation of a prototypical instrument system and are organized in accordance with the overall document organization.

1.5.1 Thermal Hydraulic Analysis Objectives

- Identification of key validation data gaps for pebble bed thermal hydraulic safety analysis methods that would benefit from development of specialized instrumentation.
- Develop environmental parameters describing the expected operating environment for sensors and transmission equipment.

1.5.2 MEMS Sensor Design Objectives

- Review of MEMS sensor design strategy for thermal sensors in harsh environments.
- Review of MEMS materials interactions for operation in harsh environments.
- Selection of basic sensor type and development of functional sensor design.
- Development of instrument fabrication and calibration sequence.
- Proposal of complete instrument design, including identification of final design parameters that can be used to simulate instrument performance and determine overall applicability of the proposed metrology strategy.

1.5.3 Simulation and Functional Applicability Evaluation Objectives

- Identification of key performance indicators for device operation to determine the effectiveness and applicability of the proposed sensor.
- Development of a simulation framework for characterizing device performance.
- Theoretical confirmation of applicability for a prototypical sensor design as a proof-of-concept for the instrument function and metrology strategy.

1.5.4 Overall Project Objectives

- Development of an instrument design which is capable of accurate collection of the target measurements over long operating periods in the specified environment and leverages the advantages of the MEMS design philosophy.
- Identification of overall performance and applicability to the intended measurement function for existing HTGR testing facilities (HTR-PM thermal environment).

1.6 Instrument Development Assumptions and Simplifications

A number of assumptions and simplifications must be made to facilitate economical and efficient development of the proposed instrumentation given the resources available. These assumptions create the boundary to the solution space explored in this research project and provide guidance regarding practical limits for digression from the primary project goals. Assumptions are separated into several groups, each pertaining to specific portions of the proposed development plan.

1.6.1 HTGR Thermal Hydraulic and Structural Environmental Assumptions

- The thermal reactor environment is isolated, no nuclear interactions are considered, as the development assumes deployment in a high-fidelity testing facility for thermal hydraulic characterization rather than deployment in an operating commercial HTGR.
- The reactor gas coolant is comprised of pure helium without contaminants.
- No particles are entrained in the coolant flow, no effects of graphite dust or other potential contaminants in structural material are otherwise considered.

- The boundary conditions of the selected heat transfer volume are constant over time and spatial dimensions, steady state operation is assumed unless stated otherwise.
- Reference material parameters provided by HTGR development authorities and fuel manufactures are accurate.
- The pebble bed fuel pebbles are essentially static, with insignificant dynamic loading.
- The fuel pebbles exhibit perfect packing structure with point contact and are not affected by boundary structures or other inconsistencies, such as broken pebbles.
- The fuel operates at a constant temperature and has no surface temperature gradient.
- The fuel surface does not have grain boundaries or directionally dependent properties.

1.6.2 MEMS Thermal Sensor Design Assumptions

- The sensor materials are a constant temperature and do not have internal temperature gradients or other asymmetrical boundary conditions unless specifically stated.
- The sensor materials have accurate material properties that are uniform and do not change over time or with increased thermal exposure, unless specifically stated.
- The sensor materials only consider radiation as a product of heat transfer.
- The sensor materials do not collect or diffuse electrical charge due to charged particle or electro-magnetic interactions, unless specifically stated.
- The sensor materials do not undergo geometric drift or diffuse into the substrate or the surrounding environment, unless specifically stated.
- The sensor material will not chemically corrode, oxidize, or otherwise undergo chemical transitions, unless specifically stated.
- The sensing material is electrically isolated from the substrate material and the substrate resistance is assumed to be constant over a wide temperature range.
- The sensor will have no significant impact on bulk fluid behavior in the local region around the fuel surface.
- The sensor will not be subject to mechanical stress from pebble contact regions and is mechanically isolated from material strain of the fuel pebble itself.

1.6.3 Other Instrument System Design Assumptions

- The sensor will utilize a six- or eight-conductor power and signal cable that is routed to an external electronics package for measurement.
- This signal cable and electronics package design and impact are outside the scope of this investigation and are assumed to be interchangeable with modular wireless signal transfer hardware for design purposes.
- The sensor will undergo thermal exposure equivalent to, at most, one trip through the reactor re-fueling system circuit before being replaced or re-calibrated.
- There are no bandwidth limits for collection or processing of measurement data.

1.7 Development Scope and Limitations

The scope of this work is limited to the development, simulation, and qualitative confirmation of applicability for a novel thermal sensor instrumentation package utilizing MEMS fabrication techniques and a novel algorithm for real-time instrument calibration correction. Simulation of the functional performance of the hardware in a representative environment provides data to characterize the relative accuracy and precision of the device compared to contemporary metrology, and is compared against manufacturer specifications for similar devices to serve as a basis for determination of conceptual design applicability for the target use case.

The simulation of device operation is meant to demonstrate the instrument sensitivity to heat transfer phenomena useful for thermal hydraulic safety analysis, to estimate the accuracy of the device in capturing these phenomena, and to determine if the proposed instrumentation system has operational advantages that meaningfully extend applicability beyond currently available instrumentation hardware. Although the general metrology strategy may be applicable for other advanced reactor environments, only heat transfer phenomena related to the pebble bed HTGR core design are considered, as this is the targeted thermal environment for deployment.

Limitations on the time and resources available for this project determined the depth and extent of simulation fidelity as well as the quality of the resulting evaluation of conceptual design applicability. Basic functional simulations have been performed; however, extensive characterization of secondary device performance, such as data transmission simulations, will not be conducted due to the additional resources required for development of a high-fidelity simulation framework. Instrument interfaces with data collection systems are defined in relatively basic terms and rely on external hardware to perform signal manipulation and derive thermal hydraulic performance metrics from the measured sensor resistance. Development of the data acquisition infrastructure surrounding the use of multiple devices is beyond the scope of this proposed project; however, multi-component calibration correlation has been analyzed for a multi-sensor array within a single device to demonstrate the key calibration drift mitigation capability of the concept.

1.8 Document Organization and Outline

This document is organized in chapters that chronologically follow the development of the aforementioned instrumentation system. Each phase of development has a distinct purpose which contributes to the overall investigation, and is described here for ease of navigation.

The first chapter has focused on introducing the concepts necessary to understand the environment which surrounds this development effort. The short background on HTGR design and the basic principles of thermal hydraulic safety analysis provides the reader with an understanding for the motivation and target environment of the research being described. A short description of MEMS-based instrumentation provides an understanding of the means by which the proposed challenges will be addressed and the basic form of the solution being developed. The remainder of the chapter focuses on the purpose, applicability, objectives, assumptions, scope, and limitations in explicit terms to identify the boundaries of the addressed endeavor and to allow the reader to clearly understand the motivations for the research presented herein.

The second chapter focuses on summarizing foundational work related to the research project and collecting information from literature concerning the current state of reactor thermal metrology development. This includes an investigation into thermal hydraulic analysis for HTGR systems and the metrology challenges presented by the pebble bed core configuration. An overview of relevant reactor components and basic safety analysis methodology provide a foundation for further investigation of a selected reference design, from which system parameters are derived as a basis for instrument design in later chapters. High temperature instrumentation systems from modern testing facilities and reactors are investigated to provide context for determination of the threshold for novelty for proposed thermal instrumentation. Investigation into different types of contemporary thermal instrumentation informs the decision to select the RTD thermal sensor class as the design basis for further development. Key challenges for RTD deployment in high temperature environments are identified and characterized. Finally, investigation into high temperature applications of MEMS-type instrumentation systems, including their materials and applicable fabrication methods, provides a contextual roadmap for further development of a novel thermal sensor array for HTGR environments.

The third chapter focuses on deriving parameters used for the characterization of pebble bed core heat transfer and extrapolating that analysis to develop target sensor design and simulation parameters. The expected heat transfer parameters for a selected reference reactor design, the HTR-PM, are derived from the reference material provided by reactor developers and primary researchers. In order to evaluate how well a given sensor will operate in the target environment, an analytical model is developed from these derived parameters which characterizes the thermal exposure which occurs in the sensor environment. Assumptions and simplifications must be made to allow for practical analysis and are determined by investigating the characteristics of the pebble bed heat transfer phenomena that are targeted for safety analysis. Finally, a determination of a range for environmental variation according to the most accurate environmental operational data found in literature is used to derive a spatial thermal exposure model, which is used in later chapters as a basis for confirmation of conceptual design applicability.

The fourth chapter focuses on MEMS-based thermal sensor array development using the environmental operating parameters determined in the previous chapter, and the steps that are required to fabricate the proposed instrument package. Techniques for correction of calibration drift due to thermal exposure are explored and a novel resistance correction algorithm based on differential thermal expansion of a reference material is described. Various designs of MEMS RTD thermal sensors and configurations for sensor arrays are derived and evaluated for performance when utilizing the described correction algorithm. A final sensor geometry, material composition, and array configuration is selected for further development and optimization. Fabrication strategies are selected based on the geometry and materials selected. A fabrication sequence which utilizes the scaling efficiency of MEMS manufacturing techniques is described.

The fifth chapter focuses on development of a simulation framework for instrument performance analysis. The instrument parameters derived in the previous chapter are extended to evaluate instrument response for an arbitrary thermal exposure profile. The mechanisms contributing to instrument calibration drift driven by thermal exposure are evaluated and a model for expected calibration drift is developed. The performance of the calibration correction algorithm is simulated using these models and a summary of performance data is presented for the test environment and expected instrument parameters described in the previous chapter.

The sixth chapter focuses on confirmation or demonstration of the applicability of the proposed sensor for HTGR thermal environments. This is accomplished by evaluating the effectiveness of the underlying calibration correction algorithm while simulating the operation of the sensor for varying thermal exposures expected for different initial locations of deployment in the HTR-PM. The metrology package is evaluated against contemporary hardware to determine the effectiveness of the sensor and if any benefits are immediately apparent which warrant further sensor development and investigation. Estimations of error bounds are developed and used as a key comparison point for sensor

applicability as it pertains to the targeted use case; collection of experimental thermal hydraulic validation data.

The seventh and final chapter focuses on conclusions drawn from the research project, a finalized instrument package design summary, a description of the overall expected performance of the device when compared against contemporary thermal instrumentation systems, and suggestions for further development. Future work is described which would further the development of the underlying novel metrology principle presented and motivate the allocation of the resources required to progress from theoretical development to prototypical deployment.

The remainder of the document includes the bibliography and engineering drawings for the proposed sensor, collected to form the appendix.

2 Survey of Literature and Selecting a Basis for Development

The survey of literature presented in this chapter will serve as a reference and basis for the remainder of the document and will provide a central location for all referenced parameters found in literature which compose the foundation of design efforts found in later chapters. A summary of design and operation parameters for the selected HTR-PM reference plant and relevant advancements in the field of HTGR instrumentation, high-temperature MEMS, passive remote sensing, and other associated technologies will also be presented to provide context for the work described in later chapters and highlight the novel aspects of the work being presented.

To properly develop a technical foundation and justify motivation for the proposed subject of study, a brief summary of modern thermal hydraulic safety analysis for HTGR systems is presented. A developmental design basis is established by identification of thermal hydraulic parameters for a reference HTGR system and development targets are established by evaluating gaps in current instrumentation technology related to this reference environment. An investigation and review of applicable modern sensor hardware provides context concerning the form and function of the proposed instrumentation and highlight the ways in which this work seeks to improve upon current technology for HTGR applications. Thin film or MEMS fabrication techniques and applicable materials which could be used to fabricate the proposed sensor hardware are reviewed to provide context and key parameters for reference in instrument design work presented in later chapters. Signal transmission mechanisms are briefly evaluated for applicability to the proposed hardware and environment and example applications to similar instrumentation systems are be explored to identify useful approaches for the proposed instrumentation system design.

At the end of this chapter, a basis for further development is selected as an RTD sensor array and specific implementation challenges are identified, which are then mitigated or contained by measures described in later chapters.

2.1 HTGR Pebble Bed Reference Design: HTR-PM

The choice of coolant is a parameter which significantly affects the applicability, safety, efficiency, and difficulty of development for a given nuclear reactor design. Although the water-cooled reactor is by far the most common reactor in use today, many alternatives exist which provide significant improvement to thermal hydraulic characteristics. Liquid metal and liquid salt coolants, for example, offer the potential for extremely high power densities and for the utilization of a fast neutron spectrum. Reactors utilizing these types of coolant can operate at atmospheric pressure and do not require massive containment structures to maintain a pressure boundary. However, this coolant creates difficulty in controlling corrosion of exposed surfaces. Gas coolants are another alternative and are used primarily in two capacities, depending on the goals of the application. Supercritical gas coolants provide favorable heat transfer parameters and high thermal efficiencies, but again may create difficulties with controlling corrosion. Inert gas coolants, such as helium, will not produce corrosion products on exposed surfaces, have a single-phase thermal cycle which greatly simplifies design and simulation requirements, and most importantly, allow for extremely high temperature operation [33].

This final advantage, the ability to operate at extremely high temperatures, is a profound extension of capability for these reactor designs. This allows for a huge expansion in applicability for these systems as co-generation plants and as industrial heat sources. The ability to withstand extreme temperatures in the core region also allows for a unique approach to reactor safety. A passive, design-driven approach is utilized, which allows the reactor to cool using free convection and radiative heat transfer without danger of damage to the barriers which prevent the releasee of radioactive materials [34]. The high-temperature gas-cooled reactor leverages a design which utilizes an inert, single-phase coolant to provide a thermal production system which has significant operational and safety advantages over reactors which utilize other coolant types. This is one of the reasons that the HTGR was chosen as the design basis for the NGNP [35], and is also the reason that development of advanced instrumentation platforms is so vital. Durable, accident tolerant

instrumentation systems must be developed so that safe and efficient deployment of HTGR-based plants can become a realizable goal in the United States and elsewhere.

The task of designing a sensor specifically suited to an HTGR core environment starts with the characterization of the thermal hydraulic parameters which define the normal and limiting operations of this type of reactor. This will allow the sensor design process to target specific heat transfer mechanisms for measurement, ensuring the efficiency and applicability of the proposed devices for the collection of vital validation measurements. The role of experimental validation and the underlying motivation for the collection of experimental data will be explored in the next sections to provide context for the motivation driving advanced instrumentation research; and to aid in the derivation of targeted performance goals, or figures of merit, which will determine the final capability of the proposed instrumentation in accomplishing the intended validation and safety monitoring functions.

To investigate thermal hydraulic processes in pebble bed flow, it is convenient to select a single reactor design so that physical parameters can be determined and the problem can be bounded by a well-defined hardware configuration. Due to the large number of variations which exist on the fundamental HTGR plant design, a number of legitimate choices exist with a range of development progress and technical challenges. A well-established, technically mature design would be preferred, as it would likely be similar to the HTGR design that is ultimately selected for deployment in the near future. The selected design branch should be highly developed and have a prototype plant or testing facility in operation if possible so that physical properties are established and operation data is available. Analysis of the prototype plants can allow for the determination of ideal heat transfer parameters for measurement and the required instrument sensitivity required for the relative scale of the physical properties which are to be measured. Developing a device with specific heat transfer parameters as a target measurement task simplifies design optimization and allows for a custom application of design principles to the selected

environment. This ensures the developed device is useful for collection of target measurement data concerning spatial scale and deployment configuration.

Because only a small number of pebble bed reactors have been constructed, the list is immediately reduced to four primary candidates; the AVR, the THTR-300, the PBMR, and the HTR-PM. Of these, only the HTR-PM prototype plant is in operation and under active testing, thus the selection of the High Temperature Gas-Cooled Reactor – Pebble Bed Module (HTR-PM) as the design basis for analysis is the most logical choice. The next section provides context for evaluating the maturity of the design with a short summary of development history and design philosophy utilized for the HTR-PM and lists useful thermal hydraulic parameters related to thermal transfer in the core region. These parameters are taken from design studies and initial testing data provided by the reactor operator. In some cases, this data has not yet been made available in literature. Although the presented instrument design study is developed with application to the HTR-PM in mind, it should be noted that operational data from the predecessor plant from which the HTR-PM is fundamentally derived, the HTR-10, is widely available and may serve to provide guidance in areas where HTR-PM data has yet to be published.

2.1.1 HTR-PM Development and System Design Overview

Currently, China is heavily involved in the development of pebble bed gas reactor designs and is the host of two facilities which will serve as a design basis for sensor development. These facilities are the HTR-10 and the HTR-PM, located at Tsinghua University and the Shidao Bay Nuclear Power Plant respectively. The HTR-10 was constructed first, as a technology demonstration plant and a testing bed for fuel development efforts. Based on the technical success of this plant, the HTR-PM was developed as a step toward expansion of the experimental program to commercial-scale power generation. As of the publication of this study, this reactor is currently under construction and will feature two 250 MW_{th} reactor modules coupled to a shared steam turbine generator module.

The HTR-10 or HTR-PM present a unique opportunity for research, as they are currently the only operating pebble bed nuclear plants in the world. Foreign research initiatives are strongly supported by the primary developer and a great emphasis is placed on multi-national research efforts. The initial success of the HTR-10 created a need for the creation of domestic fuel fabrication capability, the primary result being the expansion and development of fuel fabrication processes at the Chinese Institute of Nuclear Energy Technology (INET). INET initially supported the fabrication and testing of pebble bed fuel for the South African PBMR and was the primary industrial supporter of HTR-10 and HTR-PM development and operation [36].

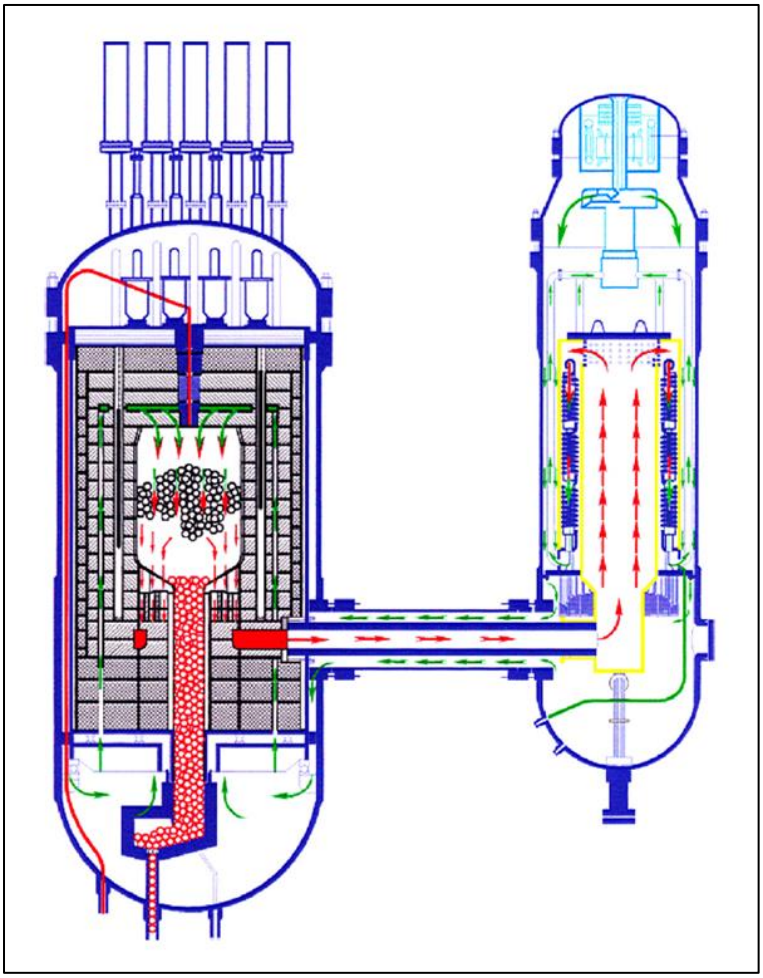

Figure 2-1: The High Temperature Reactor – 10 MW_{th} (HTR-10) [37]

Figure 2-1 depicts the HTR-10 plant layout, with two pressure vessels connected via a concentric primary coolant duct. The pebble bed power module, located on the left, contains the reactor core, graphite reflectors, control rod mechanisms, and pebble recirculation hardware. The steam generator module, located on the right, houses the coolant circulator and the heat exchanger.

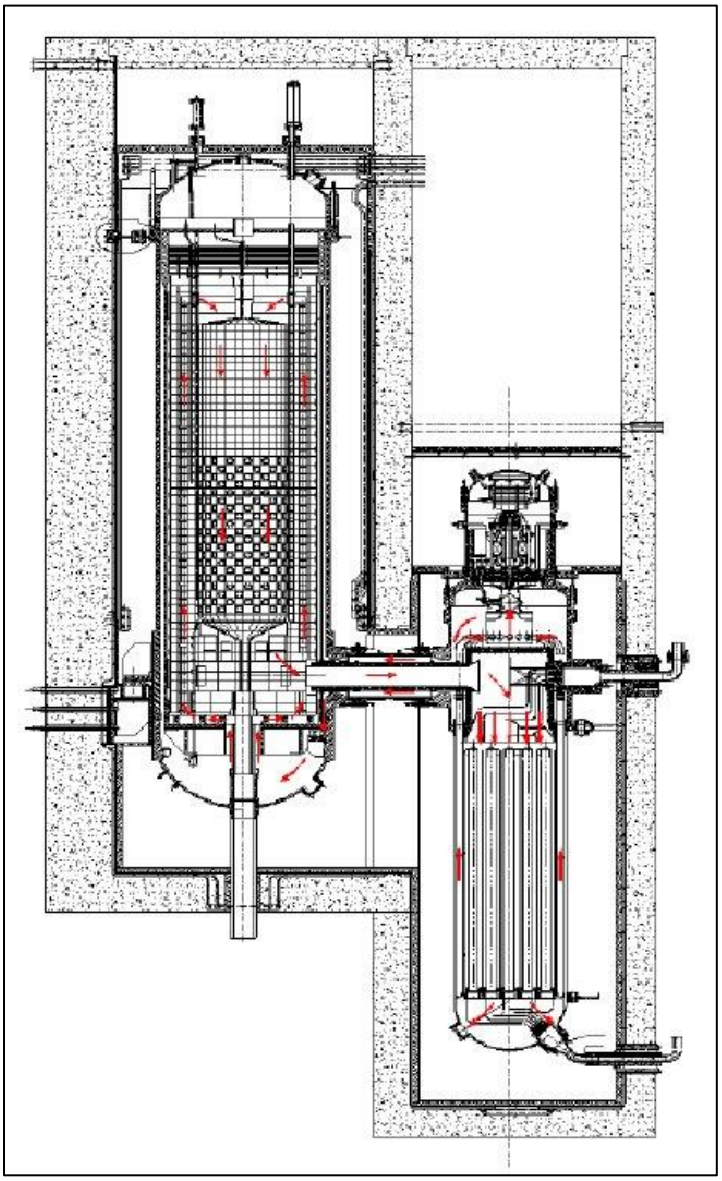

Figure 2-2: The High Temperature Reactor – Pebble Bed Module (HTR-PM) [37]

The final HTR-PM design, depicted in Figure 2-2, has many similar design features to the HTR-10. The plant still incorporates the same modular, side-by-side design philosophy used by the MHTGR, with the concentric duct serving as a connection between the primary reactor pressure vessel (RPV) and the steam generator pressure vessel. The most apparent difference between the two designs is the lowering of the steam generator module with respect to the RPV. This change promotes isolation of the natural circulation cooling loop and supports design criteria for passive cooling in accident scenarios [38]. The primary circulator is still located in the upper portion of the steam generator vessel and drives the coolant flow during normal operation. The flow direction through the steam generator is reversed with respect to the HTR-10, but internal routing of the flow path ensures that the coolant still passes through the heat exchanger first prevent thermal stress on the primary circulator components.

The HTR-PM core inlet temperature is estimated to be approximately 250 °C, with an estimated mixed outlet temperature of approximately 750 °C. The design utilizes a secondary coolant loop; thus, the thermal hydraulic cycle is a Rankine cycle as opposed to a direct Brayton cycle; which allows for some comparisons to be made with common LWR reactor designs. The reactor pressure vessel contains the pebble bed core surrounded by a carbon reflector containing control rod channels and a ceramic support structure with borings for the helium return flow. All of this is contained inside a metallic core barrel which is supported by the RPV. The fueled core is a simple cylinder, as opposed to the annular configuration utilized by some pebble bed configurations.

The design philosophy utilized in the development of the HTR-PM is similar to that which was fundamental to the MHTGR development effort, but expanded with a further focus on reducing the initial and operational costs to increase the attractiveness of the plant design to various consumer markets. The primary philosophical design concerns for the HTR-PM were for safety, design standardization, economic construction and operation, and utilization of existing proven technology. This approach is fundamentally driven by the

need for efficient and low-cost power production plants in China as economic development continues to drive electricity demand at an ever-increasing rate [39].

The inherent safety of the MHTGR and thus the HTR-PM is a result of the fuel and core design. The fuel is extremely accident tolerant and when coupled with the passive thermal transport mechanisms achieved by the core and vessel design, allows the plant to passively transition from operational conditions to safe shutdown conditions with minimal operator intervention. Standardization of the various modules utilized in the HTR-PM plant design means that the construction, verification, and integration can be done at a greatly reduced cost when compared to the high costs incurred by specialized plant designs. The design was developed to be economically competitive with traditional PWR plant designs, a feature that should increase the quantity of plant installations and thus re-enforce the cost saving mechanisms of standardization. A focus on utilization of existing technology for the gas turbine, instrumentation, and heat removal systems would further reduce costs associated with application of emerging technology and provide further support of economic goals. A large portion of the hardware designated for use in the HTR-PM plant design was initially tested and validated through use in the HTR-10 plant [40].

Development efforts for the HTR-PM began in 2001, following the initial success of the HTR-10 demonstration plant. Researchers were motivated by their previous success and the need for further research into gas turbine and process heat application technologies. Development efforts also focused on creating a plant design that was an economical alternative to traditional electrical power and process heat generation technology, hence the motivation for a modular design where multiple reactors to be coupled to one secondary electrical generation system and the emphasis on passive or ‘inherent’ safety systems which would mitigate the additional cost of auxiliary or redundant heat removal systems not used in normal operation of the plant. It was thought that the overall nuclear efficiency of HTGRs would be greater than for traditional LWRs as well, meaning electricity could be generated at a lower overall cost when compared to existing nuclear plants [36].

Around 2004, an initial conceptual design was relatively mature and ready to proceed to initial feasibility evaluation phases. The authors of the design suggested that the construction phase would be completed around 2010. The initial design featured an annular core configuration, where fueled pebbles surrounded a central reflector region comprised of non-fueled graphite pebbles or solid graphite blocks and was scaled to approximately 450 MW_{th}. These design parameters are coupled in that the annular core design allows for a higher thermal power rating due to reduction of peak fuel temperature for some accident conditions. Both of these design parameters were later adjusted, resulting in the removal of the central reflector region and lowering of the thermal power rating to 250 MW_{th} to reduce development costs [40].

An updated design summary was released in 2006, which stated that design development work was nearly complete and would be finalized that year. The report pushed back the construction completion date to 2012. A significant change in strategy for project funding was described. The project would rely on utility company investment for all costs outside the scope of technology development. This was attributed to a motivation to drive the design toward feasible adoption, but it did introduce financial uncertainty to the project that would result in additional project delays in the future, specifically the delays following the global economic slow-down in 2008 [39].

The final design for the HTR-PM was completed in 2009 and included major revisions such as the change of scaling to 250 MW_{th} per module and the abandonment of the annular core concept. The Preliminary Safety Analysis Report (PSAR) was also completed at this time, locking in the design specifications as the project proceeded to initial component manufacturing and site preparation phases. The construction completion date was pushed back to 2013, though this was extremely optimistic considering that fuel fabrication infrastructure was still relatively undeveloped. To meet the overall technology development roadmap goals, it was suggested that up to 18 power modules would be constructed simultaneously, however this plan has not been realized and only the initial demonstration plant is currently being constructed as of the most recent project planning

update (2009) [37]. Future plans for incremental power increases are mostly focused on adding additional modules onto a shared steam turbine. The next phase of demonstration plant is expected to have six power modules, initially called the HTR-PB 600.

Updates following the 2009 final design specification have mostly been concerned with analysis for the initial testing program and ramp-up of reactor operation as well as updates on construction progress. A comprehensive reactor physics assessment was released in 2013 and is reviewed in later sections [41]. An overview of the fuel manufacturing process was published by INET in 2013 and serves as a primary reference for fuel pebble parameters in later sections [42]. Additional research efforts around the helium sampling systems was detailed in a 2016 report [43], which is the same year that both reactor pressure vessels were installed into the containment building. In April of 2017, the first un-fueled graphite moderator spheres were loaded into the reactor core. In July of 2017, the thermal hydraulic parameters of the steam generator were tested and validated [44]. In 2018, a full scale mock-up of the helium circulator finished endurance testing and the resulting publication provides detailed thermal hydraulic parameters for later sections [45].

Fuel irradiation qualification was also completed in 2018, utilizing a high-flux test reactor. The parameters developed in the report are useful for determining the surface material transitions expected on the fuel pebbles as they undergo irradiation and again, the information is used in later sections of this report [46]. Reactor safety analysis specifically focused on the HTR-PM thermal hydraulic systems was summarized in updated Phenomena Identification and Ranking Tables (PIRT), which expands on initial analysis performed by the NRC for the MHTGR plant and shapes the goals of initial system testing and targeted safety system development [47]. This information shapes the analysis presented in the thermal hydraulic safety analysis section.

As described, the most recent construction updates indicate that the HTR-PM is nearing the point of being ready to be loaded with fuel pebbles and undergoing initial testing. The completion of the demonstration plant may still be many years in the future, but it is clear

that progress continues given the updates from 2016, 2017, and 2018. It is assumed that once first criticality is accomplished, the project can be considered a success and more detailed operation parameters will be published.

2.1.2 HTR-PM Reactor Core Design Overview

The High Temperature Gas Reactor is a type of reactor that differs significantly in form and function from common water-cooled reactors; and therefore, demands a different strategy for development. The design motivations differ to the extent that HTGR design philosophy focuses on the leveraging of material and coolant properties to develop an inherently safe, high-temperature thermal generation system that is widely applicable to industrial process needs and capable of a thermal efficiency greater than any commercially deployed reactor concept today, due to the high outlet temperature of the coolant.

As previously described, HTGR-based designs typically utilize helium as a primary coolant and graphite as a neutron moderator. Single phase, non-reactive coolant and core structures composed of extremely temperature-tolerant materials allow some variations of this reactor design to produce an outlet coolant temperature of up to 950 °C [10]. The higher outlet temperature increases the efficiency of the power conversion system by allowing for greater energy transport flux and an increased utilization rate when compared to reactors operating at lower temperatures, which typically utilize two-phase coolants. Attaining an increased outlet temperature also enables the reactor to be used as a generator of process heat for a number of unique industrial applications, including hydrogen production, coal gasification, fertilizer production, and seawater desalination; among other industrial manufacturing processes.

A number of design strategies are used to attain increased operating temperatures; as previously stated, HTGR designs utilize high-temperature materials for core structure and fuel cladding. Materials with stable chemical structures tend to be very resistant to high-temperature corrosion. Carbon is a great high-temperature material due to its affinity for strong, stable chemical bonds and gaseous phase change on oxidation. HTGRs utilize

different forms of carbon-based materials for specific applications. Graphite is a form of pure carbon and serves as a fundamental material for the primary core structure and neutron moderator in HTGRs, while fuel is typically contained in small, multi-layered, silicon carbide particles designed to prevent the release of radioactive material. These materials are configured in the core region according to one of the two distinct design strategies currently being developed, the prismatic block or pebble bed. Detailed discussion of the prismatic block core geometry is outside the scope of this research endeavor, but detailed discussion of the pebble bed geometry and associated hardware forms the foundation of instrumentation design efforts.

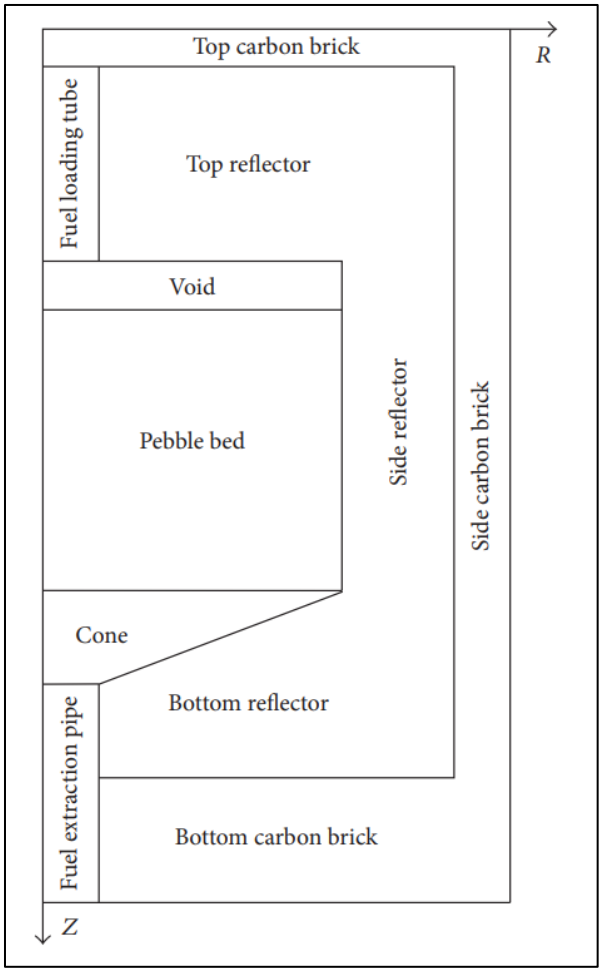

Figure 2-3: Radial diagram depicting the layout of the core structure for the HTR-PM [48]

Pebble bed HTGR cores vary between specific designs, but all designs have a number of common primary components which are functionally similar. In this section, the specific components designed for use in the HTR-PM will be reviewed. These components include the previously mentioned fuel pebbles, along with radial reflectors, axial reflectors, inlet and outlet plenums, control rod hardware, and fuel recirculation hardware. In the following sections particular attention is devoted to the structure and fabrication of the fuel pebbles, which comprise the bulk of the core region. These pebbles pose unique functional advantages, such as enabling online refueling and extremely high tolerance for structural, thermal, and neutronic variability in the core region, which are balanced by the unique challenges, specifically for instrumentation, presented by the dynamic, unconstrained movement of the pebble bed.

2.1.2.1 Fuel Pebble Design Overview

Arguably the most important component of a pebble bed reactor core is the fuel pebbles themselves. These fuel pebbles are sometimes called spherical fuel elements (SFEs) and are typically composed of TRISO fuel grains suspended in a porous pyrolytic graphite matrix, which is then encased in a durable sintered graphite shell [42]. The fuel grains are randomly distributed in the graphite substrate, but have a well-defined, homogeneous density so that they will create precise conditions for fission when many of these pebbles are collected in a large volume. The amount of fissile material must be enough to achieve critical operation, but not so dense that the reaction can't be controlled or the thermal energy can't be transported out of the core. Thus, there exists a careful balance between the surface area of the pebble and the volume of fuel contained inside, as well as between the thermal and chemical properties of the materials used.

Fuel pebble manufacturing was initially developed to fabricate SFEs for the German AVR and THTR facilities. Modern manufacturing techniques have been developed by INET, which fabricated the FSEs used in the HTR-10 reactor and will fabricate the FSEs used in the HTR-PM reactor as well. Most of the parameters used in this study are taken from

various INET publications over the last several years as they have qualified and scaled their manufacturing process to meet the demands of new pebble bed reactor construction.

The fuel pebbles used in the HTR-PM are spherical and comprised of a multi-layer graphite composite with embedded TRISO fuel particles. The fueled region of the pebble is 50 mm in diameter and composed of approximately 12,000 individual fuel particles. This region is surrounded by a 5mm thick fuel-free protective shell, producing a pebble with an overall diameter of 60 mm and a maximum operating temperature of 1,620 °C.

Table 2-1: HTR-PM Fuel Pebble Design Parameters and Initial Testing Results [42]

Parameter	**Unit**	**Specification**	**Mean Value**
Density	g/cm^3	1.70 to 1.77	1.72
Thermal conductivity (1000 °C)	$W/(m\ K)$	≥ 25.0	32.4
Corrosion rate	$mg/(cm^2\ h)$	≤ 1.3	0.79
Erosion rate	mg/h	≤ 6.0	1.55
Number of drops		≥ 50	50
Crushing strength	kN	≥ 18.0	23.7
CTE anisotropy (20-500 °C)	$\alpha_{\perp}/\alpha_{\parallel}$	≤ 1.3	1.15
Diameter	mm	59.6 to 60.2	59.9
Thickness of fuel-free shell	mm	≥ 4.0	5.0
Uranium loading	g/SFE	7.00 ± 0.35	6.95
Free uranium fraction	U_{free}/U_{total}	$\leq 6.0 \times 10^{-5}$	8.7×10^{-5}

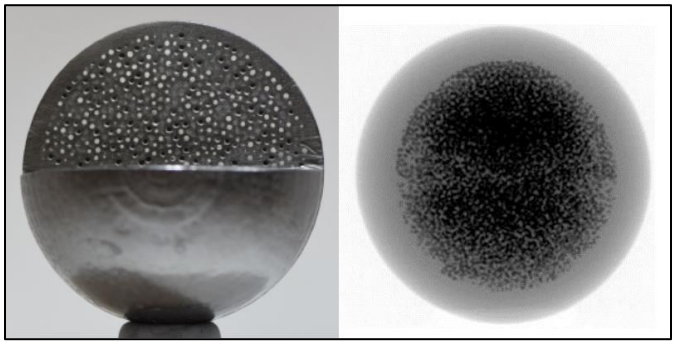

Figure 2-4: Cut-away and X-ray tomography images of an SFE [42]

As mentioned in the introductory chapter, the ideal deployment location for a specialized thermal instrumentation package would be at the coolant interface of the fuel. For pebble bed HTGRs, that would be on the outer surface of a fuel pebble. Due to the proposed use case for instrument deployment being an HTGR thermal hydraulic testing facility, the assumed instrument mounting location is on an unfueled pebble with identical dimensions to the fueled pebble utilized in the HTR-PM.

2.1.2.2 Central Reflector and Core Geometry

Initial design proposals for the HTR-PM included a central reflector composed of un-fueled pebbles or graphite blocks. The central unfueled region results in an annular fuel configuration in the reactor core. An annular fuel configuration allows for a higher core thermal power compared to a cylindrical configuration because it flattens the radial temperature profile and distributes the thermal loading across a larger area further from the center of the core. The proposal for the use of graphite blocks for this central unfueled region was abandoned because of the extremely high cost associated with replacement of the blocks at some point during the lifetime of the reactor, which was deemed necessary due to structural changes which occur in graphite materials at high levels of neutron fluence.

The approach of utilizing unfueled pebbles as a central reflector region was also considered and later abandoned due to technical challenges, which included maintaining the boundary of the unfueled pebble region as pebbles traversed the core and promoting coolant mixing between the fueled and un-fueled regions. The final design for the HTR-PM does not utilize a central reflector; thus, the maximum core thermal power rating had to be lowered. The possibility of increasing the core power by implementing an annular fuel configuration reinforces the motivations for developing thermal instrumentation which is capable of monitoring the temperature of the central core region and could serve to verify the central unfueled pebble migration boundary as the pebbles move through the fuel recirculation cycle.

2.1.2.3 Fuel Pebble Recirculation Mechanisms

The last general component of interest is the means of fuel pebble recirculation, which is a defining feature of the pebble bed design. This hardware is worth investigating for instrumentation development because it would be the primary means of retrieving a wireless variation of instrumented pebbles deployed in the core for calibration or analysis. The pebble recirculation hardware facilitates the removal of fuel pebbles from the bottom of the core region, inspection of the fuel pebbles, transport of the fuel pebbles to the top of the facility, and insertion of fuel pebbles at the top of the core region. This process is meant to enable on-line refueling and continuous re-circulation of pebbles to ensure relatively uniform fuel burn-up.

The hardware which comprises these systems does vary widely between pebble bed designs, but most designs include a 30- to 60-degree funnel at the bottom of the reactor core. This funnel routes the fuel pebbles through an inspection module and then utilizes a pneumatic transport system to return to the pebbles to a distribution system at the top of the core. Several different types of pebble distribution systems have been considered for installation in the HTR-PM. These systems range from a simple tube which drops returned pebbles in a mound at the center of the upper surface of the pebble bed, to more complex systems which distribute the pebbles in concentric rings or a symmetric star pattern to ensure even radial distribution. If an unfueled central region of pebbles is required to implement an annular fuel loading strategy, this would primarily be accomplished by precise control of placement for fueled and unfueled pebbles upon return to the core volume via the recirculation system.

Pebbles are expected to traverse the core region an average of six times before being removed and may make up to fifteen trips through the core before they reach the maximum burn-up level. It is expected that any wireless variation of instrumented pebbles would only make a single pass through the reactor before being replaced. The exact hardware used for pebble inspection and re-circulation has not yet been published for the HTR-PM, but it can be assumed that a system similar to that which was used on the HTR-10 will be

utilized, which was comprised of a centrally located outlet tube, creating a pebble mound on the upper surface of the pebble bed.

2.1.3 HTR-PM Thermal Hydraulic System Design Parameters

Thermal hydraulic parameters such as the peak core temperature, core inlet and outlet temperature, pebble surface temperature, and peak coolant temperature provide bounding thermal limits for device development and are the key constraints for the sensor design study and confirmation of applicability presented in later chapters. Design decisions such as materials selection must utilize these parameters to determine the maximum level of allowable corrosion and material degradation while allowing for consistently accurate measurements. Taking this approach allows for device design to have a basis in ensuring dependable accurate device operation in the expected conditions.

Table 2-2: HTR-PM System Design Parameters [37]

Parameter	Unit	Value
Total thermal power	MW_{th}	2×250
Total electrical power	MW_e	210
Active core diameter	m	3.0
Equivalent active core height	m	11.0
Average / max core power density	MW_{th}/m^3	3.22 / 6.57
Enrichment of fresh fuel spheres	%	8.9
Average enrichment of fuel spheres	%	4.58%
Number of fuel spheres in reactor core		420,000
Average discharge burn-up	GW_d/tU	90.0
Average power density	MW/m^3	3.22
Primary coolant pressure	MPa	7.0
Outlet mixed coolant temperature	°C	750
Inlet mixed coolant temperature	°C	250
Core coolant flow rate	kg/s	172
Maximum operating fuel temperature	°C	932
Maximum accident fuel temperature	°C	1470

Investigation of design documents for the HTR-PM indicates the thermal hydraulic parameters found in Table 2-2 were defined as the target performance indicators for the HTR-PM prior to construction. The parameters presented in Table 2-2 represent core averaged values in some cases. It should be noted that pebble beds exhibit variable packing structure at core boundaries, which creates thermal hydraulic conditions which vary significantly from the conditions found in the central region of the core, where a consistent packing structure is assumed. Thus, these parameters are useful as a starting point and as bounding conditions for material selection and initial instrument design, but the more detailed analysis presented in Chapter 3 provides a more refined estimation of the spatial distribution of these parameters.

2.2 HTGR Thermal Hydraulic Safety Analysis

Thermal hydraulic safety analysis is both the foundation and a primary motivator for advanced reactor design due to the inherent societal impact of widespread radiological contamination. All measures to confine and control the radiological material that is used and created in the reactor core are dependent upon mechanical resilience of materials utilized in construction of the implemented hardware, and the performance of that hardware in the harsh conditions of the surrounding environment. Although radiation fluence can significantly change the mechanical properties of a given material through nuclear and chemical corrosion, it is the effects of thermal stress that are far more likely to preclude catastrophic failure of containment systems. Thus, a robust validation of implemented containment measures is dependent upon thermal hydraulic safety analysis, which is comprised of a coupled system of predictive analysis and experimental validation. It is the experimental validation component of this system that could be improved with development and deployment of specialized instrumentation.

In this section, industry-standard practices for safety analysis methods are reviewed and targeted studies found in literature are explored to provide the context of experimental validation goals and limitations, as they apply to the HTGR class of reactors. The

relationship between simulation and validation is then evaluated and clearly defined. Finally, modern experimental thermal hydraulic research is reviewed and future needs for experimental validation is identified to provide guidance for creating the development roadmap of the proposed instrumentation.

2.2.1 Modern Safety Analysis Philosophy and Methodology

Thermal hydraulic safety analysis is primarily defined by a sequence of predictive analytical evaluations that can be simplified into three steps; identification, prediction, and verification. This process begins with identification and ranking of accident outcomes according to overall risk, which is evaluated by estimation of the magnitude of impact on public wellbeing and probability of occurrence. These two factors are combined to produce an estimation of risk for each given accident. The accident scenarios with the highest risk estimate are labeled design basis accidents, as they are the primary consideration for reactor design. These design basis accidents are used to identify boundary conditions for numerical simulation of reactor operation and accident mitigation performance. By simulating design basis accident transients, operational limits can be developed for various mitigation systems which are designed to prevent the occurrence of an accident transient. These mitigation systems function by controlling the flow of energy from the nuclear fuel and dissipating it in a way that doesn't exceed the developed operational limits for the constituent components. Thus, accurate simulation of energy transfer mechanisms within the reactor core is a vital prerequisite to accurate prediction of these operational limits.

Simulation of the physical processes connected with reactor operation and progression of accident transients is extremely complex because the individual processes related to the different types of energy transport throughout the reactor core are functionally dissimilar but relatively tightly coupled. This creates additional complexity in the application of the standard approach to multi-physics simulation, where each process is initially isolated and evaluated independently, before being superimposed into an integrated model. Ultimately, it is excess thermal energy that causes material failure in most design basis accidents; thus,

if simulation of an energy transport mechanism must be simplified, nuclear processes should be targeted over thermal processes.

Simulation of thermal hydraulic processes with simplified source terms for the various nuclear energy transfer mechanisms is a good compromise between complex multi-physics simulations and isolated, independent simulation of each transfer mechanism. Thermal hydraulic simulation also has the benefit of being relatively straightforward to experimentally verify, as thermal testing facilities aren't at risk of radiological release and are much simpler to design and construct than nuclear testing facilities. This experimental validation component is the final step of the sequence for safety analysis and provides confidence that the predicted operational limits are well correlated to the boundary conditions for the specified design basis accidents.

2.2.1.1 Selection of Design Basis Accident Reference (Identification)

Postulated accidents for HTGRs have been investigated as they have been observed and defined through operating experience with existing gas-cooled reactor installations. One class of these postulated accidents is characterized by the loss of the primary coolant circulator, resulting in a core inlet pressure drop and eventual flow stagnation and reversal. Uneven radial heating in the core region creates buoyant flow features which manifest into a semi-stable natural circulation flow loop within the primary pressure vessel. These types of accidents are identified as Loss of Forced Circulation (LOFC) accidents and are further identified by whether or not the reactor cavity remains pressurized during the transient. Pressurized LOFC (P-LOFC) accidents are subject to increased heat transfer via convective cooling compared to the depressurized case (D-LOFC), although both accidents are heavily dependent on radiative heat transfer for energy transport.

Both P-LOFC and D-LOFC accident scenarios have unique flow structures associated with the helium coolant, although relatively few resources have been adequately developed to characterize flow for these accidents in pebble bed core geometry. These conditions provide a unique opportunity for investigation due to their transient nature. Flow velocities

vary from full flow conditions, to stagnation, to the development of natural circulation. Thus, the flow regimes present in the core region transition from turbulent to laminar and back again over the course of the accident progression. Characterizing the development of turbulent flow in an environment with strong thermal gradients and validating predictive capability for numerical simulations of these environments is a relatively undeveloped component of thermal hydraulic safety analysis for HTGR designs.

2.2.1.2 Thermal Hydraulic Simulation (Prediction)

In the nuclear industry, numerical simulation methods which evaluate entire power conversion systems, and can predict overall characteristics and bulk parameters between individual components, are considered to be system level methods. Typically, these methods only evaluate parameters for individual components in one spatial dimension and cannot predict component-scale phenomena due to the simplified physical framework of the system. Methods which precisely evaluate only a small part of a system with a very high level of fidelity can be classified as direct simulation methods. These methods typically simulate phenomena in three spatial dimensions resolved to a series of volumes or nodes and are capable of evaluating high resolution parameter sets and predicting component-scale phenomena.

Increased accuracy and precision for simulation requires significant increases in complexity for input data, physical models, empirical correlations, and access to more advanced computational tools and hardware. Direct simulation methods can be coupled to system level simulation methods to produce high resolution parameter sets for one critical volume of a system with bulk parameter simulation for the remainder of the system. This allows for system wide effects to be evaluated as they relate to local scale phenomena in the component of interest. Validation of numerical simulation methods must be conducted according to the scope and complexity of the method in question. High resolution simulation methods should be validated with collected data of a similar resolution. As simulation methods continue to develop complexity and are able to further discretize a given volume of interest, appropriate measurement techniques must be developed to

provide adequate validation data. In the case of thermal hydraulic analysis, high resolution methods are typically designated as computational fluid dynamics (CFD) methods.

Typical safety analysis of reactor primary systems begins with systems level simulation methods which are used to evaluate the plant response to an accident condition. Bulk flow parameters can be determined from this analysis and critical safety parameters can be determined with a relatively wide margin of error due to the simplified parameters of the system. As analysis matures, error margins are typically reduced by increasing the simulation fidelity for critical components. CFD methods are used to evaluate component scale phenomena and determine critical parameters with a higher degree of certainty. In the case of HTGR thermal hydraulic simulations, particularly for the pebble bed core configuration, bulk flow parameters concerned with heat transfer in the core region are a significant source of uncertainty in system level simulations. CFD methods have been developed which can predict flow structures on the scale of the flow channels themselves, but these complex models require high quality validation data to ensure the accuracy of the simulation. If CFD methods can predict transient core flow phenomena with a high level of confidence, system level simulation methods can be improved and thermal hydraulic safety analysis for HTGR systems can provide more specialized, targeted guidance for reactor development.

Modern thermal hydraulic simulation methods which provide local scale analysis for design basis accidents are dependent on accurate modeling for each mechanism of thermal energy transfer. Conductive and radiative heat transfer account for the majority of heat flux in the core region and are relatively straightforward to model. These mechanisms allow thermal energy to flow away from the extremely hot region in the center of the core to the relatively cool outer periphery. Thermal energy also flows from the pebbles into the radial and axial reflectors. These components are typically constructed of thermally insulating materials, so conductive and radiative heat transfer declines significantly at the reflector boundary, but these mechanisms do allow the thermal energy distribution to be modeled as relatively homogeneous across the fuel pebble region.

Given the dynamic structure observed in pebble bed cores, conductive and radiative heat transfer can typically be accurately modelled using stochastic methods. Integrated analysis methods can estimate heat transfer for a given volume of pebbles rather than as a discrete, local-scale mechanism and will result in gradient distributions for thermal parameters. Convective heat transfer is less significant overall, but as gas coolant is the primary mechanism for removing heat from the core region, it is extremely important to transient simulation. Further complications arise from inhomogeneous flow structures which may develop in the core region, creating dynamic channels of bypass flow and regions of flow stagnation.

Simulation of convective heat transfer for local scale analysis is dominated by turbulence flow structure modeling and turbulence field predictions within the reactor core. When the helium coolant flows through the reactor core, the flow can be characterized by a number of parameters related to fluid and boundary properties. In the case of convective heat transfer, these parameters are grouped into two primary flow regimes. Laminar flow characterizes a velocity profile which is well developed and steady over time as it traverses the geometry in question. Turbulent flow characterizes the formation of time dependent effects and momentum dominated flow physics which results in an unsteady velocity profile and increased effective convective heat transfer. It is generally preferred to operate a reactor in the turbulent flow regime for the purpose of increased energy transport between the fuel surface and the coolant. The simulation of accident transients must correctly predict the flow parameters present in the core for the energy transport to be accurately accounted and applicable to the design in question. In the case of transient accidents such as the LOFC accident scenario, the coolant flow regime may range from laminar to turbulent over the course of the accident progression. Predicting the onset of these transitions is a valuable tool for thermal hydraulic safety analysis as it is a fundamental parameter for estimating energy transport within the core.

Turbulent flow can be characterized via a number of physical parameters. The most common parameters used for determination of flow regime are velocity profiles which are

either directly or indirectly determined from data collected from a variety of applicable instruments. Identification of temporal flow structures, described by sequential velocity profile measurements in the volume of a given flow, indicates the onset of turbulent transition. These temporal flow structures also produce slight pressure variations which can be detected with high sensitivity instruments. Slight fluid temperature variations may also be observed as a result of stratified flow entering a turbulent flow volume. Both of these methods lack the accuracy of velocity field measurements but may be useful for specific applications. Heat flux measurements can directly measure fluid velocity, but have the drawback only being applicable to surface velocity profiles. This means that inter-fluid structures which are not directly adjacent to the fluid interface will not be detected with heat flux measurements. The use of wire sensors which protrude into the flow volume of interest can capture inter-fluid flow structures, but the presence of the probe may be considered intrusive for some validation applications.

2.2.1.3 Experimental Thermal Hydraulic Validation (Verification)

Generally, dedicated experimental facilities which provide validation data can be classified into two distinct types, depending on their scope of investigation. Integrated effects test (IET) facilities utilize multiple system components to create an environment that accurately recreates the conditions under investigation. Effects which propagate through multiple systems or are associated with overall system performance can be evaluated using this type of facility. Generally, these facilities are selectively scaled to reduce construction and operational costs and may have simplified components if flow conditions can be altered without affecting system response.

The alternative to this type of facility is the separate effects test (SET) facility. Generally, these facilities are used for isolated investigation of a single physical phenomenon and are composed of only a small fraction of the system in question. Effects which occur outside the particular area of interest or are multi-component in nature are not accounted for, which can allow for elimination of disruptive effects, but may limit the applicability of the results for full system analysis. Methods of thermal hydraulic numerical simulation can be said

to generally fall within these classifications as well, regarding the isolated and multi-physics simulations discussed in the previous section.

Nuclear reactor system design is inherently driven by the need for accident mitigation. Accident mitigation techniques are supported by a safety analysis philosophy that predicts accident conditions and then verifies mitigation functions with a program of simulation coupled with experimental validation. Thus, experimental thermal hydraulic validation is the cornerstone of safety analysis for reactor design.

2.2.2 Instrumentation Requirements for HTGR Safety Analysis Validation

In support of the continued development of high temperature gas reactor technology, and specifically pebble bed thermal hydraulic experimentation, a significant gap in instrumentation for high temperature reactor systems must be addressed. Modern high temperature thermal hydraulic experimentation has considerable challenges to overcome in the application of traditional measurement systems to extremely harsh environments, such as the core of a high temperature pebble bed reactor. The pebble bed core configuration is chosen as a representative environment due to the unique difficulty presented by the dynamic geometry and high level of flow variation throughout the core. Many modern methods for measurement of coolant flow parameters such as temperature, velocity, and pressure are not effective for very high temperature gas in a complex, enclosed environment. This apparent challenge is ideal for the implementation of novel, specialized measurement methods which can meet the considerable requirements for reliable and accurate operation established by modern challenges of thermal hydraulic experimental validation.

The largest gaps in understanding, concerning high temperature reactor core thermal hydraulics, are due to poor characterization of energy transport behavior between components in the reactor core. Sensors capable of operation in these environments are perhaps most valuable for use in experimental facilities as simulation validation tools; considering the stage of development for HTGR thermal hydraulics and specifically pebble

bed reactor core design. This suggests a requirement for instrumentation which has high spatial resolution and accuracy, in addition to the rugged construction and adaptability necessary for reliable operation in a dynamic environment.

Micro Electro Mechanical Systems (MEMS) type instrumentation presents characteristics which are favorable for the environment and requirements specified. The characteristics of this instrument classification and initial development strategies are investigated in later sections to determine the feasibility of a MEMS-based instrumentation platform for HTGR core environments. In the interest of stated objectives and scope limitations of this research endeavor, only high temperature operation will be considered. Neglecting radiation is a considerable compromise for sensor development, however most experimental thermal hydraulic facilities are non-nuclear and instead utilize electric resistance heaters. Material and fabrication technique selection are the initial steps for development of a specialized sensor and investigation of these will give an early indication of MEMS applicability to high temperature thermal hydraulic instrumentation.

Thermal hydraulic experimental facilities which simulate core environments typically have the a few key characteristics which must be accommodated by the proposed sensor design. Fuel element surface temperatures can reach up to 1,600 °C for full-scale temperature facilities which investigate transient conditions, meaning if sensors are mounted directly to the surface of a heated component, they must tolerate these temperatures locally. Heating elements are typically made of graphite or various carbide ceramics to simulate a nuclear fuel pebble, which can be formed to accommodate a sensor mounting point with cable routing voids; however, accommodations must be made to ensure the differential thermal expansion between the sensor and the mounting surface does not dislodge the sensor over time or create external stress on the instrument housing. If the sensor is mounted to an unheated fuel pebble, then requirements are slightly reduced as the pebble will likely reach a reduced maximum temperature equal to the local coolant temperature.

Coolant composed of helium or nitrogen is expected to reach 1,200 °C or more in the active core region. Sensors must perform reliably at this temperature for extended periods of time to provide economic utility. Helium is an inert coolant and the assumed lack of oxygen is a large advantage for sensor design, as oxidation resistance is not a critical design criterion. However, moisture ingress has been a persistent problem for pebble bed thermal hydraulic testing facilities, with most facilities having to undergo a 'bake-in' period to drive moisture out of the core components before they can operate at high temperatures. Encasing the instrumentation in a protective sheath capable of resisting moisture penetration and oxidation is critical for durable operation of thermal sensors in this environment.

A number of instrumentation configuration strategies have been developed for application to high temperature environments. Many of these methods are based upon single point deployment of sensors around the active core periphery, reading flow characteristics at the inlet and outlet of the core coolant flow or at the core boundary. This is suitable for collection of operational data but lacks the information density required for collection of simulation validation data, which has the additional requirements of possessing both high spatial density and high local accuracy and precision to accurately characterize energy transport.

Single point measurements must be deployed in an array formation or translated across a measurement volume to produce spatially dense data. Another option exists in the form of optical measurements which collect data from images of an illuminated two-dimensional plane. These are typically classified as field-of-view measurements and require line-of-sight access to the measurement volume to capture data. This approach is very difficult for core flow measurements due to the difficulty in obtaining line-of-sight access to the core region while ensuring the sensitive optical instruments are insulated from the harsh thermal conditions. Small scale, single point instruments deployed in an array is the most straightforward method for collection of spatially dense, accurate, and dynamic data using non-optical methods and is the assumed deployment configuration for this investigation.

2.3 HTGR Thermal Hydraulic Instrumentation

A number of fundamental implementation challenges exist for pebble bed HTGR core instrumentation, specifically for thermal hydraulic sensors. Perhaps the most significant challenge is simply the high temperature of the core solid structures and coolant. Another difficulty lies in the dynamic configuration of the core and the uncertainty associated with movement of the fuel pebbles within the core. In addition to these unique challenges, we also have the typical difficulties surrounding nuclear reactor instrumentation such as high radiation flux, complex geometry creating access and routing challenges, flow invasiveness concerns, and extensive requirements for redundancy and durability.

In this section, contemporary thermal hydraulic instrumentation for HTGR systems is investigated and the basic functional design for a range of instruments is explored. Development of specialized MEMS instrumentation suited for pebble bed HTGR environments is essentially an extension of the same fundamental design concepts already utilized by contemporary instrumentation, so it is worthwhile to develop a basic understanding of these physical processes as a basis from which to begin development. Investigating and defining contemporary instrument deployment strategies also provides context for highlighting the novelty of proposed MEMS instrumentation and identifies the areas in which the proposed design improves upon currently available hardware. Finally, recent developments in instrumentation hardware are reviewed and applications of advanced or experimental instrumentation are investigated to identify the leading edge of instrumentation development efforts and determine the direction of innovation for the near future.

2.3.1 Basic Thermal Hydraulic Sensor Functional Overview

For context and initial design guidance, contemporary instrumentation utilized for HTGR applications should be investigated. A range of instrument types are required to fully characterize the thermal hydraulic parameters of a given reactor heat transport system. This hardware consists of instruments for temperature measurement, pressure

measurement, and flow measurement primarily, with additional secondary sensor classes for specialized measurements such as heat flux or wall-shear stress.

High temperature thermal sensors are primarily composed of two distinct functional classes of sensors. The first class includes the basic thermocouple, resistance temperature detector (RTD), thermistor, and other types of sensors which operate via direct physical contact with the material which is being measured. This class can be called direct thermal sensors and they share the common functional approach to placing a material with a well characterized thermal response in the region to be measured and observing the response of that material to determine the temperature. The second class of sensors does not make physical contact with the material which is being measured and instead measures electromagnetic energy which is produced by the material from a distance, often allowing the instrument to avoid direct contact with the harsh environments being measured. These sensors can be referred to as indirect thermal sensors and include thermal imaging cameras of various types and specialized radiation detectors such as gamma thermometers.

Due to the harsh environments being considered for HTGR instrumentation, indirect thermal sensors would be an ideal choice to prevent sensitive measurement hardware from being exposed to the high temperatures of the core region. However; the pebble bed geometry prevents direct optical access to the center of the core region. Fiber optic viewports have been used in some applications to route photons out of the extremely hot environments in which they are produced so that they can be measured in a more suitable environment. This approach is not possible in a pebble bed reactor core due to the dynamic nature of the core structure and the relatively sensitive optical transmission materials, which must be insulated from the core environment.

More durable and perhaps more suitable materials are used by direct thermal sensors, such as thermocouples. Contemporary HTGR process instrumentation utilizes direct measurement instruments due to the difficulties encountered when attempting to implement indirect measurement techniques to the pebble bed HTGR environment. The

development effort presented will follow this same direction and focus on direct measurement methods only. In this class of instrumentation, the thermocouple and RTD are the most common hardware types for the HTGR environment being investigated.

2.3.1.1 Thermocouple Functional Overview

Contemporary high-temperature thermal instrumentation hardware for process monitoring is almost entirely comprised of two basic functional types, thermocouples and resistance temperature detectors (RTDs). Each of these sensor types has key benefits and drawbacks which must be considered when determining the instrument applicability to a given measurement environment, as each of these instruments function by measuring fundamentally different physical processes. By a large margin, the most utilized instrument type is the thermocouple, which is employed extensively in reactor instrumentation systems. This is primarily due to the high durability, stability, wide measurement range, and relatively low cost of the instrument hardware when compared to RTDs.

Thermocouples operate primarily via measurement of two separately identified physical phenomena called the Seebeck effect, or Peltier effect, and the Thomson effect. Both of these effects in combination describe the electromotive force (EMF) generated between two differentially heated nodes of an electric circuit comprised of dissimilar metals. The magnitude of this EMF is relatively small, in the millivolt (mV) range, and depends on the metals selected for the circuit as well as the temperature difference between the two nodes being measured. The mV signal is typically measured at one node at a known temperature and the temperature of the other node can be derived from an established calibration curve between the signal magnitude and the node temperature difference.

A large range of functional metal alloy combinations are characterized and used as thermocouple probes in industrial applications. These alloy combinations are known as thermocouple types and are usually denoted with a single letter, such as ‘K’-type or ‘S’-type. The selection of the most appropriate thermocouple type for a given application

depends primarily on the measurement environment, the desired measurement accuracy, and the cost of materials. In addition to type, thermocouples are also described by their measurement error tolerance over a given temperature range, called the thermocouple class. For example, a commonly used thermocouple in reactor systems is a K-type, class 1E thermocouple, which refers to a Nickel-Chromium to Nickel-Aluminum junction with an error tolerance of ± 1.5 °C from 0 °C to 375 °C and ± 0.4 °C from 375 °C to 800 °C.

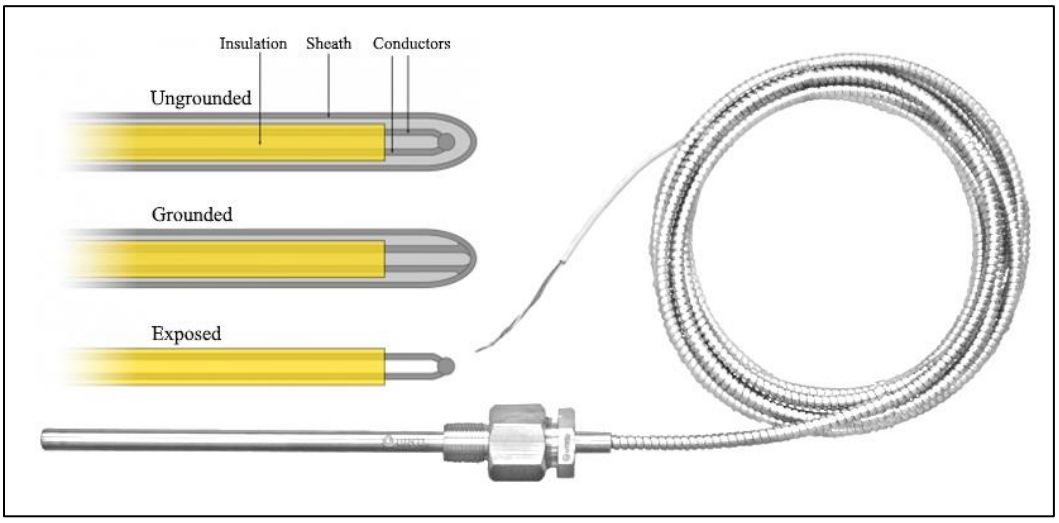

Figure 2-5: Example thermocouple construction and hardware [49]

Thermocouples are relatively delicate instruments and must be electrically and chemically insulated from the surrounding environment to reduce signal noise and drift. Typically, thermocouple probes are sheathed in a durable metal tube with an inert insulator isolating the thermocouple probe from the sheath. Common materials for these components are 316L stainless steel alloy or Inconel for the sheath and magnesium oxide (MgO) or alumina (Al_2O_3) ceramic powder for the insulation. In very high temperature environments, ceramic sheaths can be used to provide more durable protection for the thermocouple probe, however a trade-off between durability and thermal responsiveness must be evaluated, as insulating materials will prevent temperature fluctuations in the surrounding environment from quickly propagating to the thermal probe. For metallic sheathed thermocouples, the hot junction of the probe can be welded to the sheath; depicted as the

grounded configuration in Figure 2-5, which improves instrument response time but may decrease probe mechanical durability.

To accurately measure a given environment, one node of the thermocouple circuit must be at a known reference temperature, which is measured by an accurate independent process in a relatively benign environment. Typically, this reference temperature environment is located far from the harsh process environment and thus the thermocouple probe must be routed through complex geometry and across pressure boundaries to properly isolate the two measurements. An RTD is typically utilized for the reference temperature measurement because they do not require a known temperature reference and can provide extremely accurate temperature measurements.

For the specialized application to pebble bed HTGR environments being investigated, the primary functional difference between thermocouples and RTDs is the type of signal being measured and what electronic hardware is required to accurately measure that signal. If a primary design goal is to realize an implementation that could be extended with wireless signal transfer at some point in the future, thermocouples are not a viable choice. Thermocouples output a relatively small differential voltage signal that requires specialized electronics to measure accurately. This requirement, in addition to the reference junction mentioned previously, makes it impossible to implement a remote sensing system which utilizes thermocouples because the reference junction and measurement electronics must be physically connected to the measurement probe and must be located in a benign environment.

Thermocouples do offer the advantage of being more resistant to neutron radiation when compared to RTDs, which is a primary motivator for their widespread use in reactor instrumentation systems. This is because RTDs are prone to calibration drift when impurities are added to the sensor material, which increases the electrical resistance of the sensor conductor. Impurities also cause thermocouple calibration drift, but not to the same extent, due to the underlying physical process being only weakly coupled with the

resistance of the sensor conductor. Both instruments are prone to electromagnetic noise caused by exposure to radiation; however, the high signal to noise ratio of the RTD is better suited to filtering techniques to remove this noise.

Although thermocouples do offer a range of functional advantages compared to RTDs, the limitations of the supporting measurement hardware limit their possible extension mechanisms and thus, their applicability, for the pebble bed HTGR thermal environment being investigated.

2.3.1.2 Resistance Temperature Detector (RTD) Functional Overview

RTDs are primarily comprised of a length of fine-gauge conductive wire wrapped around a structural insulator, which is then encased with powdered inert insulating material in a protective metallic or ceramic sheath. The conductive wire is fabricated from a material which has a well-characterized, temperature-dependent electrical resistance; such as platinum, copper, or nickel. The resistance of the conductive wire is measured and thus the temperature of the wire can be derived by comparing the recorded resistance against a known calibration curve. Due to the relatively simple components which comprise an RTD, the probes themselves are inexpensive and relatively easy to fabricate using a variety of methods. RTD probes are usually very fragile due to the fine gauge of wire used for the sensing element and must be insulated from corrosive environmental effects to prevent measurement errors.

RTD probes are commercially available in three distinct forms; the wire wound probe, the wire coil probe, and the thin film probe. The wire wound probe was previously described and is comprised of a sensing wire wound around a supporting ceramic structure. The wire coil probe is similar except the sensing wire is first tightly coiled to create a helical shape, before being loosely packed inside voids of a central ceramic encasement. The coiled wire is allowed to float freely, being suspended by fewer contact points on the central insulator when compared to the wire wound sensor. This reduces mechanical stress and measurement drift caused by differential thermal expansion between the wire and

supporting ceramic structure, but introduces sensitivity to vibration and reduces the mechanical durability of the probe. The final type, the thin film probe, is the type that is most applicable for MEMS or semiconductor fabrication methods as it consists of a thin metallic film trace deposited onto a given support substrate. The substate must be carefully matched to the probe material so that mechanical stress resulting from differential thermal expansion can be minimized across a given temperature range.

The accuracy of an RTD temperature measurement ultimately depends on the accuracy of the resistance measurement of the sensing wire and the stability of the temperature dependence of resistance. Electrical resistance is dependent upon a variety of environmental and material factors, such a conductor stress, chemical composition, length, and cross-sectional area, among other factors. Isolating the effects of temperature variation on the resistance can be difficult, even in relatively benign environments. In harsh environments, this can be almost impossible if the various external factors cannot be quantified and compensated for. Even if a given probe is well insulated from the surrounding environment, slow-acting effects such as material diffusion and thermal creep will slowly cause the resistance-to-temperature dependency curve to shift, introducing error in the measurement.

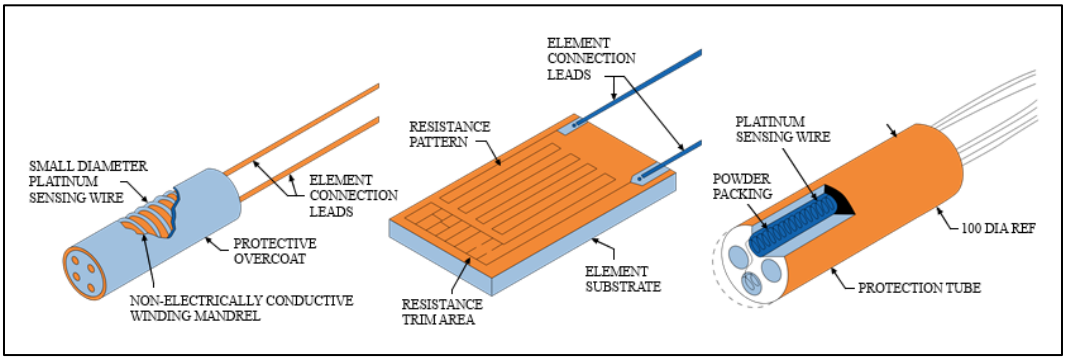

Figure 2-6: Wire and thin film RTD construction diagrams [50]

Different RTD probe material combinations offer stable operation over various temperature ranges. The mechanical and chemical properties of a given material will

usually predict the operating temperature range, as structural transitions within the sensing element and chemical reactions such as oxidation will often be the primary drivers of transition to non-liner resistance-to-temperature response at high temperatures. Platinum is commonly used for RTD sensing elements because it has good mechanical properties across a wide temperature range, thus resulting in stable operation and high repeatability in resistance measurements.

The rate at which the electrical resistance of a given material changes per degree of temperature change is denoted by the Greek letter alpha (α) with units of $\Omega/(\Omega\,°\mathrm{C})$, and should remain constant over a given temperature range if the temperature-to-resistance relationship is linear. Pure platinum is commonly defined to have $\alpha = 0.003925\ \Omega/(\Omega \cdot °\mathrm{C})$ in the 0 °C to 100 °C temperature range, although standards for RTD measurements, such as IEC 60751 and ASTM E-1137, specify a value of $\alpha = 0.00385\ \Omega/(\Omega \cdot °\mathrm{C})$, which reflects probes created from industrial grade platinum or by intentionally doping pure platinum with contaminants to achieve the specified value.

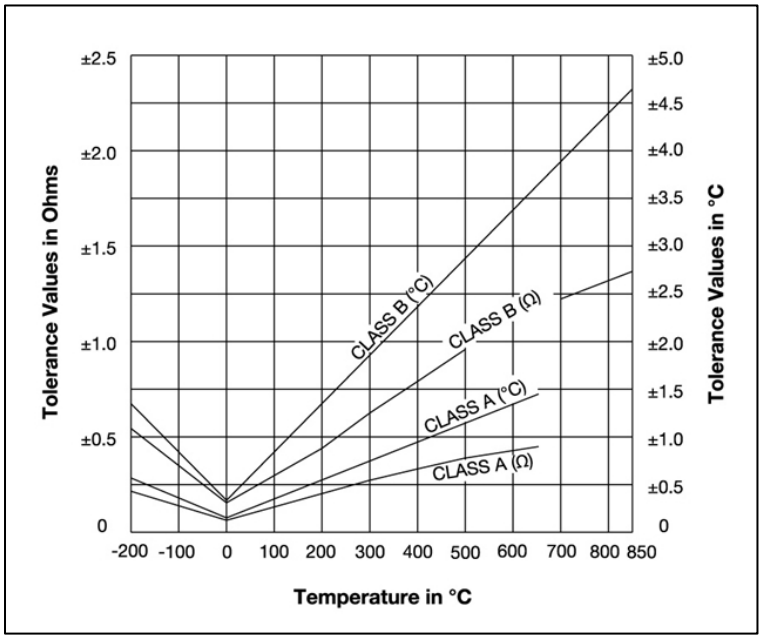

Figure 2-7: RTD accuracy class definitions [51]

Resistance of an RTD element is typically measured by flowing a small amount of current (~1.0 mA) through the probe and determining the voltage drop across the probe. Probes are typically fabricated with resistances of 100 Ω or 1000 Ω at 0 °C and have a class designation which refers to the probe accuracy and repeatability, class A for 0.06% and class B for 0.12%, with fractional classes for specialized, high accuracy RTDs.

The choice of nominal resistance is dependent on the application and available measurement hardware. The use of a 1000 Ω RTD results in larger variations in voltage than for a 100 Ω RTD over the same temperature range, so the accuracy of the measurement can be higher if the voltage measurement hardware is identical. However, 1000 Ω RTDs would have a thinner and more fragile sensor trace when compared to a 100 Ω RTD, making them potentially more susceptible to signal distortion from external sources. Another consideration for high resistance probes is the self-heating effect, called joule heating, which is induced by the resistance heating of the excitation current required to collect a voltage measurement. This effect can be minimized if the excitation current is limited or if measurements are taken only periodically, allowing the sensor to return to equilibrium with the surrounding environment before another measurement is taken.

RTD probes used in nuclear environments must be regularly calibrated to maintain their accuracy due to the doping effect encountered in high-flux environments. This typically means that a probe must be removed from service and placed in a controlled, well-characterized environment to determine new calibration coefficients which accurately describe the temperature-to-resistance relationship for the current state of the probe. Methods of in-situ calibration are a subject of ongoing research, as functionally independent methods of measuring temperature are possible for some applications and can greatly reduce the maintenance burden of utilizing RTD sensors, which is the typically cited justification for the choice of thermocouples over RTDs in industrial applications.

RTDs are generally more accurate and offer better repeatability when compared to thermocouples. Platinum RTDs are slowly replacing thermocouples in many industrial

applications for environments below 600 °C and some specialized platinum probes are capable of operating in environments up to 1000 °C, although thermal diffusion of impurities at elevated temperatures can cause accelerated calibration drift. Routine calibration of the RTD sensor can mitigate this effect. RTDs can also offer improved response time when compared to thermocouples, although this is heavily dependent on the insulating materials used in the probe construction.

The signal magnitude of an RTD can be varied depending on the initial resistance of the chosen sensor, whereas thermocouples have a fixed, relatively small signal magnitude. Generally, RTDs have a 10x increase in signal magnitude when compared to thermocouples (~100 mV compared to ~10 mV). RTDs do require a power source for voltage measurement; however, for high resistance probes, the excitation current is extremely small and, in some cases, can be provided by the surrounding environment when utilizing wireless signal transfer. Thermocouples do not require an external power source, but colleting the mV scale signal requires specialized electronics that do require power, so the instrument package as a whole does not benefit from the passive nature of the sensor.

2.3.1.3 Signal Transmission

Contemporary methods of signal transmission in harsh environments focus on the use of an extremely durable mineral insulated, metallic sheathed wire which is routed from the harsh environment of the probe to a more benign environment for signal analysis.

For thermocouple probes, this routing path is sensitive to temperature due to the underlying physical phenomena being driven by temperature differences between two nodes in a sensing circuit. Effects such as thermal conduction in the sensor wire and the high resistance of long lead wires can cause measurement drift. In addition, the lead wire must be comprised of a compatible material, as the underlying physical phenomena are also dependent upon the materials used in the probe circuit. Transition junctions can be used, but the temperature of the junction must be known, otherwise the offset caused by this material change cannot be compensated for.

For RTD probes, lead wire routing is comparatively simpler. If a three- or four-wire configuration is used, the resistance of the lead wire can be compensated for in the final measurement, making the wire less sensitive to length, temperature, and other physical properties. High resistance of the lead wire compared to the probe can again introduce measurement error when utilizing a three-wire connection, but if a 1000-ohm probe is used, this can usually be avoided or significantly reduced.

The wiring configuration utilized to connect the RTD probe with the measurement electronics has a significant impact on the resulting accuracy of the sensor if the lead wire resistance is not eliminated. If a four-wire measurement configuration is used, also called an ohm measurement, the lead wire resistance will not impact the voltage drop measured by the instrument electronics. This configuration is implemented by using four lead wires, two of which will carry the excitation current and two of which are utilized for the voltage measurement. Since the current path does not include the lead wires used for the voltage measurement, the resulting voltage drop is only dependent on the resistance of the sensor. This configuration is depicted in Figure 2-8.

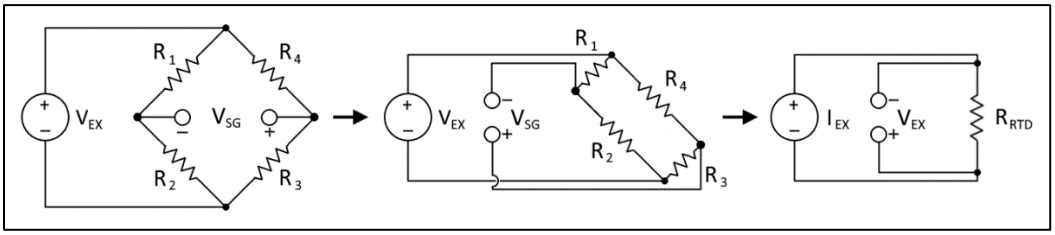

Figure 2-8: Wheatstone bridge circuit (left) compared to an ohm measurement circuit (right)

Figure 2-8 is also useful for identifying the primary difference between a n RTD probe and a strain gauge. Both of these instruments utilize a thin metallic trace with high resistance to measure a physical property. Strain gauges measure differential resistance between two sensors, which comprise the legs of a Wheatstone bridge (WSB) circuit (R_2 and R_4), while RTD sensors measure the magnitude of resistance for a single sensor which comprises the Ohm measurement circuit (R_{RTD}). Figure 2-8 illustrates how these circuits are related, as

they have similar features, but ultimately serve two distinctly different functional purposes. Note that the strain measurement utilizes a constant voltage excitation source while the RTD measurement utilizes a constant current excitation source.

The most significant challenge of instrumentation deployment in a pebble bed core is implementing a flexible method of signal transmission. Routing a mineral insulated wire through the dynamic structure of an operating pebble bed is simply not practical, thus alternative methods of signal transmission must be considered to achieve widespread deployment. Wireless signal transmission has been demonstrated for RTD instruments in some harsh environments and is a subject of ongoing research and development. Removing the need to route a wire through the active core region would greatly increase the potential applicability for specialized thermal instrumentation and will be the eventual target hardware configuration for widespread deployment.

2.3.2 Contemporary Reactor Instrumentation Systems

To determine the current state of thermal hydraulic instrumentation development, it is useful to investigate the thermal hydraulic instrumentation hardware deployed at various contemporary HTGR plants. In the following sections, a summary of instrumentation utilized at the Peach Bottom and Fort St. Vrain plants is presented, along with an investigation of the instrumentation system of the HTR-10 and expected instrumentation system for the HTR-PM.

2.3.2.1 Peach Bottom and Fort St. Vrain Thermal Hydraulic Instrumentation

The thermal hydraulic in-core instrumentation utilized in early prismatic core gas reactor pilot programs, such as those at Peach Bottom and Fort St. Vrain, were comprised of specialized K-type (NiCr-NiAl), E-type (Chromel-Constantan), C-type (WRe5%-WRe26%), N-type (Nicrosil-Nisil), and Geminol-P/N thermocouples clad in a molybdenum or Inconel sheath. High-purity magnesium oxide powder was commonly used as an isolation element. In-core instruments were placed at the outlet coolant channels of the core as well as in channels created the graphite reflectors of the core periphery [52].

Some alternative thermal sensors were also utilized to support extended functional diversity, such as acoustic thermometers, however the vast majority of thermal instruments were thermocouples.

Peach bottom had 97 K-type thermocouples, for temperatures below 538 °C, and 59 C-type thermocouples, for temperatures up to 1310 °C, initially installed in the core region. The C-type thermocouples were identical to those utilized in the first HTGR in the UK, the Dragon reactor. Most of the C-type thermocouples failed via open circuit during the installation process due to tungsten embrittlement [53]. The deployment of a large number of instruments created redundancy for the high failure rate that was expected due to radiation exposure of the thermocouples. For thermocouples near the reactor fuel assemblies, the expected lifetime was approximately three years. A second, functionally independent, thermal measurement system was installed for eight of the fuel compacts in the form of an acoustic thermometer. This redundant system allows for in-situ calibration of the core thermocouples and to provide a means for temperature monitoring after the thermocouples failed.

Fort St. Vrain utilized specialized Geminol-P and Geminol-N type thermocouples, for temperature measurement up to 1093 °C, as well as E-type thermocouples for temperatures up to 538 °C. The plant utilized 429 Geminol thermocouples for in-core and primary circuit measurements, as well as more than 300 E-type thermocouples in the secondary coolant circuit and at selected points in the support structure inside the pre-stressed concrete reactor vessel (PCRV). An additional 235 thermocouples were installed outside the pressure vessel to monitor the structural parameters of the PCRV, as this was the first commercial deployment of the technology and the service life and degradation characteristics were under investigation.

Additional instrumentation was sometimes deployed in control rod tubes that were otherwise not occupied and could provide very accurate temperature measurements close to the active core regions. In fact, these temperature measurements are some of the most

accurate thermal hydraulic measurements made in gas reactor core environments, due to the ability to easily insert and remove the instrumentation via the control rod tube maintenance access ports [25]. New instrument hardware could be used for each measurement with the expectation that the instrument would fail quickly due to radiation exposure.

Technical specifications concerning the thermocouple calibration procedures and operational lifetime observed for the Fort St. Vrain and Peach Bottom plants are not available in meaningful detail, but investigations which seek to summarize the lessons learned through the construction and operation of the plants indicate that the thermal hydraulic instrumentation was not adequate for long term operation of the plant [54]. Although some measures, such as locating coolant temperature measurement instrumentation in the steam generator section of the plant to shield the instruments from radiation exposure, were successful and utilized by later instrumentation system designs.

2.3.2.2 HTR-10 Thermal Hydraulic Instrumentation

The HTR-10 thermal hydraulic instrumentation system was developed to serve three distinct functional purposes, to measure process parameters to allow for operation of the plant, to detect conditions which indicate abnormal reactor conditions and provide a trigger for reactor safety systems, and to collect validation data during system testing. Researchers Wei and Zhong provide an excellent overview of the HTR-10 instrumentation system in their presentation at the 18th International Conference on Nuclear Engineering (ICONE18) in 2010, which serves as the primary source for the information on this topic [23].

The primary thermal hydraulic measurement parameters for the HTR-10 are coolant temperature, primary loop pressure and mass flow rate, feedwater pressure and mass flow rate, in-core component temperature, and pressure vessel temperature. Of these parameters, the most applicable to this investigation are the core temperature measurements. For the hot-leg helium coolant temperature, the designed operating range

of the instrumentation is 0 °C to 800 °C. For core component temperature, the designed operating range of the instrumentation is 0 °C to 500 °C.

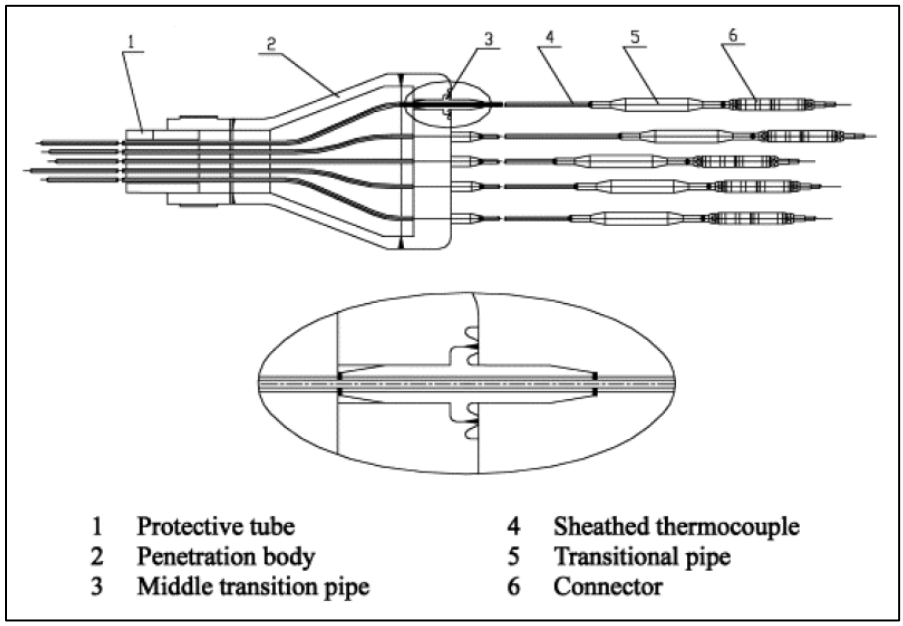

Figure 2-9: In-core thermocouple bundle for the HTR-10 [23]

Similar to the configuration utilized in other HTGR instrumentation systems previous to the construction of the HTR-10, core temperature measurements are concentrated at the inlet and outlet coolant channels as well as at the periphery of the core outer reflectors. The coolant instrumentation consisted entirely of K-type (NiCr-NiAl), class 1E thermocouples, with a diameter of 3.17 mm, sheathed in a 316L stainless steel tube, and internally insulated with high purity magnesium oxide powder. The expected error for class 1E thermocouples is ±1.5 °C from 0 °C to 375 °C and ±0.4% of the reading from 375 °C to 800 °C. The coolant measurement instruments are inserted directly into the coolant flow channel and anchored by swage lock type tube fittings at the wall of the pressure vessel.

Instrumentation measuring the surface temperature of the core barrel and other reactor components also consisted of K-type thermocouples, identical to the coolant measurement

instrumentation, but also included additional thermocouples with unspecified thermocouple error class. These are only described as surface thermocouples bolted to the core barrel and pressure vessel outer surfaces. Fifty-seven of these surface temperature thermocouples were attached at various points in the primary and secondary pressure vessels.

In-core instrumentation consisted of four bundles of ten thermocouples, which were routed to gaps between the outer reflectors of the core via specialized penetration hardware assemblies designed to prevent helium leakage at pressure vessel boundaries. A diagram of one of these bundles is depicted in Figure 2-9.

The primary failure mechanism for these instruments is signal quality degradation due to radiation exposure. To mitigate this issue, instrumentation for measurement of coolant temperature was typically placed as far from the reactor core as possible, with most measurement points being in the secondary pressure vessel near the steam generator. The instruments used for in-core temperature measurements could not be shielded in this way, and required frequent replacement to ensure measurement accuracy. It is stated that following the completion of 568 days of operation, for a total of 2,498.95 MWd of power production, only ten of the forty in-core thermocouples initially installed were still functional within the accepted error limits for operation of the facility, which were stated as being ± 2.5 °C for temperatures up to 500 °C and ± 5.0 °C for temperatures from 500 °C to 800 °C. Thus, the failure rate was 75% over 568 days of operation.

2.3.2.3 HTR-PM Thermal Hydraulic Instrumentation

The documentation released regarding the design of the instrumentation system hasn't specifically identified the layout or density of core thermal hydraulic instrumentation. Some investigations have been released which assume a similar instrumentation layout as that which was utilized by the HTR-10 [55], which is likely a safe assumption. Given that the proposed power monitoring system for the HTR-PM is based on a Harmonics Synthesis Method (HSM) which relies on neutron detectors at the core periphery to determine the

power level, which then provides an estimate of core temperature, no additional thermal instrumentation capability is specifically required for the HTR-PM relative to the system implemented in the HTR-10 [56].

A number of issues exist with this approach, mostly concerned with a lack of certainty and a very slow response rate when utilizing derivative methods such as HSM to monitor core thermal hydraulic performance. This topic is further explored in Chapter 3, which focuses exclusively on estimating the thermal hydraulic environmental parameters of the HTR-PM for establishment of target performance metrics for instrument development efforts. In summary, it will be assumed that the HTR-PM will have a thermal hydraulic instrumentation system identical to the HTR-10.

2.3.3 Advanced Thermal Sensors for HTGR Core Environments

Although proving to be exceptionally difficult, there are a number of projects which are moving forward with pebble bed technology development and as such, require validation data. Thus, we have a range of examples of instrumentation strategies currently being deployed across a number of high-temperature thermal hydraulic test facilities. It is worthwhile to review these approaches to determine their effectiveness and draw conclusions from published performance data which will shape the instrument development process in the following chapters.

2.3.3.1 Approach to Mitigation of Instrumentation Challenges for HTGRs

In facilities such as Fort St. Vrain and HTR-10, thermocouples were used to monitor the core temperature. These thermocouples were placed in the outer reflector and plenum regions to measure the inlet and outlet temperature of the coolant and structural material surrounding the core. These measurements relied on other data sources, such a radiation detectors and coolant flow sensors, to create an on-line thermal hydraulics simulation to derive an extrapolated estimate of the core temperature. The obvious issue with this indirect measurement system is that it is prone to measurement error due to the high variability of the input parameters as well as a very slow response rate due to the distance

and thermal mass separating the thermocouples from the region of interest for measurement.

Due to the relatively narrow cylindrical design of the reactor pressure vessel in these two systems, the thermal flux between the RPV and RCCS is relatively high and can be useful in measuring reactor output. Coolant in the RCCS can be accurately measured to determine the thermal load on the system, which is then derived to create core temperature estimates. Again, this methodology is both far removed from the region of interest and slow to respond due to the large thermal mass of the systems being monitored.

A vital measurement for estimation of core thermal efficiency is the ratio of fission power to helium flow. Primary system helium flow rate is difficult to measure and cannot be measured directly in the systems described. Instead, a derivative estimate is made using operating parameters such as the circulator motor speed and pressure drop across the circulator turbine, as well as coolant temperature. This estimate is also prone to high error due to spatial variability in coolant temperature due to flow stratification. A means to measure the fluid velocity profile at the circulator would be ideal, but implementing the hardware required for this measurement is challenging due to the harsh conditions.

The current best practice for estimating fluid velocity profiles involves the use of optical techniques to capture motion of free-floating particles or fluid structures such as voids. This observed motion is a direct representation of the velocity vector of the local fluid volume. Optical methods can also collect extremely high-resolution data at a very high frequency over a two-dimensional flow plane. This allows for evaluation of features with very short temporal periods and of a range of spatial scales. Optical methods do require a direct line of sight from the instrument to the volume of interest for operation, meaning that the technique is not appropriate for pebble bed HTGR core environments due to the complex structure of the pebble packing, but may be applicable for regions such as the primary circulator inlet and outlet. High temperatures also pose difficulty for optical

methods due to the optical interference and noise produced by Brownian motion and radiative heat transfer from the surface of the geometry surrounding the flow of interest.

Pebble bed configurations in particular are extremely challenging from a core thermal instrumentation standpoint. There is currently no instrumentation available to address the challenge of collecting temperature measurements in the dynamic structure and extreme environment that the pebble bed HTGR core presents. This fact is highlighted in a number of reports which assess the current gaps of instrumentation for advanced reactor development [57] [53]. The specific challenges identified in these reports include the coolant temperature (~1000 °C), coolant flow rate (~110 kg/s), and primary system pressure (~5 MPa). Although a number of attempts to bypass the need for direct thermal measurements have been investigated, these mitigation strategies have significant drawbacks which must be considered. Ultimately, the development of durable and accurate direct thermal instrumentation hardware for the core region remains a priority for advanced HTGR development.

2.3.3.2 Advanced Thermal Sensors for HTGR Core Environments

As described previously, current methods using derived estimations of core temperature are prone to large error ranges due to the variability observed in the primary heat transfer loop. This effect is greatly amplified by instrumentation drift, which is common in high temperature thermocouples and resistance temperature sensors due to material degradation over time in harsh environments. Precious metal thermocouples, such as platinum-rhodium (S-type), are useful outside of high neutron flux regions as they provide relatively high accuracy (+/- 200 mK above 500 °C) and good resistance to corrosion. Rhodium does have a large cross section for neutron absorption however, which creates instabilities when used for near-core measurement applications.

An alternative is pure gold-platinum thermocouples, which can produce very precise measurements (± 10mK up to 1000 °C), even in relatively high neutron flux environments. The drawback for these sensors is that they have not been shown to be durable enough for

safety related instrumentation due to the large difference in thermal expansion between the two metals. One method of relieving this thermal stress is to use a very fine bridge wire, which ultimately makes the sensor more susceptible to mechanical stress. As with all high-temperature thermocouples, the signal-to-noise ratio is relatively low and prone to electromagnetic interference. The use of a controlled cold junction does help to increase signal stability, but the cold junction must be local and isolated from any accident conditions, again creating difficulties for implementation as safety instrumentation.

Various functional alternatives to basic voltage or resistance measurements exist and can be implemented as a functionally independent, in-situ calibration reference for RTD sensors, so that the expected measurement drift can be corrected periodically. By measuring the electronic resonance of the Brownian motion of a heated material, Johnson noise thermometry provides an independent, first-principles–based, extremely accurate measurement of the sensor temperature. The RTD sensor can be coupled to a Johnson noise thermometry circuit in such a way that both measurements can take place simultaneously. The difficulty is that JNT measurements are slow and require very sensitive electronics to be placed near the measurement location due to the small magnitude of the measurement signal, making radiation hardening and reduction of thermal signal noise very difficult. Since the fuel pebbles in the core are continuously cycled, intermittent calibration of wireless sensors as they pass through the fuel recirculation loop may be a good application for JNT/RTD coupled thermal sensors.

As described in the section detailing instrumentation for the Peach Bottom HTGR, acoustic thermometers have been in use for several decades as redundant thermal instrumentation in areas where thermocouple instruments are expected to have a relatively short operating lifetime. These devices operate by measuring the acoustic resonance of material, which has a strong correlation with the material temperature. A more modern variation of these devices is the ultrasonic guided wave thermometer, which utilizes a time-of-flight measurement for a compression wave across a waveguide, such as a metallic cylinder. Acoustic thermometers are developmentally mature, but do require specialized hardware

to guide the input of the acoustic transducer from the high temperature environment to a more benign area. This guide may undergo some material transformation due to thermal and radiation exposure, requiring the device to be periodically recalibrated. In addition, the devices are susceptible to acoustic noise and must operate in a relatively stable environment. The dynamic motion of pebbles in a pebble bed core HTGR would not be suitable for implementation of such a device, as the noise created by the shifting pebbles would likely create too much interference with the wave guide hardware.

Another technology which has a similar deployment concept to the RTD sensors presented in this investigation is the vacuum micro-triode. In a 2016 study prepared by Oak Ridge National Laboratory (ORNL), these were identified as a leading candidate for advanced thermal instrumentation in HTGR cores due to their extreme durability in high radiation environments, which was attributed to their ceramic and refractory metal components [57]. The most challenging aspect for deployment of these sensors was the establishment of a wireless signal transmission system, which is also a considerable challenge recognized by a similar deployment of an RTD array sensor.

Fiber optic Bragg thermometry is an instrumentation approach that provides extremely high tolerance to electromagnetic noise and is suitable for high temperature environments. The instruments function by measuring the wavelength reflected by Bragg grates fabricated on a fiber optic sensing line. Many grates can be fabricated on a single line, allowing for a dense linear array of sensors to be deployed across a coolant channel, for example. The drawbacks of fiber optic sensors in HTGR environments include the clouding of optical materials under high radiation flux conditions and the difficulty of routing the delicate fiber optics out of the core region to a more benign area where the measurement electronics would be located. These instruments are not able to utilize wireless signal transmission, making them difficult to apply to a pebble bed core configuration.

Gamma thermometers have been in use for many years, primarily as flow instruments. They can utilize thermocouples or RTDs, with the temperature sensor measuring the

differential voltage between an isolated and exposed measurement junction to determine the effects of coolant flow and radiation heating. As these devices are an extension of applicability for other fundamental temperature sensor types, rather than a functionally independent instrument, they will not be specifically investigated for this project. They may, however, be a possible functional extension of the RTD sensors presented herein.

Other advanced instrumentation currently being investigated for application to HRGR core environments includes various types of pressure and flow measurement devices. Pressure measurement instrumentation consists of SiCN composite ceramic diaphragms, liquid metal impulse lines, polarization rotation sensors, and extrinsic Fizeau cavity sensors. Flow measurement instrumentation includes ceramic and carbide hot-wire and hot-film anemometers, heated lance probes, and projection laser Doppler velocimetry systems in addition to adaption of various optical systems used in low temperature environments. While these instruments are interesting on their own technical merit, further discussion is outside the scope of this investigation.

2.3.3.3 Advanced Signal Transmission Methods

Modern reactor instrumentation relies on extremely durable, metal-sheathed, ceramic-insulated nickel alloy wiring to withstand a large range of harsh environments and deliver reliable operation, even in accident conditions. This type of wire is typically referred to as MI (mineral insulated) or pyro cable and is commercially available in a variety of conductor materials and number of conductors per cable. A single 4-wire RTD sensor, for example, would likely utilize a single MI cable with four isolated conductors for signal transmission. Multiple sensors can share a single signal transmission wire if they are located in the same general area. A common example would be four RTD sensors, each requiring fours signal wires, all sharing a single, sixteen conductor MI cable. The metal sheath of the cable has the ability to be welded to create a hermetic seal for pressure vessel penetrations. There are also a number of non-permanent seal types which can be utilized; however, most reactor instrumentation primary coolant system penetrations require the use of a welded seal to reduce the probability of primary coolant leakage. Wired communication utilizing

traditional conductive signal transmission cable is, by far, the most common means for instrument communication and is the only method widely supported by safety related standards.

Another type of cable often used for wired instruments is fiber optic cable, which consists of one or more strands of a transparent medium individually wrapped in a reflective sheath. Fiber optic cable is typically regarded as fragile and must be isolated from vibration and mechanical stress, but because it utilizes photons instead of electrons for signal transmission, it is not affected by electromagnetic fields. Fiber optic cable is gaining popularity, especially for redundant reactor safety systems, because it offers a functionally independent method of signal transmission when coupled with MI cables. The latency of signal transmission is also shorter for fiber optic cables compared to traditional conductive cables. This property is useful for instrumentation that serves as a trigger for a control process or other time-sensitive function. Fiber optic cables typically are not utilized in high radiation flux applications because the transparent medium becomes cloudy and transmission signal strength is reduced as a function of total exposure.

Wireless communication has recently become a topic of interest for the development of safety-related instrumentation within the reactor confinement building. Wireless instruments would be functionally independent from wired instruments and may avoid the possible signal disruption from structural damage that would destroy signal cable bundles routed through conduits in the building walls and floors. Challenges which must be addressed for the deployment of wireless instrumentation in this manner include network security, harsh environment durability, and functional verification and validation in accident conditions. Of these challenges, harsh environment durability is the most difficult to achieve, as wireless transponders typically require an RF generator or antenna coupled with a relatively sensitive electronics package. The signal electronics are typically comprised of silicon semiconductor electronics, which cannot operate at elevated temperatures due to the large amount of thermal noise observed in low-bandgap semiconductor materials.

Semiconductor materials are being developed to address this challenge, such as those which utilize silicon carbide as a basic substrate rather than pure silicon. These devices should allow for operation at elevated temperatures, such as those observed in the confinement building of a reactor under accident conditions [58]. Extending wireless communication to core instrumentation is much more difficult and requires a specialized, targeted approach to mitigate the effects of environmental induced noise.

No commercially-available semiconductor can operate at the elevated temperatures expected in an HTGR core environment. The only feasible method to utilize wireless signal transmission for core instrumentation is to place the signal transmission electronics in an isolated, benign area and route wires to an antenna or similar passive signal transducer to the harsh environment just outside the core region, likely somewhere within the outer reflector volume. Passive wireless instrumentation in the core can then communicate via the passive antenna and the signal would then be processed with the attached electronics package and sent to a central control interface via traditional instrument wiring. This reduces the wireless portion of the signal transmission to a relatively short distance from the central core region to the antenna in the outer reflector, which mitigates the need to pass the wireless signal through the primary pressure vessel. The challenge of developing a passive wireless sensor that could harvest energy from the surrounding environment and communicate with the proposed antenna is significant, if it is even possible; however, it is the only feasible route for implementing wireless signal transfer for core instrumentation at this time.

Recent developments in passive, harsh environment thermal instrumentation have demonstrated that the technology could eventually be mature enough to operate in the manner proposed. Techniques such as inductive coupling between an RTD sensor package and an RF antenna have been utilized to demonstrate passive wireless thermal and strain sensors in a range of harsh environments [59] [60] [61] [62]. An example of a surface acoustic wave (SAW) passive transducer is depicted in Figure 2-10. This type of passive transducer could be adapted for use with an RTD sensor, but due to its integral reliance on

a piezoelectric crystal for mechanical-to-electrical signal conversion, it would still be limited by its mechanical response to environmental conditions. If a method of wireless signal transmission could be developed for HTGR core environments, it would enable key functional advantages that are not achievable with traditional wired signal transmission methods.

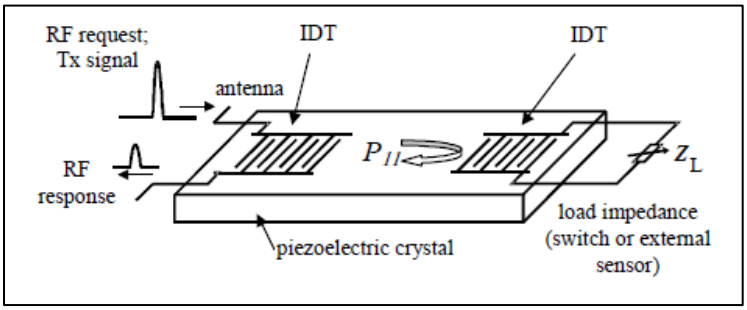

Figure 2-10: Diagram of a SAW wireless signal transducer [63]

Pebble bed HTGR instrumentation in particular would benefit a great deal from wireless signal transmission, as a key design feature for this configuration is the dynamic motion of the fueled pebbles. The utilization of a passive wireless sensor would enable direct measurement of core thermal parameters without impeding the movement of pebbles, which is not currently possible with contemporary instrumentation hardware. Indeed, the benefits of wireless signal transmission are significant for HTGR instrumentation and this is recognized by researchers involved in HTGR instrument development at national labs in the United States. Oak Ridge National Lab in particular has repeatedly presented the need for wireless signal transmission for pebble bed instrumentation. Current technology summary reports compiled in 2010 and again in 2016 state that this approach is necessary and possible but would take significant development resources. The intended instrument proposed to be coupled with this system would be the micro vacuum-triode, which has similar functional characteristics to the RTD sensor proposed by this investigation. This similarity provides a degree of reassurance that the approach presented herein is, at the very least, feasible; and that a means for passive wireless communication in HTGR core environment will eventually be realized [53] [25] [57].

2.4 Micro Electro Mechanical Systems (MEMS) Instrumentation

MEMS devices are identified as having a characteristic length of less than millimeter but more than a micrometer and utilizing micromachining fabrication methods derived from silicon semiconductor manufacturing techniques used for integrated circuit development. These devices have demonstrated usefulness in a number of applications but are primarily defined by use as mechanical actuators and small-scale sensor assemblies. The primary investigation for the purpose of HTGR thermal hydraulic instrumentation development is into their use as thermal sensors. Relevant modern applications have been demonstrated for the aerospace, automotive, and industrial power production industries; however, applications for nuclear thermal hydraulic instrumentation have yet to be demonstrated, despite a number of key opportunities created by recent improvement in MEMS device fabrication precision and extended durability enabled by the introduction of new materials.

These devices are typically minimally invasive with very small power requirements, meaning they are ideal for instrument array applications. This is meaningful for thermal hydraulic experimentation applications because the data collected from a micro-scale instrument array can be used to validate high resolution numerical results common for modern thermal hydraulic simulation efforts. The potential advantages of MEMS devices when deployed in an array formation are a key motivation for development of this approach. Future safety monitoring instrumentation goals such as passive wireless communication and local environment or carrier signal power scavenging are enabled by low power consumption; a defining characteristic of modern MEMS applications. Other more considerable advancements such as distributed flow control systems have been demonstrated for various use-cases and may prove to be applicable to reactor thermal hydraulic instrumentation and control hardware as well.

An in-depth review of literature pertaining to modern and innovative MEMS applications, materials, and methods is available in a de-facto reference text for the industry; a three-book series called the MEMS Handbook. Information summarized in this section, unless otherwise cited, is derived from the second edition of this collection [26].

2.4.1 MEMS Development Background and Applicability Basis

A short overview of MEMS development history, design philosophy, and modern high temperature device development is presented to provide a basis for further analysis of design options related to HTGR instrumentation development. Traditional MEMS materials and fabrication techniques are also explored so that key high temperature performance characteristics can be established based on the known operation limits of these contemporary devices.

Advanced manufacturing processes capable of producing micro-scale devices have seen considerable development interest since the early 1980's, corresponding to key advancements in batch processing for integrated circuit manufacturing. These devices are designed to operate under micro-scale-domain physical forces, often leveraging the non-linearity of applied force balance with relation to size. For example, gravity is almost non-impacting at the micro-scale; whereas forces such as surface tension and electrostatic attraction are far more significant. Some unexpected benefits can be gained through exploitation of this force imbalance, reinforcing the attractiveness of very small-scale device manufacturing applications to novel sensor development.

Traditionally MEMS devices have been composed of silicon or silicon composites, although an increasing amount of interest is being directed toward various carbides, oxides and other durable ceramics. The prominence of silicon as a substrate material is again due to the origin of the technology being connected to miniaturization of integrated circuits on silicon substrate. This poses a problem for high temperature reactor applications, as silicon has a commonly defined semiconductor operating limit of around 300 °C and experiences physical deformation and deterioration around 1,400 °C. Ideally a sensor developed for application to HTGR environments would be operable even at the highest expected core temperatures, which is around 1,200 °C for coolant interfaces for a number of HTGR core designs. It should be noted that the reference design selected for this investigation, the HTR-PM, has a maximum operating fuel temperature of 932 °C, with a maximum accident fuel temperature of 1,470 °C, indicating that some designs may have environmental

parameters which fall within the mechanical operating range of silicon and would be well within the operating range of the various refractory ceramics currently being investigated.

2.4.1.1 Key Benefits of MEMS Instrumentation

As previously alluded, the key benefits of implementing MEMS fabrication methods for the development of thermal hydraulic instrumentation are significant and include precise micro-scale dimensioning and placement of sensor components, reduced cost for high volume manufacturing applications and highly complex variable geometry, direct integration into the fuel pebble manufacturing process for integrated sensors, favorable physical response due to non-linear scaling effects, and many more minor benefits related to material compatibility and harsh environment durability. MEMS fabrication has the benefit of an immense amount of commercial investment to push the constituent technologies to a level that exceeds development innovation rate of nearly all other modern technologies. By implementing MEMS processes and taking advantage of these technological advancements, thermal hydraulic instrumentation applications can be pushed forward to a new generation of data availability, reliability, and accuracy.

The most obvious benefit to MEMS fabrication methods is the micro scale of the components which can be accurately produced. The direct benefits of production at this scale are significant. Small scale sensors are minimally invasive, have inherently lower power consumption rates, can be deployed in high density arrays and benefit from non-linear scaling of physical forces and material properties. Small scale components also require less material to manufacture and are highly applicable to high volume semiconductor manufacturing methods, which significantly lowers the cost per sensor and allows for almost zero marginal cost for manufacturing variability, even for very complex sensor geometry.

The indirect or secondary benefits are less intuitive but provide significant advantages which are not present with larger scale sensor hardware. These benefits include application of stochastic numerical methods for cross-calibration and error correction due to the large

number of sensors which can be deployed in a local region and derived differential measurements enabled by parameter variation between sensors in a local array. Local environmental power scavenging and wireless communication are also much easier to implement due to the aforementioned low power consumption and high geometric precision for fabrication of integrated antenna and RF attenuators.

The non-linear scaling of physical forces can also result in some additional difficulties. Thermal and electrical insulation between components can be very difficult or impossible, given the close proximity of materials. Attaching interface components such as signal wires or mounting hardware can be extremely difficult, as any component not integrated into a single unified manufacturing process will have very large uncertainty with regard to differential alignment of components.

Overall, the benefits observed are a compelling reason to pursue MEMS fabrication methodology for production of thermal hydraulic instrumentation. If even a fraction of these benefits can be realized and applied to HTGR instrumentation systems, massive improvements in instrumentation accuracy, reliability, durability, and density could push measurement systems forward to a more prominent and useful role within reactor development and operation practices.

2.4.2 MEMS Design and Fabrication Philosophy

To best utilize the benefits previously described, the design philosophy of sensor development using MEMS fabrication methods is significantly different than those implemented for fabrication methods for contemporary instrumentation. These differences in philosophy can be attributed to the batch processing methods used for semiconductor manufacturing, the extremely high material quality and environmental standards of the manufacturing processes, integrated measurement and testing processes inherent to integrated circuit electronics manufacturing, and the application of the fabrication process as direct integration to the target substrate. Each of these differences are explored to determine how they might inform the specialized development effort presented.

Batch processing used in semiconductor manufacturing typically relies on highly accurate, repeatable processing steps sequentially applied to a monolithic substrate, such as a silicon wafer, that is transported to each processing station and can produce hundreds of unique components from a single substrate unit. Due to the primary driver of development of this manufacturing strategy being the highly complex geometry found in integrated circuits, the resulting batch processing methodology is highly automated and capable of producing a high volume of complex components with extremely tight geometric and material tolerances at a very low cost per unit. Design-driven features such as geometric parameter variation between sensors are reduced in cost so significantly as to make them practically free, due to the use of automated pattern lithography and chemical etching and deposition sequences that gain no efficiency benefit from geometric uniformity between sensor components. Hundreds of sensors, all with unique geometry, can be fabricated in a single sequence for nearly the same cost of hundreds of sensors with identical geometry. Measurement and verification of unique geometry also imposes no additional cost when compared to identical geometry, as the methods employed are again not sensitive geometric complexity variations with respect to throughput efficiency.

Because integrated circuits are electronic components which are extremely sensitive to variations in material composition and are of such a small size that even nanometer-scale variations in substrate geometry or foreign contamination can be detrimental to the manufacturing process, an entire industry has been developed to provide ultra-high-quality crystalline substrate at a very low cost. The substrates typically used in semiconductor manufacturing are extremely pure and have a well-defined crystalline structure which enables highly repeatable processes and reduces manufacturing defects. The environments in which photolithography is performed is almost entirely free from contamination and very low pressure, again reducing deviations in the manufacturing process and decreasing the probability of defects. This high confidence in process and environmental variables enables design strategies in which confidence in material properties is very high and testing for functionality which is sensitive to material variations can be reduced or eliminated if a geometric verification can be performed instead. This simplifies the manufacturing

process and again helps to drive costs per sensor even lower. This benefit may not be realized for this specific application, as it depends on the functional parameters of the final sensor design. If contemporary fuel pebble manufacturing methods must produce the initial sensor mounting substate because the approach of attaching independent sensor hardware to unfueled pebbles can't be utilized, then these benefits related to material composition would obviously not be realized.

The process of semiconductor manufacturing must integrate measurement and testing functions into the manufacturing sequence and this integration provides some benefits for design philosophy. Because silicon wafers are typically moved to various machines to perform specific steps of the fabrication sequence, each machine must be able to measure the features of the wafer extremely accurately to align processing steps to substrate geometry. This enables measurement and verification of geometric features as an integrated function which can be utilized to again simplify the fabrication process and ensure calibration of sensor performance without the need to functionally verify each individual sensor after manufacturing is complete.

Finally, the concept of direct fabrication onto the surface of the target measurement substrate, in this case an unfueled pebble, provides some design advantages that could be realized. Application of the sensor material directly to the heat transfer surface being investigated removes any uncertainty regarding relative instrument positioning and thus improves confidence in measurement validity with respect to differential analysis. Integration of sensor components into the measurement substrate also inherently links the sensor to the material processing steps required for manufacture and can greatly simplify the overall production of the resulting instrument assembly. The benefits of direct fabrication must be evaluated against the drawbacks of possible material uncertainty to determine the design philosophy which will be ultimately implemented for this investigation.

2.4.3 MEMS Materials

MEMS instruments are often referred to as “a system of materials” because they depend so heavily on material parameters for operation. The scale at which the instruments function is highly sensitive differential material response to thermal and environmental exposure. In fact, many instruments leverage this response as their driving functional measurement method. Materials useful for MEMS fabrication are reviewed in this section, including both contemporary materials and specialized materials for use in high temperature or harsh environment applications.

The primary substrate material used with MEMS fabrication methods is silicon. This is the origin of many early fabrication techniques and is still the most widely used material for sensor fabrication, especially for semiconductor-based sensors. Silicon is available in a number of forms with varying chemical, structural, and electrical characteristics which make them uniquely suited and useful for a variety of purposes related to semiconductor and micro-scale mechanical device fabrication. Alternative substrate materials which are more suitable for high temperature applications include a range of carbide and oxide ceramics. These materials have strong resistance to chemical corrosion and thermal degradation, making them stable at high temperatures, but these properties also make traditional MEMS fabrication processes more difficult. A balance must be found between operational durability and ease of fabrication when utilizing these alternative substrates.

Many MEMS thermal devices utilize thin metal films as conductors, actuators, sensing elements, or shielding elements. These metal films are typically applied via a range of deposition techniques; including plasma evaporation, sputtering, electroplating, and chemical vapor deposition (CVD); all of which will be covered in the next section. For the stated purposes of this investigation, only sensing element and masking metals compatible with high temperature operation, such as platinum or nickel will be reviewed, as those are the most likely metal materials and film applications for thermal hydraulic instrumentation development.

Although a few of the following substrate and sensor materials are considered to be useful at low temperatures only, understanding their properties and applications will be useful for comparison to high temperature materials. Many of the fabrication techniques proposed for high-temperature materials still utilize silicon composites for molds structures; etch masks, and electrical insulators, so reviewing these materials is still applicable, even if these low temperature materials are not utilized directly in the final sensor assembly.

2.4.3.1 Mono- and Poly-Crystalline Silicon (Si)

Identified primarily by possessing a single, continuous lattice crystal structure, single-crystal silicon is the most well characterized material used in semiconductor applications and is typically used as a base substrate in MEMS fabrication due to widespread availability and low cost. Silicon crystal has a band gap of 1.1 eV and a cubic crystal structure. The material is very stable and performs well in benign environments. Silicon can be easily doped with impurities to alter its conductivity and is readily machined using isotropic or anisotropic chemical, plasma, or laser etching procedures.

Silicon is considered to have a semiconductor operating temperature limit of around 300 °C, but is mechanically useful to much higher temperatures. Silicon begins to deform and deteriorate around 1400 °C, which could make it useful as a structural material in relatively high temperature applications.

Poly-silicon or poly-crystalline silicon is the most widely used structural material for MEMS devices and has a wide base of support for micro-machining operations. This is due to the convenient application methods using film deposition which allow for rapid fabrication of surface machined structures. Poly-silicon can be doped with impurities to alter its conductivity for sensing features used in MEMS instruments. It is also highly resistant to silicon dioxide etching compounds (hydrofluoric acid), allowing precise chemical etching processing when the two materials are used for etch boundary control. This technique allows very fine geometric structures to be created and parted from substrate with relative ease.

2.4.3.2 Silicon Dioxide, Silica, and Quartz (SiO_2)

Silicon dioxide, or silica, is the most commonly used sacrificial and masking material for MEMS devices. It can be thermally developed on silicon substrates or deposited using a variety of processes. Silicon dioxide is typically produced in the temperature range of 900 °C to 1000 °C in environments with an oxygen or steam atmosphere. Deposition techniques utilizing this temperature range are often referred to as thermal methods. The maximum practical film thickness is approximately 2.0 μm due to the self-limiting nature of the high temperature growth process. A low-temperature oxidation (LTO) deposition process can be used to create film thicknesses greater than 2.0 μm, however the deposition rate is reported to be considerably reduced when compared to the high temperature alternative. Including a doping gas, such as phosphorous, into the deposition process can create a distinct form of silicon dioxide with altered material properties called phosphosilicate glass (PSG).

These materials, thermal SiO_2, LTO deposited SiO_2, and PSG, are the are the three most applicable forms of silicon dioxide for MEMS fabrication and are all electrical insulators useful for different specialized applications. Quartz, which is a single crystal variant of SiO_2, is finding increased application thanks to its electrical insulation characteristics in addition to piezoelectric properties created by its unique crystalline structure. Alternative fabrication methods, such as nickel mold deposition, enable creation of very large structures composed of SiO_2. Silicon dioxide and quartz substrate wafers are also commercially available in various grades and crystal orientations, simplifying the process of MEMS fabrication utilizing these materials if the required processes do not require an initial silicon substrate to be used.

2.4.3.3 Silicon Nitride (Si_3N_4)

Silicon Nitride is the most widely used electrical isolation material for MEMS devices. It also has uses for surface passivation, etch masking, and as a mechanical material. It has very high hardness and good thermal stability, as well as being relatively chemically inert.

Two deposition methods are commonly used to deposit silicon nitride films, low-pressure chemical vapor deposition (LPCVD) and plasma-enhanced chemical vapor deposition (PECVD) which will both be described in the fabrication techniques section. Deposition rates are relatively low, around 30 Å/min. Specialized source gasses are used with a specific feed rate and feed location depending on the geometry of the deposition chamber, typically relying on process-limited deposition to ensure even film thickness.

Thick films of silicon nitride tend to crack due to high tensile stress in the resulting film, limiting maximum thickness to a few hundred angstroms. This can be overcome by injecting extra silicon source gas into the deposition chamber, resulting in silicon doping in the material that reduces tensile stress in the film.

2.4.3.4 Silicon Carbide (SiC)

Silicon carbide has long been the ideal choice for harsh environment semiconductor development. Silicon carbide is naturally polymorphic, meaning that multiple crystal structures share a common stoichiometry. Cubic, hexagonal, and rhombohedral polytypes exist, with 6H-SiC being the most temperature insensitive material for semiconductor applications with a band gap of 3.2 eV. Silicon carbide is very resistant to chemical processing, meaning wet etching is limited to aggressive techniques such as high temperature baths in strong base solutions such as KOH. Dry etching (fluoride-based plasma) is generally preferred, but material removal rates are significantly slower than with other silicon composites.

Deposition of single-crystal SiC onto silicon substrate for the purpose of surface machining fabrication can be accomplished only via 3C-SiC deposition onto silicon, due to the shared cubic crystal structure. Polycrystalline SiC, however; can be deposited onto a number of substrates, including poly-silicon, silicon dioxide, and silicon nitride. A number of deposition methods are also possible, meaning fabrication options are varied and can be device specific.

A number of complex geometries comprised of SiC have been demonstrated through the creation of micro-scale pumps and gas-turbines, among many other complex, three-dimensional shapes. These are typically produced using a silicon mold fabrication technique (discussed in the fabrication techniques section) along with 3C-SiC or poly-SiC deposition.

2.4.3.5 Carbon, Graphite, and Diamond (C)

Diamond is a very attractive material for MEMS development due to its extreme hardness and large semiconductor band gap at 5.5 eV. Un-doped diamond is a relatively good insulator; alternatively, the addition of boron as an in-situ dopant results in a p-type conductor. Thermal oxidation does not develop on diamond surfaces thanks to carbon monoxide and carbon dioxide being gaseous and diffusing readily under normal conditions. Passivation coatings can also be used to limit oxidation rates in high temperature environments. Diamond possesses an extremely high young's modulus, meaning that it is an ideal material for resonator construction; which can be useful for wireless communication applications. Oxides can be deposited via other means if necessary, although an additional fabrication step is then required.

Diamond deposition is limited to polycrystalline and amorphous material structure. Diamond epitaxy is relatively undeveloped and large-scale single crystal growth has yet to become a realization. Polycrystalline diamond can be deposited onto silicon or silicon dioxide surfaces provided the surfaces have been prepared properly. Typically, this involves surface roughing and seeding or a process called 'bias enhanced nucleation' which produces a strong negative charge on the deposition surface. Silicon and silicon carbide molding practices can produce complex geometry utilizing differences in carbon deposition rates for the two materials. Because of the relative ease of doping the polycrystalline structure as it is being deposited, insulating and semiconducting regions can be used to produce single material sensors, useful for avoiding sensor distortion via differential thermal expansion.

Chemical etching is practically ineffective for diamond substrates, having a material removal rate that is extremely slow. Oxygen plasma etching techniques are effective for thin diamond films, but significantly slower than for other substrate materials, requiring a durable metallic etching mask such as aluminum or nickel to protect un-etched surfaces. Previous attempts at surface machining of diamond thin films have sometimes resulted in high surface stress in the components, an effect that is not well understood and may be a considerable difficulty to overcome for these fabrication techniques.

2.4.3.6 Aluminum Oxide, Alumina, and Sapphire (Al_2O_3, α-Al_2O_3)

Aluminum oxide, or alumina, is widely used as an electrical and thermal insulator in instrumentation applications. The powdered insulation used in metal sheathed thermocouples and RTDs is commonly comprised of alumina or magnesium oxide. Although alumina is not widely used in MEMS fabrication, it is well characterized as a deposition material commonly used for electrical insulation and surface passivation.

Alumina is very chemically inert and is commonly used to encapsulate platinum thin films to prevent platinum silicate from forming on platinum structures deposited on silicon substrate. Alumina pairs well with platinum for thermal instrumentation because it has a similar structural epitaxy and coefficient of thermal expansion.

Alumina is widely considered to be an excellent high temperature insulator, although it does undergo grain-phase transition to its alpha phase during prolonged exposure at high temperatures. Mono-crystalline alpha alumina (α-Al_2O_3) is also called sapphire and is widely utilized as an optical material for high temperature instrumentation. Sapphire is extremely stable at high temperatures and exhibits an optical-axis-dependent coefficient of thermal expansion. Natural sapphire contains trace amounts of chromium, which has good epitaxial compatibility with alumina and is sometimes used as an adhesion promoter at material interfaces. This is especially common when using platinum thin films on sapphire substrate, although chromium does thermally diffuse into the platinum film at high temperatures.

Wafers of alumina are widely available for direct fabrication processes utilizing the material as a substrate. Sapphire wafers are also available in a variety of crystal orientations, although the material is very expensive in large diameter wafer form and only available in relatively small wafer sizes due to the difficulty of growing very large crystals without interstitial lattice defects.

2.4.3.7 Platinum and Platinum Alloys (Pt, Pt-Rh, Pt-Mo)

Platinum has seen widespread use in flow instrumentation due to favorable material characteristics when used as a sensing element. High resistance to corrosion limits instrument drift and a nearly-linear temperature dependence of electrical resistivity enables its use as a resistance temperature sensor over a wide temperature range.

MEMS based thermal sensors typically utilize pure platinum as a sensing element. This includes resistance temperature detectors (RTD), strain gauges, and thermal anemometers. Hot wire anemometers specifically are limited to operation below approximately 1,100 °C due to the mechanical material limitations of pure platinum.

Various platinum alloys can increase this temperature range, as demonstrated by industrial refractory thermal instrumentation, such as B-, S-, and R-type thermocouples, which utilize varying concentrations of platinum-rhodium alloy to achieve operating ranges of up to 1,800 °C. Alloys of platinum and molybdenum are also useful for high temperature operation, with thermocouples utilizing this alloy capable of operation at up to 1,600 °C. These types of thermocouples are preferred over rhodium alloy types for nuclear reactor core environments, as molybdenum has a relatively low neutron cross section compared to rhodium and results in greatly reduced radiation-induced calibration drift.

2.4.3.8 Nickel and Nickel Alloys (Ni, Ni-Ti)

Nickel is commonly used as an etching mask for dry etching processes in MEMS fabrication, as well as a high temperature material for heating elements and strain gauges. Nickel is a very hard, chemically resistant material that can be deposited in thin or thick

films via a number of application methods. Alloys of titanium and nickel are used as micro-actuators due to the alloy's shape memory (spring) characteristics.

Nickel may be useful as a masking agent for high temperature processing due to its relatively high melting temperature. Deep reactive ion etching (DRIE) is a useful dry etching technique for high temperature materials and utilizes nickel masks extensively due to the relative ease of application when using electroplating or other rapid deposition techniques.

2.4.4 MEMS Fabrication Methods

MEMS fabrication techniques are somewhat unique in that complex geometry can be created by repeating a series of relatively simple processing steps. MEMS fabrication methods are derived from silicon manufacturing processes and are similar to other additive manufacturing techniques in that the object geometry is slowly built in layers. A key difference is that MEMS fabrication also employs material removal processes which increases the possible range of material and geometric complexity significantly. Essentially all MEMS fabrication methods can be classified as additive, subtractive, or transformational. Chemical or physical deposition and doping are considered to be additive because they add material to the substrate. Plasma or chemical etching and micromachining are considered to be subtractive because they remove material from the substate. Curing, annealing, and thermal purification are all considered to be transformational because they alter the chemical or crystalline configuration of the substrate without actually adding or removing any material.

Examples of well established, MEMS-based fabrication techniques for complex geometry are available from a number of closely related industries with similar operating requirements at lower temperatures. Devices such as resonators, cantilever beams, bridge structures, capillary channels, and micro-scale turbine blades have been efficiently manufactured from poly-crystalline diamond and other rugged materials using variations of these techniques. Each process was novel in some respect, requiring the exact process

parameters and sequence to be adjusted depending on the geometry and composition of the final component. This would also be the case for development of a MEMS sensor, as the specialized geometry and substrate is unique when compared to those in literature.

Deposition techniques for MEMS fabrication are primarily composed of chemical vapor deposition (CVD) and physical vapor deposition (PVD) methods. CVD relies on a chemical bonding process that occurs between the target surface and an injected source gas while physical vapor deposition relies on thermal vaporization of the deposition material which then diffuses onto the target and condenses. Both of these methods have significant variation in process parameters depending on the deposition and target material.

Practical techniques for material removal concerning MEMS device fabrication fall into two distinct categories. These are wet etching techniques (chemical) and dry etching techniques (plasma). High temperature materials are typically extremely resistant to chemical corrosion, so plasma etching is often the most practical material removal technique. Other processes include micromachining, which utilizes a cutter or grinding disc to mechanically remove material, and laser drilling and machining, which utilizes a high-power laser to cut or selectively melt material.

In addition to these stand-alone processes, a number of specific process sequences are important to recognize. These are processing steps that are pre-formed in a defined order to achieve a specific goal. The primary process sequences useful for review are the lift-off and silicon molding sequences, which both combine multiple steps of deposition of a masking agent with lithography and other chemical processing steps to create a selective region in which material is added to the substrate. The lift-off sequence in particular is a process which is widely utilized in MEMS fabrication and varies slightly depending on the exact materials selected, but the basic steps are reviewed in this section for later reference.

2.4.4.1 Chemical Vapor Deposition (CVD) and Thermal Oxidation Deposition

Low Pressure CVD (LPCVD) is used for deposition of a wide variety of relatively low-temperature materials, but is most widely developed as a deposition method for poly-silicon thin films. A reaction-controlled deposition process is preferred for large batch machining using automated tube furnaces with specialized source gas injection lines. Typical deposition rates are on the order of 100 Å/min. Maximum film thicknesses for MEMS applications are typically limited to 5.0 μm using this technique.

Epi-poly deposition is a CVD process used for deposition of poly-crystalline films with thickness in excess of 10.0 μm. This is achieved through elevated heating of the substrate material (beyond 1000 °C) and can produce deposition rates in excess of 1.0 μm per minute. A LPCVD seed structure deposited on a sacrificial oxide film can be used to control material properties such as nucleation, grain size, and surface roughness.

The thermal oxidation deposition process is considered a unique form of CVD and is used to deposit silicon dioxide films around 2.0 μm in thickness. It is highly adaptable and self-limiting due to the limited material availability at the surface of the substrate. The deposition rate is on the order of 100 Å/min using a hot-wall low-pressure procedure. Typically processing temperatures are on the order of 900 to 1000 °C when using oxygen or steam as an oxidizing material source.

Low temperature oxidation is an LPCVD process that can be used for film thicknesses in excess of 2 μm. The material is deposited rather than created at the surface of the substrate and is performed at significantly lower temperatures, typically around 400 to 500 °C with pressures from 200 to 400 mtorr. Extra source gasses can be included to produce as-deposited doped films. This technique is commonly used to produce phosphosilicate glass (PSG) using phosphorous seed gas.

2.4.4.2 Thermal Evaporation Physical Vapor Deposition (PVD)

Evaporation deposition techniques are PVD techniques useful for relatively rapid deposition of material onto a given surface. Material is exposed to a very high temperature heat source, such as an electron beam or plasma arc, in a vacuum chamber and forms a vapor in the immediate area where it evaporates. This vapor diffuses and is deposited in a line-of-sight, Maxwellian distribution on the target surface as it collects and condenses. This technique is applicable for a wide variety of materials, but metallic elements tend to the most appropriate materials for this technique.

2.4.4.3 Wet Etching (Chemical Etching)

Material removal techniques which submerse the work piece in an agitated, sometimes heated, chemical bath which chemically corrodes exposed material are collectively termed wet or chemical etching techniques. A large number of chemical compositions, temperatures, pressures, and exposure times have been employed to etch a wide variety of materials. Typically, these techniques are most suitable for etching silicon and silicon composite materials due to their distinct chemical characteristics, allowing selective removal of a precisely measured amount of material.

The major benefit of chemical etching techniques is the ability to etch single-crystal substrates along selective crystal planes, this is called anisotropic etching and is used to produce very well-defined cavities with sharp walls and corners. There are limits to the applicability of this technique, determined by the crystal structure of the target material and the specific chemical makeup of the etching solution; however, this advantage over dry etching techniques, which are mostly considered to be isotropic, is significant and very important for specific MEMS fabrication practices.

Patterning and masking techniques are extremely important to chemical etching methods due to the complete immersion of the work in the chemical solution. Photolithography has long been the choice for patterning but does have scaling limitations when fabricated features reach the order of the wavelength of the exposure light source. Masking and

etching materials and chemicals are applied for specific applications and are often metallic or oxide thin films (masks) and highly caustic chemicals (etchants). Undercutting and corner compensation techniques constitute a well-developed body of knowledge within wet-etching literature. Careful selection of specific crystal lattice orientations ([100] or [110] typically) depending on the etching geometry required is an important consideration among many other parameters to consider.

Etch stop techniques allow selective depth or volume etching depending on the application. Selective doping, electric currents, laser-assisted etching, and timing techniques among others can allow for the etching process to be finely controlled in three dimensions when the proper preparation steps are taken.

2.4.4.4 Dry Etching (Plasma Etching)

Material removal techniques which utilize energized free radical particles which attack the target surface and remove material in all directions (isotropic etching) are commonly classified as dry or plasma etching techniques. Initial development of plasma etching techniques was limited to isotropic etching because the plasma dynamics and control mechanisms were not well understood until relatively recently. This is especially true for high volume plasma etching processes, where radical production is focused on delivering a high etch rate, rather than precise control of the radical interaction with the substrate.

Modern development of plasma etching techniques which selectively remove material in a single direction (anisotropic) has resulted in relatively new methods which can produce features similar to anisotropic wet etching. This process is collectively known as reactive ion etching (RIE) and is the result of a specialized approach which produces ions approaching the target from a single direction. A variant on this approach, a called deep reactive ion etching (DRIE) can be used to etch deep pockets and high aspect ratio holes in the target medium. These methods are typically highly specialized depending on the target material being etched and are relatively slow compared to isotropic etching methods.

When machining silicon, etching gases typically contain chlorine or fluorine, which when radicalized, will react with the silicon in the target. Oxygen etch gasses are typically used to remove photoresist films and have seen recent use as the most effective method of plasma etching diamond substrate.

Although dry etching is more effective than wet etching techniques for very inert materials, the material removal rate is still very slow for diamond or silicon carbide. A small amount of material removal is possible, but fabrication processes which require large amounts of material removal should be avoided for a number of reasons, all of which are related to the slow material removal rate causing localized stress on the substrate being processed.

2.4.4.5 Laser Etching, Micromachining, and Drilling

Laser drilling techniques are the method of choice for producing high aspect ratio holes in diamond and other chemically inert substrates. A wavelength of laser transparent to the target material is selected and a thin layer of carbon or another appropriate thermal target is applied to the surface. The laser then burns a fine hole though the substrate as it heats the surface carbon and continues to produce opaque thermal target materials as the hole is developed. Holes can change direction within the substrate if naturally occurring fractures are used as transition points or if additional layers of thermal target material are added between drilling operations.

Laser cutting, micromachining, and welding are also common processes for MEMS fabrication of metallic thin films. The process is similar to that of laser drilling; however, the wavelength of laser is less important comparatively. Laser cutting of thin films can offer significant advantages for some MEMS fabrication processes, as no lithography step is required to develop a masking layer. Utilizing laser machining processes does introduce a significant thermal load onto the material being machined, which could induce oxidation or other unwanted chemical transitions if not accounted for.

2.4.4.6 Silicon Molding and Selective Annealing Fabrication Sequences

Materials useful in extremely harsh environments, such as the carbide ceramics presented in the previous section, are durable because the chemical bonds between the constituent atoms are very strong. This means that some traditional fabrication techniques, such as chemical etching and micromachining, aren't effective in removing material from the substrate. To effectively shape these materials, alternative methods must be used. Methods which avoid the need for material removal or selectively alter the material to remove have proven to be the most effective methods for MEMS fabrication utilizing very durable materials.

Silicon-molding is a very clever and useful process for shaping very hard or inert materials. This technique utilizes silicon to create a cavity or mold which is then filled with a selected durable material. The silicon is then removed via chemical etching processes, leaving only the durable material shaped by the mold geometry. Creating a silicon mold can be done in various ways, but is usually performed by etching an outer mold cavity out of a standard silicon wafer. This mold is then seeded and the polycrystalline substrate of choice is deposited. The surface is then mechanically polished and the silicon is etched away using a wet etching method, releasing the deposited product as a freestanding component.

If the component needs to be attached to the substrate surface, an alternative method is to start with the chosen substrate and then alternately deposit silicon and the durable substrate to shape the resulting geometry in layers. This process can be more difficult, as each layer of silicon must be processed before the substate material can be added, but it does enable more complex geometry than is possible with simple molds. The final step is to etch away all silicon and reveal the deposited substrate as a freestanding object.

Another option for shaping durable materials is to use selective annealing to alter the properties of a material to allow for easier etching or mechanical removal of material. The final geometry would then be hardened via doping or a thermal process to transform the material and make it more resistant to operational environments.

2.4.4.7 Lift-off Fabrication Sequence

A lift-off fabrication sequence refers to the use of selective deposition of material to create a three-dimensional structure in layers. Essentially, any deposition process that is not intended to cover the entire surface of the substrate will likely use a type of lift-off sequence to remove the areas of material deposition which are not intended to be included in the final structure being developed.

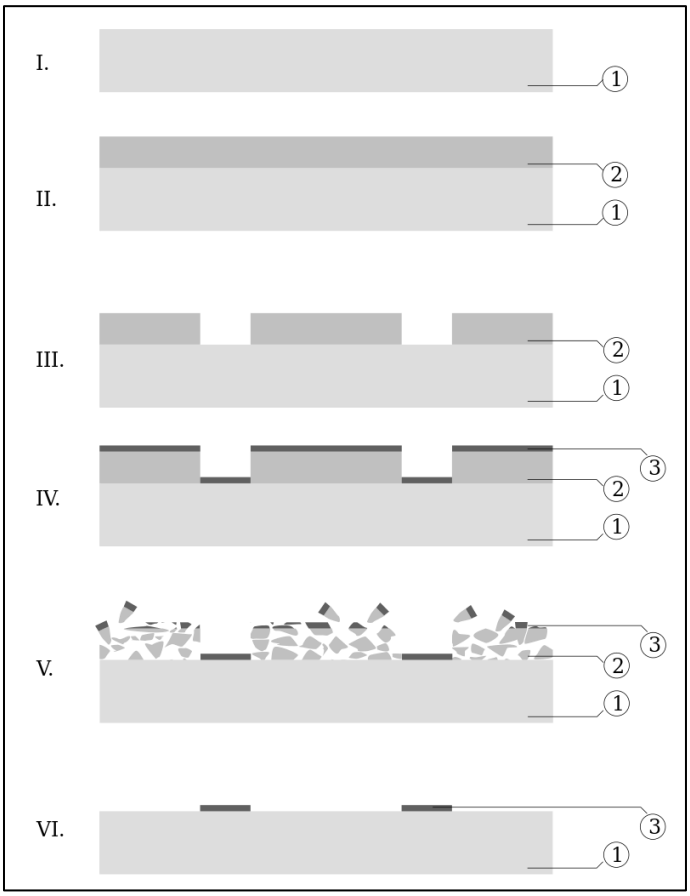

Figure 2-11: Diagram of lift-off sequence (1: substrate, 2: photoresist, 3: deposited material) [64]

Utilizing a lift-off sequence begins with coating the substrate in a photoresist fluid, identified as step II in Figure 2-11. This fluid is typically selected to have chemical properties compatible with the substrate and material being deposited, as well as good

transition characteristics which are compatible with the lithography system selected for developing a pattern on the photoresist. The fluid is added to the top of the substrate wafer, then the substrate wafer is spun to create a uniform film thickness of photoresist. The photoresist is then 'baked' by placing the substrate wafer in a heated chamber to dry. This process causes the layer of photoresist to adhere to the substrate wafer and form a semi-solid, gel film.

This film is then exposed to a specific wavelength of light by a lithography machine. A lithography mask is used to selectively expose areas of the film for a specified period of time, which causes the exposed area to harden or cure. The substate wafer is then cleaned with a chemical solution which only removes the un-hardened photoresist, leaving only the exposed, cured photoresist in place. This process is depicted in step III of Figure 2-11.

In step IV of Figure 2-11, a layer of material is then deposited across the entire substrate wafer via one of the deposition processes described in the earlier sections. This layer adheres to the substrate in the areas where the photoresist was removed, and adheres to the photoresist in the areas that were exposed to the lithography light source and hardened.

Finally, in step V of Figure 2-11, the substrate wafer is placed in a chemical bath to selectively dissolve the hardened or cured photoresist. This removes the deposited layer from the areas which were covered by the photoresist and leaves on the areas in which the deposited layer adhered directly to the substrate. This process can then be repeated many times to selectively add material in layers of precise thickness.

The lift-off process sequence is very inexpensive, accurate, and adaptable to a wide variety of materials and structure geometries. Some common difficulties arise from very narrow features or from unintended adhesion of the deposited material layer to areas covered by photoresist. These problems can typically be avoided by adjusting the processing parameters, such as type of photoresist or chemical bath temperature and solvent concentration, to suit the specific geometry of the part being fabricated.

2.4.5 Advanced MEMS Instrumentation Applications and Innovations

Integration of MEMS sensors into environments or processes which would be otherwise difficult or impossible for contemporary instrumentation is the best demonstration of the unique advantages presented by MEMS fabrication methods. MEMS sensors, particularly those which utilize wireless data transfer, are being used in harsh environments and enabling new monitoring and analysis methods to increase the safety and efficiency of processes which were previously difficult to accurately characterize. A selection of innovative MEMS and thin film instruments are reviewed in this section to provide a contextual overview of the state of development for harsh environment and wireless MEMS instrumentation which utilizes the materials and fabrication processes presented in the previous sections.

2.4.5.1 MEMS Thermal Hydraulic Instruments for Harsh Environments

Many innovations in MEMS development are concerned with the utilization of ceramic carbide and oxide materials for instrument construction. Innovations concerning the development of silicon carbide semiconductor electronics for wireless communication in harsh environments are progressing, demonstrating operation at temperatures of up to 450 °C when coupled with a Pt-Pb thermocouple [58], or operation at temperatures of up to 300 °C when utilized directly as a semiconductor temperature sensing diode [65]. Silicon carbide semiconductor temperature sensing diodes have also been paired with silicon carbide heaters to create a robust ceramic flow sensor [66].

Many different types of thermal hydraulic instrumentation are possible to deploy via MEMS instrumentation packages. The most basic of these are thermal sensors such as RTD- and thermocouple-based heat flux sensors, often in array formations [28] [67]. NASA has recently developed multiple types of multi-functional MEMS instrument packages for use in propulsion testing facilities, depicted in Figure 2-12 [68]. The use of Nickel, as well as other alternative sensor conductor materials, has yielded good results for applications in chemically corrosive environments [69]. Recent demonstrations of innovative pressure sensors utilizing MEMS fabrication include a high-sensitivity

capacitive pressure sensor for ultraclean environments [70], as well as a very clever zero-temperature-coefficient diaphragm pressure sensor that leverages complementing material properties to mitigate the effects of thermal expansion [71].

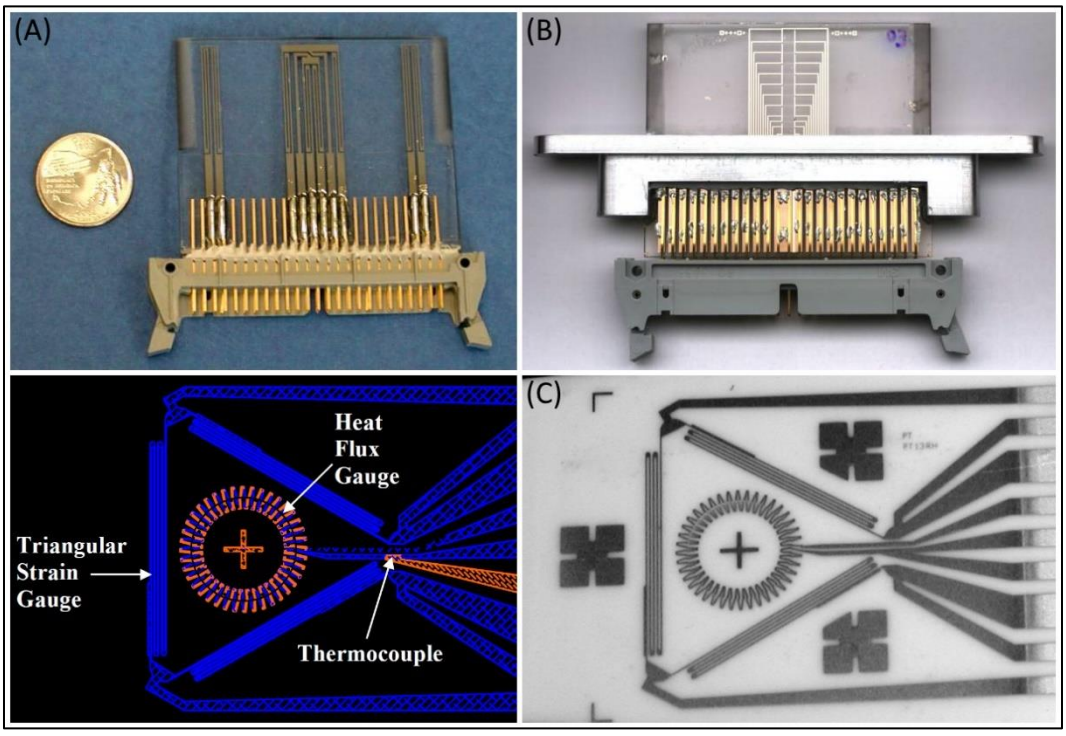

Figure 2-12: MEMS (A) mass flow, (B) boundary layer, and (C) multi-sensor instruments [68]

Harsh environment flow sensors, such as those developed for use in internal combustion engines and jet engines, must be durable and minimally invasive, providing an ideal application for MEMS flow sensors utilizing durable materials for structural and sensing elements. A range of thermal anemometers have been developed for various applications in this area. These include temperature compensated hot film anemometers which utilize platinum thin film resistors on rigid and flexible substrates [72] [73] [74] [75], and with bi-directional flow sensitivity, depicted in Figure 2-13 [76] [77], thermopile sensors comprised of titanium-tungsten and p-doped polysilicon, which are depicted in Figure 2-14 [78], silicon carbide thermal anemometers in porous silicon substrate [79], and polysilicon hot wire thermal anemometers [80].

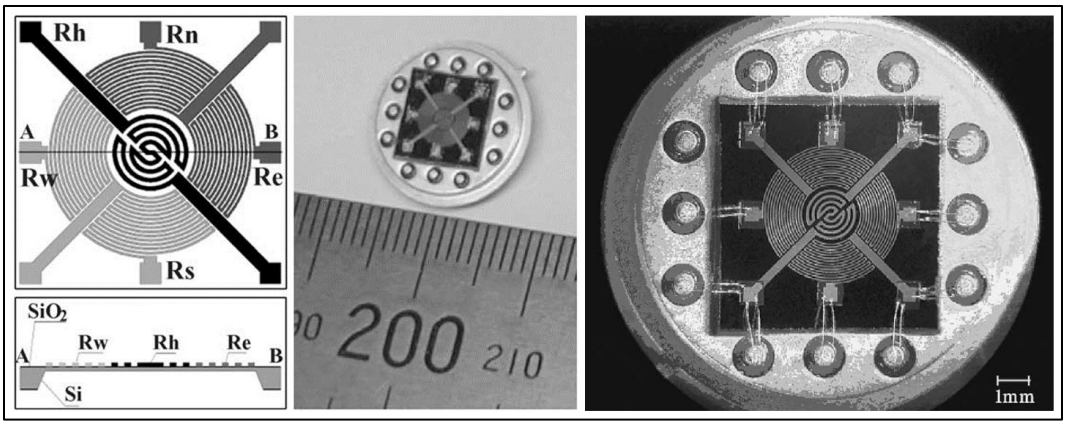

Figure 2-13: A MEMS platinum RTD bi-directional flow sensor [76] [77]

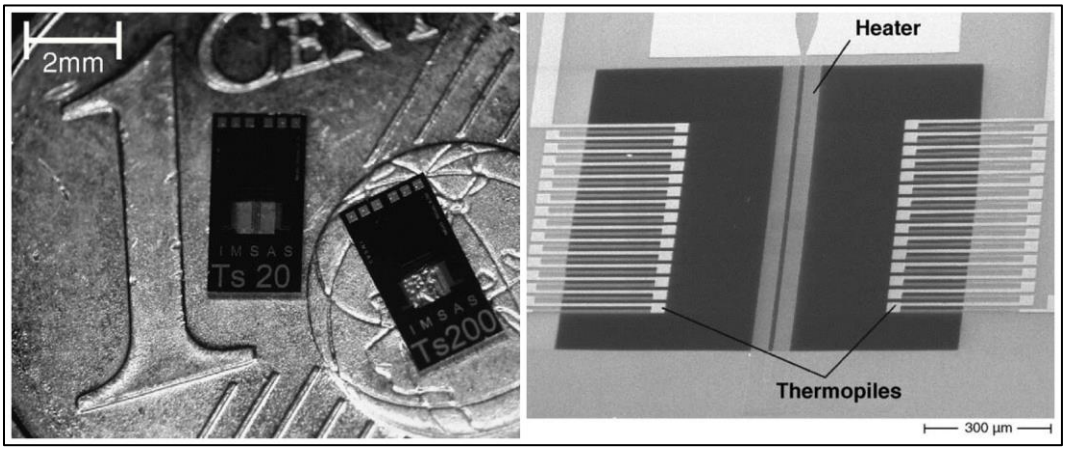

Figure 2-14: Titanium-tungsten and p-doped polysilicon thermopile flow sensor [78]

2.4.5.2 Alternative MEMS Fabrication Method Applications

Another recent innovation includes sensors which are fabricated without using the traditional lift-off method described in the previous section. Instead, these sensors utilize a direct-write fabrication process in which the sensor material is deposited as a powder suspended in a fluid, which is then sintered to produce the final sensor geometry. Examples of innovations in this area include gold RTDs developed on flexible polyimide with laser sintering, depicted in Figure 2-15 [81], flexible Cr-Ni-Pt and pure nickel RTDs on polyimide [82] [83] [84], and platinum or gold thick-film RTDs developed on curved alumina substrate [85] [28].

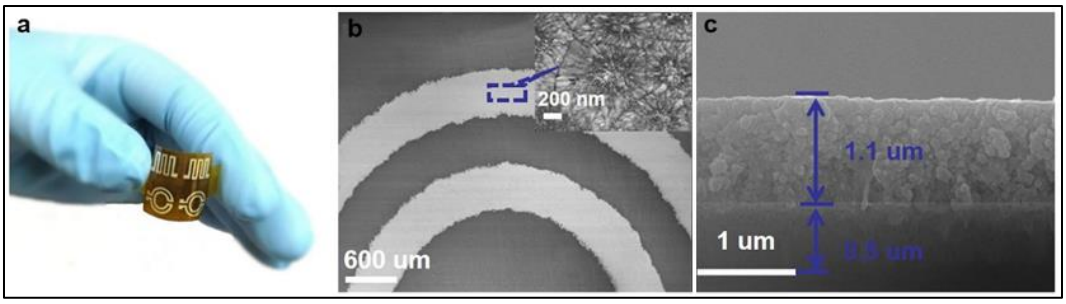

Figure 2-15: Gold-PI flexible film RTD with SEM imaging of sensor trace geometry [81]

2.4.5.3 MEMS Wireless Sensors for Harsh Environments

Innovations in wireless sensing for MEMS instrumentation have demonstrated by a range of studies over the last decade which focus on passive inductance capacitive, or LC, sensing. This method utilizes inductive coupling of a transmitter with a passive receiver, with the signal being transduced by an impedance analyzer, as depicted in Figure 2-16. This technology is commonly employed in capacitive touch screens for mobile devices and track pads for HMI devices. This method of communication can also be employed as a wireless signal transmission mechanism for RF powered, passive thermal sensors [86] [59]. High temperature pressure sensors which utilize this means of wireless communication have been demonstrated [87] [88], as well as multiplexing of a low frequency signal to read multiple devices simultaneously in this manner [89]. Multiplexing of multiple passive sensor instruments has also been demonstrated with passive RFID resonators [90].

Temperature sensors are a relatively new innovation for coupled capacitance remote sensing, but several applications have been demonstrated. These include direct fabrication of wireless sensors on turbine blades [60], flexible sensors fabricated on HTCC tapes [62], and a very promising resonance based thermal instrument that is capable of wireless operation at up to 1,400 °C [59]. All of these are promising advancements toward applicability for HTGR thermal instrumentation deployment. Commercial products have also recently become available which utilize RFID technology for various methods of threshold sensing, although their temperature range is very limited [91] [92] [93]. These

innovations support the idea that this passive capacitance coupled wireless signal transmission strategy could eventually be adapted for use in HTGR core environments.

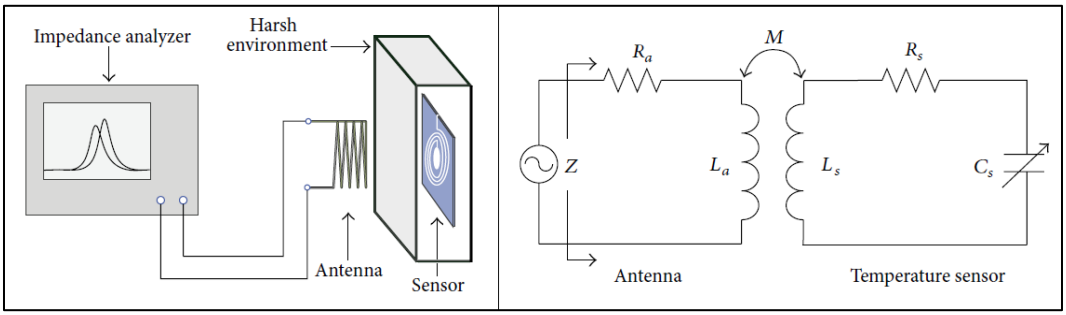

Figure 2-16: Inductance coupling system diagram [62]

2.4.5.4 MEMS Enabled Self-Calibration and Error Reduction

As mentioned previously, a key advantage of the small scale of MEMS instrumentation is that cross-correlation among local instruments can enable increased instrument accuracy and prevent the calibration drift often encountered in harsh environment applications. Several investigations of this concept have resulted in algorithms for calibration correction for thermal instrument arrays applicable to MEMS instrumentation. A good example of this approach is summarized in a 2019 study presented by Miczulski et al., in which a range of techniques were utilized to reduce the total instrument error for previously published studies. The uncertainty for measurements from 0 to 200 °C was reduced from 49.21 °C to 0.03 °C in the most significant case [94].

Another approach to calibration correction for MEMS devices is to include electronics to allow a temperature transducer to monitor parameters associated with environmental drift and correct them in-situ, before relaying the measurement signal outside of the device. This so-called “smart sensor” approach has been demonstrated with a nickel RTD sensor on alumina substrate for low temperatures [95] and may be applicable to high temperature applications if SiC or GaN semiconductors can be utilized.

2.4.5.5 Autonomous MEMS Instrument and Control Systems

The capability of MEMS extends much further than what is envisioned in this investigation for HTGR thermal instrumentation. An exciting area of development for MEMS also includes autonomous MEMS instruments which are used for active flow control on aircraft. In a 2012 investigation, a MEMS device was developed which included thermal, pressure, and shear stress sensors coupled with a MEMS actuator assembly. The instrument package could independently identify the local flow conditions and position the actuator to control the boundary flow separation point from the surface of an aircraft wing [96].

This type of autonomous response mimics organic systems, in which cellular automata describes the ability for isolated cells to recognize the conditions around them and respond accordingly, without centralized coordination. If MEMS instrumentation could be extended to exhibit this behavior with instrumentation in pebble bed core environments, wireless communication with a central safety system would be unnecessary. Active, autonomous flow control could be realized, drastically extending the possible functional thermal hydraulic range of a pebble bed core and enabling a truly progressive form of safety monitoring as well as considerable thermal efficiency improvements derived from control of bypass flow through the pebble bed core.

This application is obviously very far from realization, but the initial deployment of MEMS thermal sensors could be the first step down the path that leads to that next generation of core instrumentation and the true realization of the variable operation potential inherent in the pebble bed design concept.

3 Pebble Bed HTGR Thermal Hydraulic Analysis

In this chapter, thermal hydraulic analysis methods for pebble bed HTGR heat transfer are reviewed and are applied to the selected pebble bed reference design (HTR-PM) described in the previous chapter. From the results of this analysis, a number of parameters are derived. These include environmental parameters, which are used as bounding conditions for instrumentation development, and performance indicators, which provide targets for thermal sensor design and criteria for simulation and confirmation of functional instrument applicability. The target criteria for confirmation of applicability evaluates the functional performance of the final proposed instrument package in the target environment and identifies the apparent advantages of the proposed deployment approach relative to the contemporary HTGR instrumentation reviewed in the previous chapter.

The foundation of thermal hydraulic analysis is the characterization of the heat transfer phenomena which drive energy transfer in the pebble bed core. Thus, the first point of investigation is the primary mechanisms for pebble bed heat transfer. Key heat transfer phenomena related to safety analysis are identified and presented to provide context for later design justifications.

After a list of key equations is identified, these application of these equations to the selected HTGR reference design is explored by reviewing the most recent thermal hydraulic investigations published by the reactor developer. Using data derived from initial design studies for the HTR-PM, a continuous solution of the phenomena of interest, which is the effective thermal exposure in this case, is developed as an extension to the initial published analysis. Instrumentation development efforts then utilize this continuous characterization to target specific, realized parameters and better relate the final instrument system design to the needs and conditions of the actual reactor environment being targeted. This hybrid extension approach should provide a high level of certainty concerning the long-term applicability for the proposed instrumentation package and deployment strategy by using the high-quality analysis already published as a basis and making the extension of that analysis targeted to the specific implementation proposed.

Although the final instrument design is not specifically meant for deployment in an operating reactor, developing the instrumentation package to be deployed in an environment with similar thermal characteristics allows for the use of the proposed instrumentation in testing facilities and other full-scale research systems. These facilities don't typically don't utilize nuclear heating, but do have similar heat transport parameters and are often used to validate safety analysis for HTGR reactor systems.

Another key component of instrumentation design is development of limiting conditions for sensor operation. By using operation data from the selected HTGR installation, we can define the operating environment with a high level of confidence and initiate instrumentation design with realistic operating conditions in mind. Conditions present in different areas of the core vary greatly, thus it is critical that an envelope of operating conditions is selected which best represents the most likely conditions present for various measurement locations.

Once environmental parameters are established, we can then identify instrument accuracy, resolution, and durability requirements for operation in the proposed environment to a degree which will produce measurement output which is ultimately useful for thermal hydraulic analysis. Thermal hydraulic parameters of interest, coupled with boundary conditions derived from the expected environmental parameters, helps to define these performance indicators to a high level of confidence in later chapters. This approach is vital to ensure that parameters selected during sensor design ultimately produce data which is useful for thermal hydraulic analysis and fulfills the primary motivation of expanding safety analysis capability.

The synthesis of environmental boundary conditions along with simulated performance metrics for the proposed sensors allows for the sensor design to be theoretically functionally validated, affirming that the design is capable of producing useful output for the given operation environment and furthermore, justifying and validating the underlying approach to instrument fabrication and deployment.

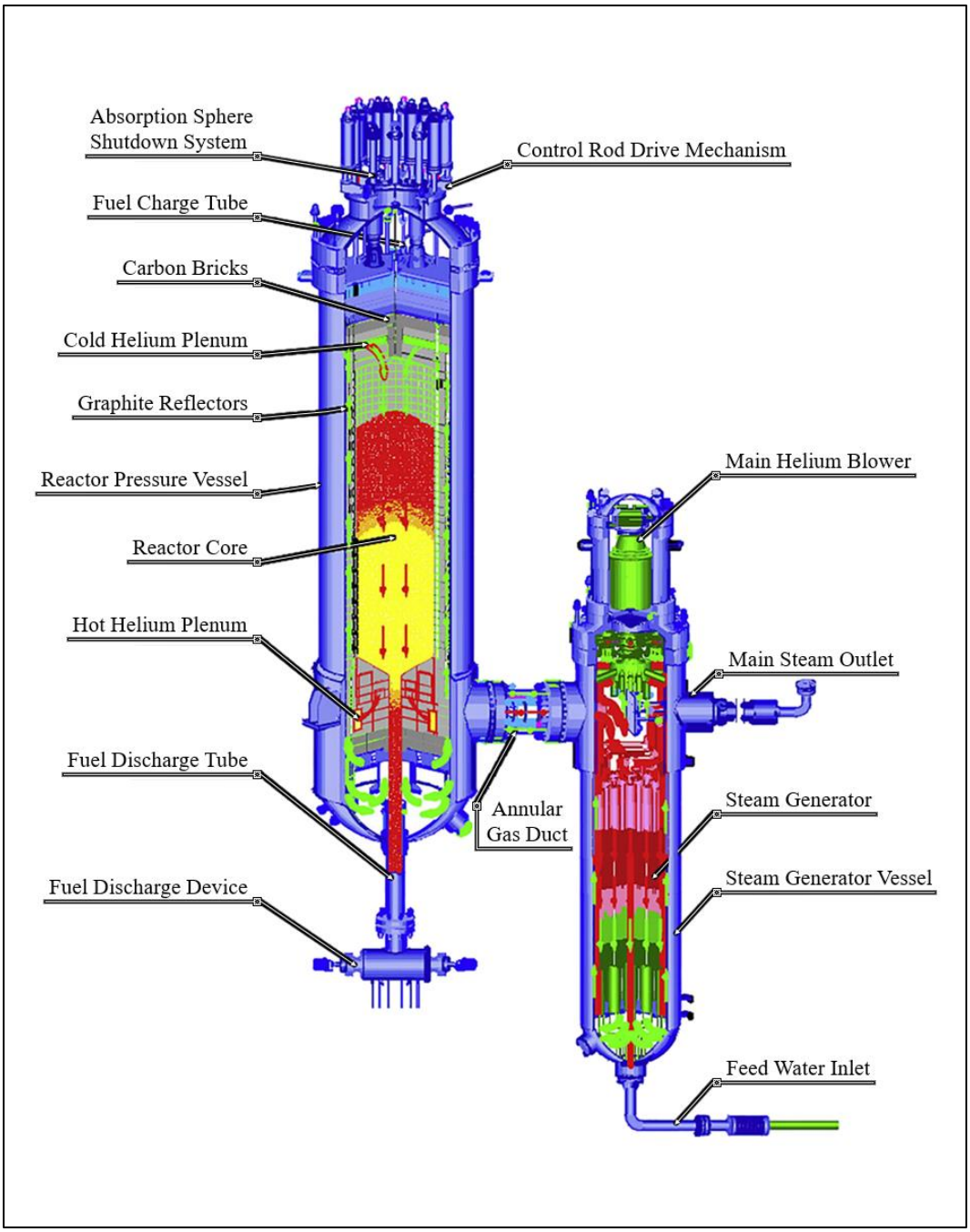

Figure 3-1: An overview of HTR-PM primary system components [97]

3.1 Pebble Bed HTGR Heat Transfer Analysis

In this section, primary mechanisms for pebble bed HTGR heat transfer are identified and key variables useful for instrumentation design are derived by considering how these heat transfer mechanisms affect phenomena of interest for thermal hydraulic safety analysis, which is a key driving motivation for reactor core instrumentation and thus, instrument development efforts. Analytical assumptions and simplifications are made and justified. The final outcome is a selection of key variables for heat transfer phenomena, which is then correlated by selection of key equations for pebble bed HTGR heat transfer. Previously documented HTR-PM environmental parameters collected from literature are applied to these equations to generate instrumentation operation targets relative to the key variables identified.

3.1.1 Primary Mechanisms for Pebble Bed HTGR Heat Transfer

The three primary mechanisms of thermal energy transfer are radiation, convection, and conduction and each of these are explored in the context of HTGR thermal hydraulic analysis. The relative fraction of energy transferred by each of these mechanisms is influenced by the temperature, composition, and geometry of the reactor system materials, the pressure, velocity, and thermal characteristics of the coolant, and the contact pressure and thermal characteristics of the fuel pebbles and support materials which constitute the reactor core. All of these variables create an extremely complex, interdependent system that is challenging to analyze. Ultimately, effective analysis of pebble bed heat transfer requires simplification of these mechanisms. The degree of simplification required and justification for the various required assumptions should be understood, so that investigation of simulation results in later sections has fundamental physical context against which it can be evaluated.

3.1.1.1 Conductive Heat Transfer

Heat transfer via conductance at solid interfaces and across stagnant gas volumes surrounding solid interfaces is significant for pebble bed core configurations and is sub-divided into several interactions. Solid contact between individual pebbles and structural

components of the reactor, such as the side reflector, are modeled as a point contact that is dependent on mechanical force as well as the differential temperature of the bodies considered. Mechanical force varies axially as lower pebbles must support the weight of the pebbles above, and radially as the pebbles expand due to temperature and material transitions due to radiation fluence effects. In addition, dynamic forces are created between pebbles and at material interfaces of the pebble bed as the pebbles flow from the re-fueling circulation system, which removes pebbles from the bottom of the core and relocates them to the top of the core.

In the volume immediately surrounding solid contact points, the surrounding gas is often modelled as conductive heat transfer, as convective effects are minimized due to low fluid velocity caused by boundary layer shear stress for flows against the narrow pebble surface gap between adjacent pebbles. This simplification is somewhat dependent upon coolant pressure, which varies axially across the core volume.

Heat transfer via conduction is commonly simplified and modeled using Fourier's Law, which defines the heat flux ($\dot{q}_{cond}, W/m^2$) and heat transfer rate ($\dot{Q}_{cond}, W$) as functions of thermal conductivity ($k, W/(m\,K)$), one-dimensional spatial temperature gradient (dT/dx), and cross-sectional area (A_c, m^2).

$$\dot{q}_{cond} = -k\frac{dT}{dx} \quad \text{Eq. 3-1}$$

$$\dot{Q}_{cond} = \dot{q}_{cond}A_c \quad \text{Eq. 3-2}$$

In this case, the cross-sectional area can be adjusted to an apparent value, which accounts for the stagnant gas conduction in the gap and the variable pebble-to-pebble compression force across the core volume. The coefficient of thermal conductivity is more difficult to estimate and depends on the degree of simplification being utilized for the core volume being considered. Estimating effective thermal conductivity for pebble bed heat transfer

is an ongoing subject of numerical simulation research. Thus, this variable will be selected from the body of research that was utilized for design calculations for the HTR-PM.

3.1.1.2 Radiative Heat Transfer

Heat transfer via thermal radiation is primarily considered as a line-of-sight interaction between the fuel pebbles and the surrounding materials. Most models for this heat transfer mechanism utilize averaged environmental and material parameters for a subsection of the core volume which are dependent on a given surface temperature gradient for the immediate surroundings and an estimate of the surface emissivity for various materials and temperatures.

For a simplified model, the net radiative heat flux ($\dot{q}_{rad}, W/m^2$) and radiative heat transfer rate ($\dot{Q}_{rad}, W$) from a surface can be defined as a function of the surface emissivity ($\varepsilon, 0 \leq \varepsilon \leq 1$), the Stefan-Boltzmann constant ($\sigma = 5.67 \times 10^{-8}\ W/(m^2K^4)$), the differential temperature between an emitter surface (T_E, K) and receiver surface (T_R, K), and the emitter surface area (A_E, m^2).

$$\dot{q}_{rad} = \varepsilon\sigma(T_E^4 - T_R^4) \quad \text{Eq. 3-3}$$

$$\dot{Q}_{rad} = \dot{q}_{rad}A_E \quad \text{Eq. 3-4}$$

At high temperatures, radiative heat transfer becomes increasingly significant, as the exponential relationship between energy transfer rate and material surface temperature indicates. For HTGR reactor core environments, radiative heat transfer is extremely important for this reason. Many thermal hydraulic simulation codes go to great lengths to ensure the radiative heat transfer is modeled accurately, often by attempting to produce a precise estimate of the surface emissivity for a given homogenized volume of the core. Like the effective thermal conductivity coefficient for conductive heat transfer, the effective emissivity will also be selected from the body of research that was utilized for design calculations for the HTR-PM.

Another obvious means of radiative heating for nuclear systems, radiation absorption by the coolant gas and the materials, such as the graphite moderator of the pebbles, introduces an additional heat source term that is isotropic, but dependent upon the expected radiation flux gradient for the core and the various material properties that are correlated with a material absorption cross-section for a given flux spectrum. A significant amount of 'self-heating' would occur in sensor materials, electronics, and support materials due to these effects. As mentioned previously, the scope of this investigation precludes the discrete addition of this analysis as a component of instrument design. Instead, an integrated nuclear heating term will be collectively accounted for by an isotropic heating power parameter which is derived from the nuclear power density and radiation transport simulated by the various codes explored in later sections.

3.1.1.3 Convective Heat Transfer

Convective heat transfer in reactor core environments is a very complex energy transfer mechanism to analyze due to the non-linear nature of heat transport efficiency for a range of identified coolant flow regimes. Various geometric and material properties of the core structure and coolant gas create transitions between these flow regimes in different regions of the core, such as the lower and upper plenum and inter-core cavities, that can be extremely difficult to predict and model effectively.

Convective heat transfer is a primary driver of core temperature distribution transients due to the inherent flow instabilities of the gas coolant and the dynamic structural nature of the pebble bed core environment. For steady state analysis, a constant boundary condition and static core structure prevents system-scale instabilities from cascading toward temperature distribution transients, which can simplify modeling and analysis to the extent that bulk flow analysis can be effectively implemented. These methods homogenize and divide the core region into sub-volumes with varying bulk flow boundary conditions. These volumes are highly dependent on flow velocity distribution and pressure drop across their surface planes, but can effectively estimate general flow conditions within the core and predict average heat transfer for a given region, greatly reducing the resources required for analysis

when compared to an equivalent pebble-scale simulation of convective heat transfer effects.

Bulk flow analysis utilizes two primary flow regimes, forced convection and free convection. In the forced convection regime, the primary coolant circulator is providing increased coolant pressure at the inlet plenum and is driving coolant through the core at a high average velocity. In the free convection regime, the primary coolant circulator is not actively affecting the coolant flow and relatively slow flow paths are established within the core volume. The coolant behavior is driven by thermal pressure differential between heated and un-heated gas, causing the aforementioned flow instabilities. Convective heating can also be further divided between bulk flow turbulent heating and the solid-to-gas heating that occurs in the core as the gas coolant flows through the fuel pebbles, modeling each of these separately allows for some simplification to be made.

The subject of convective heat transfer analysis for HTGR cores is incredibly deep and much of it resides outside the scope of this investigation. To greatly simplify what is perhaps a fundamental challenge for HTGR thermal hydraulic development and allow for the material to focus on instrumentation rather than flow simulation, a similar bulk flow model to that which was used for initial reactor design efforts will be utilized and application validity will be assumed.

To provide a basis for understanding the model utilized, it is helpful to define convective heat transfer in relatively basic terms. Using Newton's Law of Cooling, the convective heat flux ($\dot{q}_{conv}, W/m^2$) and convective heat transfer rate $\left(\dot{Q}_{conv}, W\right)$ can be defined a function of the convective heat transfer coefficient ($h, W/(m^2K)$), the heated surface area (A_s, m^2), and the differential temperature between the heated surface (T_s, K) and the coolant (T_∞, K).

$$\dot{q}_{conv} = h(T_s - T_\infty) \quad \text{Eq. 3-5}$$

$$\dot{Q}_{conv} = \dot{q}_{conv} A_s \quad \text{Eq. 3-6}$$

In this greatly simplified case, all the information concerning the flow regime and surface parameters, among other variables, is encapsulated in the convective heat transfer coefficient. Similar to the other forms of heat transfer, estimating this parameter for pebble bed HTGR core conditions is extremely difficult and will again, be provided by the literature which describes the initial modeling use for reactor design.

For transient analysis utilizing a control volume approach, it is also useful to define the energy which can be carried by a coolant as it is heated and flows into and out of the control volume. This net energy transfer rate $(\dot{Q}_{tran}, W)$ is defined as a function of the coolant mass flow rate $(\dot{m}, kg/s)$, the coolant specific heat capacity $(c_p, J/(kg\ K))$, and the average temperature difference between the inlet (T_{in}, K), and the outlet (T_{out}, K) coolant.

$$\dot{Q}_{tran} = \dot{m} c_p (T_{in} - T_{out}) \qquad \text{Eq. 3-7}$$

3.1.1.4 Energy Balance for Pebble Bed HTGR Thermal Hydraulics

If all the previously described forms of energy transport are combined for a selected volume of interest, the Law of Conservation of Energy allows for these terms to be related and analyzed as a complete system. All energy transfer must be accounted for, thus for a volumetric cell which includes the entire core volume of a pebble bed, the (greatly simplified) energy balance can be described as a functional relationship between the conductive heat transfer rate $(\dot{Q}_{cond}, W)$ of the pebbles to the core cavity, the radiative heat transfer rate $(\dot{Q}_{rad}, W)$ between the pebbles and the core cavity, the convective heat transfer rate $(\dot{Q}_{conv}, W)$ between the heated coolant and the core cavity, the net energy transfer rate of the coolant flow $(\dot{Q}_{tran}, W)$, and the core thermal power (Q_{th}, W).

$$\dot{Q}_{cond} + \dot{Q}_{rad} + \dot{Q}_{conv} + \dot{Q}_{tran} = \dot{Q}_{th} \qquad \text{Eq. 3-8}$$

Extrapolating this basic premise to include minute detail in accounting for the various forms of energy transfer is what leads to the highly complex thermal hydraulic simulations

which form the basis of safety analysis for reactor systems. The relations presented here are greatly simplified, but understanding this accounting scheme should allow for greater understanding of the complex simulations presented in the next sections which ultimately form the basis for instrument design presented in later chapters.

3.1.2 Phenomena of Interest for Thermal Hydraulic Safety Analysis

Thermal hydraulic safety analysis focuses on a number of selected design basis accident transients which influence the environmental control mechanisms of the reactor core. The primary thermal transfer mechanism for HTGR systems is forced convective cooling, thus most design basis accidents are correlated with coolant flow transients. The most direct method of safety analysis investigation for HTGR systems is determining the thermal response of the core for the worst-case design basis accident. This would be the thermal response of the core if the primary coolant circulator fails and the primary coolant pressure drops to atmospheric levels, which is primarily an investigation of convective cooling transients as passive flow regimes are established while the system progresses from a nominal operational state to an equilibrium shut-down state. This set of transients, referred to as a depressurized-loss-of-circulation-accident (DLOCA) is assumed to result in the highest peak fuel temperature when compared to other design basis accidents [98]. Thus, if only a single transient parameter is considered as an upper boundary for thermal hydraulic safety analysis, the critical parameter for determining the probability of fuel cladding failure would be the core temperature profile for the DLOCA transient.

As previously stated, the investigation of convective heat transfer mechanisms is extremely complex for pebble bed core systems and ultimately outside the scope of this research endeavor. Instead, a focus on the result of these flow transients, a transition of fuel temperature distribution, is selected as the link between the driving motivator of safety analysis and the primary deliverable proposed; a thermal sensor capable of operation in HTGR core thermal environments.

Although safety analysis is organized by design basis flow transients, the fundamental safety parameter that must be evaluated is the maximum temperature of the fuel. This is the measure by which safety is ensured, as the underlying goal of safety analysis is the prevention of radiological release, which for HTGR systems, is prevented by keeping fuel temperatures below an established failure threshold. Thus, the development of a sensor capable of directly measuring this critical safety parameter fundamentally validates the goal of thermal hydraulic safety analysis, and the intermediate focus on flow analysis can be effectively bridged without sacrificing the applicability of the overall project.

A focus on fuel temperature being clearly justified, the next step is to identify how the thermal hydraulic phenomena of interest for safety analysis affects the fuel temperature and identify design parameters which can be used to guide instrumentation development efforts. The goal is to identify temperature ranges for operation in a steady state nominal environment and the environmental variations expected under flow transient conditions, as this will inform the determination of applicability of proposed instrumentation. In addition to simple temperature ranges, an important additional consideration is the time which fuel will be exposed to these temperature ranges, as a key operational aspect of the instrumentation design is dependent on estimating probable calibration drift, which is a function of total thermal exposure, as will be further explored in the next chapter.

3.1.3 Key Thermal Hydraulic Variables for Instrument Design

Thus far, the primary methods of heat transport within the HTGR core have been investigated and common methods of analysis have been briefly explored. The relationship between the goals of thermal hydraulic safety analysis and the applicability for proposed core instrumentation has been clearly defined. Key variables have been identified, with the primary design variable being the time dependent fuel temperature for nominal steady state and accident transient scenarios. The HTR-PM has been selected as the reference design for determination of this primary design variable.

Determination of the sensitivity of the time-dependent fuel temperature for the selected HTR-PM system for the operating scenarios is accomplished by combining two fundamental components. The time-dependent fuel temperature profile for the reactor core is the most significant component and will be determined by investigation of design-basis simulations performed by HTR-PM primary investigators. The second component is an estimation of the probability distribution for pebble migration and corresponds to the dynamic fuel structure design component of the pebble bed concept.

Due to the movement of pebble fuel elements through the core, it is assumed that proposed instrumentation should be capable of dynamic movement as well, a feature that is enabled by the assumed development of wireless signal transfer at some point in the future. This goal adds an additional consideration for determination of thermal exposure, as a given instrument will not remain in a fixed location during operation. Thermal exposure is then dependent upon a probability distribution for the pebble migration path, which provides an estimate of the time the fuel pebbles resides in the various temperature zones found throughout the reactor core.

The time-dependent core temperature profile and probability distribution of pebble migration paths are combined to create an environmental exposure model, which is the key deliverable of the thermal hydraulic analysis presented in this chapter and will be used in the next chapter to drive instrumentation design, as well as the sixth chapter to evaluate the overall functional applicability of the instrumentation deployment configuration being proposed.

3.2 HTR-PM Thermal Hydraulic Analysis

Development of instrumentation hardware capable of functioning in the target HTR-PM environment requires the integration of an HTR-PM environmental model to provide a functional basis for selection of performance indicators. Thermal hydraulic simulations of HTR-PM core heat transfer for steady state and transient operation is a complex topic in

its own right, having a wide range of variance for possible operating conditions, some of which haven't been well established in design literature. To simplify the process of developing a functional environmental model and to avoid shifting the focus of the investigation from instrument design to development of a valid pebble bed thermal hydraulic simulation, simulations performed previously by a range of investigators will be summarized and integrated to create an environmental model which is appropriate for instrument design considerations and should not require additional validation, as the constituent models have been peer-reviewed and independently validated.

3.2.1 HTR-PM Primary Coolant Flow Path

Of primary importance to the thermal hydraulic simulation of the HTR-PM heat transport system is the path of the primary helium coolant as it circulates through the reactor core and primary system components. As mentioned in the previous section, convection is the primary means of heat transport from the reactor core to the secondary cooling system, thus the parameters related to the path the coolant traverses are critical to the function of the reactor plant and are well defined for the purposes of investigation via thermal hydraulic simulation.

The primary coolant flow path for the HTR-PM is typical for HTGR systems and utilizes a standard coupled vessel approach. It includes an elevated primary vessel with an integrated cross-duct connection to a secondary vessel which contains the steam generator and primary coolant circulator. Coolant is diverted from the primary loop for targeted cooling of various hardware systems. The core region has coolant flowing downward towards the lower plenum, which has structural components designed to encourage thermal mixing before exiting the primary vessel via the annular cross-duct. This coolant path does have some simplifications when compared to the as-built facility hardware, as some additional components are included in the steam generator to accommodate the HTR-PM design goal of connecting multiple reactors to a single steam generator, but these components are not reflected here.

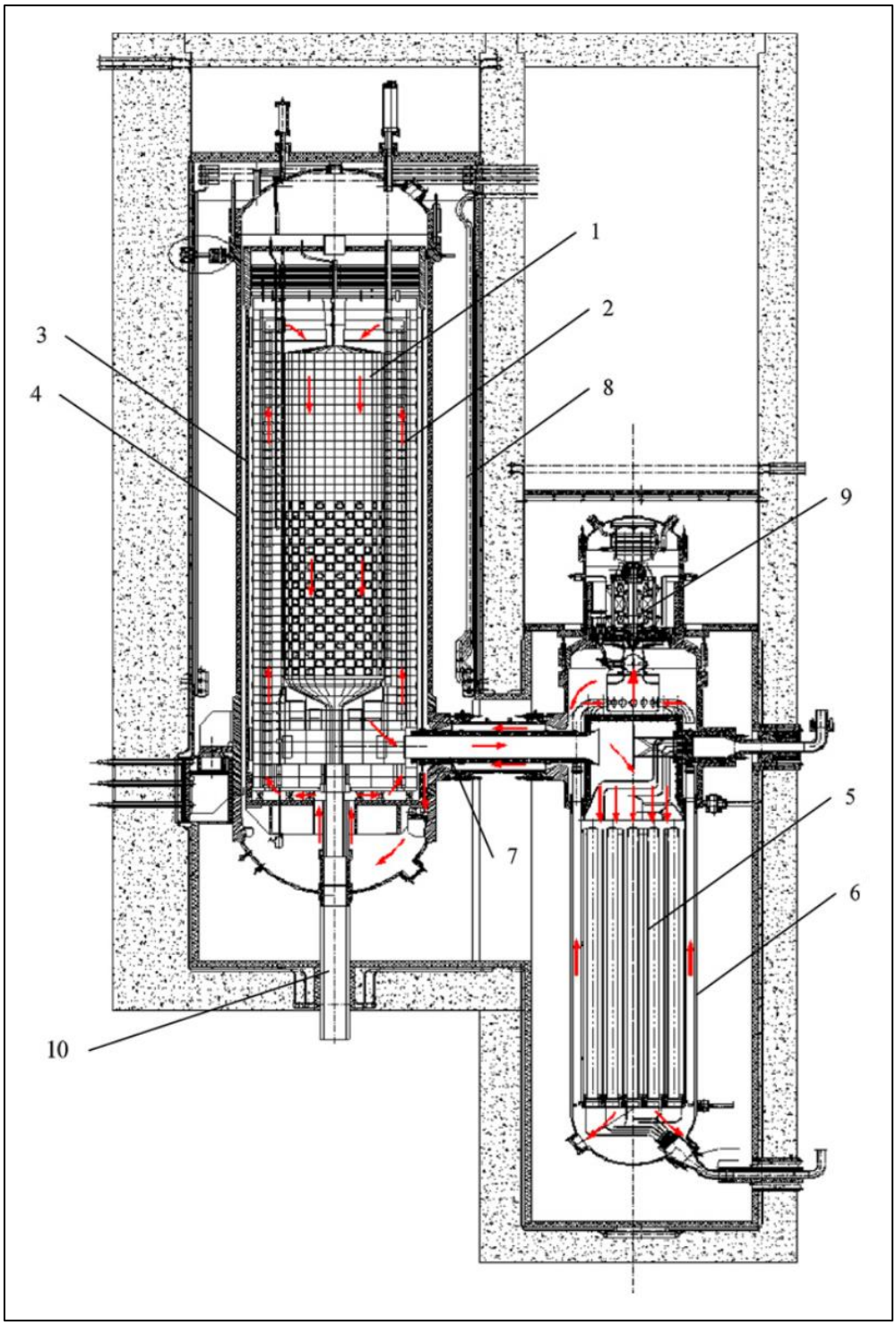

Figure 3-2: The HTR-PM primary coolant flow path [100]

The simplified flow path is depicted in Figure 3-2. It begins with the primary coolant circulator (9) pushing helium through the outer annulus of the integrated duct (7), then downwards to the bottom of the RPV. Some coolant is deflected to cool the fuel element recirculation loop (10), while the bulk of the helium flows upwards though the channels in the outer reflector (2). Helium reaches the upper plenum, where again a small portion of the helium is used to cool the control rod hardware and the rest flows into the upper core cavity and down through the pebble bed (1). Finally, the helium flows through the center portion of the integrated duct (7), into the steam generator and back to the primary coolant circulator (9).

3.2.2 Thermal Hydraulic Simulation Reference Study

The primary thermal hydraulic simulation to be investigated herein will be the results published in 2012 by Zheng et al. using ATTICA3D and THERMIX simulation codes [99]. These simulations provide two- and three-dimensional models of the core environment at steady state operation and under transient conditions. Zheng et al. also explore asymmetrical loading conditions to demonstrate the three-dimensional analysis capability of ATTICA3D, however these studies aren't generally useful for this application and will be omitted, focusing instead on the two-dimensional simulation of THERMIX, which has undergone more thorough validation when compared to ATTICA3D.

The two-dimensional simulation results will provide a baseline from which we can begin to develop a specialized model for application to instrument design. It should be noted that the data presented in the 2012 publication has not been experimentally verified, as no experimental data exists for the HTR-PM at the time of writing. However, the results have been compared against other CFD simulations of similar complexity and appear to be in agreement, supporting the initial validity of these specific simulation results.

3.2.2.1 Initial and Boundary Conditions

Initial and boundary conditions used for the simulations performed by Zheng et al. are in general agreement with the initial design parameters listed in the previous chapter. The

relevant system parameters utilized are described in Table 3-1 and the fuel pebble parameters are summarized in Table 3-2. Note that additional information on fuel pebble parameters, including estimates for parameter variance for the expected manufacturing processes, can be found in Chapter 2, under the fuel pebble review section.

The concrete comprising the foundation and structure of the facility, which is the boundary condition outside the residual heat removal system (RHRS), is kept below 100 °C via a water-cooling circuit. This comprises the ultimate boundary condition for the outer boundary of the simulation. The annular area between the reactor pressure vessel (RPV) and core barrel is also filled with helium which is maintained at or below 250 °C by an auxiliary cooling circuit, which comprises an additional intermediate boundary condition for the thermal hydraulic simulation.

Table 3-1: HTR-PM System Design Parameters [99]

Parameter	**Unit**	**Value**
Reactor power	MW_{th}	2×250
Active core diameter	m	3.0
Active core height	m	11.0
Reactor pressure vessel inside diameter	m	5.7
Helium pressure of primary loop	MPa	7.0
Helium mass flow rate	kg/s	96.0
Mean / maximum power density	MW/m^3	3.22 / 6.57
Inlet / outlet helium temperature	°C	250 / 750
Type of steam generator (once-through)		helical
Main feed-water temperature	°C	205
Main steam temperature	°C	571
Main steam pressure	MPa	13.9
Steam generator feed-water flow rate	kg/s	98

Other design features of note include the fuel reloading system, which consists of a worm-screw or auger style fuel loader at the bottom of the reactor core to remove fuel pebbles. These fuel pebbles are then inspected and either diverted to a spent fuel storage facility or returned to the top of the core using a pneumatic transport system. The returned fuel elements are distributed at the top of the core via a centrally located ejection tube, with an expected radial Gaussian distribution. More information on fuel element migration can be found in the following section of this chapter, in which fuel loading is investigated in detail.

Table 3-2: HTR-PM Fuel Pebble Design Parameters [99]

Parameter	**Unit**	**Value**
Number of fuel elements in equilibrium core		420,000
Number of TRISO fuel particles per element		12,000
TRISO fuel particle diameter	mm	0.92
Spherical fuel element diameter	cm	6.0
Fueled region diameter	cm	5.0
Un-fueled shell thickness	cm	0.5
Metal U loading per fuel element	g	7.0
Average number of cycles per fuel element		15
Average fuel burnup	MW_d/tU	90,000
TRISO particle failure temperature	°C	1,700
Maximum accident fuel temperature	°C	1,620
Estimated DLOCA maximum fuel temperature	°C	1,470

Nuclear kinetic conditions for steady state simulation include the insertion of control rods, located in the outer reflectors, to a uniform depth to ensure a radially symmetric power shape. It is assumed that no small absorber spheres are present in the core or the in the dedicated channels of the outer reflector. A steady state nuclear power distribution, as defined by the VSOP neutronics code, depicted in Figure 3-3, with a maximum power density of 6.35 MW/m^3, is then justified as the assumed initial neutronic condition for transient simulation. It is also assumed that the initial core thermal power distribution is

closely coupled with the neutronic power distribution, if not offset slightly in the axial direction due to the influence of the coolant flow through the core region. Another likely deviation between nuclear power density distribution and thermal power density distribution is the small rise in nuclear power density near the outer periphery of the core, which is due to the reflection of neutrons from the graphite outer reflector.

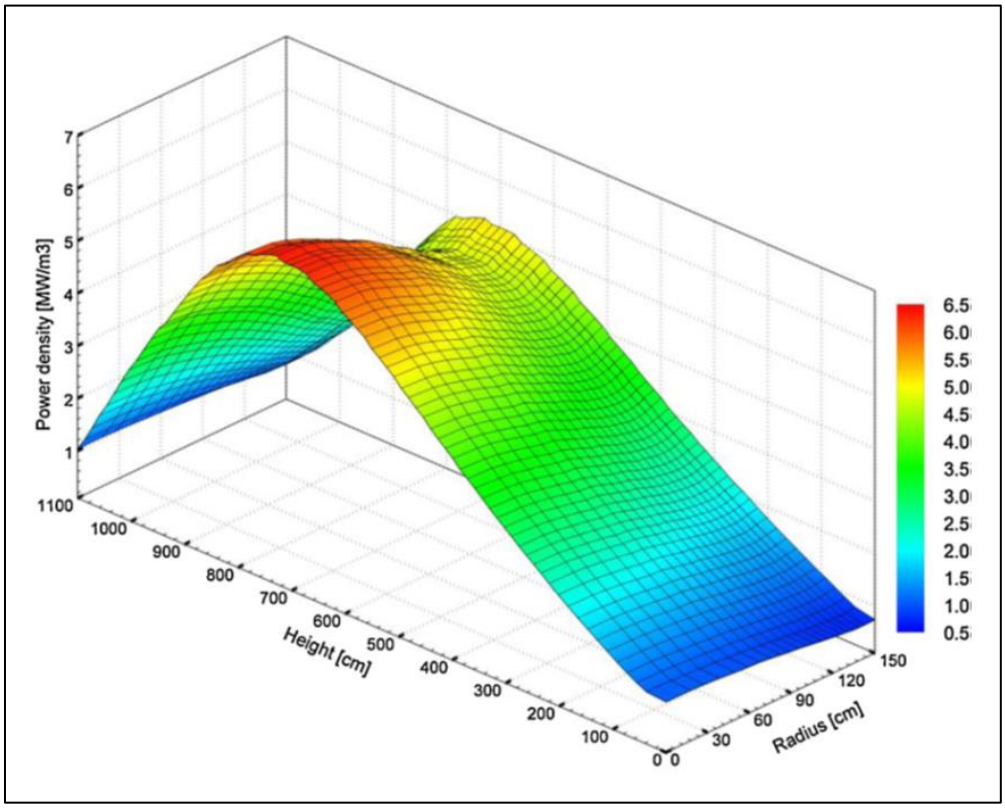

Figure 3-3: VSOP HTR-PM initial condition for steady state nominal power density [99]

3.2.2.2 Thermal Hydraulic Simulation Methods

THERMIX has been in development and widespread use for decades and has a well-established record of validation for HTGR thermal hydraulic simulation. It was used in thermal hydraulic design efforts for a range of experimental HTGR systems, including the AVR, THTR, HTR-500, PBMR, HTR-10, and of course, the HTR-PM [99]. The details of the underlying models utilized by THERMIX can be investigated in the referenced work

of Zheng et al. and others who have utilized the code for first-order HTGR thermal hydraulic analysis and will not be repeated here outside of generic description.

However, of particular interest are a number of additional correlations incorporated into the THERMIX code to increase the fidelity of the simulation for the HTR-PM system. In many cases where data pertaining to the Chinese manufactured spherical fuel elements could not be utilized, parameters for German manufactured spherical fuel elements, such as those utilized in the AVR, are substituted. It is assumed that many aspects of these fuel elements will be similar, having almost identical thermal hydraulic and nuclear kinetic performance characteristics.

In general terms, THERMIX utilizes a coupled general-purpose thermal conduction simulation with a quasi-steady-state convection simulation on a two-dimensional cylindrical field of interest. A gas flow model defines the primary coolant loop and is included as an inlet/outlet gas flow boundary condition and ultimate heat sink for the simulation, in addition to the RHRS boundary mentioned earlier. Additional modifications to this code for specific application to the HTR-PM include a refined heat conductivity model for the graphite matrix of the fuel elements, a refined effective heat conductivity model for an idealized uniform pebble bed which considers fast neutron kinetic heating as well as thermal transport, and specialized graphite reflector and carbon brick thermal properties for the material and geometry utilized in the HTR-PM. Properties for which German manufactured fuel or fuel systems served as a reference includes fuel element surface heat transfer coefficients, a specialized model for pebble bed friction resistance loss, and a specialized helium thermal physical property model. Details on these modifications can be found in the referenced work by Zheng et al.

All of these independent updates and refinements produce a collective overhaul of the THERMIX code suited specifically for the materials and geometry of the HTR-PM. It is assumed that these refinements would serve to increase the precision of the simulation and lower the expected error range of the simulation results, however it should be reiterated

that any improvements offered by these alterations have not been experimentally verified due to a lack of operational data from the HTR-PM.

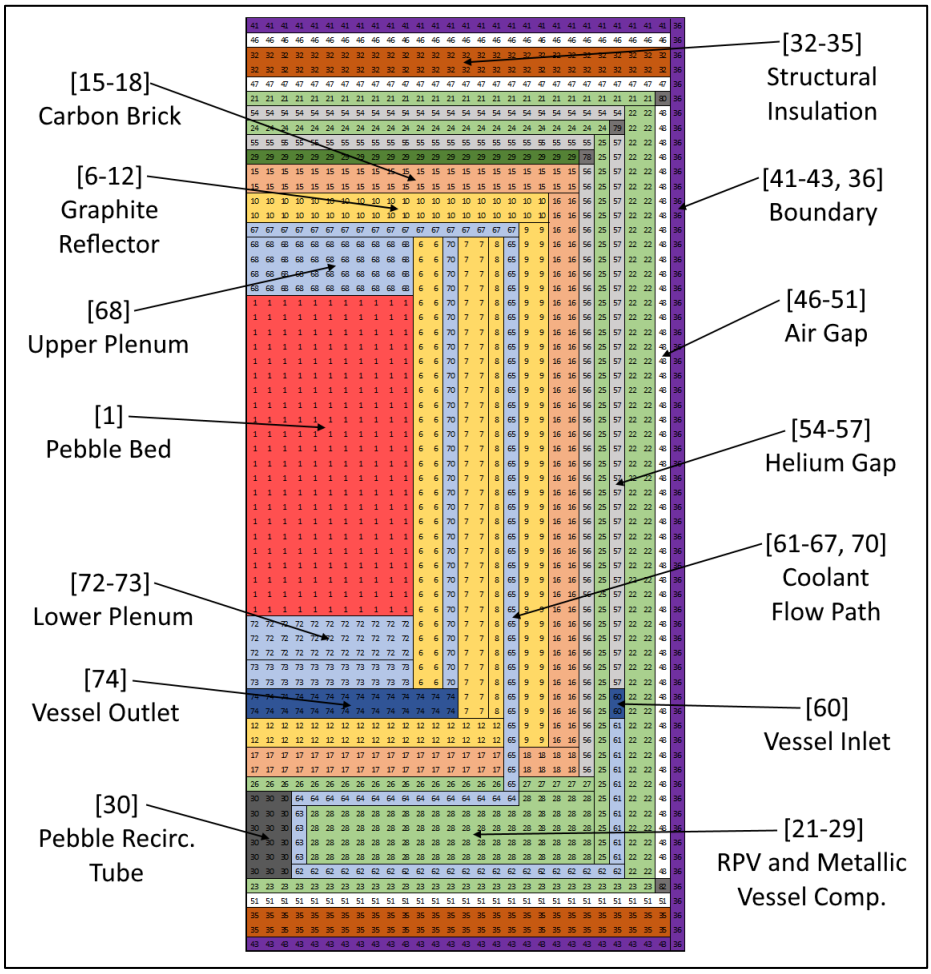

Figure 3-4: HTR-PM primary vessel discretization scheme [99]

Simplification of the HTR-PM core geometry into a two-dimensional cylindrical field of interest is not a trivial operation and can have significant effect on the resulting simulation fidelity. In this case, this translation was accomplished by dividing the primary vessel volume into 50 two-dimensional cells, with an air gap between the pressure vessel wall and the RHRS boundary condition. The integrated cross-duct is modeled as a gas flow boundary condition internal to the pressure vessel, which is a straightforward simplification

to better focus the model on thermal hydraulic performance of the core, rather than vessel exchange phenomena occurring in and around the cross-duct volume. The various regions used in the simulation are illustrated in Figure 3-4.

The THERMIX code steps through time by solving the region-specific thermal transport via solution of the continuity, momentum and energy conservation equations for fluid convection based on a time-dependent solid structure temperature profile for materials in the region of interest. Inter-region dynamic gas flow phenomena are homogenized via void fraction simplification and correlation models for areas such as the upper and lower plenums, reflector flow channels and core region. The spherical fuel elements are modeled on a one-dimensional spherical space with five subdivisions with diameters of 6.0 cm, 5.0 cm, 3.0 cm. 1.0 cm, and 0.3 cm, which is the assumed location of maximum fuel temperature. These subdivisions are depicted in Figure 3-5.

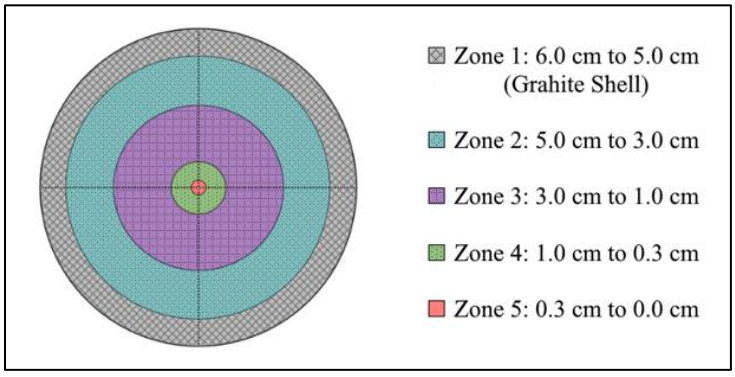

Figure 3-5: Discretization scheme of spherical fuel elements

3.2.2.3 Summary of Thermal Hydraulic Simulation Reference Study Results

The primary THERMIX simulation results produced and published by Zheng et al. which are applicable to the creation of an environmental exposure model for instrument development are the two-dimensional temperature profiles for steady state operation and the peak temperature profile estimated for the DLOCA accident scenario. Note that the referenced figures depicting the simulation results also include data from the ATTICA3D code, which provides a degree of verification for the results, but will not otherwise be

analyzed. Please refer to the referenced investigation for further detail; as only broad generalizations regarding the steady state spatial temperature distribution of the core region will be utilized, which served as the basis for comparison of DLOCA simulation results produced by the two codes being compared in the referenced study.

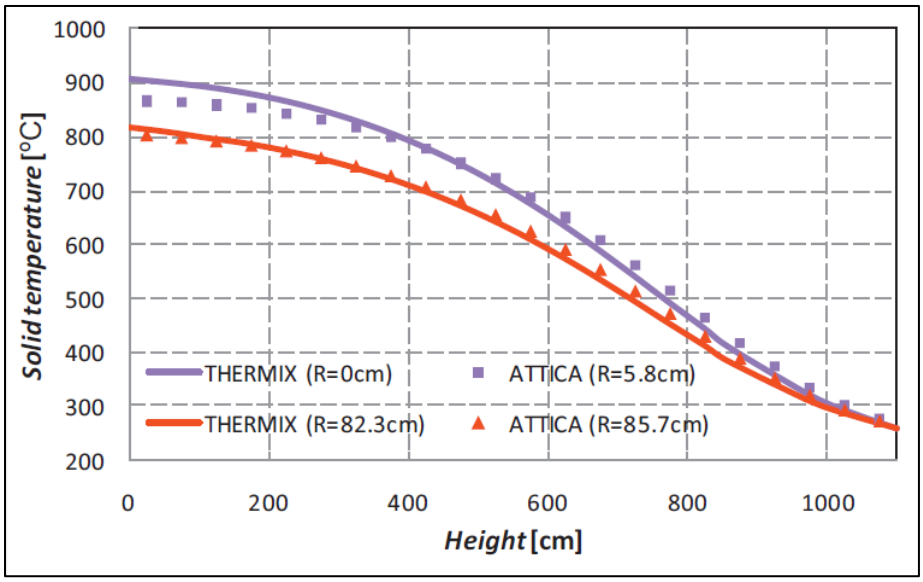

Figure 3-6: Steady state solid fuel axial temperature profile [99]

The axial solid temperature profile for the centerline and outer core periphery is depicted in Figure 3-6. This data predicts a radial thermal gradient of approximately 90 °C between the centerline and the selected radial location at the core outlet. Figure 3-7 depicts the radial helium coolant temperature profile at the core inlet, center, and outlet. As expected, the largest temperature gradient is found at the core outlet, with a 200 °C difference observed between the core centerline and the outer periphery.

Accident conditions for the DLOCA scenario are also analyzed by Zheng et al., resulting in estimates for the fuel temperature distribution and RPV thermal loading at various times as the transient progresses toward equilibrium. The peak fuel temperature when the fast neutron dose is included in the effective heat conductivity model for the THERMIX code was determined to be approximately 1,531 °C with an error of 1.5%. This estimate is well

below the design basis for the spherical fuel elements, but is considerably higher than the predicted peak steady state operation temperature of the fuel elements.

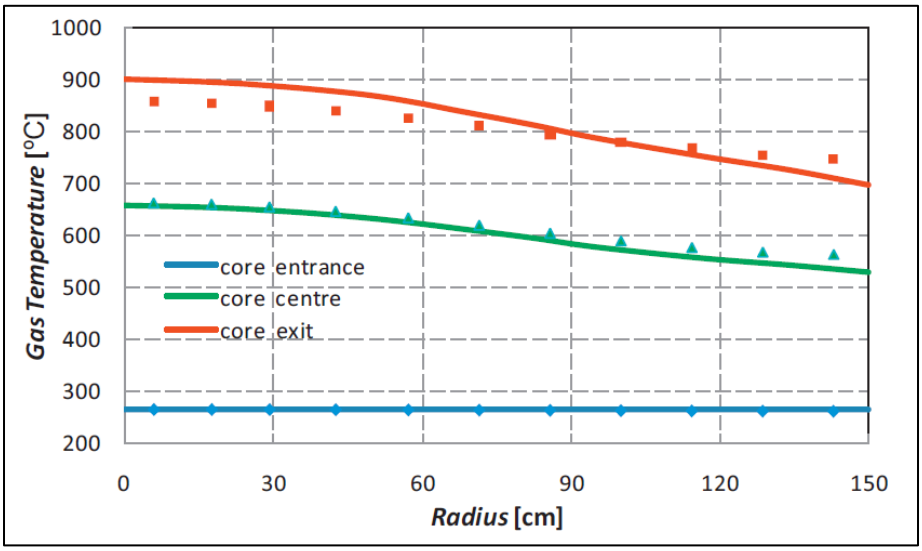

Figure 3-7: Steady state radial helium coolant temperature profiles at various core heights [99]

The details of the DLOCA accident transient simulation can be found in the referenced publication, with a complete description of the decay heat model utilized. This data will not be used for instrument design, as the maximum temperature is nearly twice the targeted operating temperature for steady state conditions and presents a considerable design parameter adjustment for what is essentially an edge case for analysis. Even for thermal hydraulic test facilities, it is unlikely that this temperature would be routinely reached. If DLOCA cases are investigated, instrumentation can be deployed outside the centerline, which will likely be considerably cooler and more aligned with the typical temperature range for steady state operation. However, it is useful to have an estimate of the maximum temperature the core may reach under accident conditions, to understand the operating bounds of the system which instrumentation is being developed for.

3.3 HTR-PM Pebble Migration Analysis

Assuming the ultimate applicability case for instrument design is a deployment goal of wireless on-pebble instrumentation, capable of traversing the HTR-PM core in the same manner as a typical spherical fuel element, additional data in addition to the core temperature distribution is needed. Of particular interest to the determination of the operating conditions to which proposed instrumentation will be exposed is determining the time the instrument will be deployed in the various temperature regions the spherical fuel elements will traverse as they flow through the core volume and are recycled through the fuel recirculation system. Together, these parameters constitute the thermal exposure of the instrument array for any probable fuel cycle and will determine the rate of material transitions which account for progression of the calibration drift of the instrument over time.

The environmental model has been developed in the previous sections, which gives an approximation of the fuel temperature for any given point in the core region. The second component, the amount of time a given fuel element might spend in each of these regions, must be approximated for a range of pebble loading locations. The most direct method of accomplishing this is to develop a pebble migration model. This model includes an initial pebble probability distribution as an initial condition coupled with a fluidized bed flow model to account for pebble movement from the initial placement to the ultimate destination of the pebble recirculation channel at the bottom of the reactor core. Similar to the method for selecting an environmental model in the previous section, a primary source will be selected, in this case the 2020 publication from Gui et al. [101], and will be verified by comparison to other contemporary investigations of fluidized pebble bed flow.

3.3.1 Initial Pebble Loading Distribution

A number of models are used to estimate the pebble distribution mechanisms for the HTR-PM. Although the distribution mechanism hasn't been specified in design documents beyond an 'insertion tube', a number of hardware implementations have been suggested to

change the distribution of fresh pebbles to the top of the core, with differing effects on the pebble distribution as the pebbles flow through the center core region.

For the simplest case, a single tube ejection site where pebbles are centrally released and allowed to settle atop the core without attempting to evenly distribute them along the radial profile, the pebbles are expected to have a normal distribution if the top of the core were assumed to be a flat initial condition. However, as the pebbles naturally build and collect toward the center, additional pebbles are not placed via this distribution. If an initial condition of a gaussian curve is used to model the pebble mound, then the distribution looks quite different. In fact, the distribution would seem to be flatter across the radial profile, as pebbles are spread throughout the upper surface relatively evenly due to the sloped sides of the mound carrying new pebbles away from the mound center.

Adding to this simple model, we can take in to account the effects of pebble flow dynamics demonstrated by the proceeding simulations of pebble migration for HTGRs. These effects tend to pull pebbles in faster in the center region and more slowly in the outer regions, with the magnitude of this difference being highly dependent on the angle of the lower core support structure and the friction coefficient of the pebbles and the graphite reflector surface [102]. This effect serves to flatten the assumed mound found at the top of the core and is a counter-balance to the mounding effect for an assumed static, single central point loading system. Ultimately it is the equilibrium of these forces which creates the initial loading conditions, more centerline pebble flow creates a flatter upper pebble surface, while less centerline pebble flow creates a mound atop the pebble surface.

For the purposes of instrument design, an idealized case for initial loading will be assumed. The instrumented pebbles will be separated from the fueled pebbles after being removed from the core via the pebble recirculation system and transferred into a separate reloading pipeline. This pipeline will be assumed to be capable of dropping the instrumented pebbles at the core center, at various points along the outer periphery of the core, and at various points in the intermediate radius range. The point of initial placement is assumed to remain

static during the reloading movement, meaning the instrumented pebble will have an initial loading condition directly below the insertion point, and will not roll or otherwise move laterally as the pebble settles atop the core mound.

This assumption can be justified if the upper core mound is reasonably flat, which can be assumed if centerline pebble flow is significantly faster than pebble flow at the outer core periphery, based on the equilibrium described above. If the centerline pebble flow is equivalent to the periphery pebble flow, then a pebble placement system must be used to have certainty regarding the initial placement of the instrumented pebbles, as this would allow a flat initial distribution to be deliberately maintained by avoiding the mounding effect caused by a central loading scheme.

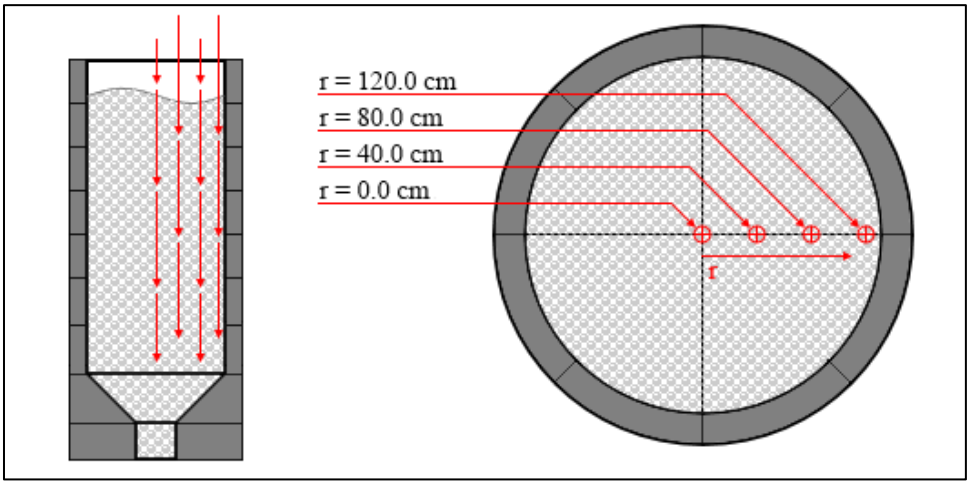

Figure 3-8: Initial instrumented pebble loading locations for pebble migration analysis

Obviously this loading scheme would be unrealistic in practice due to the additional hardware required to distribute the instrumented pebbles at multiple points, but it does have value to assume this configuration for the purposes of instrument design so that the ideal loading point can be determined based on optimization of the fundamental functional characteristic proposed, the ability to correct for calibration drift, which has an assumed dependency on the environmental exposure, which is highly dependent on initial core

loading position, as the following analysis illustrates. The loading positions selected for migration analysis are at distances of 0.0, 40.0, 80.0, and 120.0 cm from the core centerline, as depicted in Figure 3-8.

3.3.2 Pebble Flow Reference Study

Using coupled static and kinematic model, a study published in 2020 by Gui et al. [101] analyzed the pebble flow expected in the HTR-PM for a variety of core support base angles, pebble recirculation modes, and coefficients of friction for the fuel element surface. This study represents the best available estimations of pebble flow distribution for the HTR-PM at the time of writing and will form the basis of the analysis used to create the pebble migration model used for instrument design.

The analysis technique utilized by Gui et al. is split into two distinct models, a kinematic model utilizing a Eulerian approach to determine the granular flow velocity of the pebble bed, and a discreet element method (DEM) model utilizing a Langrangian approach to determining the distributions of forces for pebbles in a quasi-static pebble bed. The study presented by Gui et al. is the first effort to create a hybrid model using the most recent estimates of material properties for the fuel elements as well as the first to explore the particular variation of parameters illustrated in Figure 3-9, specifically the variation of the base angle of the core support structure (30, 45, and 60 degrees) and the variation of pebble distribution mode (star, point, and ring) for labels a, b, and c, respectively.

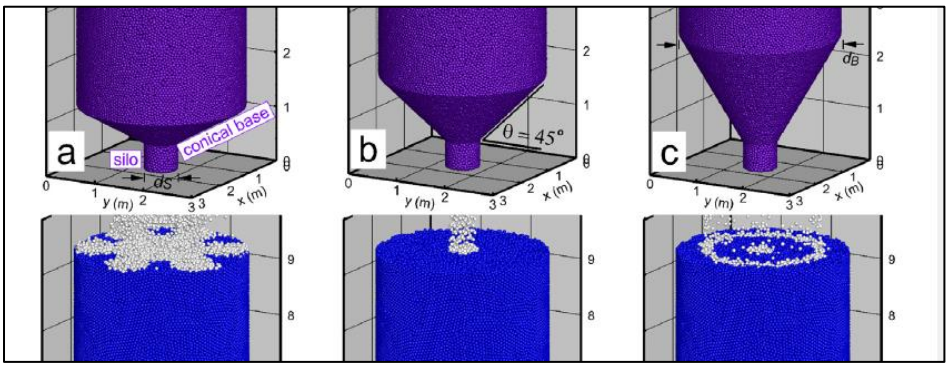

Figure 3-9: Conical base and pebble loading variations for the HTR-PM [101]

3.3.2.1 Initial and Boundary Conditions

The initial conditions used for the pebble flow simulation are presented in Table 3-3. If these conditions are compared with the initial and boundary conditions utilized by Zheng et al. in the previous section, good agreement between the two data sets is observed, supporting the validity of conclusions drawn by joining of these models into a hybrid environmental model coupled with a pebble migration model.

Note that the silo parameters presented in Table 3-3 represent the fuel removal tube at the base of the core. The variation of the conical core support structure is anchored at the upper rim of the silo, with larger angles reducing the cylindrical portion of the core volume as the conical portion increases in height, as shown in Figure 3-9.

Table 3-3: Initial Conditions for Pebble Flow Simulation [101]

Parameter	**Variable**	**Unit**	**Value**
Core diameter	D_g	m	3
Core height	H_g	m	11
Silo diameter	D_s	m	0.6
Silo height	H_s	m	0.5
Angle of conical core base	θ	°	$30, 45, 60$
Number of fuel elements	N_p		420,000
Fuel element diameter	d_p	mm	60
Fuel element density	ρ_p	$\mathrm{kg/m^3}$	1,750
Stiffness factor	k_c	N/m	10^5
Poisson ratio	ν		0.3
Restitution coefficient	e		0.30
Friction coefficient	μ		$0.3, 0.5, 0.8$
Time step	δt	s	10^{-4}
Pebble loading rate (inverted)	t_s	ms	$0.3, 1, 2$
Simulation time	T_s	s	$126,420,840$

3.3.2.2 Methods of Pebble Flow Analysis

The solution method utilized in the reference study for discrete pebble motion in a granular bed assembly is relatively well established [103] and models elastic collision, viscous damping, and friction between particles and the core support structure. These forces are formulated as described in Equations 3-9, 3-10, and 3-11, utilizing variables as defined in Table 3-4.

Table 3-4: Pebble Flow Simulation Variable Definitions [101]

Parameter	**Variable**
Contact force normal, tangential	$\int_{p,n}^{c}$ $\int_{p,t}^{c}$
Inter-element displacement normal, tangential	χ_n χ_t
Contact force vector	$\vec{\int}_p$
Radius vector (centroid to contact point)	$\vec{r}_p$
Collision torque	$\vec{T}_p^{\,c}$
Damping Coefficient	β
Newtonian contact force	$\vec{F}_p^{\,c}$
Fuel element mass	m_p
Fuel element inertia	I_p
Gravity acceleration vector	$\vec{g}$

$$\begin{cases} \int_{p,n}^{c} = -k_n\chi_n - \beta_n\dot{\chi}_n \\ \int_{p,t}^{c} = -k_t\chi_t - \beta_t\dot{\chi}_t \\ \text{if } \left|\int_{p,t}^{c}\right| \geq \mu\left|\int_{p,n}^{c}\right|, \text{ then } \left|\int_{p,t}^{c}\right| = \mu\left|\int_{p,n}^{c}\right| \\ \vec{T}_p^{c} = \vec{r}_p \times \vec{\int}_p^{c}, \text{ or } T_p^{c} = r_p\int_{p,t}^{c} \end{cases} \quad \text{Eq. 3-9}$$

$$\begin{cases} \ddot{\vec{x}}_p = \dfrac{\vec{F}_p^{c}}{m_p} + \vec{g} \\ \ddot{\alpha}_p = \dfrac{\vec{T}_p^{c}}{I_p} \end{cases} \quad \text{Eq. 3-10}$$

$$\vec{F}_p^{c} = \int_{p,n}^{c}\vec{n} + \int_{p,t}^{c}\vec{t} \quad \text{Eq. 3-11}$$

3.3.2.3 Summary of Results of Pebble Flow Analysis

The primary results of the analysis performed by Gui et al. are estimated pebble migration paths and probability density distributions for vertical and lateral pebble movement over a complete reloading cycle, which is defined as the loading and removal of a complete nominal fuel inventory from the reactor core. The pebble migration paths for 30-, 45- and 60-degree conical base angles (a, b, and c, respectively) are depicted in Figure 3-10.

It is observed in Figure 3-10 that the pebble migration paths have very little lateral motion across the cylindrical portion of the core height. Significant radial displacement is observed, as expected, near the bottom of the core where the conical base narrows. The degree of this displacement for different radial starting locations appears to be relatively uniform across the different conical base angles. The pebble migration path in the upper cylindrical portion of the core appears to have very little dependence on conical base angle.

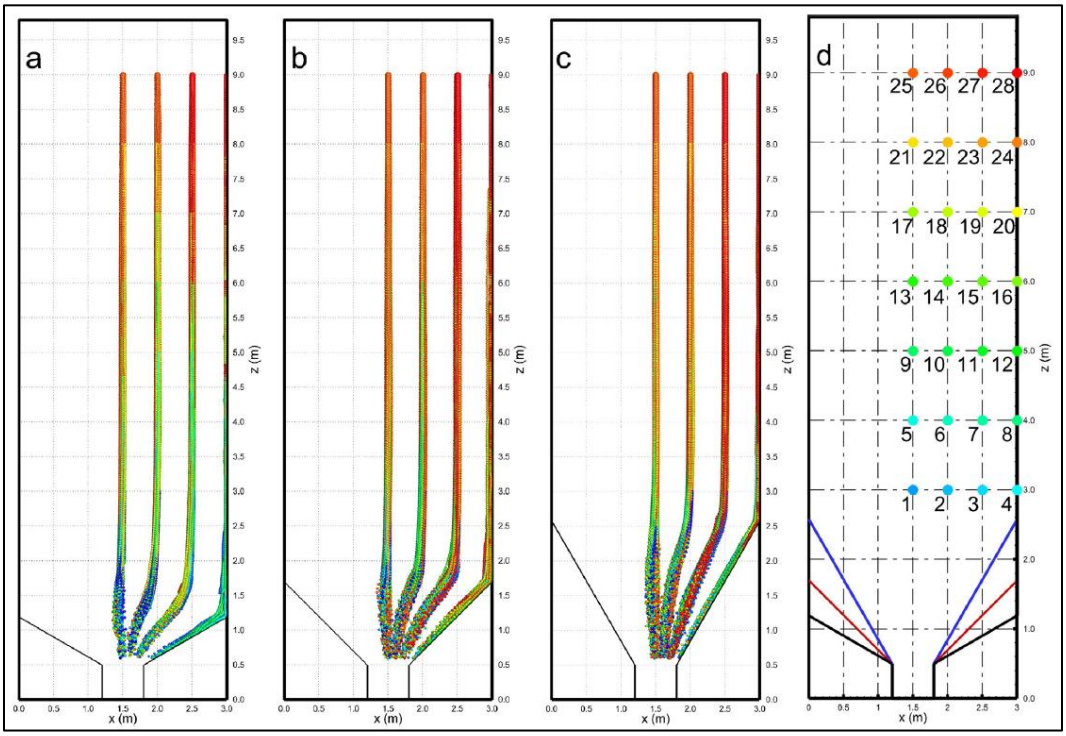

Figure 3-10: Pebble migration paths for 30-, 45-, and 60-degree conical base angles [101]

The referenced investigation also develops estimates for the probability density distributions for radial displacement of pebbles starting from various initial positions for the 30-degree conical base angle case. The distributions are generally narrow, indicating that very little lateral motion is predicted as the pebbles traverse the axial core height. Pebbles at the core periphery travel nearly straight down, likely due to the proximity of the wall preventing random settling motion observed the other radial locations. No significant lateral displacement is observed until a height of 1.5 to 1.0 m, which corresponds to the height at which the conical base structure begins to narrow, forcing fuel pebbles to move toward the central collection silo.

Figure 3-11 depicts the height dependent vertical velocity of fuel pebbles with different radial starting locations, again for the 30-degree base angle case. The variance in vertical velocity as the pebbles descend is very low, narrowing slightly at the lower elevations as compared to the upper region of the core. The vertical velocity is generally very uniform across the range of radial locations, with the only significant deviation observed, again, at the last 1.5 m of core height. At the bottom of the core, near the fuel removal silo, a funneling effect is observed. Fuel pebbles closer to the center of the core accelerate quickly while those on the periphery accelerate more slowly.

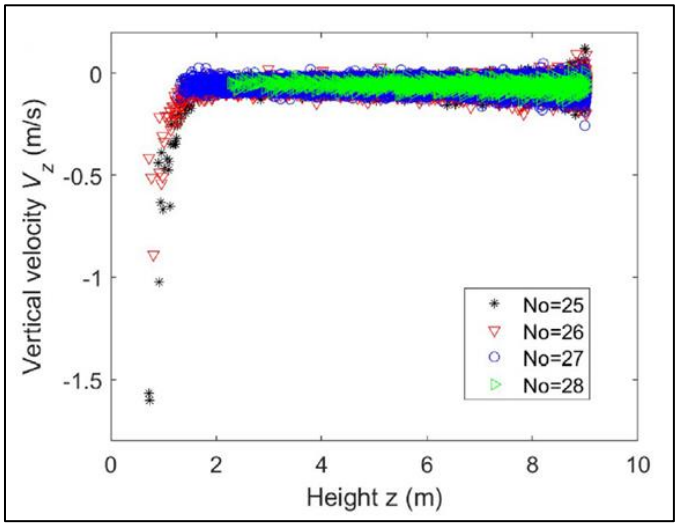

Figure 3-11: Vertical velocity for pebbles at various radial locations. [101]

Other results presented by Gui et al. include a minimal, almost indiscernible pebble motion dependency on pebble-to-pebble friction coefficient, pebble reload speed, and pebble loading mode, indicating that shear forces between pebbles and inertial forces of pebble motion are nearly negligible when analyzing the migration paths through the core region for pebbles at various radial loading locations. These results are expanded upon in the referenced publication.

3.3.3 Pebble Migration Analysis Impact on Instrumentation Design

It can be concluded that the radial position stays relatively constant throughout the pebble refueling migration and is not highly dependent on the core support structure angle, inter-pebble friction coefficient, pebble reload speed, or loading mode for the regions of the core above the conical core support geometry, which comprises the majority of the core region. The axial velocity does vary significantly in the conical region of the core, resulting in large variations in the time which a given pebble is subject to the environmental conditions found at the lowest elevations in the steady state core. The lower elevations near the conical region are also subject to a relatively high variance of solid material temperatures across the radial dimension. Both of these factors considered together may create significant variation for thermal exposure for pebbles with similar initial loading locations, however, this is only for the very end of the pebble migration path. To avoid the complications that may arise from this variation, the lower conical portion of the core region will be omitted from analysis. Only the upper cylindrical region will be considered for instrumentation design functional applicability investigations.

Overall, the investigation predicts relatively uniform ‘mass flow’ migration in the upper cylindrical portion of the core volume, with the relative pebble position for a radial slice of pebbles staying almost static as the slice moves in the axial direction. Once a radial slice of pebbles approaches the conical region of the core support structure, radial diffusion increases as a function of structure angle and initial radial pebble position, resulting in pebbles closer to the center of the core being discharged more quickly. This effect seems to be proportional to the rate of cross-sectional reduction in radial area however, resulting

in negligible effects on the pebbles above the conical region, and avoiding a central void from forming above the center of the core. Indeed, the mass flow rate of the pebbles is uniform despite the conical region causing significant variation in axial pebble velocity.

The impact of this analysis on the development of an environmental exposure model is the justification of two simplifications which can be made. The first is that a straight vertical pebble migration path can be utilized for the cylindrical region of the core. The second is that the vertical velocity is approximately constant for all loading locations and is proportional to the pebble recirculation rate for nominal operation of the HTR-PM.

3.3.4 Verification of Simulation Results

The results obtained by Gui et al. are in good agreement with similar studies from other authors in most respects. The key parameters which should be verified are associated the determination of the impact of the coefficient of friction between the fuel pebbles and the reactor cavity as well as the pebble-to-pebble coefficient of friction, as these drive lateral pebble motion by causing the fuel pebbles at the periphery to be slowed and allowing this perturbation to propagate via inter-pebble interactions in the radial direction.

A 2016 study by Li et al. [102] presents similar findings when utilizing DEM simulation methods in that it is determined that a low coefficient of friction for these aforementioned interactions does indeed result in a radially consistent, mass-flow of pebbles, without significant lateral motion in the cylindrical portion of the reactor cavity.

Methods of controlling the coefficient of friction at the lower conical surface, which was found to be the most significant determinator of the magnitude of lateral pebble motion, were explored for the HTR-PM. This provides confidence that aversion to pebble stagnation, which is the result of high centerline pebble flow relative to the periphery pebble flow, will drive design considerations to ensure that the conical coefficient of friction is low enough to ensure minimal lateral pebble motion. Thus, verifying the results

by Gui et al. and the determination that initial radial placement of instrumented pebbles will remain constant as the pebbles are circulated through the core region.

3.4 Development of an Integrated Environmental Exposure Model

Integration of the presented thermal hydraulic analysis and the pebble migration model allows for a model of pebble thermal exposure to be derived with a high degree of confidence. This thermal exposure model can then be used to determine the applicability of the proposed instrument for use in a pebble bed HTGR environment and ultimately determines the validity of the design approach and target performance criteria. In this section, data from the previous sections is summarized, extended, and combined, resulting in continuous, three-dimensional temperature distribution map of the steady state HTR-PM core and thermal exposure models for a range of radial pebble loading locations.

3.4.1 Derivation of a Steady State Temperature Distribution Model

Fitting curves to the axial surface temperature data presented in Figure 3-6 for the centerline and at a radius of 82.3 cm provides continuous functions of axial centerline $(T_{AC}, °C)$ and axial intermediate $(T_{AI}, °C)$ solid structure temperature. These are defined as a fourth-order polynomial function of core height (h, cm) in Table 3-5 and depicted in Figure 3-12. This is then combined with similar curve fits of the radial solid structure temperature distribution provided in Figure 3-7 at an upper $(T_{RU}, °C)$, middle $(T_{RM}, °C)$, and lower $(T_{RL}, °C)$ core height, which are defined as fourth-order polynomials with coefficients listed in Table 3-5 and depicted in Figure 3-13.

Combining these functions and interpolating between the referenced defined data sets produces an estimate of the axial solid structure temperature at the core periphery $(T_{AP}, °C)$, which is also depicted in Figure 3-12 and has polynomial coefficients listed in Table 3-5. These six axial and radial data sets are then extrapolated via sequential axial polynomial progression to generate a three-dimensional temperature distribution model for the HTR-PM fuel surface temperature at steady state operation, depicted in Figure 3-14.

Table 3-5: Polynomial Coefficients for Spatial Temperature Distribution Map

Name	h^4	h^3	h^2	h^1	h^0	R Value
T_{AC}	1.135E-9	-1.838E-6	2.727E-4	-1.753E-1	9.084E+2	0.999946
T_{AI}	1.038E-9	-1.738E-6	3.925E-4	-2.170E-1	8.182E+2	0.999944
T_{AP}	1.035E-9	-1.802E-6	4.576E-4	-9.904E-2	6.988E+2	-
T_{RU}	-	-	-	-3.091E-5	2.6150E+2	0.937501
T_{RM}	-1.333E-7	1.366E-4	-2.444E-2	3.118E-1	6.896E+2	0.998062
T_{RL}	-1.902E-7	1.366E-4	-2.737E-2	3.119E-1	9.054E+2	0.999274

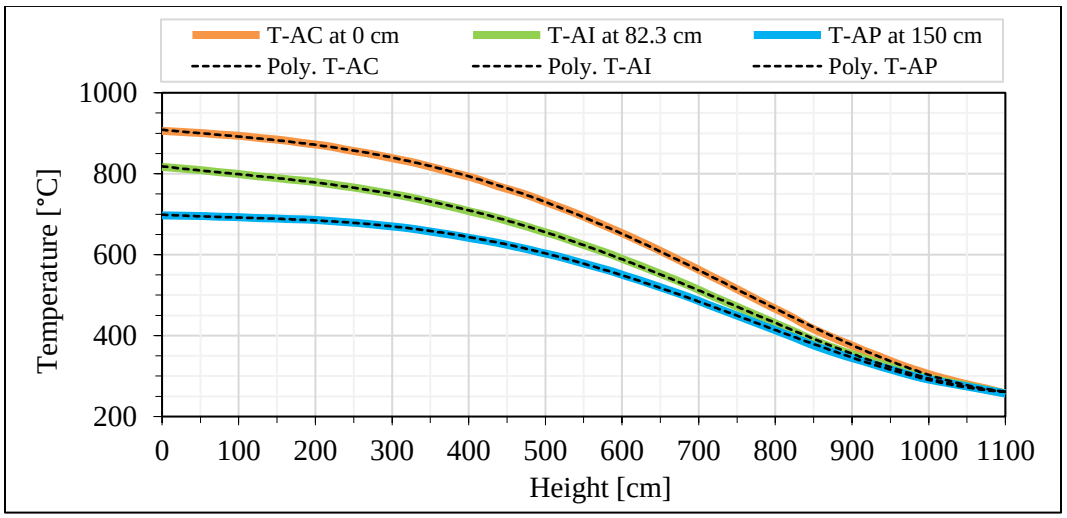

Figure 3-12: Derived axial solid structure temperature distributions

This derived temperature distribution map is generally consistent with the data presented by Zheng et al., but does have some irregularities. The centerline temperature peaking is slightly more exaggerated than can be expected in a real pebble bed core and the peak solid structure temperature is at the extreme bottom center of the core. A real pebble bed core would likely have a flatter radial temperature distribution across the centerline and some mixing of the coolant after it passes through the region of greatest nuclear power density would likely raise the location of the highest structural temperature to just above the bottom of the core volume. However, these features are evident in the data provided by Zheng et

al., so it will be assumed that any deviation from a real thermal system is not significant enough to affect the design parameters and thus, will not be investigated further.

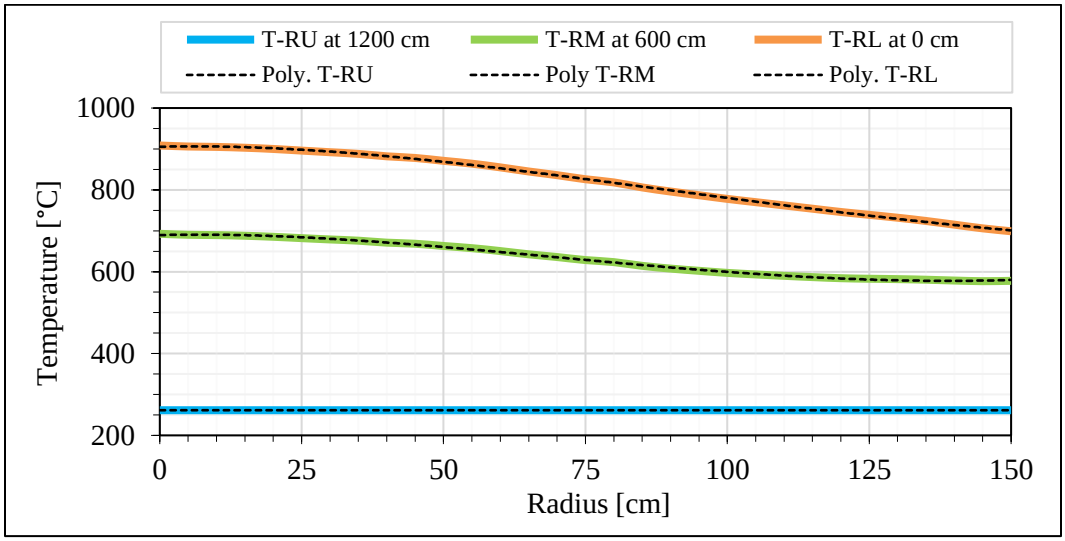

Figure 3-13: Derived radial solid structure temperature distributions

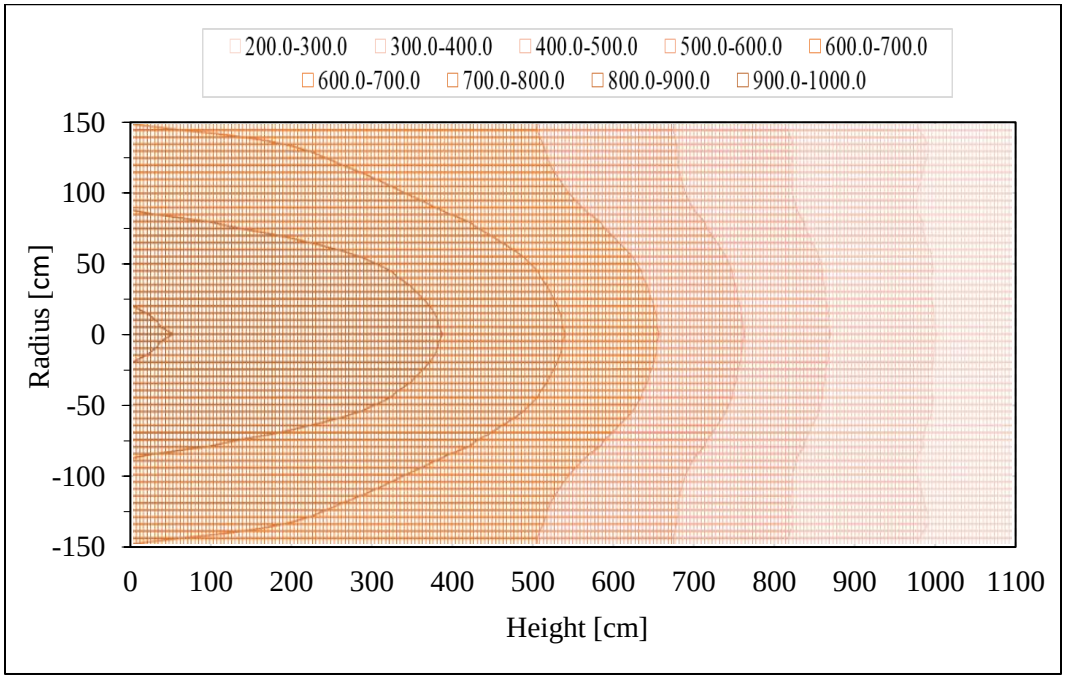

Figure 3-14: Derived two-dimensional temperature distribution in HTR-PM core region

3.4.2 Derivation of a Steady State Pebble Migration Vector Approximation

The cumulative results obtained in the Gui et al. study, which were confirmed by the Li et al. investigation, indicated that estimating the fuel pebble migration would be fairly straightforward. The fuel pebbles flow via a radially uniform velocity distribution for the cylindrical portion of the core. Thus, it will be assumed for the purposes of estimating the thermal loading on instrumented pebbles, that the pebbles will have a velocity vector which is straight downwards from their initial placement on the upper surface of the pebble bed.

The fuel pebbles will undergo lateral motion upon entering the lower conical portion of the core volume, which is roughly parallel with the slope of the conical face with some offset from the wall. This portion of the pebble travel is not necessarily impactful to instrument design however, as it is assumed that the instrumented pebbles will be replaced after traversing the core a single time. Thus, this last section of the migration path has very little impact on the overall performance of the device, as it has already traversed the volume where thermal measurements are considered to be most critical.

The magnitude of the velocity vector is determined by the pebble recirculation rate. The expected amount of time for an individual fuel pebble to remain in the core is estimated at 1057 days by the IAEA [104], although this value would depend on the fuel loading and the burn-up of the core, which varies considerably over the system integration period. If the active core height is approximately 1,100 cm, as indicated in Table 3-3, and the assumed velocity vector is straight downwards. Then the magnitude of the velocity vector would be equal to 1.041 cm per day or 0.1204 μm per second. Additionally, if the core contains 420,000 fuel pebbles, this results in an average fuel recirculation rate of approximately 16.56 pebbles per hour.

3.4.3 Integrated Pebble Thermal Exposure Model

Integrating the spatial temperature distribution and the pebble migration vector approximation is fairly straightforward. For the initial loading points defined previously, a time dependent estimate of the total thermal exposure can be depicted in a graph of time

and temperature. The path travelled by the pebble as it slowly flows downward through the core is described by the time-dependent temperature profile. This profile is depicted for a range of initial starting locations in Figure 3-15. This time dependent temperature profile can then be integrated to estimate the total thermal exposure profile for each of the selected initial radial positions.

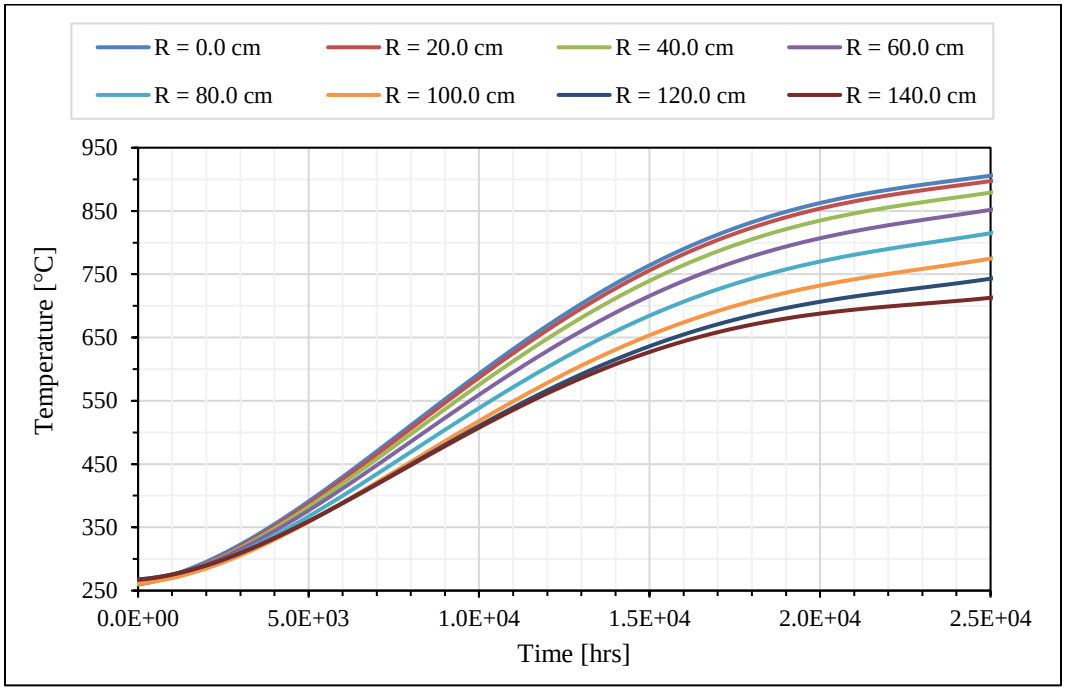

Figure 3-15: Thermal exposure for pebbles with varying initial radial position

The impact that this thermal exposure will have on the functional performance of the proposed instrumentation will be explored in later chapters. As a general simplification, it can be assumed that the thermal exposure will impact the sensor material structure in a similar way to annealing processes for various metals. Being exposed to a specified temperature for a period of time creates a known pattern of grain growth, which contributes to the material's physical parameters. In this case, those parameters affect the innate ability of the material to resist the flow of electricity.

4 MEMS Thermal Sensor Design, Fabrication, and Deployment

The fundamental deliverable of this research endeavor is a novel MEMS thermal sensor array that can mitigate the environmental effects which typically prelude instrument failure in HTGR thermal environments. The fabrication of the proposed instrument is not trivial and requires a complex series of thin film or MEMS fabrication processes to produce a sensor with precise geometry and material properties required for robust, accurate operation in the target environment. The level of precision achieved for a range of instrument parameters is a strong predictor for the final sensitivity of the instrument, which is a primary driver for the functional applicability being investigated. This chapter is devoted to exploring MEMS thermal sensor design, describing the fabrication processes and materials utilized, and defining a sensor geometry to be further analyzed in later sections.

4.1 Harsh Environment Calibration Drift Mitigation Strategy

MEMS thermal sensors can be developed to utilize several different types of physical processes to measure thermal properties for a wide range of applications. The type of sensor which is selected or this investigation is the resistance temperature detector (RTD), which measures the electrical resistance of a sensing element to indirectly determine the temperature of a target environment.

RTDs provide extremely precise and accurate measurements of temperature with fast response times and good signal quality in ideal environments, but have operational constraints which limit their applicability in harsh environments. This is mostly due to a range of environmental effects that cause the resistance-to-temperature calibration curve to drift over time. These effects can be mitigated by utilizing two distinct instrument design strategies, one passive and one active.

The first is the traditional way in which harsh environment instrumentation is developed, by designing instrumentation specifically suited for a given harsh environment and

including various hardware alterations to passively isolate the instrument from specific environmental effects which distort measurement accuracy. Another method of mitigating these calibration drift effects is to actively monitor the instrument for calibration drift, and when it occurs, to update and adapt the known calibration curve to the properties of the instrument. With this method, if the instrument does undergo some material transition which affects the calibration, that effect can be actively accounted for. The difficulty in this strategy is knowing when this drift has occurred and how the instrument has changed.

4.1.1 Functional Design Concept Overview

The purpose of this investigation is to determine if those effects which cannot be mitigated completely can be effectively compensated by estimating the onset and propagation of material transitions that ultimately lead to calibration drift. This estimate is calculated through the use of an instrument array consisting of four linked RTD sensor traces with well-characterized and predictable signal deterioration mechanisms. These traces are also utilized by another, fundamentally different, method of temperature measurement to provide a reference from which the accuracy of the RTD measurement can be determined and the material properties of the sensor traces can be monitored.

Various types of instrumentation have been evaluated to determine their applicability for this approach to drift mitigation. An ideal configuration concept has been developed, which has favorable characteristics for the specified target environment. The proposed instrument consists of a coupled platinum RTD and thin-film strain sensor, fabricated atop an alpha-alumina (sapphire) substrate base. Because both the RTD and thin-film strain sensor both utilize resistance measurements, they can share a single sensor trace. The method by which this resistance is sensitive to temperature is fundamentally different however, which is the key to determination of the onset of calibration drift.

Sapphire is an extremely durable material and is often utilized for high temperature instrumentation applications because it is very stable and does not corrode or otherwise deteriorate in harsh conditions. Although that is an excellent property to utilize, it isn't the

key reason for choosing sapphire as an instrument base. Sapphire also has the unique property of demonstrating axially dependent thermal expansion. This property allows for a properly configured strain gauge to measure the temperature of the sapphire substrate by measuring the magnitude of the differential strain created by this anisotropic thermal expansion.

If a single instrument trace is used to measure both absolute resistance and differential resistance between two portions of the sensor trace, both of which can be correlated to temperature, then the variance between the two measurements can be used to determine the geometric and material condition of the sensor trace. If the sensor trace has changed in such a way that would cause the temperature calibration curve to drift away from the previously established standard, then an updated calibration standard can be estimated and applied.

To ensure the new calibration standard is accurate, the sensor trace must have a well characterized response to the material transitions which cause the drift to occur. This accuracy can be further assured if numerical methods can be used to reduce the measurement uncertainty, which requires many independent samples from a local area with similar environmental exposure. This can be accomplished by a deployment configuration which allows for high local instrument density, such as those demonstrated by MEMS instrumentation.

For these reasons, among many others which will be explored in this chapter, a novel **H**ybrid-**E**lectrical-**R**esistance-**T**h**E**rma**L** sensor, hereby referred to as a HERTEL sensor, is proposed.

4.1.2 Identifying the Root Causes of RTD Calibration Drift

RTD calibration drift is caused by a variety of processes. These are mostly concerned with physical material transitions which occur inside or near the sensing element. This includes external stress on the sensing element from surrounding materials, variation of electrical

conductivity due to structural material transitions, internal stress of the sensing element from grain formation or differential thermal expansion of constituent materials, material contamination of the sensing element via thermal diffusion or in the case of the proposed application, nuclear interactions resulting in material transmutation [105]. Other effects, such as electromagnetic interference, electron pair production due to high energy particle interactions, and interactions with other parts of the measurement hardware, such as the sensor leads or resistance measurement package, are not being considered as they are outside the narrow, thermal-effects scope of this investigation.

If the various processes which contribute to RTD calibration drift can be well-characterized and estimated, then the resulting signal can be corrected to remove the noise caused by these mechanisms and an accurate measure of temperature can be determined. A good place to start an investigation of RTD calibration drift mechanisms is the ITS-90 platinum resistance thermometry standard and its accompanying guide, presented by the BIPM [106]. This guide presents the effects described in the following sections as the primary drivers of calibration drift.

4.1.2.1 Chemical Transition of Materials (Oxidation)

A common source of calibration drift is the chemical reaction of the sensing element or substrate material with contaminates or free gas molecules in the sensing environment. The chemical reaction rate can be characterized by the partial pressure of the contaminate gas, the solid temperature of the material, and the orientation and size of grain structure within the material.

These effects are most common with free environmental oxygen, which is typically produced by the various insulating materials in the reactor cavity structure as they heat and produce off-gas from material restructuring, grain growth, etc. Some free oxygen is actually beneficial, as it may more readily react with other contaminates in the environment and form passivation oxides, but an overabundance can cause an oxidation reaction in platinum at high temperatures. These oxidation reactions are complex, with up to a dozen

possible oxides and allotropes. The general effects can be summarized into groups of reaction progression for various temperature bands.

At temperatures up to approximately 350 °C, a single surface layer of platinum oxide slowly forms, with the exact reaction rate being highly dependent on the partial pressure of free oxygen. This progression will saturate with a cumulative permanent room temperature calibration drift of approximately 1.0 to 2.0 mK for a standard 25 Ω RTD.

For temperatures between approximately 350 °C and 600 °C, the formation of oxide extends beyond the surface at a rate that is a function of the partial pressure of the free oxygen and the temperature. No apparent saturation limit is observed for this reaction, with typical effects including a permanent room temperature calibration drift of approximately 10 mK for a 25 Ω high-temperature standard platinum resistance thermometer (HTSPRT) resistor. More significant effects are observed at long operating times in this environment.

At temperatures above 600 °C, the platinum oxides will disassociate and the oxygen will typically migrate out of the platinum material lattice, returning the calibration drift offset to near zero in most situations, if a long dwelling period above 600 °C is utilized. Thus, it is vital that the time the instrument is exposed to temperatures between 350 °C and 600 °C is minimized, or if it does occur, the instrument should be either heated to above 600 °C for a period of time or the calibration reference should be adjusted to compensate for the oxide formation.

The substrate chosen for this investigation is alpha-alumina, which is a form of aluminum oxide. Thus, a certain amount of free aluminum and oxygen will be present near the platinum sensor trace and may cause some initial chemical deterioration. This is expected to reach an equilibrium point in which relatively rapid chemical reaction no longer take place, instead replaced by the slower process of thermal diffusion. The direct effects of chemical reactions outside of the oxidation described above will be assumed to be isolated

to the initial annealing phase of the instrument fabrication sequence, and is not expected to occur during normal operation of the device.

4.1.2.2 Thermal Diffusion of Impurities

Any two materials which are placed in contact with one another at high temperature will exhibit some level of thermal diffusion. This process occurs when the thermal energy of the material is great enough to break the grain or lattice bonds that typically hold a material together. As these bonds are broken, the material sheds free atoms into the surrounding surfaces, which can either recombine in the origin material or may travel a short distance in to the adjacent material. Once this occurs, the free atoms are relatively unlikely to ever return to the origin material and will instead either combine to form a new substance within the adjacent material or may simply occupy a lattice void and create an interstitial defect.

As electrons flow through an ideal conductor, the electrical resistance is primarily driven by the scattering of electrons by the thermal motion of the conductor atoms. The introduction of impurities in the conductor will increase this scattering rate and thus increase electrical resistance. This increase is not significantly dependent on temperature and corresponds to a calibration drift similar to that which is observed for oxidation reactions.

Both of the thermal diffusion outcomes described above will marginally change the electrical resistance of the instrument and must be accounted for in a similar way to the oxidation adjustments described in the previous section. The rate which is expected for this drift is highly dependent on the materials which insulate the platinum wire from the environment and the substrate chosen. Typical HTSPRT probes with a quartz insulation sleeve have been characterized as having a calibration drift rate of approximately 5 mK per 100 hours of exposure to temperatures above 450 °C for process monitoring environments. The specific rate of thermal diffusion for the platinum and sapphire material pairing will be estimated by investigation of the literature on this topic, as this is the primary thermal diffusion mechanism which is expected to occur.

4.1.2.3 Strain and Hysteresis

Strain, which is defined as the elastic distortion of the atomic lattice of the platinum material which comprises the sensor element by applied stress, will alter the resistance of the platinum sensor trace until the strain is removed. Hysteresis is defined as the combination of strain with thermal energies great enough to alter the lattice bonds under strain and permanently plastically reform the crystal structure, which relieves the strain and causes a permanent alteration of the calibration reference. This permanent alternation must then be accounted for with a correction factor. Thus, strain is considered a dynamic factor and hysteresis is regarded as a static factor.

The rate at which the elastic deformation transitions into plastic deformation, a process similar to mechanical or thermal 'creep', is highly dependent on the thermal exposure of the instrument. For a high-temperature, isothermal, static measurement over long time periods, this transition rate has only a slight impact the resistance measurement, as the fundamental mechanism by which the resistance is changed is very similar for both strain and hysteresis. The lateral strain in the material serves to constrict the cross-sectional area of the sensor trace, increasing the resistance as a purely geometric function of Poisson's ratio for the material and the applied strain.

A key difference between the resistance change caused by strain and that caused by the geometric deformation of hysteresis is that the resistance change due to strain also includes an extra piezoresistive effect, which is more significant than the geometric effect for strain-induced resistance variation of platinum and most semiconductor materials. The resistance change for platinum due to the piezoresistive effect at low temperatures is more than twice the magnitude of the resistance change due to geometric affects. This difference is observed to be even greater for thin film geometries and mono-crystalline films. The piezoresistive effect is induced by the widening of the electron bandgap due to the distortion of the lattice bonds, which restricts electron mobility in the material. Like other bandgap-based effects, the influence of this effect is reduced with temperature, as thermal noise reaches an energy equivalent to the bandgap energy at high temperatures.

For RTD sensors, it is when transitioning between temperatures that this rate of change between strain and hysteresis is especially important, as elastic deformations will be variable and induced by differential thermal expansion, but any plastic deformations will be static and will remain in the material. This causes the so-called 'hysteresis effect', which generates a different resistance curve for each temperature transition in which the rate of temperature transition is faster than the rate of complete deformation transition and residual strain remains in the material.

The fundamental operating concept for the proposed sensor configuration will utilize a measurement of strain to provide an alternative measure of temperature, so the actual strain on the sensing element will be known and can be directly accounted for in-situ, via a similar adjustment of the reference calibration curve as was described in earlier sections concerning oxidation and impurity migration. The characterization of this resistance change as a function of measurement temperature and thermal exposure is important to determine the maximum temperature transition rate as well as the permanent correction factors which will need to be applied to the calibration reference curve.

It should be noted that this approach to measuring strain at high temperatures is fundamentally opposite of the typical approach for strain measurement. In this approach, the piezoresistive portion of the resistance change is expected to slowly diminish over time and geometric transition is encouraged, which will offset the strain calibration curve permanently as the elastic deformations in the material lattice are slowly replaced with permanent plastic deformation, bringing the expected resistance change into alignment with a purely geometric approximation. The typical approach to measuring strain seeks to suppress this hysteresis effect and maximize the piezoresistive effect, gaining higher sensitivity and repeatability by preserving the material lattice and preventing plastic deformations.

For RTDs which utilize an AC or fast-switching DC measurement mode, this effect can be significant. As each measurement cycle heats the element slightly, allowing it cool

between measurements, this transition between temporary and permanent deformation accounts for approximately 0.1 mK to 1.8 mK of calibration drift from peak-to-peak. This effect can be mitigated by slowing the measurement cycle rate or by limiting the measurement current to reduce self-heating. However, this would also reduce the data density and accuracy obtained by the signal processing electronics, so a trade-off between these effects must be evaluated.

4.1.2.4 Vacancies and Defects

Vacancies and defects in the material lattice of the resistance sensor serve to increase the measurement resistance in the same manner as thermal diffusion of impurities, in that they create more electron scattering at the defect location. These vacancies and defects are primarily created by two distinct processes, described as either thermal or mechanical.

At temperatures above approximately 450 °C, the thermal energy of the constituent atoms is great enough to break lattice bonds and cause atomic displacement of the atom, resulting in a lattice vacancy, interstitial defect, or plane dislocation defects. The rate of this effect increases exponentially with temperature and can create multi-atom defects at high temperatures, as multiple atoms are dislocated and form a new lattice which is offset from the original lattice, essentially creating a new ‘grain’ in the material. This effect is on the order of tens of mK at 962 °C, which is a common reference calibration temperature.

The vacancy creation rate is balanced by the annealing rate, which is when the displaced atoms return to their original location, again due to the thermal energies driving lattice bond re-formation. These two rates will reach an equilibrium at a given temperature and will not result in permanent alteration of the calibration reference if the temperature transitions are slow. If platinum is suddenly cooled, by quenching for example, these vacancies do not have an opportunity to anneal, and will be permanently included in the material lattice, causing a permanent increase in resistance for the sensor. To avoid this effect, the maximum cooling rate for platinum is recommended to be no more than 50 °C per hour for temperatures above 500 °C. Once the 500 °C threshold is reached, the sensor

can be cooled more rapidly to avoid undue oxidation, as vacancies are less prevalent in this temperature range.

Mechanical defects are similar to hysteresis in that the material lattice is plastically deformed, in this case by mechanical impact or vibration, which causes the calibration reference curve to shift. These effects are additive in nature, with every impact raising the sensor resistance marginally. These defects can be annealed to return the sensor to its original calibration reference; however, a large number of defects will require proportionally longer exposure times at high thermal energies to re-form the surrounding lattice bonds, which will return to their most energetically favorable formation. Very large mechanical defects can't be practically annealed because the material lattice will have shifted beyond the previous 'ground state' or fully annealed formation, and a different formation will be formed once all lattice bonds are fully annealed and reach their most energetically favorable state. If this new formation has significantly different geometry when compared to the original formation, the alteration to resistance would be permanent.

Mechanical defects are common for newly fabricated sensors and are characterized by internal stress in the sensor material. These defects must be annealed to return the material lattice of the sensor to the 'ground' or stress-free state, from which the most accurate and stable calibration curve can be developed.

4.1.2.5 Thin Film Effects on Electron Mobility (Electron Mean-Free-Path)

In addition to the previous effects reviewed in the ITS-90 standard, additional parameters have been identified by researchers investigating the impact of annealing on the thermal coefficient of resistance (TCR) for platinum thin films. Among these are the effects which are assumed to be more prominent in thin film devices, such as that which is proposed in this investigation. These effects include the density of grain boundaries in a material as well as variation in current transport density, which results in a non-linear scaling of electron mobility as the mean-free-path length nears the film thickness.

It is generally observed that longer annealing times will lower the thermal coefficient of resistance due to grain growth. For alumina substrate, this includes grain re-orientation, as growth in the (111) crystal lattice orientation is preferred due to the epitaxial material boundary shape of the alumina substrate. As the grains are re-oriented and grow in size, electron mobility, measured by mean-free-path, tends to increase as the grain boundary density becomes lower. This effect is generally well understood but characterization is heavily dependent on the materials utilized. If this mean-free-path nears a magnitude which is equivalent to the film thickness, additional constraint on electron mobility results in a non-linear reduction in TCR for additional annealing time, even as grain size continues to grow. This is only a concern for very thin films (nanometer scale), such as those used for transistor fabrication; thus, this effect is only marginally applicable in this case.

4.1.3 Applicable Calibration Drift Mitigation Techniques

If the effects explored in the previous section can be accurately characterized in the target environment, calibration reference adjustment is simply a matter of applying the right factors as a function of instrument thermal exposure. Mitigation should be approached in the two ways previously described, both passively by reducing the impact of the calibration drift effect, and actively by measuring the onset and magnitude of the drift effect so that it can be compensated for. The following strategies will be utilized to mitigate each of the effects previously described.

4.1.3.1 Sapphire Substrate Structural and Chemical Durability

The material chosen for the substrate and thin protective film surrounding the sensor is alpha-phase, mono-crystalline alumina, also called sapphire, and has a range of desirable characteristics for the intended application and environment.

A high Young's modulus indicates the material will resist strain due to the impact of external forces, such as the point loading of compression from surrounding fuel pebbles. The mono-crystalline structure of the material provides consistent thermal expansion and heat conductance characteristics. Sapphire has a high lattice bond energy, meaning it

requires relatively high thermal energy to prompt material transitions such as vacancy formation or off-gassing of oxygen. The electrical insulation characteristics are also very stable, even at high temperatures, reducing the amount of leakage current expected to flow through the insulator.

4.1.3.2 Platinum Corrosion Resistance and Thermal Stability

The material chosen for the resistive trace on the instrument is platinum, which has long been an ideal material choice for high temperature instrumentation due to its resistance to corrosion and high thermal stability. Particular interest in the material compatibility between alumina, aluminum, and oxygen are of a concern, as these materials will be readily available as thermal diffusion contaminants due to the close proximity of the platinum sensing element and the surrounding substrate.

Alumina itself does not thermally diffuse into platinum as a coherent molecule, but oxygen and aluminum do disassociate at the material boundary and may thermally diffuse as free atoms. While platinum does form an oxide layer at high temperatures, this layer disassociates readily and does not contribute to long term calibration drift at temperatures above ~600 °C. Aluminum is the primary concern, as it will readily diffuse through platinum if the concentration of free atoms at the material boundary is large. One method of preventing this is to allow a small amount of oxide formation on the platinum surface, which acts as a passivation layer and preferentially reacts with the free aluminum atoms to re-form alumina, rather than allowing the aluminum to pass further into the material.

Platinum will form platinum silicate when paired with silicon-based materials, such as silicon carbide, at high temperatures. This is a primary difficulty with platinum-on-silicon instruments and will be avoided in this case by utilizing alumina instead of silicon or silicon carbide as a substrate material.

Two key concerns for the use of platinum are the bonding strength to the sapphire substrate and the physical material limitations of pure platinum. Bonding strength is primarily a

function of similarity in crystalline epitaxial structure, which is a good match between platinum and alumina. If the bonding strength needs to be increased, a metallization layer of chromium, zirconium, or molybdenum can be used as an adhesion layer between the two materials. This interstitial material can introduce additional considerations for effects such as thermal diffusion, so they will not be considered unless they prove to be a necessary addition.

Concerns regarding the material properties of pure platinum can be addressed by adding a small amount of molybdenum, rhodium, or rhenium to produce a platinum alloy with considerably higher melting temperature. Again, the alloying of these materials creates additional complexity in predicting the thermal response of the instrument, due to additional thermal diffusion between the adjacent materials. Thus, these alloying elements will also not be considered unless deemed necessary for the function of the instrument.

4.1.3.3 The Benefits of Utilizing a MEMS Instrument Array

A key component of the proposed instrumentation approach is the use of an instrument array. MEMS fabrication techniques are uniquely suited to the fabrication of sensors in an array formation because many sensors can be fabricated with batch processing. The various fabrication methods mentioned previously and expanded upon later in this chapter are sequential, layered techniques that can be easily scaled across large areas. In addition, the material geometry for each sensor in a given layer can be easily varied, meaning that a large number of sensors with unique, precise geometry and material characteristics can be fabricated at very low cost. This high confidence in the final sensor parameters coupled with the low cost of variation and ease of scaling to high volume manufacturing makes the approach of utilizing MEMS instrument arrays a key component of the novelty of the presented research.

Because the MEMS fabrication process enables the use of micro-scale sensor arrays, a key assumption can be made regarding the environmental exposure of each sensor in the array. Due to the close proximity of the proposed array, it is assumed that the temperature of each

sensor is identical and the possible radiation exposure for each sensor is likewise very similar in magnitude. This allows for varied parameters of these sensors to be isolated as the primary motivator of differential measurements between the sensors, and allows for the fundamental capability of leveraging this differential response to estimate environmental exposure, which then enables an estimate of sensor drift to be made.

The differential response to environmental conditions can be realized in several unique ways. One example is the inclusion of a thermal diffusion agent in varied concentrations on the upper surface of the platinum trace, then comparing the differential resistance as the agent diffuses through the platinum material would allow for a determination of thermal exposure for the instrument. In this case, a differential strain measurement is utilized to provide a functionally independent measurement of sensor resistance, which allows the estimation of thermal exposure to be made based on the comparison of the RTD measurement against the strain derived temperature.

Another key benefit of an array sensor deployment configuration is that sensors in close proximity can be cross-correlated to reduce the uncertainty in measurement accuracy. If two sets of sensor arrays are mounted to the same pebble, and it is known that a single pebble will only undergo a limited thermal gradient due to heat conduction of the material and bounds on the expected environmental profile, then the measurements from these two arrays must lie within a specified range of each other. This allows for the standard error to be analyzed with additional boundary conditions, increasing the overall confidence in measurement when applied across an entire instrumentation system.

The benefits of instrument arrays are significant, but a number of challenges are also created. Although the long-term application for the instrumentation approach presented is assumed to utilize wireless signal transmission, the practical development of this approach will utilize a wired connection initially. Having a large number of sensors in an array creates significant challenges regarding the signal wire connections and routing of the signal wires out of the harsh environment the sensor is exposed to. It is assumed that multi-

conductor, mineral insulated wire will be utilized as the signal lead wire in this case. Each sensor will need at least four terminal connection pads, each of which is around a millimeter in diameter. This allows the mineral insulated wire to be bonded, via silver soldering or similar high temperature brazing technique, to the pad after the sensor is fabricated and the batch processed wafer is diced into individual units. Even a small sensor array will thus require a large area just for termination connections and cable routing, relative to the characteristic dimension of the sensor, which is the size of the sensor trace in this case.

4.2 MEMS Thermal Sensor Design

In this section, the design decisions which determine the sensor geometry and material selection will be examined and a final instrument design will be defined. This process begins with a clear description of the design targets, philosophy, and key equations; followed by a summary of the instrument materials and geometry selection process. The final design is then described in detail and key parameters are identified based on their functional impact. Finally, the sensitivity of these key parameters is investigated to determine the allowable variation for manufacturing processes.

4.2.1 Primary Design Target Parameters

The goals for design are twofold. The first and primary goal is to create a functional sensor array that can accurately measure the temperature in the target environment. The second goal is to isolate the mechanisms of calibration drift so that thermal exposure becomes the primary, well-characterized means of measurement drift.

Creation of a functional sensor array can be achieved simply by creating a sensor geometry that is comprised of pure elemental platinum and has an ultimate resistance in the range of 25 Ω at the TPW (273.16 K or 0.01 °C). This range is chosen so that SPRT calibration interpolation standards can be utilized. The sensor portion of the instrument is functionally complete by providing stable termination points for the connection of power and signal analysis components. Isolating the various causes of instrumentation drift is a more

difficult endeavor, as a range of effects can cause the resistance to temperature relationship to be unstable, as explored in the previous section.

For HTSPRTs, a TPW resistance from 0.2 Ω to 2.5 Ω is commonly used, with a measuring current of 5 mA to 10 mA with wire diameter of 0.3 to 0.5 mm. This lower initial resistance and larger measurement current are used to compensate for the relatively large leakage current observed for mica insulation, which is used for construction of HTSPRTs used for process monitoring. The selection of sapphire as a substrate removes this requirement, as it does not exhibit the same large leakage current at high temperatures. To ensure low power requirements and high measurement accuracy by avoiding self-heating of the sensor wire, a 25 Ω initial resistance will be used unless thermal leakage is demonstrated to be a significant contributor of measurement error.

4.2.1.1 HTGR Environmental Parameter Review

As described in the previous chapter, the target environment for instrument deployment will include a range of temperatures depending on the deployment location within the reactor core. Thus, we have an expected core-wide temperature variability described by the thermal exposure profile identified in Figure 3-15. This predicts an operational exposure of 25,368 hours across a range of approximately 250 °C to 910 °C for steady state operation, which will be the functional environment for the proposed instrumentation.

Axial coolant pressure drop is described by the primary thermal hydraulic simulation reference as being approximately 80 kPa across the core height, applying this 80 kPa gradient to the design coolant pressure of 7.0 MPa indicates a height dependent environmental pressure of between 6.92 MPa and 7.0 MPa. Mechanical pressure from adjacent fuel pebbles will be assumed to be isolated by the sensor mounting and will not be considered outside of the analysis done for the pebble migration study in the previous chapter. The environment being considered will include pure helium coolant, with carbon freely available at the instrument surface due to off-gassing of carbon oxides and free carbon dust which is expected in the operating environment.

Other environmental parameters for a functional reactor would be the expected radiological exposure for the instrumentation. However, it should be recalled that those effects are not being considered in this case, as the initial use case is for thermal hydraulic experimental facilities only. In addition, the effects of electromagnetic field noise typically created by the high voltage heating system of such facilities will not be considered here, as it is highly variable and dependent on the specific type of heating system utilized for the test facility.

Considerations of effects on signal transmission wires, external power and signal analysis equipment, and all other components external to of the sensor assembly will be considered stable and not analyzed for response to the assumed environment.

4.2.1.2 Target Instrument Accuracy

The targeted accuracy will be equivalent to what is currently implemented for contemporary HTGR thermal hydraulic instrumentation systems. The thermocouples utilized for the HTR-10 instrumentation system are K-type, class 1E thermocouples, with an expected accuracy of ± 1.5 °C or ± 0.4% of measured temperature, whichever is greater. Thus, this will be the minimum acceptable accuracy variation for the thermal exposure range specified.

4.2.1.3 Target Instrument Response Rate and Measurement Frequency

The instrument response rate is highly dependent on the thermal insulation properties of the shielding layer of sapphire which protects the sensitive resistive element from environmental exposure. A trade off must be evaluated between the level of protection offered by this layer against the impact on instrument response rate.

As a reference, the target will again be set to provide an equivalent performance to what is typically used for contemporary HTGR instrumentation systems. The response rate for the K-type thermocouples utilized in the HTR-10 is a function of the insulation parameters of the magnesium oxide powder which protected the probe tip as well as the probe construction, grounded or ungrounded.

For an ungrounded probe diameter of 3.17 mm, it can be assumed that the layer of magnesium oxide is no greater than 1 mm in thickness when accounting for the diameter of the thermocouple wire and stainless-steel sheath. Given that the response time is a function of the heat transfer properties of measurement media and environmental temperature, a conservative estimate would be in the range of 2.5 seconds for an ungrounded probe to 0.5 seconds for a grounded probe. Thus, a target of 0.5 seconds is selected for response time of the developed sensor.

The measurement frequency of an RTD sensor is limited by the self-heating of the resistance trace during measurement. If a square wave, 2.0 Hz, DC excitation current profile with a variable up-time is used for measurement, this would result in a measurement frequency equivalent to the targeted response rate of 0.5 seconds. Thus, 2.0 Hz is the targeted instrument measurement frequency.

4.2.1.4 Target Instrument Durability

Initial design efforts will assume an environmental exposure equivalent to a single pass through the pebble bed core fuel recirculation system. Thus, the target instrument durability target is defined as maintaining the target accuracy throughout this single-pass cycle.

4.2.2 Primary Design Philosophy and Key Equations

The design philosophy utilized in the development of the presented instrument arrays are focused on isolation of the effects of thermal exposure which influence calibration drift for RTD sensors. The design of each sensor and each array package should not be overly complex, as the geometry is somewhat limited by the fabrication techniques selected. Thus, the simplest geometry is chosen and unnecessary complexity in features is avoided when possible.

Generally, design features which were demonstrated to be successful in literature are chosen. Which is the origin for selection of the meander type sensing element and the

determinator for geometry of the vias and termination pads. Geometric complexity is isolated to two layers, a top layer which faces away from the mock fuel pebble and a bottom layer which routes the traces to convenient locations for connection of the meander sensing element above to the lower termination pads required to connect the signal wire leads. Between these two layers, a number of channels (called vias) are utilized to route connections through the sapphire substrate.

The thickness of each insulating layer and the of the sensor circuit components are initially selected from various successful fabrication operations described in literature, then adjustments are made to ensure compliance with the design targets described previously. The sensing element geometry is motivated by the desire to achieve a sensor resistance of 25 Ω, which is an industry standard for SPRT elements. The substrate thickness is motivated by commercial availability, with 725 μm (±25 μm) 1120 (A-plane) sapphire wafers in 100 mm and 150 mm diameters being widely available from industrial suppliers.

4.2.2.1 Fundamental Equations for Circuit Analysis and Design

A fundamental equation for design of a resistance-based instrument is defined in Equation 4-1. It describes the relation of the electrical resistance (R, Ω) to the resistivity $(\rho, \Omega\, m)$, length (L, m), and cross-sectional area (A_c, m^2) of a conductor. Note that the resistivity is a function of temperature, with the triple point of water (TPW, 297.15 K) being chosen as the reference temperature for selection of the generic value.

$$R = \frac{\rho L}{A_c} \qquad \text{Eq. 4-1}$$

Most equations useful for electronic design are derived from Ohm's Law, defined in Equation 4-2, which relates the resistance (R, Ω), current (I, A), and electric potential or voltage (V, V). These factors are related to power (P, W) as described in Equation 4-3.

$$V = IR \qquad \text{Eq. 4-2}$$

$$P = I^2R \quad \text{Eq. 4-3}$$

Ohm's Law is extended to circuit analysis via Kirchhoff's Current and Voltage Laws, which state that the sum of currents entering and exiting a circuit node must be equal and that voltage increases and decreases must be equal in a closed loop circuit, respectively. The equivalent resistance of resistors in series or parallel, defined in Equations 4-4 and 4-5, is a matter of adding either the resistance value or the inverse resistance value for each component.

$$R_{Series} = R_1 + R_2 + R_3 + \cdots + R_N \quad \text{Eq. 4-4}$$

$$\frac{1}{R_{Parallel}} = \frac{1}{R_1} + \frac{1}{R_2} + \frac{1}{R_3} + \cdots + \frac{1}{R_N} \quad \text{Eq. 4-5}$$

Extending this circuit analysis further to the specific case of the WSB circuit as applied to strain gauges, Equation 4-6 defines the ratio of change in resistance $(\Delta R, \Omega)$ over the initial resistance (R_0, Ω) as equivalent to the product of strain gauge factor (k) and strain (ε). The strain is defined in Equation 4-7 as being equivalent to the ratio of a change in a spatial dimension, such as length $(\Delta L, m)$, over the original dimension (L_0, m), or as the ratio of stress $(\sigma, N/m^2)$ to the Young's modulus $(E, N/m^2)$ of the material.

$$\frac{\Delta R}{R_0} = k\varepsilon \quad \text{Eq. 4-6}$$

$$\varepsilon = \frac{\Delta L}{L_0} = \frac{\sigma}{E} \quad \text{Eq. 4-7}$$

The strain gauge factor is commonly assumed to be equal to 2.0 for most thin-film metallic strain gauges and is typically uniquely defined for each individual strain gauge during calibration. The theoretical basis for gauge factor is described in Equation 4-8, which relates the gauge factor (k) to the Poisson's ratio (ν) for a given material, the strain (ε) and the piezoresistive effect, which is defined as the ratio of change of resistivity $(\Delta\rho, \Omega\, m)$ over the initial resistivity $(\rho, \Omega\, m)$, per unit of strain.

$$k = \frac{\Delta R/R_0}{\Delta L/L_0} = 1 + 2\nu + \frac{\Delta\rho/\rho}{\varepsilon} \qquad \text{Eq. 4-8}$$

Fundamental to the analysis of RTD elements is the effect of temperature on resistance. This relation is a function of the temperature offset $(T, °C)$ from an initial temperature $(T_0,\ °C)$ and the temperature coefficient of resistivity $(TCR\ or\ \alpha, °C^{-1})$ and is defined by Equation 4-9. It should be noted that TCR also varies with temperature.

$$R(T) = R_0[1 + \alpha(T - T_0)] \qquad \text{Eq. 4-9}$$

As a reminder of the specific circuit configuration being proposed for this hybrid resistance instrument, an example of the WSB and Ohm measurement circuits is depicted in Figure 4-1, which was previously presented as Figure 2-8.

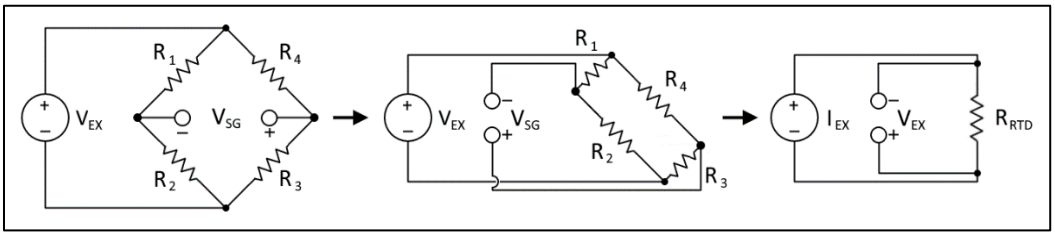

Figure 4-1: WSB circuit (left) compared to Ohm measurement circuit (right)

A number of standardized equations exist for calculating the parameters of the 4-wire Ohm measurement and WSB circuits, all of which are derived from Ohm's and Kirchhoff's Laws. These include is a simplified equation for the bridge voltage (V_{SG}, V) as a function of the four resistance values (R_{1-4}, Ω) which comprise the four balanced legs of the WSB circuit, and the bridge excitation voltage (V_{EX}, V) defined in Equation 4-10. A similar relation can be derived for the expected voltage from the 4-wire Ohm measurement, with the measured voltage (V_{RTD}, V) as a function of the four equal resistance values which comprise the sensor element and the excitation current (I_{EX}, A), defined in Equation 4-11.

$$V_{SG} = \left[\frac{R_3}{R_3 + R_4} - \frac{R_2}{R_1 + R_2}\right] V_{EX} \quad \text{Eq. 4-10}$$

$$V_{RTD} = I_{EX} R_{RTD} \quad \text{Eq. 4-11}$$

These equations can be simplified for the hybrid instrument which is proposed, as the resistance of the RTD is equivalent to the combined resistance of the WSB, as long as the two halves of the bridge remain balanced. This simplification is defined in Equations 4-12 and 4-13. At the calibration basis point of TPW, all legs of the WSB will be equal because this is also the assumed zero strain point. Thus, at this point the RTD resistance is equivalent to any one of the bridge resistances, as defined in Equation 4-14.

$$V_{RTD} = V_{EX} \quad \text{Eq. 4-12}$$

$$\frac{1}{R_{RTD}} = \frac{1}{R_1 + R_2} + \frac{1}{R_3 + R_4} \quad \text{Eq. 4-13}$$

$$R_{RTD@TPW} = R_1 = R_2 = R_3 = R_4 \quad \text{Eq. 4-14}$$

4.2.3 Summary of the Instrument Development Process

In this section, the development process is reviewed and key decisions concerning the selection of instrument materials and geometry are described in detail. The motivations for the design choices are made clear and support is provided through contextual references to the literature used to develop the initial sensor parameters. Any design decisions not detailed in this section are assumed to be made according to the design philosophy presented earlier in this chapter.

4.2.3.1 Sensor Material Selection

MEMS instruments are often described as “systems of materials” due to the impact of inherent material properties at the spatial scales being considered for instrument design. Large temperature gradients and harsh environmental conditions drive material transitions

which can significantly alter instrument calibration and reduce signal quality. Thus, the selection of materials should be carefully considered. Materials must be selected for three primary functional classes; a substrate, sensing material, and a protective shielding material. An additional three functional classes are also considered; a thermal diffusion material, a thermal conduction material (heat spreader), and a metallization material (adhesion promoter). Several materials are considered for each of these applications in the following section and the most desirable materials are selected for initial design efforts.

It is vital that the materials chosen for sensor design share similar material properties, such as coefficient of thermal expansion (CTE) and epitaxial crystal structure. This prevents internal stress from being created at material boundaries, which reduces unwanted strain or hysteresis effects, and promotes good bonding at material boundaries. In addition to these structural inter-material concerns, the materials chosen should also be corrosion resistant, have stable grain formation at the expected operating temperatures, and resist unintended thermal diffusion across material barriers. The materials must be readily available at high purity and be capable of being manipulated using common MEMS fabrication techniques.

Metallic thin film RTD sensors commonly feature a platinum, nickel, silver, or gold thin film sensing element deposited on an insulating substrate comprised of silicon dioxide, alumina, quartz (fused silica), sapphire, titanium dioxide, tungsten oxide, or various other refractory insulating materials. An outer corrosion inhibitor or shielding layer is typically used to seal the instrument and prevent intrusion of contaminants or corrosive elements. The choice of materials is affected by the environment of deployment and the expected interaction between the sensing material, the selected substrate, and the shielding barrier.

Additional interstitial material may be used to promote mechanical adhesion of the sensing material to the substrate, to provide an auxiliary function, such as grain growth inhibition, through the addition of a thermal diffusion agent, or to ensure isothermal operation though the addition of a high thermal conductance layer near the sensing element. These

secondary materials can introduce additional variables that must be accounted for when analyzing sensor performance and may cause significant reliability issues for operation at high temperatures if their thermal and mechanical response is not well characterized. To avoid this, additional materials should only be added if absolutely necessary and a preference for simple geometry and fewer material interfaces is advised.

If the instrument is incorporated into a manufacturing process which already utilizes a silicon wafer as the substrate material, such as for embedded sensors in integrated circuit electronics, then a thin insulating layer of silicon dioxide is typically utilized to create a suitable foundation for a platinum sensing element to be deposited on top of. Silicon dioxide has two primary drawbacks however, the CTE difference in these materials is significant and platinum does not adhere well to the silicon dioxide substrate at high temperatures, requiring the use of an intermediate material to aid adhesion. For this reason, silicon dioxide will not be considered for this investigation.

More exotic and durable substrate materials, such as silicon carbide, titanium dioxide and tungsten oxides, have been investigated for applicability to high temperature environments, with some promising results. All of these materials demonstrate excellent resistance to thermal diffusion and corrosive chemical attack, but exhibit significant hysteresis effects due to the large differential thermal expansion between the two materials and typical metallic sensing materials, such as platinum. Adhesion at material boundaries is also poor, requiring interstitial materials to be used. Silicon carbide in particular has shown promising results in applications as a ceramic thin film thermocouple when coupled with platinum. However, silicon carbide reacts adversely with platinum if thermal diffusion barriers are not used. Platinum silicide is formed if no oxidized passivation layer is present to contain silicon migration at high temperatures. Thus, these materials will also be excluded from further investigation as possible substrate materials.

Thermal sensors for high temperature or harsh environments typically utilize a metallic sensing element comprised of platinum or nickel alloys due to their high melting

temperature and good resistance to corrosion. Common choices for the insulating substrate include alumina or silicon dioxide, both of which have high melting temperatures and very stable material structure across a wide temperature range. Platinum and alumina have similar coefficients of thermal expansion (CTE in Table 4-1), and are commonly paired together for this reason.

Sapphire, which is the monocrystalline form of alumina, has also been recently investigated as a high temperature substrate for RTD sensors and demonstrates some beneficial properties when combined with platinum specifically, as they share the same epitaxial crystalline structure. The difference in CTE between mono- and poly-crystalline alumina may cause increased hysteresis effects or adhesion failure for operation across large temperature ranges. Additional investigation is required, as the initial results published in 2019 by Wang et. al [107] were very promising for high temperature applications, but is one of relatively few investigations into the material pairing. An additional consideration is that sapphire CTE varies significantly with temperature; however, in the range of ~900 °C, the CTE of sapphire and platinum are relatively closely matched.

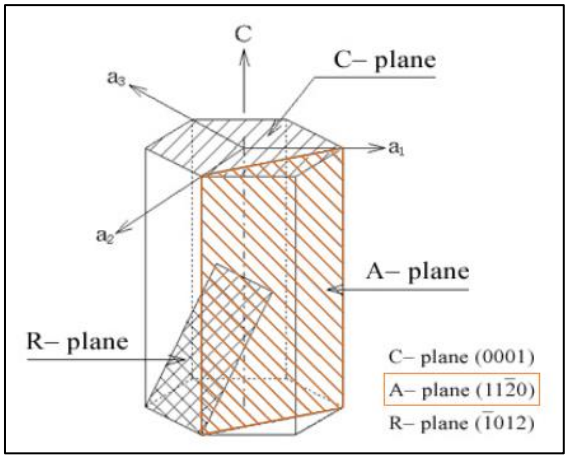

Figure 4-2: Structure and lattice planes of sapphire with A-plane highlighted [108]

Sapphire has been utilized for MEMS fabrication processes for many years, as it is the primary substrate utilized in silicon-on-sapphire (SoS) CMOS electronics for harsh

environments. This approach is fundamentally enabled by the identical crystal epitaxy spacing of silicon and sapphire, when cut on the R-plane, as described in Figure 4-2. Silicon-on-sapphire construction utilizes sapphire as a substrate and insulator for the addition of doped silicon thin films to form semiconductor components, such as piezoresistive pressure sensors, which have extremely high chemical corrosion resistance.

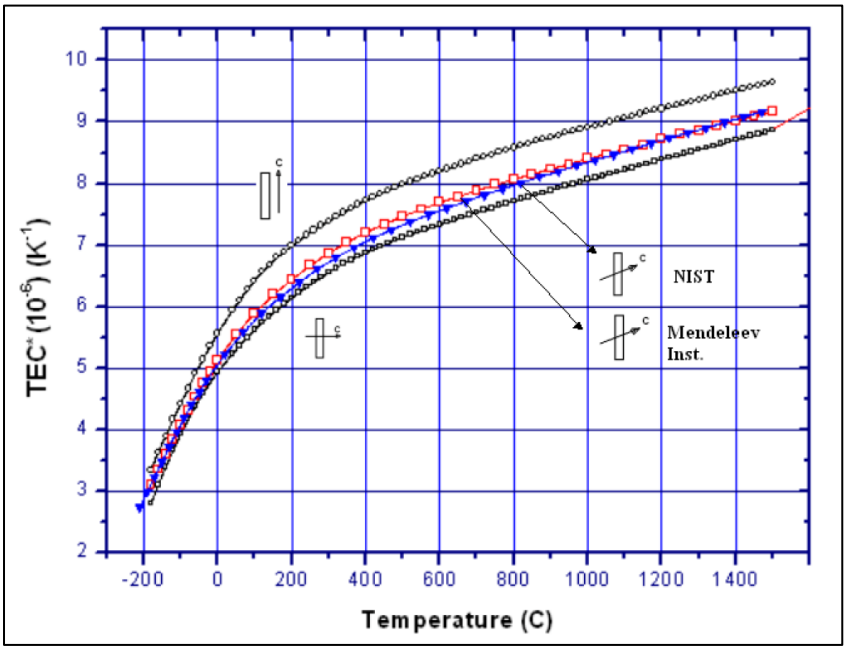

Figure 4-3: Temperature dependent CTE for sapphire par. and perp. to the C-axis [109]

When cut on the A-plane $(11\bar{2}0)$, also depicted in Figure 4-2, sapphire exhibits an anisotropic coefficient of thermal expansion. Although this differential expansion rate is marginal at very low temperatures, it amounts to approximately 7.5% differential CTE at the targeted operating range for high temperature instrumentation, as depicted in Figure 4-3. This creates the opportunity to utilize this substrate as an additional measure of temperature, if the differential thermal expansion can be measured accurately at high temperature. A common way that this is done is through the use of strain gauges oriented along perpendicular axis [110].

High temperature strain gauges typically utilize nickel or platinum alloys, although semiconductor strain gauges are typically preferred for harsh environments due to their high gauge factors, which is linked to their coherent lattice structure. If the piezoresistive contribution of the gauge factor is ignored, and the strain gauge is operated assuming a purely geometric gauge factor, as is expected at very high temperatures, then a wide range of metals provide similar response and the primary design criteria is shifted to preference for highly corrosion resistant materials.

Alternative sensing materials composed of monocrystalline non-oxide ceramic materials, such as doped silicon carbide, have also been investigated. Although these materials demonstrate good durability and very low hysteresis effects in harsh environments, the non-linear resistance-to-temperature profile exhibited by many of these materials results in poor instrument accuracy and low measurement precision. In addition, the difficulty of developing and preserving a mono-crystalline structure for operation in harsh environments requires specialized fabrication considerations. Research in this area will likely be possible in the future, but the current state of development is not mature enough for the limited scope of this project.

As an initial choice of materials to create an instrument sensitive to both temperature and axially dependent differential thermal expansion, platinum and sapphire are selected. Pure platinum exhibits a linear TCR across a wide temperature range, is highly corrosion resistant, has a massive amount of high-quality reference and characterization material available, and has good performance demonstrated at high temperatures due to the use of pure platinum for platinum thermocouples and RTDs for definition of calibration standards. Sapphire is chosen as the substrate for high mechanical and chemical stability, ease of manufacture, high epitaxial and thermal compatibility with platinum, and most importantly, the property of axially dependent differential thermal expansion. In addition to this, studies on the high temperature characteristics have indicated that poly-crystalline alumina does not thermally diffuse into platinum at temperatures below 900 °C [107] [111] [111]. Sapphire is expected to have a slightly higher barrier for thermal diffusion, with

some investigations indicating a threshold of 1,100 °C or more. Material properties are listed in Table 4-1 for comparison to materials with similar functional applicability and later reference.

The final choice of primary material is the shielding or capping barrier which is deposited on top of the sensor element to protect it from the surrounding environment. To keep material interfaces as uniform as possible, the obvious choice for this is alumina. The capping layer would ideally be thermally deposited so that the crystal lattice is continuous. If this proves to be too difficult to realize, poly-crystalline alumina could also be deposited via a sputtering system, although the expected performance in that case is expected to be slightly worse than if a mono-crystalline capping layer is utilized.

Table 4-1: Primary and Secondary Material Parameters [107] [112] [113] [114]

Material	**Resistivity (ρ) [nΩ m] at TPW**	**TCR (α) [K^{-1}]**	**CTE [10^{-6} / K]**
Platinum (Pt)	97.65	0.00393	8.90
Rhodium (Rh)	43.30	0.00445	8.35
Chromium (Cr)	125.0	0.00301	4.90
Alumina (Al_3O_2)	1.0×10^{25}	-	8.40
Sapphire (α-Al_2O_3)	1.0×10^{25}	-	9.03 – 8.31 *
Silicon (Si)	2.3×10^{12}	-	2.60
Silicon Dioxide (SiO_2)	1.0×10^{25}	-	0.60
Silicon Carbide (SiC)	2.3×10^{12}	-	4.00

* Note: Sapphire CTE varies with optical axis alignment and temperature (at ~1,270 K)

In addition to the platinum and alumina materials chosen for the sensing material and substrate, additional secondary materials should be selected for the optional inclusion of metallization, thermal diffusion, and thermal conducting layers. As stated previously, these additional materials should not be included in the sensor design unless necessary, as they will increase the complexity of analysis and will likely contribute to failure mechanisms

associated with thermal diffusion of the additional material into the platinum sensing material.

One of the concerns identified in literature for the deposition of platinum onto alumina substrate is poor adhesion of the metal to the substrate, leading to delamination and the sensor material pulling away from the substrate. These investigations were primarily focused on the utilization of poly-crystalline alumina rather than mono-crystalline sapphire, but it is still a concern which should be addressed. Although this is not desirable, it doesn't necessarily present an immediate failure mode for the instrument if other mitigation measures are taken. These measures could include the deposition of the platinum into a deep channel, carved out of the substrate by anisotropic DRIE etching methods, rather than on the surface of the sapphire, or alternately ensuring the capping layer of alumina has good adhesion in the areas not covered by platinum. This would ensure that the strain measurement is still accurate, as the material may delaminate but will not move, because no gap exists for it to translate into.

If this kind of mechanical bounding isn't possible or creates unforeseen errors, then a metallization layer can be added to promote adhesion. Studies into this material combination indicate that chromium would be an ideal choice for this purpose, promoting good adhesion across a wide temperature range without significant thermal diffusion into the platinum. Titanium is another option, although this has been shown to diffuse into platinum at relatively low temperatures, starting around 400 °C [115].

Although thermal diffusion is an effect that is best avoided if possible, there are a variety of extended functions that could utilize a degree of well-characterized thermal diffusion. Grain growth in platinum, which has been shown to occur at high levels of thermal exposure, can be controlled via a thermal diffusion agent, such as yttrium [116]. Another possibility is utilizing measurement of a thermal diffusion agent as an alternative to strain measurement as a means of estimating the thermal exposure. If two sides of a bridge circuit have differential exposure to a thermal diffusion agent, then the thermal exposure can be

estimated via differential signal decay. Rhodium would be an ideal choice for this application, as the material is widely used as a platinum alloy for high temperature thermocouples and diffuses at a relatively slow rate without creating lattice defects in the platinum material. Rhodium and platinum also have similar a similar CTE, meaning undue strain can be avoided.

Thermal diffusion for a variety of materials has been studied to better understand the performance of thermal barrier coatings for applications such as jet turbines, discharge nozzles, and other applications where metallic components must be protected from rapid oxidation or corrosion. In particular, aluminum and titanium have been well characterized, as these materials are commonly utilized in aircraft engines. Platinum is used as an interstitial material to promote thermal barrier coating adhesion, and the thermal diffusion rate is well characterized as a function of thermal exposure and shared surface area. In particular, a thorough study by Marino et al is used as a primary reference on this topic [117], which characterizes the thermal diffusion rate via first-principles quantum mechanics calculations. This source provides a basis for characterizing the rate of thermal diffusion for the selected material in a platinum substrate, if that functionality is desired.

The final secondary material application is the addition of a heat spreader or thermal conductivity layer to ensure that the primary assumption of identical temperature across all parts of the sensor is possible. This could be accomplished by the inclusion of a metallic surface layer on the front of the sensor, deposited above the capping layer. Many materials would be applicable for this purpose, with the primary design criteria being a good match of CTE with the sapphire substrate so that no additional strain in created. Alternatively, the conducive material could be applied in a line or grid formation, to ensure that the material doesn't impact the strain profile. Additional platinum would be a good choice of material for this purpose, as it would resist corrosion and is obviously already used in the sensor construction.

4.2.3.2 Sensor Geometry Selection

Thin film RTD sensors typically utilize a "meander" type geometry in which the sensing material is deposited in a thin trace which traverses multiple times across a given surface to create a very long, thin conductive path. Considerations must be taken to ensure that the substrate supporting the sensor does not undergo material transitions which would induce irregular or non-repeatable strain on the sensing element across a given temperature range. Regular, repeatable thermal induced strain, such as that produced by a mono-crystalline substrate is expected and, in this case, encouraged. A thin film RTD is presented in Figure 4-4 to provide a visual reference for a common trace geometry.

For traditional RTDs, the sensing element is usually coiled around a central support pillar to prevent differential expansion between the substrate and sensing material from inducing stress in the sensing element. Thin film RTDs must be applied directly to the substrate surface, so this mitigation technique is not applicable. Some attempts at emulating this approach have been investigated, by creating a small cavity under the sensing material and allowing it to float freely, anchored by only a few points of contact. This technique produces a sensor which is then more vulnerable to dynamic forces, such as vibrations or impacts which cause the unsupported sensing element to deform and thus changes the calibration curve of the instrument in ways that are difficult to predict.

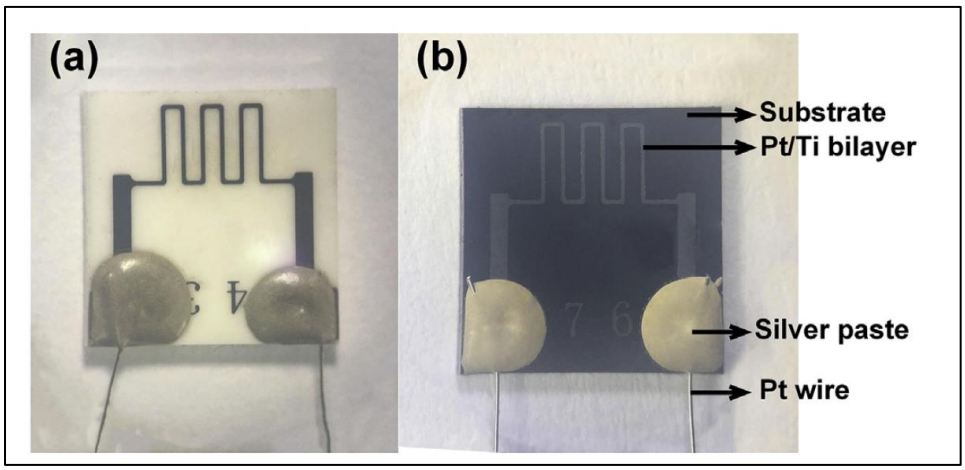

Figure 4-4: MEMS Pt/Ti RTD on (a) alumina and (b) silicon dioxide substrates [115]

For this investigation, it will be assumed that the thin film sensor must be created directly atop the supporting substrate and uses a meander geometry which is comprised of a thin sensing element connected to terminal pads. If a two-sided fabrication process can be realized, then one side will have the resistive trace deposited and the other side would have the connection points for signal wire leads, as depicted in Figure 4-5. The sensor would be mounted to the surface of an unfueled graphite pebble, with the resistive trace facing outwards and the wire termination points facing inwards. This mounting configuration would be identical for both wired and wireless operation, with the center volume of the pebble reserved for signal wire routing or to house a wireless signal transmitter. This configuration is depicted in Figure 4-6.

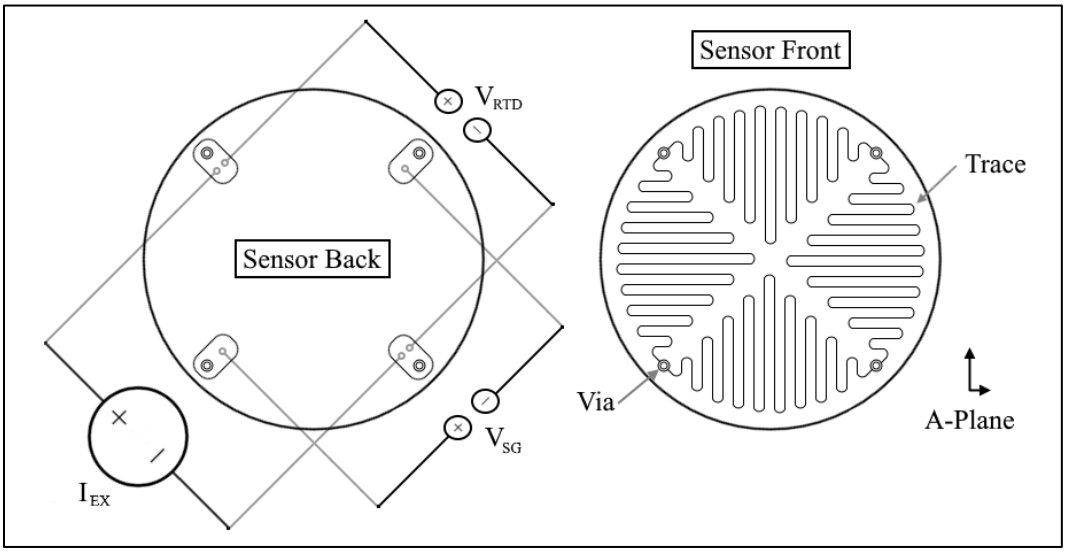

Figure 4-5: Proposed double-sided HERTEL sensor feature layout and connection scheme

Ideally, these terminal pads are deposited atop vias which route the electrical connection to the back of the sensor, where it would then be connected to a signal wire or to terminations for a wireless antenna for remote sensing applications. If this approach is not possible due to difficulty creating the vias or unintended effects of the three-dimensional strain that vias create as they undergo thermal expansion, then an alternate single-sided geometry can be used. In this alternate configuration, termination pads are instead included

on the upper surface of the sensor, adjacent to the resistive trace. If this configuration is utilized, the sensor would be installed with the resistive traces and termination pads facing toward the center of the fuel pebble so that the signal wire lead terminations can be protected from the harsh environment. The trade-off for this configuration is a reduced sensor response time, as the sapphire substrate would then insulate the sensor from the surrounding environment.

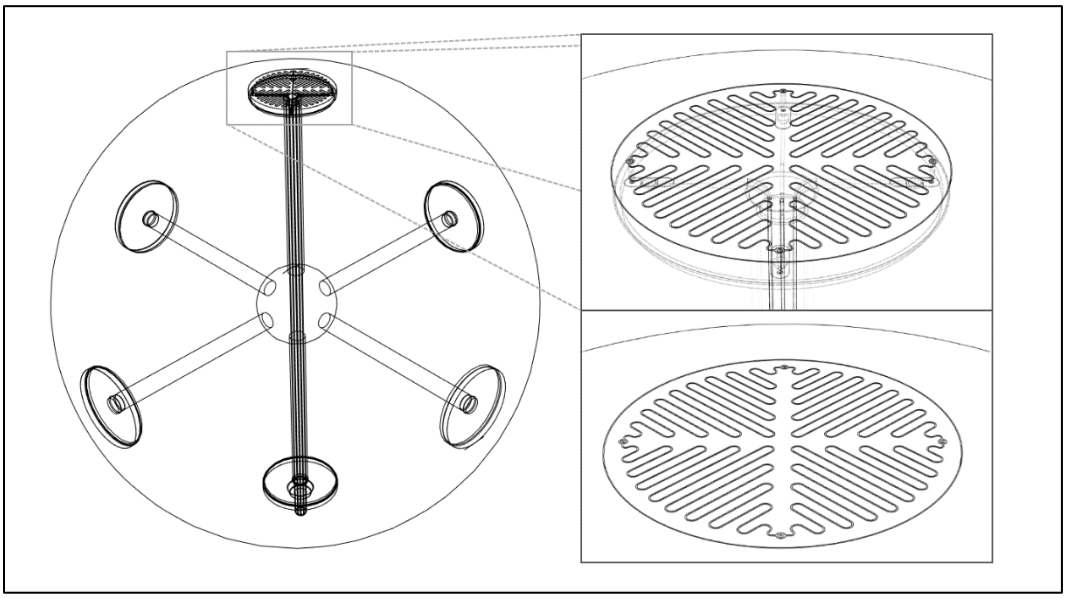

Figure 4-6: Proposed HERTEL sensor mounting configuration and signal wire routing

For this investigation, the instrument leads are assumed to be wired, but the interaction of the signal wire with the surrounding environment is not considered, as the intent of the research is to pave the way for future implementation of wireless signal transfer. Thus, the sensor being proposed is a simple resistive element with exposed signal wire termination pads. All other portions of the instrument are assumed to operate ideally and will not be further analyzed for design considerations.

The resistance of an RTD sensor is most accurately measured using a 4-wire Ohm measurement circuit, while the resistance of a strain gauge is measured using a Wheatstone

bridge, or WSB, circuit. These circuits measure different parameters of resistance, with a 4-wire Ohm circuit measuring the absolute resistance of a sensor trace while a WSB circuit measures differential resistance between two identical legs of the sensor trace. These two measurement circuits are comprised of similar components and are directly comparable, with the 4-wire Ohm measurement essentially being a special configuration of a WSB, as depicted in Figure 4-1. A more detailed circuit configuration is depicted in Figure 4-7.

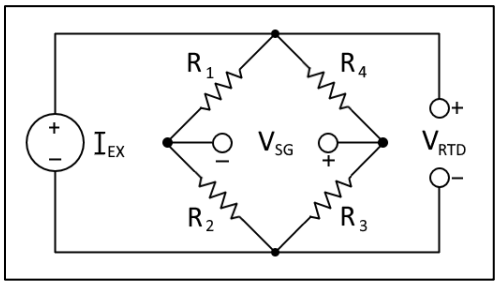

Figure 4-7: Detailed hybrid Ohm measurement and WSB circuit diagram

The proposed single array formation is depicted in Figure 4-5, with the continuous resistive trace comprising a dual RTD element as well as a full bridge strain element. Each array is self-contained as an independent unit, with one or more of these units installed onto a single graphite sphere, although it is assumed that only one array will be utilized for each graphite pebble in this case.

As the temperature of the instrument rises, the differential thermal expansion of the sapphire substrate X- and Y- axis causes the resistance of the four legs of the WSB to diverge, with the voltage measurement between the two sides of the bridge rising proportionally to the magnitude of the differential thermal expansion. A key feature of this circuit configuration is that the full-bridge WSB circuit generates a differential voltage at the indicated measurement points, but the resistance of the two sides of the circuit will stay balanced, as the axis-dependent resistance increase is equally divided by both sides of the circuit. This allows the resistance measurement of the entire circuit to be used to determine the temperature via the 4-wire Ohm measurement. If the two sides of the circuit did

become unbalanced, the RTD measurement would not be accurate, as both sides of the circuit must be equal for the flow of current to be equally divided, thus making the integrated resistance proportional to the instrument temperature.

For this measurement scheme to operate accurately, the four legs of the WSB must be identical in both geometry and materials and they must all be exposed to the same environmental temperature and material transitions. The use of a mono-crystalline substrate should enable the strain created from thermal expansion to be uniform across the device. As mentioned earlier, a heat spreader, or thermal conduction layer, could be added to the instrument if a temperature gradient is expected. However, for this initial investigation, it will be assumed that these deviations do not occur and the device will be as simple as possible to avoid the complex analysis required for additional materials.

The key geometric parameters which will be varied for sensitivity analysis are few, due to the simplicity of the sensor geometry. These include the trace cross-sectional dimensions and length, the meander path of the trace, the minimum radius of trace bends, and the dimensions of the substrate and capping or shielding layer above the trace. The specific dimensions of the vias and terminal pads will not be analyzed, as these do not contribute to the operation of the instrument directly.

Given the target resistance of each of the sensor legs at TPW being 25 Ω, the calculation of the trace length is straightforward, utilizing Equation 4-1 and material properties taken from Table 4-1. The trace length and cross-sectional area are dependent upon each other, with a larger cross-sectional area resulting in a longer trace and vice-versa. assuming a similar trace profile to those found in literature, so that the same annealing and thermal diffusion parameters can be applied, a platinum film thickness of 4.0 μm is selected, with a trace width of 40.0 μm, creating a rectangular cross-sectional profile. This results in a cross-sectional area of 1.6×10^{-10} m^2, which requires a trace length of 40.96 mm to achieve the desired TPW resistance.

The meander path and bend radius of the trace is dependent upon the area being covered by the trace. If the trace is assumed to cover 25% of the sensor surface area, with approximately 20% of the total area being reserved for buffer regions between the sensor traces and around the outer edge of the sensor, that leaves approximately 20% of the surface area to be covered by the instrument trace. For an instrument diameter of 10 mm, this would be an individual trace area of 15.71 mm^2 with a distance of approximately 6.36 mm from via-to-via and an average perpendicular traverse of approximately 0.3 mm between trace switchbacks. This would allow for approximately 18 switchbacks with a maximum minimum bending radius of 0.19 mm. This results in an axial strain sensitivity ratio, defined as the ratio of parallel to perpendicular trace traverse length, of 5.54 for the targeted strain axis. These dimensions are depicted in Figure 4-8.

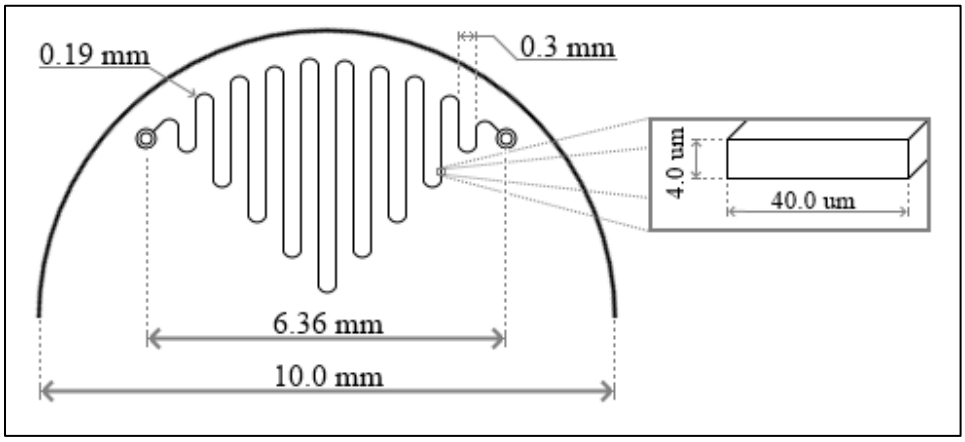

Figure 4-8: Trace geometry dimensions

As previously described, the complete instrument would be comprised of four of these resistive traces, each connected with a terminal pad of arbitrary dimensions. The next sections summarize the critical parameters and provide renders of the final sensor, array, and instrument configuration.

4.2.4 Final Proposed HERTEL Instrument Design Parameters

The final HERTEL sensor design parameters are summarized and listed in Table 4-2. The sensor trace geometry detail is depicted in Figure 4-9 and the sensor front and back are depicted in Figure 4-10.

Table 4-2: Final Instrument Design Parameters

Parameter	Unit	Value
Trace material / purity		Platinum (Pt) / 99.999% (5N)
Resistivity (TPW)	nΩ m	97.65
Film thickness	μm	4.0
Trace width	μm	40.0
Trace cross-sectional area	mm^2	1.6×10^{-4}
Trace length	mm	40.96
Resistance (TPW)	Ω	25.0
Axis parallel legs		18
Axial strain sensitivity ratio		5.54
Substrate material / purity		α-Alumina (Al_2O_3) / 99.999% (5N)
Substrate thickness	μm	725 ± 25
Crystal lattice orientation		A-Plane $(11\bar{2}0)$
Instrument package diameter	mm	10.0

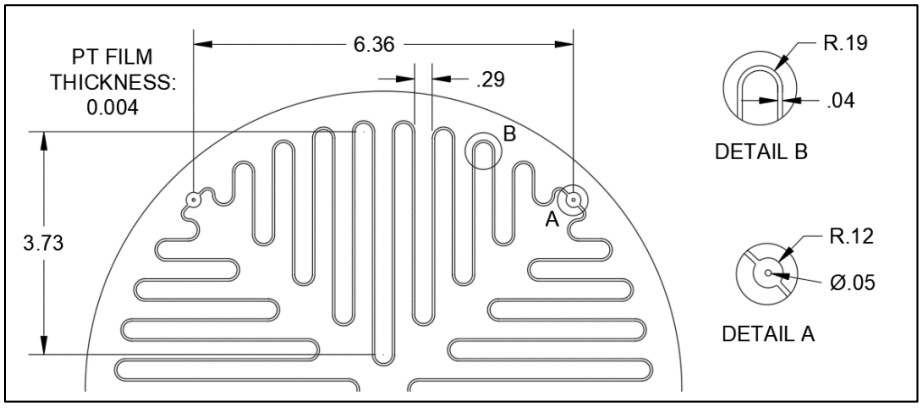

Figure 4-9: Final HERTEL sensor trace geometry (units: mm)

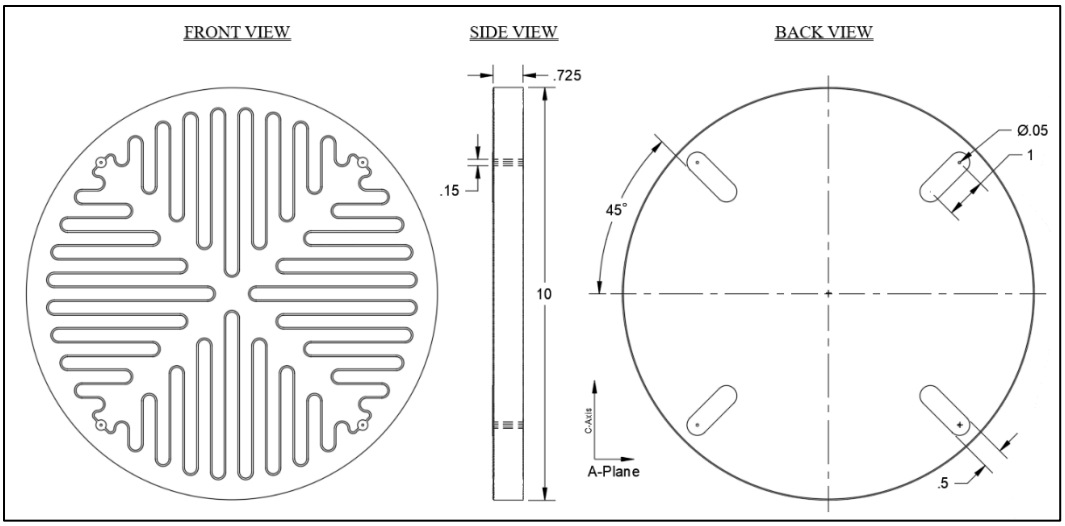

Figure 4-10: Final HERTEL sensor front, side, and back views (units: mm)

A CAD model of the proposed sensor was constructed to create engineering drawings and images of the final geometry. A rendered model of a HERTEL sensor installed on an unfueled pebble is presented in Figure 4-12. A rendered model of the upper and lower faces of the HERTEL sensor is depicted in Figure 4-12, note that the capping layer is not included. Additional drawings and renders are available in the appendix.

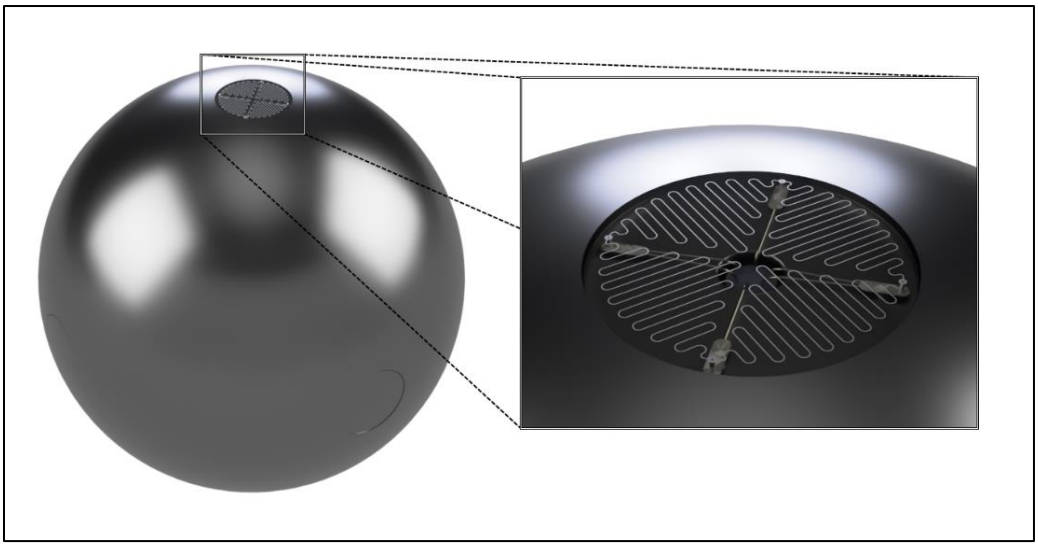

Figure 4-11: CAD model render of a single HERTEL sensor mounted on a fuel pebble

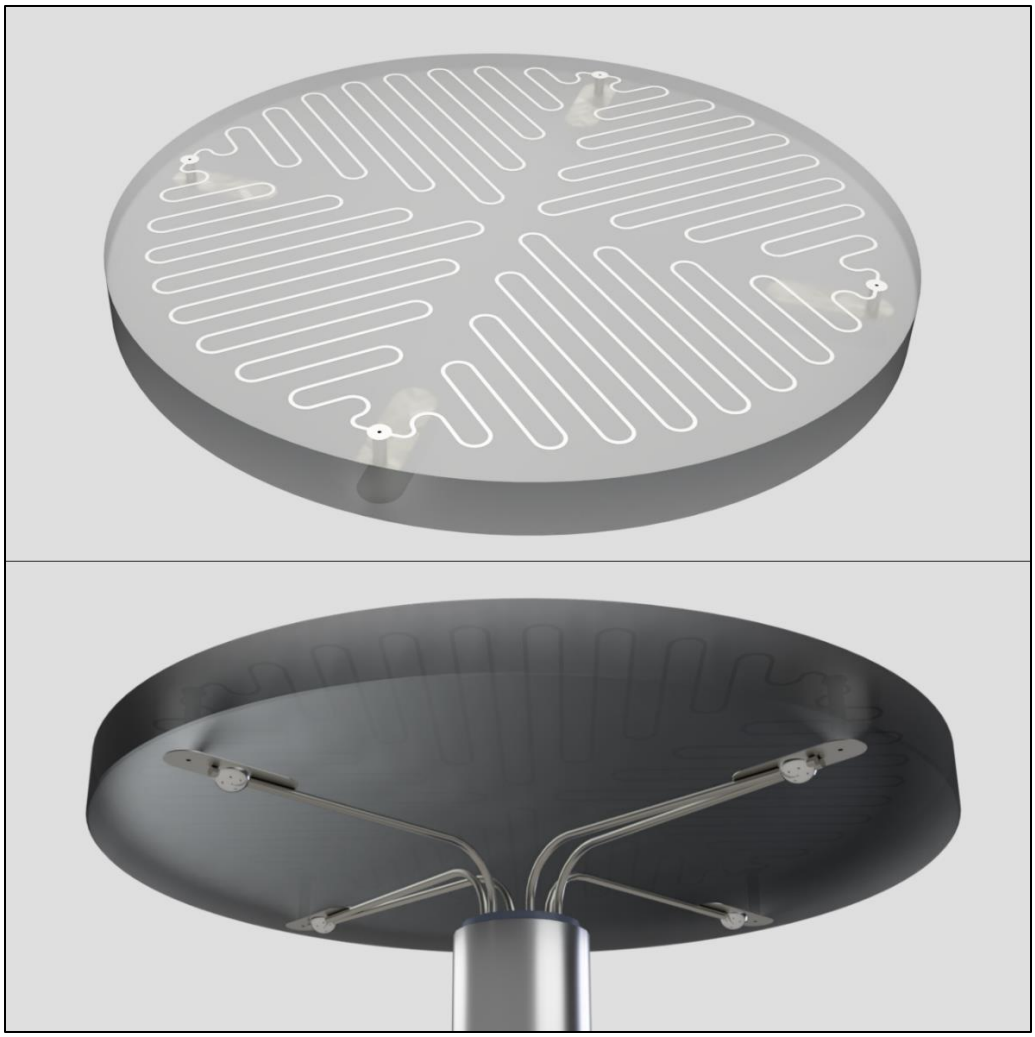

Figure 4-12: CAD model render of the proposed HERTEL sensor, top and bottom faces

4.3 MEMS Thin-Film Fabrication Sequence

Fabrication of the proposed instrument is relatively straightforward. The A-plane sapphire substrate is available from commercial suppliers and can be ordered with a surface finish that is ready for processing. If no secondary materials are required, the process follows the general steps of applying the lift-off technique to deposit the desired geometric pattern of platinum in the thickness desired on the front and back of the substrate, laser drilling and deposition of the via channels, followed by the deposition of the capping or shielding layer,

and concluding with an annealing process to resolve any lattice defects or residual stress. Following these steps, the wafer is diced into individual sensors, which should be calibrated to establish the reference relation between the RTD and strain gauge sensors before being placed into service.

4.3.1 Overview of Proposed Fabrication Sequence and Processes

Each of the following sections investigates a specific portion of the fabrication sequence, with parameters taken from a collection of primary references which have characterized the process thoroughly. Investigation of fabrication techniques and annealing times by Han et al. [111], Lin et al. [115], as well as Yi et al. [118] were heavily influential in developing this fabrication process. All of these investigators experimented with various deposition pressures, plasma temperatures, masking agents, and annealing profiles. The results of these investigations have informed the process described herein.

4.3.1.1 Selection of Bulk Materials for Substrate and Deposition

Instrument design and development assumes commercial availability of sapphire substrate wafers and pure platinum stock for deposition. Although platinum is readily available at purities of 99.9% and 99.99%, the absence of contaminants is vital to the function and accuracy of the sensor, making 99.999% (also called 5N) material highly desirable. This same standard should be applied to the selection of the sapphire substrate, for the same reason. Platinum is able to be zone refined with a vacuum furnace, which may be a viable option for further purification if adequate purity of platinum cannot be procured.

Companies such as American Elements have high purity platinum sputtering targets available in a variety of sizes and electrode backings under the product code PT-M-05-ST (CAS#: 7440-06-4, MDL#: MFCD00011179, EC#: 231-116-1), although any high purity stock material should be appropriate. The form of the sputtering target and backing material depends on the requirements of the plasma sputtering system utilized for fabrication.

High quality sapphire wafers are available for shipment from a wide variety of vendors, although it can be difficult to get the A-plane cut that is required for this application, as it is not regularly used for standard CMOS processes. The material parameters presented in this investigation are specifically referring to the wafers available through MolTech GmbH, which are grown via the Kyropoulos method. A variety of other growth methods are available as well as alternate sizes, surface finishes, and dopants. The assumed surface roughness for this investigation is less than 2 nm; although, an alternate surface finish could aid in sensing material and capping layer adhesion.

Alumina sputtering targets can be purchased at the same purity and from the same vendors mentioned above, to be used as the capping or shielding layer. Again, contamination control is vital and material purity should be a primary consideration.

4.3.1.2 Lithography and Masking

The patterning process begins with spin-coating of a positive photoresist, such as AZ-4620, followed by a short baking period to set the photoresist, according to the manufacturer's recommendations. A shadow mask pattern is then applied by an UV lithography system. The photoresist is cured and developed fully, followed by a bath in pure acetone to remove any unexposed photoresist. A final rinse and dry cycle in an automated wet bench system will prepare the wafer for deposition. This entire sequence can be performed without operator intervention and with photo-inspection verification via a Tokyo Electron automated wafer handling system coupled with an ASML or Nikon DUV lithography node.

4.3.1.3 Thin -Film Metal Deposition

A LEYBOLD Z550 or equivalent RF/DC magnetron sputtering system is then used to deposit the chromium metallization layer, if it is to be used, to a film thickness of approximately 20 nm. This is followed by the 4.0 μm thick platinum layer, which is applied in short bursts of no more than 3 to 5 minutes at 600W sputtering power or lower to keep the wafers from heating more than 50 °C. The chamber should be at a vacuum pressure of approximately 2.0×10^{-6} Pa to 5.0×10^{-4} Pa with approximately 300 sccm of argon

purge flow. Higher vacuum pressure typically results in larger grain size before annealing, with examples from literature suggesting a nominal size of approximately 40 nm expected for the higher-pressure range and approximately 20 nm expected for the lower-pressure range described.

Although the exact pressure and power used for the plasma sputtering process can be variable, if a chromium adhesions layer is used, various investigators have shown that the lower power sputtering process can help to aid long term stability by allowing a thin oxide film to form between each layer of deposition. This oxide film can act as a passivation layer and delay the effects of thermal diffusion, although an exact characterization of this effect is not well developed. If the chromium metallization layer is not used, then a wider range of sputtering power and pressure can be used, as any internal defects will be resolved in the annealing phase and the initial grain size isn't preserved through the annealing process.

4.3.1.4 Lift-off Technique

Following the material deposition process, additional layers of photoresist masking can be used to continue building up material, or to cover the sensor if plasma etching is desired to shape the underlying substrate. After all deposition is complete, the wafer should be placed in a heated bath of acetone or sodium hydroxide to remove the remaining cured photoresist as well as any material deposited on the zero-layer mask.

At this point, the wafer should be inspected for conformance to the geometric pattern, as lift-off defects can be common if the process isn't well established for the geometry being developed. Defects include areas which were not removed completely by the photoresist masking, which could allow a short to form between legs of the resistive trace. Once the geometric tolerances are verified, the wafer should be cleaned and dried once again in preparation for the addition of the capping or shielding layer.

4.3.1.5 Capping or Shielding Layer Ceramic Deposition

The final layer to be added to the material stack is the capping or shielding layer of alumina, which is applied via the same sputtering method as the metallic thin films. Again, the use of low plasma power and short bursts is recommended, as it will help to adhere the capping layer to the underlying substrate and prevent delamination. The target film thickness should be in the range of 10.0 μm, although a thicker capping layer can be utilized if needed. A trade-off between sensor responsiveness and corrosion resistance should be evaluated for thicker insulating films.

4.3.1.6 Annealing

The final step of preparation includes annealing to relieve any residual stress in the resistive trace and capping layer and to allow any voids or lattice vacancies to be filled. A wide range of annealing temperatures and times have been investigated, with various recommendations from different authors. The general consensus is that annealing should be performed at a minimum of 700 °C and a maximum of 900 °C, in a tube furnace utilizing an ultra-pure nitrogen or argon purging gas, at a ramp rate of no more than 3.0 °C per minute, for a thermal soak period of approximately two hours to allow the metallic films to reach an equilibrium state regarding lattice vacancies and defect concentration. Grain size will continue to grow in the (111) orientation for times longer than two hours, however this is not expected to have a large impact on the initial calibration of the sensor.

After the annealing period is complete, the temperature should be reduced by no more than 50 °C per hour until a temperature of 600 °C is reached, at which point a faster cooling rate of up to 180 °C per hour can be utilized to avoid undue oxidation.

4.3.1.7 Post-Processing and Initial Calibration

The final step following annealing is the post processing. This includes the dicing of the large wafer into individual sensors, trimming the edges of the substate to reach the final instrument diameter of 10 mm, brazing the lead wires into place, and mounting the sensors into unfueled graphite fuel pebbles.

The lead wires are typically brazed with a platinum paste with a mass fraction of 82.6% or higher to prevent residual flux from contaminating the sensor. The lead wires should be set with a high temperature sintering oven, at a temperature of at least 800 °C for 10 minutes, following the same cooldown sequence used for annealing.

After the lead wires are attached, the instruments should be affixed in their mounting position. A multi-mount mock fuel pebble, such as is depicted in Figure 4-6 can be used. Consideration should be given to instrument signal wire routing and the isolation of external forces on the surface of the instrument, given that the position and orientation of the fuel pebble within the testing space may be uncontrolled, it is expected that some instruments may have external forces applied. By recessing the surface of the instrument slightly below the fuel pebble surface, this loading should be minimized.

Once the instrument is installed in its service location, a precise final calibration should be precisely performed to develop an accurate initial calibration curve for the instrument. A high accuracy and very stable calibration oven should be used with a SPRT or HTSPRT calibration reference, following standard procedures for process instrument calibration. The soaking times for each calibration point above 200 °C must be extended dramatically to ensure that all residual thermal stress in the film is annealed. The instrument should not exhibit significant temporal error if a long soak time is used. If these effects are present, additional annealing may be required to ensure the platinum film has reached equilibrium or ‘ground state’ for each calibration point.

4.3.1.8 Alternative and Additional Non-Critical Fabrication Processes

Additional fabrication steps are necessary if a thermal conduction layer, adhesion promoter, or thermal diffusion layer is desired. Each of these components will follow the same general approach described previously, utilizing a similar lift-off technique, although the specific parameters of the deposition and annealing steps may be slightly different with these extra components included.

Another key design variation which may be necessary is the deposition of the platinum resistive trace in a recessed channel of the sapphire substrate rather than simply on the surface of the substrate. A channel approximately the same size of the sensor trace would then need to be etched in the substrate before the deposition of any metallic materials. The recommended approach for this is to utilize a DRIE anisotropic plasma etching technique to etch a channel straight down along the lattice axis in the substrate. This process is relatively well established for sapphire, with various examples available in literature, but will not be further explored, other than to acknowledge that it may be needed if the sensor material delaminates or behaves differently than is assumed in the performance simulation utilized in later chapters. This alternative geometry may allow the shielding layer to better adhere to the substrate as well, as it would be deposited on a flat plane instead of the varied geometry of the trace element atop the substrate.

Also not included in the preceding fabrication sequence is the use of laser drilling and material deposition required for the development of the vias which connect the front and back of the sensor, nor are the steps required to deposit the termination pads on the back of the sensor. These steps are not trivial and would require some specialized processes to ensure that the addition of these features does not impact the overall function of the sensor. However, these features can easily be excluded if an alternative layout is used which places the termination pads on the same side of the substrate as the sensor trace, as described in the previous sections. Thus, because these features are not vital to the performance of the instrument, but would require significant additional investigation, they are not further explored in terms of development of a fabrication sequence in this section due to the limited resources of the project. The layout utilizing the vias and termination pads on the back of the sensor will be assumed, but the fabrication process described is only applicable for a single sided sensor design.

4.3.1 Fabrication Parameter Variation

Variation in parameters during fabrication is somewhat expected and unavoidable, however MEMS manufacturing processes have an extremely high precision ceiling, if

advanced processes are utilized, accuracy and precision can be increased dramatically, but at increased marginal manufacturing cost.

Assuming that initial variance of the sapphire wafers meets the manufacturers specifications, no more than ~5% of geometric variance was observed in the investigations which informed the manufacturing process summarized here. This variance was primarily derived from errors in the lithography and lift-off processes, including focus instability on the shadow mask and cases in which the lift-off process 'chipped' off unintended material.

Lithography errors can be reduced by utilizing an immersed DUV lithography system as opposed to the dry system utilized by the initial researchers. These systems have a resolution in the tens of nanometers and would provide adequate precision to ensure lithography errors are minimized, if not eliminated entirely.

Errors stemming from the lift-off technique can be solved by breaking the process up into multiple layers, with each layer being slightly thinner and thus, less likely to remove unintended material. If this is ineffective, a plasma etching process can be implemented instead, where an additional mask is used to cover the sensor trace and the unwanted platinum is removed with targeted plasma oxidation. This process offers increased accuracy at the cost of a slower processing rate and possible thermal stress on the surrounding materials.

Another source of error is in the rate of deposition, with an average film thickness error of 1.2% to 1.6% observed in a single film and less than 0.3% average film thickness error observed across multiple devices. The film thickness dimensions from the source investigations were typically validated using X-ray fluorescence spectroscopy, although other methods are available. If film thickness variation must be avoided, then lowering the sputtering power to decrease the material deposition rate should allow for better control of this parameter.

5 Functional Performance Analysis

In this chapter, the physical processes which determine the performance of the HERTEL sensor package proposed in the previous chapter are explored. A set of relations which allow for simulation of instrument performance are developed and the effects of environmental exposure are characterized. The various effects which impact the electrical resistance variation as a function of the thermal exposure are integrated into a single performance model, which is then used to develop an estimate of instrument accuracy over the expected deployment lifetime.

5.1 Simulation of Nominal Steady State Instrument Performance

In this section, the various parameters which impact instrument performance are characterized or estimated. These parameters are then combined into a temperature-dependent performance model for steady state nominal operation of the instrument. This model does not include any expected degradation modes and is not time-dependent, as the idealized nominal performance would not degrade over time in absence of these expected material transitions.

The estimate of nominal performance begins with an estimate for RTD response to temperature. The idealized response would be equivalent to the ITS-90 standard for platinum resistance thermometry; however, this standard is for SPRT probes only, which have different operational characteristics when compared to the response expected from a thin-film instrument. Additional considerations of differential thermal expansion, material parameters specific to thin-film sensors, among other unique characteristics should be included in the nominal performance estimate. Thus, the following sections will investigate these characteristics and attempt to build a performance model from basic principles of material interactions.

The second primary function of the proposed instrument is to measure the differential strain caused by axially dependent thermal expansion of the instrument substrate. Thus, this is

also modeled for nominal performance. These two models are then integrated to give a complete simulation of expected performance in an ideal environment with no calibration degradation mechanisms.

5.1.1 Estimation of Temperature Dependent Operating Parameters

The performance of the proposed instrument is dependent upon a variety of parameters which are temperature dependent to varying degrees. Thus, the first task of simulating the performance of the proposed instrument is the estimation of these parameters across the full range of expected environmental temperature exposure.

5.1.1.1 Linear Thermal Expansion Coefficient (TEC)

The temperature dependent linear coefficient of thermal expansion ($\alpha_L, 10^{-6}\,°C^{-1}$), which is a measure of the change in length of a material with respect to the original length ($\Delta L/L_0$) per degree of temperature change ($\Delta T, °C$) is defined in Equation 5-1 and is commonly simplified as being constant for most materials. Typically, this is an effective approximation, and is reflected in the value provided in Table 4-1. However, in the case of modeling the performance of the proposed HERTEL sensor, a more accurate approximation is needed.

$$\alpha_L \Delta T = \frac{\Delta L}{L_0} \qquad \text{Eq. 5-1}$$

For platinum, a number of standards bureaus and other organization concerned with highly precise determination of material properties have developed detailed approximations of the temperature dependent thermal expansion coefficient across a wide temperature range. The model selected for this investigation is that which was developed by Kirby et al. [119], which is an integrated relation combining many different investigations on the topic into one definitive characterization. This model is approximated by the fourth-order curve fit defined in Equation 5-2 and depicted in Figure 5-1.

$$\alpha_{L,Pt}(T) = 1.360 \times 10^{-12}T^4 - 3.204 \times 10^{-9}T^3 + 3.167 \times 10^{-6}T^2 + 1.500 \times 10^{-3}T + 9.034 \quad \text{Eq. 5-2}$$

Although sapphire is utilized as a material for construction of dimensional standards by NIST and other standards organizations, finding reliable data on the thermal expansion of the axis perpendicular to the optical axis (C-axis) is difficult. The best estimate that could be found in literature is from a 2016 summary investigation of thermal expansion measurements in solids by S. T. Kompan [109], which provides the and linear thermal expansion coefficient parallel $\left(\alpha_{L,\parallel}, 10^{-6}\,°C^{-1}\right)$ and perpendicular $\left(\alpha_{L,\perp}, 10^{-6}\,°C^{-1}\right)$ to the C-axis as an approximated fourth-order polynomial, depicted in Figure 5-1, with constants as defined in Equation 5-3 and Equation 5-4, respectively.

$$\alpha_{L,\parallel}(T) = -1.560 \times 10^{-12}T^4 + 6.427 \times 10^{-9}T^3 - 9.809 \times 10^{-6}T^2 + 8.169 \times 10^{-3}T + 5.660 \quad \text{Eq. 5-3}$$

$$\alpha_{L,\perp}(T) = -1.163 \times 10^{-12}T^4 + 5.074 \times 10^{-9}T^3 - 8.081 \times 10^{-6}T^2 + 7.231 \times 10^{-3}T + 4.974 \quad \text{Eq. 5-4}$$

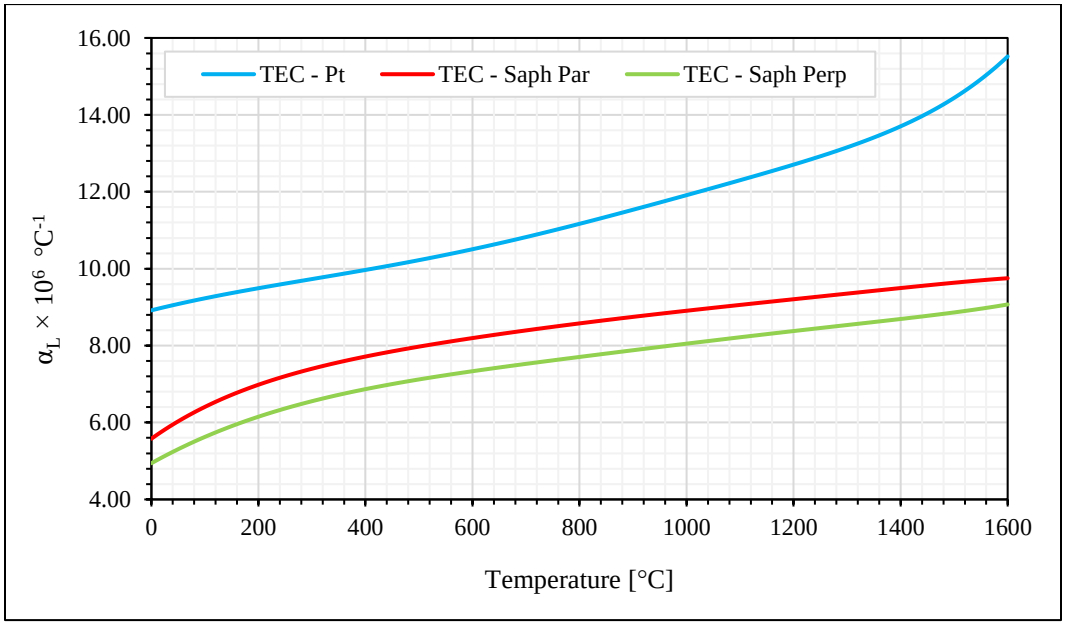

Figure 5-1: Temperature dependent coefficient of thermal expansion for platinum and sapphire

5.1.1.2 Temperature Coefficient of Resistivity (TCR)

The fundamental parameter which enables the functionality of RTD sensors is the temperature dependence of resistance for an electrical conductor. This effect is primarily driven by the scattering probability for an electron as it travels through a conductor. If the effects of lattice defects, vacancies, and impurities are isolated or otherwise mitigated, then the increase in resistance as a function of temperature is primarily due to electron scattering from thermal energies, often characterized as collisions with phonons, which are the quantum unit for thermal energy transport. This effect cannot be mitigated as it is a fundamental property of a materials response to temperature, but is predictable and can be accurately modeled as a function of temperature, utilizing bulk material parameters.

The other primary factor which influences the temperature coefficient of resistivity is the influence of grain boundaries, which also cause electron scattering within the conductor. Although these effects cannot be isolated or mitigated, they can be characterized. The modelling of grain boundary interactions is vital for accurate simulation of instrument performance, as these effects increasingly impact instrument resistance as conductor cross-sectional area is reduced to the same order of magnitude as the material granularity. Obviously, this is not a problem for classical characterization of TCR, as conductor geometry is much larger than the grain size of the material, but for thin film devices, it has significant impact.

To simulate the steady state operation of the proposed instrument, the impact of grain boundary scattering must be determined. It is known that the frequency of grain boundaries is reduced as grain size is increased, either via annealing or during operation in a high temperature environment. Thus, a model which describes the impact of grain boundary scattering as a function of grain size would be useful in determining if bulk material parameters can be used for simulation, or if these parameters must be adjusted.

A useful group of these thin film resistance characterizations is utilized by Schössler et al. in an investigation of the effects of high-temperature annealing on thin film resistance

parameters. From this investigation, an experimental approximation of the grain boundary reflection coefficient for thin platinum films is derived [120], which serves as a primary reference for investigation of the impact of grain boundary effects for the proposed instrument geometry.

A basis for thin film resistance analysis is commonly derived from an investigation of the application of the Boltzmann transport equation for electrons in thin polycrystalline films by Mayadas and Shatzkes (MS), which indicates the resistance of thin films is highly influenced by electron scattering at grain boundaries within the conductive material. This introduces an alternate parameter for resistivity, called gain boundary resistivity, that is defined in Equations 5-5, 5-6, and 5-7, with parameters described in Table 5-1.

$$\frac{\rho_{MS}}{\rho_{bulk}} = \frac{1}{f(a)} \qquad \text{Eq. 5-5}$$

$$f(a) = 1 - \frac{3}{2}a + 3a^3 - 3a^3 ln\left(1 + \frac{1}{a}\right) \qquad \text{Eq. 5-6}$$

$$a = \frac{\lambda}{d_{grain}} \frac{r}{1-r} \qquad \text{Eq. 5-7}$$

Table 5-1: Thin Film Resistance Characterization Parameters

Parameter	**Units**	**Symbol**
Bulk electron mean-free-path	m	λ
Phenomenological electron reflection coef. at grain boundary		r
Mean grain size	m	d_{grain}
Bulk material resistivity	nΩ m	ρ_{bulk}
Grain boundary resistivity, as def. by M. and S.	nΩ m	ρ_{MS}
Bulk material thermal coefficient of resistance or TCR	$°C^{-1}$	TCR_{bulk}
Grain boundary dependent TCR, as def. by T. and T.	$°C^{-1}$	TCR_{TT}

Another similar investigation by Tellier and Tosser (TT) can be used to extend the MS model to produce an estimate of the TCR for polycrystalline films as it relates to the bulk

material TCR. This relation is defined in Equations 5-8 and 5-9, with parameters again described in Table 5-1.

$$\frac{TCR_{TT}}{TCR_{bulk}} = 1 + \frac{g(a)}{f(a)} \quad \text{Eq. 5-8}$$

$$g(a) = -\frac{3}{2}a + 6a^2 + \frac{3a^3}{1+a} - 9a^3 ln\left(1 + \frac{1}{a}\right) \quad \text{Eq. 5-9}$$

In platinum, the mean-free-path of an electron is approximately 20 nm at room temperature. This is much smaller than the proposed film thickness of 4.0 μm, thus this thin film consideration of resistivity would not directly impact the function of the proposed device via geometric constraints, and bulk parameters should reflect accurate instrument performance. However, this is true only if the grain size is within the margins specified by the previous relations to ensure the thin film resistivity is similar to bulk value. For small grain sizes, the impact of grain boundary reflection is more significant, and the assumed resistivity must be adjusted to reflect this.

Platinum films deposited in the manner described in the previous chapter should have a grain size of approximately 20 to 40 nm before annealing, as verified in the primary reference by XRD peak broadening, with an estimated error band of ±10%. It is reported that the grain size grows to approximately 60 nm if an annealing temperature of 600 °C is utilized, compared to more than 140 nm for annealing at 800 °C, although the capping layer appears to impact grain size more significantly at higher annealing temperatures. It is also worth noting that this grain size is approaching the maximum possible for the reference study [120], which utilized a film thickness of 140 nm.

The results of this primary investigation were used to determine the reflection coefficient of resistivity for platinum thin films, utilized in the relations presented for thin film TCR and resistivity, as being approximately 0.58 ±0.03 and 0.49 ±0.03, respectively. These coefficients can then be input into the presented models to determine the effect of the

material grain size on the parameters required for steady state simulation of instrument performance.

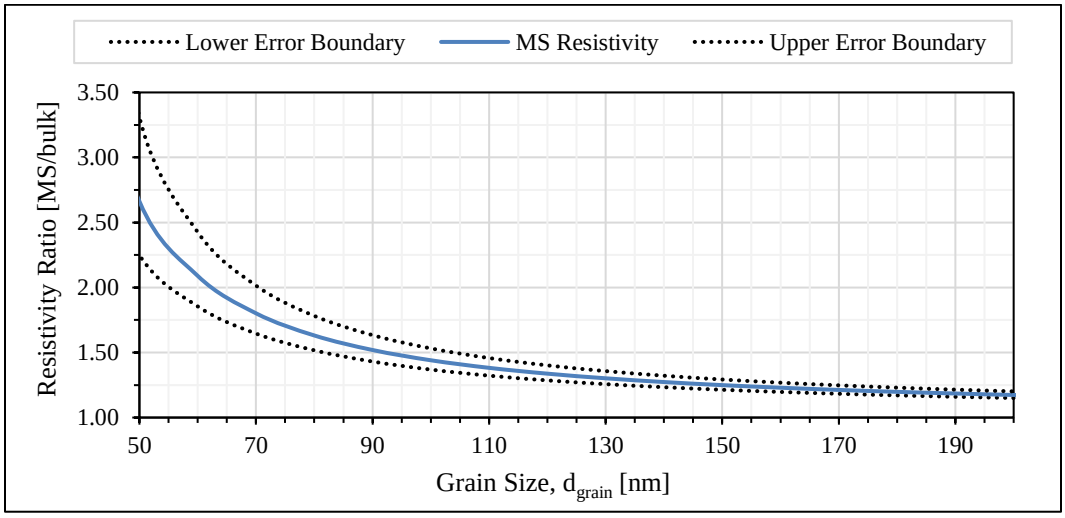

Figure 5-2: MS to bulk resistivity ratio as a function of grain size from 50 to 200 nm

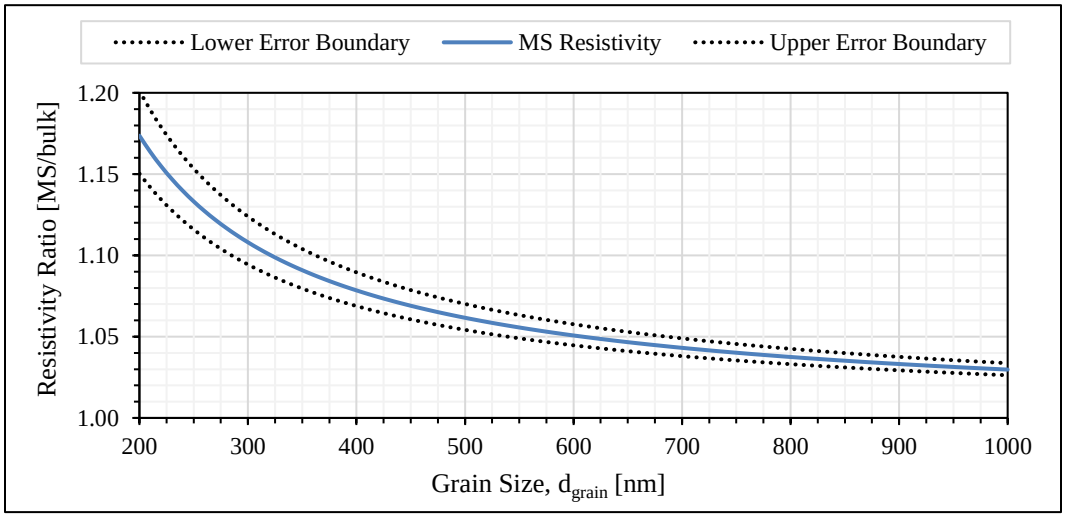

Figure 5-3: MS to bulk resistivity ratio as a function of grain size from 200 to 1000 nm

The estimated increase in thin film resistivity for the MS model is depicted as a function of grain size in Figure 5-2 and Figure 5-3. Note that for small grain size, the expected resistivity increases by a factor of 3.25 at the upper bounds of error. This grain boundary

effect is reduced considerably with larger grain size, gradually reaching a limit at approximately 1.03, or 3.0%, for grain size on the order of 1.0 μm and approximately 1.007, or 0.7%, for grain size on the order of the proposed resistive trace thickness of 4.0 μm. The effect can be approximated as linear in the range of 1.0 μm to 4.0 μm.

Note that this approximation is only valid for room temperature, with an assumed electron-mean-free-path of approximately 20 nm. As the temperature rises, the mean-free-path would be reduced due to the increased probability of phonon scattering. Due to the linear nature of platinum bulk TCR in the target temperature range, it can be assumed that the mean-free-path of electron transport has an inverse, linear relationship with temperature in that range. Thus, the result of rising temperature is a depression of the MS resistivity approximation, which is depicted in Figure 5-4. At high temperatures, the film resistivity ratio approximation is further reduced to a factor of 1.0018, or 0.18%, for grain size on the order of proposed film thickness.

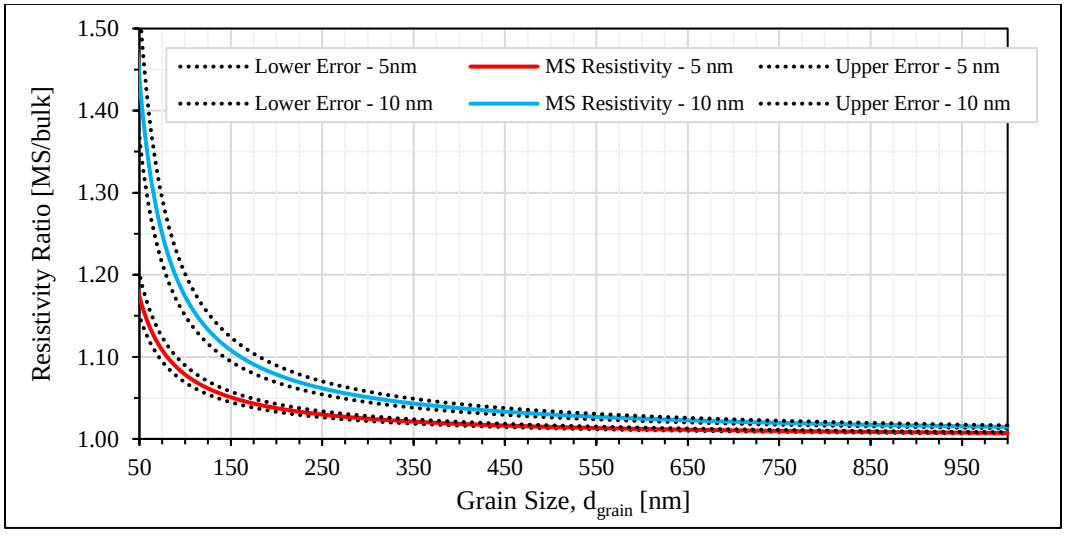

Figure 5-4: Impact of temperature on MS grain boundary resistivity

Utilizing the same reflection coefficients and variation in electron mean-free-path as a function of temperature, the TT model for thin film TCR as a function of grain size can be investigated in the same manner. The results are depicted in Figure 5-5 and Figure 5-6.

The grain boundary TCR ratio approaches 1.0 as the grain size grows, with an estimated reduction factor of 0.8, or a 20% reduction in TCR for a grain size of 60 nm for pure platinum at room temperature. At a grain size of approximately 1.0 µm, the expected TCR reduction factor is estimated to be 0.96, or a 4.0% reduction from the bulk parameter TCR. This is further reduced to a reduction factor of 0.991, or a 0.9% reduction from the bulk parameter TCR, at a grain size of approximately 4.0 µm, pure platinum at room temperature.

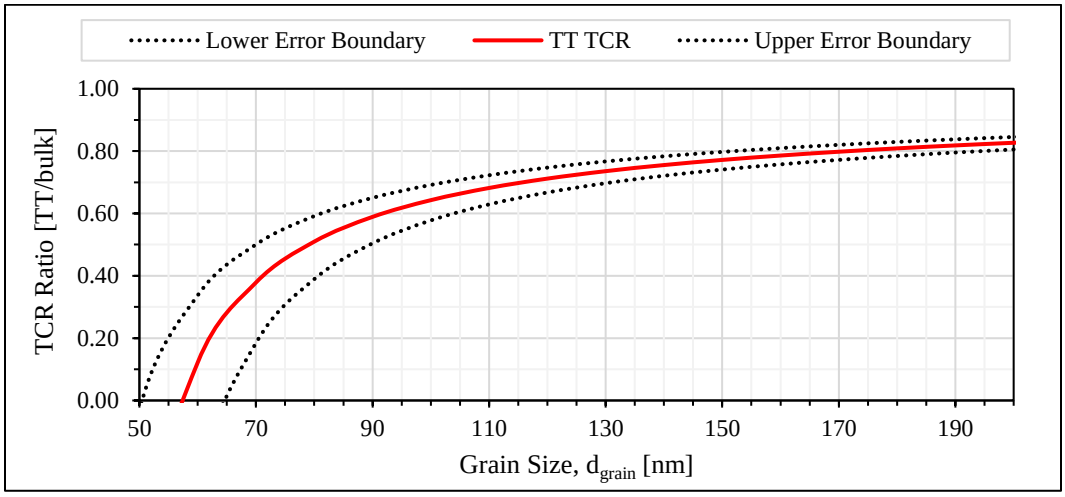

Figure 5-5: TT to bulk TCR ratio as a function of grain size from 50 to 200 nm

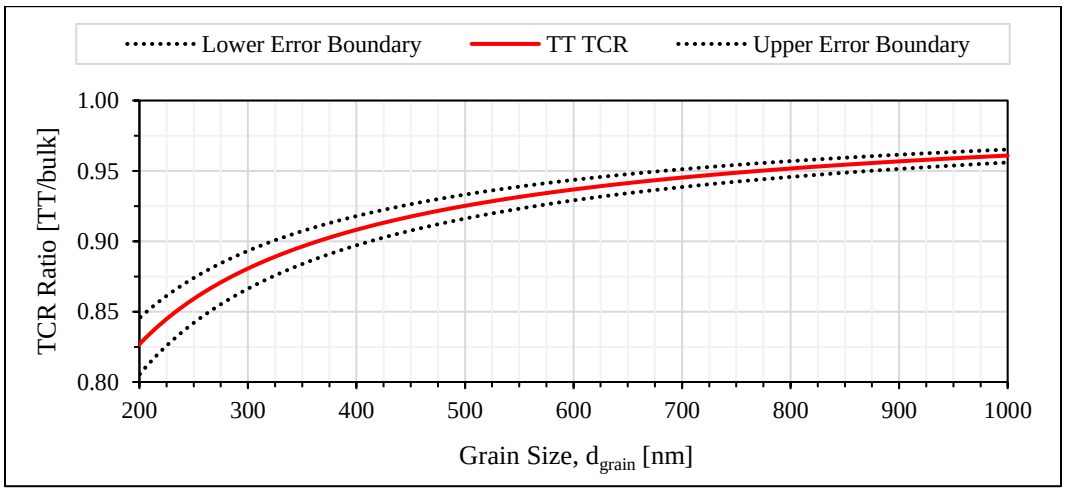

Figure 5-6: TT to bulk TCR ratio as a function of grain size from 200 to 1000 nm

The impact of the reduced the mean-free-path of an electron with rising material temperature is reflected in Figure 5-7. The TT approximation estimates a reduction factor of 0.99 and 0.998, or 1.0% and 0.2%, for grain sizes of 1.0 μm and 4.0 μm, respectively, for pure platinum at high temperature.

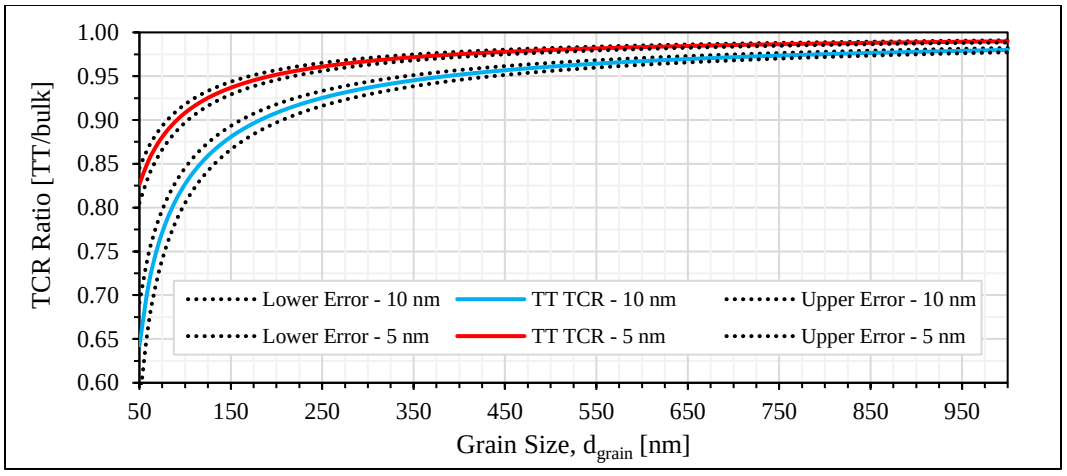

Figure 5-7: Impact of temperature on grain boundary induced TCR reduction

These estimates for the impact of grain size on material resistivity and TCR provide a means of associating the thermal exposure, or annealing time, of an instrument with the expected change in functional performance. These models also reinforce the idea that long annealing times eventually create a 'ground state' in which the resistance to temperature calibration curve should no longer be affected by grain boundary transitions.

Thus, determination of the temperature dependence of resistivity or TCR for a pure platinum thin film is a matter of taking the effects of grain size into account and applying a correction factor to the well-established bulk parameter tables found in literature. The primary reference chosen for this investigation is the bulk temperature dependent resistivity tables published by The Platinum Group Metals (PGM) Database. This reference is derived from the 1984 edition of Platinum Metals Review, which in turn is derived from a data set established for the IPTS. This reference data set is widely considered to be the definitive characterization for platinum resistivity and has a degree of accuracy (0.1%)

which enables it to be used as a reference for instrument functional performance simulation. This standard bulk resistance ($\rho_{PMR}, n\Omega\, m$) as a function of temperature ($T, °C$) is depicted in Figure 5-8 and defined by the fourth-order polynomial described in Equation 5-10.

$$\rho_{PMR}(T) = 1.3960 \times 10^{-11}T^4 - 3.3960 \times 10^{-8}T^3 - 2.9570 \times 10^{-5}T^2 + 3.8686 \times 10^{-1}T + 98.3781 \quad \text{Eq. 5-10}$$

This reference can be compared to the ITS-90 standard for SPRT measurements, which is approximated by a fourth-order polynomial as defined in Equation 5-11 and also depicted in Figure 5-8.

$$\rho_{ITS}(T) = -2.8863 \times 10^{-12}T^4 + 3.4412 \times 10^{-9}T^3 - 5.8529 \times 10^{-5}T^2 + 3.8935 \times 10^{-1}T + 97.6468 \quad \text{Eq. 5-11}$$

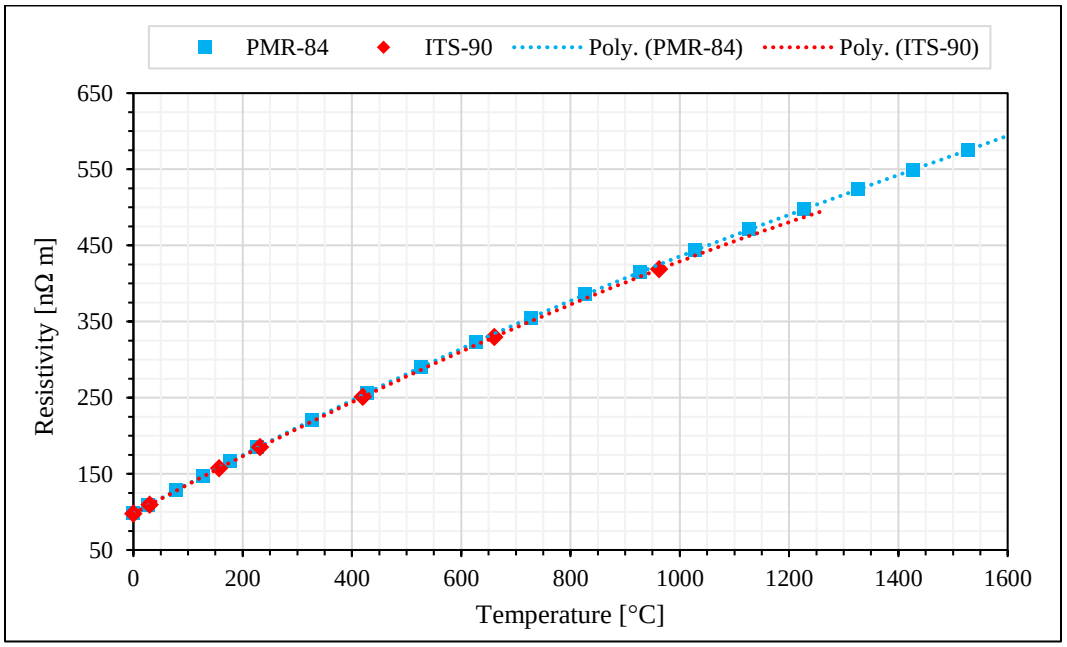

Figure 5-8: Comparison of standards for bulk resistivity as a function of temperature

The deviation observed between the ITS-90 standard and the PMR-84 standard is primarily a result of the ITS-90 standard not utilizing pure platinum. Instead, the platinum used for the ITS-90 standard is doped with an impurity to achieve an exact resistivity of 25.0 Ω at the TPW. Thus, the resistivity deviates slightly from the characterization for pure platinum. The reason for this intentional offset is to account for the variation in platinum purity that has been utilized in the past to construct SPRT instruments.

5.1.1.3 Temperature Dependence of Other Parameters

It is assumed that parameters such as the insulating value of the sapphire substrate, or any other parameter not specifically addressed here, does not vary appreciably with temperature and thus, does not require additional analysis. For these parameters, the bulk room temperature value will be assumed to be constant over the operating temperature of the device.

The determination of the gauge factor used in strain measurements is fundamentally a sum of the geometric effects of Poisson's ratio and the piezoresistive effect. At temperatures above approximately 500 °C, which is the recrystallization threshold for pure platinum, atomic mobility is such that internal lattice deformations which cause the piezoresistive effect will be resolved relatively quickly by annealing. This would result in the piezoresistive portion of the strain-driven resistance increase to decay over time. Thus, for strain measurements over long time periods at or above a threshold temperature representing significant atomic mobility, it is assumed that the strain will be solely a geometric factor primarily driven by Poisson's ratio, which is in turn driven by Young's modulus and the modulus of rigidity for the material.

Both of these parameters exhibit a temperature variability in platinum, as is expected for most metals, due to the softening that occurs at high temperatures. However, a number of investigations into this topic indicate that Poisson's ratio for platinum is not temperature dependent when measured via a standard oscillation damping method and only weakly temperature dependent when calculated directly from the temperature-dependent modulus

of rigidity and Young's modulus [121]. The reason for this is not well characterized, but is attributed to anisotropic recrystallization which occurs in pure platinum at elevated temperatures. Due to this variation in literature, it will be assumed that Poisson's ratio, as it pertains to the impact on strain resistance, is not dependent on temperature.

5.1.2 RTD Nominal Steady State Performance Model

Simulation of nominal RTD performance at steady state for the geometry and materials selected is a matter of utilizing a range of material parameters to estimate the measured RTD resistance across one leg of the instrument. This model assumes that no material transitions take place during operation, such as grain boundary transitions, temperature induced differential strain, vacancy generation or thermal migration of impurities, thus the RTD performance of all legs of the instrument should have equivalent response to temperature. Dynamic factors are considered in the next section, when the nominal strain gauge performance model is integrated with this RTD performance model and the expected performance of the overall instrument is considered with the addition of time-dependent effects.

Recalling design Equation 4-1, a temperature dependent model of resistance is developed as defined in Equation 5-12. The RTD performance is modeled, starting at the TPW and marching step-wise through the expected operating range, considering only steady state operation for a single leg of the instrument. The parameter values are provided as described in Table 5-2 and the results of the simulation are depicted in Figure 5-9.

$$R(T) = \frac{C_{MS}(d_g)\rho_{bulk}(T)L(T)}{d_f(T)w(T)} \qquad \text{Eq. 5-12}$$

As expected, the RTD resistance response is nearly linear, following the same general trend as described by the PMR-84 and ITS-90 characterizations for resistivity. The contributions of geometric thermal expansion account for approximately 1.071 Ω of reduced resistance at 1000 °C, equivalent to a 0.963% variation from a static geometry approximation.

Table 5-2: Steady State Nominal Performance Parameters

Parameter	Symbol	Units	Value
Initial calibration resistance	R_0	Ω	25.0
Operating temperature range	$T - T_0$	°C	1,600.0
Sensor trace length at TPW (single leg)	L_0	mm	40.96
Sensor trace length (single leg)	$L(T)$	mm	$f(T)$
Sensor trace width at TPW	w_0	µm	40.0
Sensor trace width	$w(T)$	µm	$f(T)$
Sensor trace film thickness at TPW	$d_{f,0}$	µm	4.0
Sensor trace film thickness	$d_f(T)$	µm	$f(T)$
Bulk, temperature dependent resistivity	$\rho_{bulk}(T)$	nΩ m	$f(T)$
Assumed fixed material grain size	d_g	µm	4.0
Thin film resistivity correction factor	$C_{MS}(d_g)$		1.00643
Poisson's ratio (PGM Database)	ν		0.39
TEC for sapphire, par. to C-axis	$\alpha_{s,\parallel}(T)$	$°C^{-1}$	$f(T)$
TEC for sapphire, perp. to C-axis	$\alpha_{s,\perp}(T)$	$°C^{-1}$	$f(T)$
TEC for platinum	$\alpha_{Pt}(T)$	$°C^{-1}$	$f(T)$
Sensor trace axial sensitivity ratio	γ		5.54

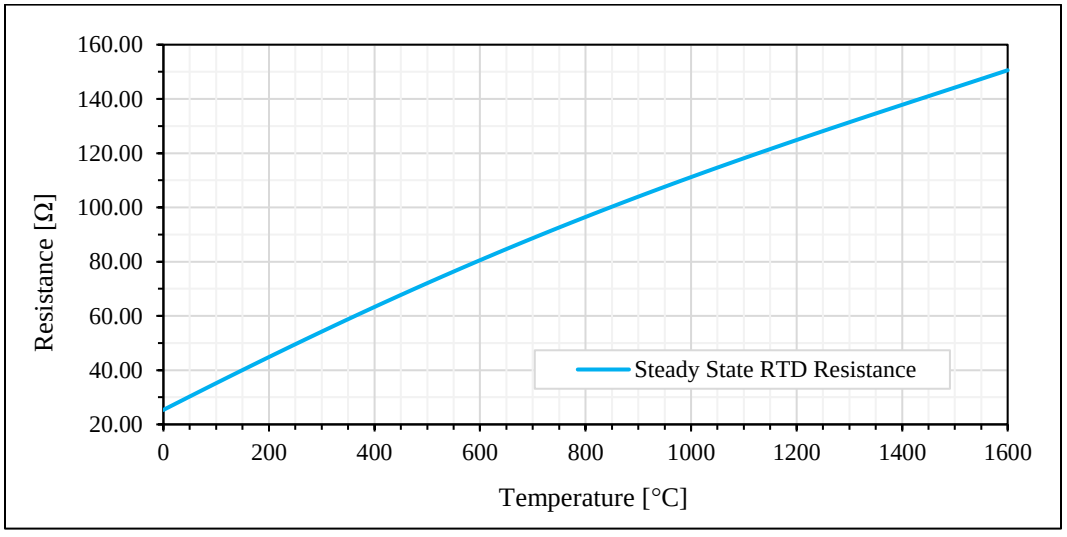

Figure 5-9: Steady state RTD resistance across the expected operating range

5.1.3 Differential Strain Gauge Nominal Steady State Performance Model

A similar approach can be utilized to determine the nominal steady state performance of the differential strain gauge contribution to the resistance measurement. Recalling Equation 4-6, Equation 4-7, and Equation 4-8 from the previous chapter, a temperature dependent model of the strain gauge response can be developed and is defined for a single resistive trace by Equation 5-13 and Equation 5-14, with parameters provided as described previously by Table 5-2.

This resistive response is primarily driven by the expected axis-dependent differential thermal expansion of the sapphire substrate and the platinum resistive trace across the operating temperature range. Thus, the length change parameter is defined as function of integrated thermal-induced trace length variance, utilizing the axial sensitivity ratio (γ) as described by Equation 5-15 and Equation 5-16. Note that the parallel $(\Delta L_{\parallel}, m)$ and perpendicular $(\Delta L_{\perp}, m)$ thermal-induced length variance components are evaluated separately, as they correspond to the orientation of the strain gauge relative to the C-axis of the substrate. This integration could also be performed by breaking the initial trace length into parallel and perpendicular portions and evaluating them separately.

$$\frac{\Delta R(T)}{R_0} = k\varepsilon(T) = \left(1 + 2\nu + \frac{\Delta\rho/\rho}{\varepsilon}\right)\frac{\Delta L(T)}{L_0} \quad \text{Eq. 5-13}$$

$$\Delta L_{\parallel,\perp}(T) = \alpha_{\parallel,\perp}(T)\Delta T L_0 \quad \text{Eq. 5-14}$$

$$\alpha_{\parallel}(T) = \alpha_{s,\perp}(T)\gamma^{-1} + \alpha_{s,\parallel}(T)(1-\gamma^{-1}) \quad \text{Eq. 5-15}$$

$$\alpha_{\perp}(T) = \alpha_{s,\perp}(T)(1-\gamma^{-1}) + \alpha_{s,\parallel}(T)(\gamma^{-1}) \quad \text{Eq. 5-16}$$

To simplify this characterization, two essential assumptions will be made. The first is that the piezoresistive term of the strain response is assumed to be zero, with the resistive trace creating a purely geometric response to strain. This assumption is only valid for very long measurement periods at temperatures near or above the platinum recrystallization temperature, which is approximately 500 °C. The piezoresistive term can be characterized

as an additional resistance term with a temperature dependent temporal decay and will be analyzed in the next section, as it is a dynamic response rather than a steady state response.

The second assumption is that the platinum trace will deform according to the thermal expansion characteristics of the sapphire substrate and any force that will be created due to this mechanical strain will be mitigated by the deformation of the platinum trace. Thus, the typical balance of forces used when determining the integrated displacement exhibited by two materials undergoing differential thermal expansion is assumed to be dominated by the much higher Young's modulus of the sapphire substrate when compared to the thin platinum film. This is a valid assumption for operation at high temperatures, due to the softening that occurs in platinum and the full encapsulation of the trace inside the substrate, but may not be valid at low temperatures.

Another simplification is the omission of shear forces at the material boundaries and bending moments at the curved portion of the resistive trace. This approximation is again valid for operation at high temperatures, as the softening of the platinum resistive trace would readily yield to these forces and deform at a rate proportional to the magnitude of the force; a transition process similar to thermal-mechanical creep. This transition ultimately produces a geometric deformation driven by the initial stress distribution over long time periods at high temperature. Thus, the geometric equivalent of liner strain is used as an approximation for these effects for steady state operation.

The resistance response of a single leg of the strain gauge both parallel and perpendicular to the C-axis of the sapphire substrate, as defined by Equation 5-15 and Equation 5-16, is depicted in Figure 5-10. Note that the differential resistance between the parallel and perpendicular sets of strain gauges is proportional to the temperature of the instrument. As the temperature increases, the differential thermal expansion of the substrate creates a nearly linear response due to the differential lengthening of the strain gauge traces. Because the WSB circuit only measures differential variation between the two sets of

gauges, the effects of temperature do not directly impact the strain measurement, other than via the thermal expansion of the substrate.

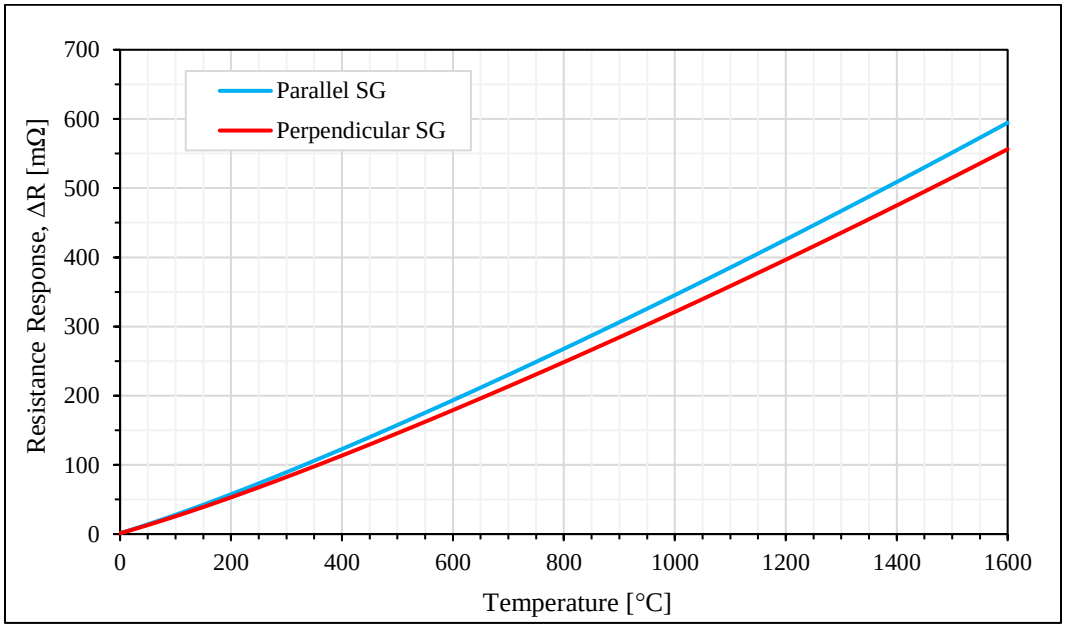

Figure 5-10: Strain induced resistance change as a function of temperature for a single trace

5.1.4 Integrated Nominal Steady State Instrument Performance Model

The instrument voltage response function for full bridge strain measurement is calculated using a modification of Equation 4-10 and Equation 4-11, defined in Equation 5-17, and is depicted in Figure 5-11 for both constant and variable excitation voltage. Note that for the full bridge configuration, the response of the two parallel gauges and the two perpendicular gauges are added together, increasing the sensitivity of the full bridge by a factor of two when compared to the voltage response of a single trace.

$$V_{SG}(T) = \left[\frac{R_{\perp}(T)}{R_{\perp}(T) + R_{\parallel}(T)} - \frac{R_{\parallel}(T)}{R_{\perp}(T) + R_{\parallel}(T)}\right] V_{EX} \qquad \text{Eq. 5-17}$$

The relation depicted in Figure 5-11 is the output of the WSB voltage with a constant instrument excitation voltage of 1.0 V. Combining Equation 5-17 with Equation 4-11 and Equation 4-12, the coupling of the RTD and strain gauge into a single instrument is described by Equation 5-18, where the excitation voltage for the WSB is a function of the total instrument resistance, which is equivalent to the RTD resistance. Evaluation of the integrated instrument output requires the inclusion of the RTD resistance characterization as the driver of strain bridge excitation voltage and assumption of a constant instrument excitation current of 10.0 mA.

$$V_{EX}(T) = V_{RTD}(T) = I_{EX}R_{RTD}(T) \qquad \text{Eq. 5-18}$$

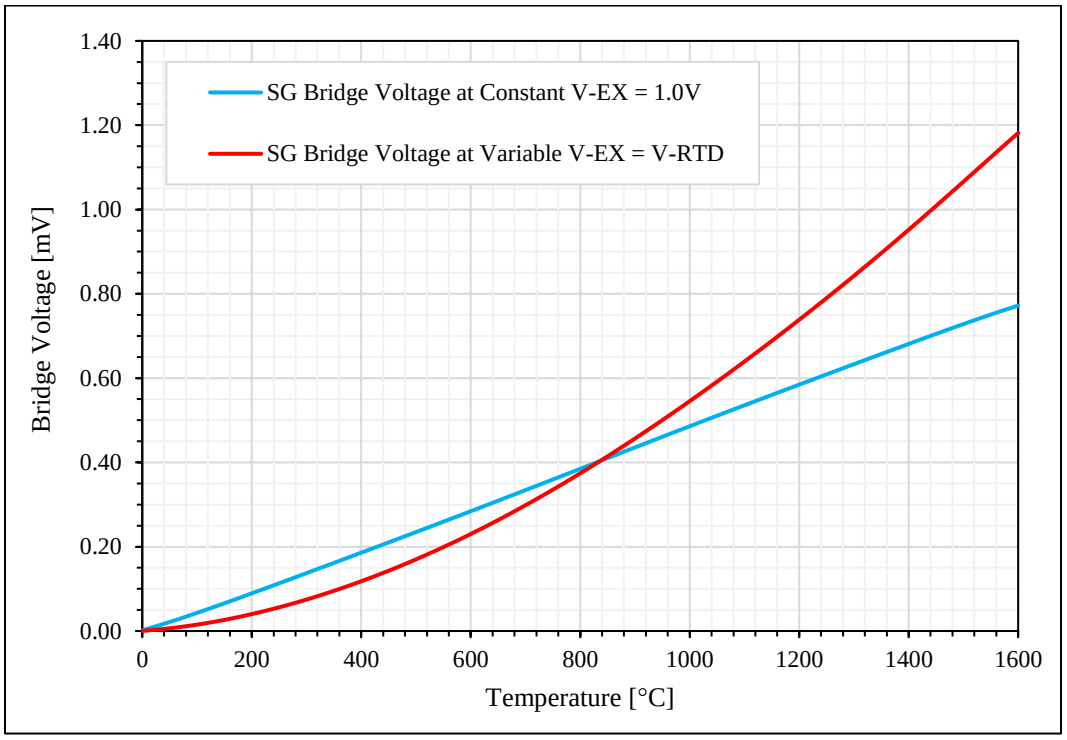

Figure 5-11: Bridge voltage output with constant and variable excitation voltage

The results of this evaluation are depicted in Figure 5-11, in which the strain gauge output for a constant excitation and variable excitation voltage are compared, and Figure 5-12, in which the two voltage outputs for strain and RTD functions are compared. Note that the

two voltage outputs are significantly different in magnitude, with the RTD voltage output being approximately three orders of magnitude larger.

This coupling of the two types of instruments also means that the strain gauge output is no longer independent of temperature, as the resistance of the RTD increases due to rising temperature, the excitation voltage of the WSB also increases, which drives the output bridge voltage of the WSB higher, as described by Equation 5-17.

This effect can be removed by dividing the WSB output voltage by the RTD measurement voltage, again removing the direct influence of temperature. The question of whether to operate the instrument in this way should be considered carefully, as a higher output voltage may be beneficial by increasing the sensitivity of the strain measurement, but may also increase measurement noise due to differential temperature vs strain sensitivity of resistance modifiers such as material contamination or grain boundary effects.

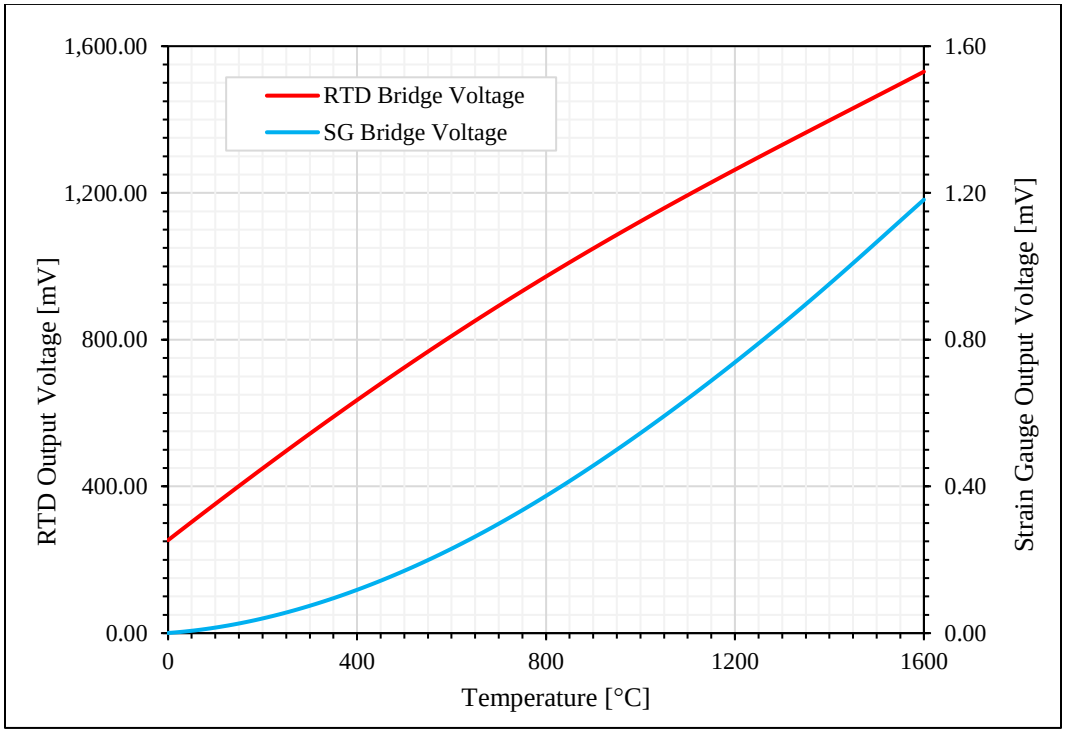

Figure 5-12: HERTEL instrument output voltage for RTD and strain measurements at 10.0 mA

5.2 Modeling of Temporal Material Transition Effects

In this section, the various temporal processes which contribute to drift of the temperature dependent electrical resistance curve of the proposed instrument are identified, evaluated for their temporal impact, and characterized if their impact is significant to simulation of the fundamental instrument operation concept. These include the processes explored in the previous chapter, which were identified by the ITS-90 platinum resistance thermometry standard, as well as the addition of processes unique to thin-film resistance instruments, such as grain-size-dependent electron scattering effects.

The addition of time to the already explored thermal performance model is essentially the development of a thermal exposure model. Thus, the various processes already identified to contribute to steady state performance will be extended in a manner which accounts for properties of the materials, environment, and thermal exposure model developed in previous chapters. The identified processes which contribute to resistance variation are explored and characterized as a function of time and temperature. These effects include chemical transitions such as oxidation, thermal diffusion, piezoresistive strain, annealing, lattice defects such as vacancy and new grain formation, and grain boundary transitions.

This analysis will result in a high-fidelity, integrated model of the expected HERTEL sensor performance in the target thermal environment of the pebble bed HTGR core. This performance characterization will then be used to evaluate the functional applicability of the instrument for the intended target environment in the next chapter.

5.2.1 Assumptions for Estimation of Temporal Effects

A number of fundamental assumptions already stated elsewhere are pertinent to recall for this investigation. These include the limiting of chemical reactions and thermal diffusion processes to interactions between the platinum trace the alumina substrate. The assumption of pure helium as the coolant and the lack of carbon interactions, including carbon dust. The simplifications made regarding strain and mechanical forces in the previous section are also significant, including the assumption that the device is perfectly isolated from

external forces such as pebble movement, vibration, and non-uniform temperature gradients. Finally, it should be recalled that the environment being considered is limited to the expected thermal characteristics of a pebble bed HTGR core, as radiation effects are being ignored, and only the performance of the sensor trace itself is being evaluated, any external electronics, including the signal transfer cable, are excluded from analysis.

5.2.2 Chemical and Oxidation Reaction Rate Model

Chemical reactions affecting the material utilized in the construction of the HERTEL sensor are assumed to be limited to oxidation reactions which take place at the platinum and alumina boundary. It is assumed that the pure helium coolant will not react or diffuse into the alumina substrate or capping layer. Carbon will readily react with free oxygen in the alumina material lattice to form carbon monoxide and carbon dioxide. However, it is assumed that the gaseous nature of these reactions will not produce latent lattice defects, as these molecules will be quickly carried away by the coolant gas. Carbon reactions will not otherwise be considered.

The oxidation reaction rate for platinum has a specific threshold temperature, as bulk aluminum oxide does not readily react with pure platinum. Thus, oxygen must first disassociate from the alumina material and migrate into the platinum material lattice. Aluminum does not form a preferential chemical bond with platinum over oxygen, but it does readily alloy and diffuse into platinum, the rate of which is characterized in the next section.

The chemical bond which holds oxygen and aluminum together in the material lattice has a strength which is determined by the sum for forces which hold the units of alumina together, as well as the individual molecules to each other. This value is experimentally defined as the Schottky defect energy (E_{Sh}, eV) and is evaluated as being approximately 9.1 eV for aluminum atoms and 3.5 eV for oxygen atoms [122]. The energy required for diffusion (E_d, eV) of oxygen through the sapphire material matrix is defined in Equation

5-19 as a relation to the lattice defect energy and lattice migration energy (E_M, eV), which has been experimentally evaluated as equivalent to 2.5 eV.

$$E_d = \frac{1}{5}E_{Sh} + E_M \qquad \text{Eq. 5-19}$$

These energy thresholds are dependent on the length of the material lattice bonds, which is a linear function of temperature. Thus, it can be observed that the availability of oxygen is approximately 33% higher than the availability of aluminum at temperatures above the migration threshold for both materials, which has been experimentally determined to be in the range of approximately 900 °C to 1150 °C [111] [107].

Once free oxygen is available to combine with platinum, it will readily do so at room temperature, but a surface passivation level only a single atom thick will prevent any further oxidation. At temperatures between 350 °C and 600 °C the oxide formation proceeds through the passivation layer and forms penetrating oxides that accumulate as a function of time and temperature and can penetrate completely through the platinum material structure, resulting in the electrical failure of the instrument trace.

At temperatures above 600 °C, the oxide disassociates and migrates out of the platinum material lattice. Thus, oxide formation can typically be reversed by long exposures above this temperature. The rate at which the oxide disassociates is not well characterized and is highly dependent upon the formation geometry, but soak times of more than 150 hours are commonly cited in literature to completely disassociate platinum oxide formations [123].

The overall impact of this analysis is that oxygen availability at the sapphire to platinum material interface will be very low at temperatures below 900 °C, so the temperature range in which oxide formation penetrates the platinum surface, 350 °C to 600 °C, will not result in oxide diffusion because there are no oxygen atoms available to diffuse into the platinum at this temperature. Additionally, since oxygen readily disassociated from platinum at

temperatures above 600 °C, once the 900 °C threshold is reached, no significant oxidation is expected to occur in the platinum material.

The only situation which would result in oxygen migrating from the sapphire substrate into the platinum resistive trace would be for a heating cycle above 900 °C for a long period, where oxygen is freed from the sapphire substrate and migrates to the platinum surface interface and collects. If the sensor is then cooled, as it passes through the 600 °C to 350 °C temperature range, the oxygen which has collected at the material interface could then readily permeate into the platinum material and oxidize. This can be avoided by traversing this temperature range quickly, with a cooldown time of less than 10 minutes recommended for SPRT instruments [123] to avoid the oxidation reaction with free oxygen.

This reaction can be avoided all together if the instrument is only heated once during the expected operating lifetime, as would be the case for an instrument deployed in the core region of a pebble bed reactor. If oxidation does accumulate in the platinum trace, this can be driven out by long periods of operation above 900 °C. Because this effect is easily mitigated, it will not be considered for further temporal performance analysis. However, a key takeaway is that free aluminum atoms will be available at the material interface once the sensor has been heated above the 900 °C threshold and will likely thermally diffuse into the platinum material if it does not preferentially reform aluminum oxide.

Considering that the energy threshold for formation of aluminum oxide is significantly lower than the energy threshold for platinum oxide, this should prevent free aluminum from collecting if the free oxygen concentration is proportional. It remains to be seen if this is the case for long operation in at high temperatures, but it will be assumed to be non-significant for simulation purposes.

5.2.3 Thermal Diffusion Rate Model

Thermal diffusion is assumed to take place for all materials which do not chemically react with platinum. This includes, in theory, alumina molecules which have broken away from

the substrate or capping material lattice as well as free molecules. In practice, macro molecules of alumina have not been observed to migrate into platinum, even at high temperatures, but free molecules of aluminum have been observed to diffuse in platinum thin films at high temperatures when aluminum is utilized as an interstitial adhesion promotion layer [107] [124]. These reactions have a theoretical threshold temperature, as the thermal energy of the environment must be great enough to break the material lattice bonds and create a free molecule, which will then diffuse from the platinum and aluminum interface.

The threshold energy for the production if free aluminum atoms is the same as for chemical reactions, equal to a material temperature of approximately 900 °C. The threshold for diffusion of platinum unto the material lattice of the sapphire is theoretically around 1,100 °C, as this is the temperature at which chromium and iron in natural sapphire and natural ruby begins to diffuse within the alumina material lattice. However, platinum does not have the correct ionic characteristics to readily diffuse at this temperature, and like magnesium and nickel, platinum has not been observed thermally diffusing into alumina more than one atomic layer, even at very high temperatures [122]. Thus, the only diffusion material which must be modeled for temporal response is the diffusion of aluminum into platinum at temperatures above the migration threshold for alumina of approximately 900 °C. Again, this is assuming that he free aluminum atoms will not preferentially re-from aluminum oxide rather than alloy with platinum.

For experiments which characterized the thermal diffusion of impurities in platinum to develop an understanding of uncertainties for the ITS-90 calibration standard, no significant impurity migration was observed via thermal diffusion at temperatures below 450 °C [123]. Thus, it is assumed the thermal diffusion rate is zero at or below this temperature.

Investigations into the interactions of various adhesion layer materials for platinum thin films characterize the thermal diffusion rate of metals such as titanium and tantalum in

platinum as being significant at temperatures over 700 °C, resulting in the formation of platinum alloys above this temperature which were detectable with x-ray diffraction [118]. However, the presence of oxygen, even in trace amounts, preferentially reacts with the metallic adhesion layer and prevents alloy formation, essentially bonding with the metal and remaining at the surface of the platinum, rather than diffusing into the platinum material lattice.

Although some diffusion of aluminum into platinum thin films is reported when the two materials are combined in adjacent thin-films, this diffusion rate is not well characterized. The presence of oxygen at the material interface suggests that aluminum may preferentially re-combine with oxygen rather than diffuse into the platinum, although aluminum does readily alloy with platinum under the right conditions to form Pt_2Al_3. The absence of a meaningful characterization in literature leads to the necessity of either an isotropic approximation or the assumption that the presence of oxygen will prevent this effect entirely. The complex characterization of lattice migration across grain boundaries does not support an isotropic molecular diffusion approximation, therefore it will be assumed that the free aluminum at the material interface is preferentially re-combined with oxygen rather than migrating into the platinum material, similar to the observed behavior for titanium and tantalum [124].

5.2.4 Piezoresistive Strain Decay, Creep, and Annealing Rate Model

The rate at which stress created by differential thermal expansion transitions from temporary elastic deformation of the material lattice to permanent plastic deformation of the material lattice is defined as the piezoresistive strain decay or creep rate.

Creep is commonly understood as the slow process by which material settles under a mechanical load, often characterized in terms of time, applied stress magnitude and temperature. Although the focus for this investigation is on internal stress created by differential thermal expansion rather than external mechanical stress, the basic concept is very similar.

Annealing is included in this functional group because it is dependent on the same fundamental process as creep, which is the breaking and reformation of lattice bonds due to absorption of thermal energy. Each of these processes is characterized as a function of time and temperature for the platinum sensing material, with piezoresistive strain decay and creep having a functional dependence on spatial stress distribution as well.

Due to the difference in Young's Modulus between platinum and sapphire, depicted as a function of temperature in Figure 5-13, the magnitude of material lattice transitions due to stress for the sapphire substrate approximately one third of the magnitude for platinum material. Sapphire also exhibits an axially dependent Young's modulus, however the characterization of the temperature dependence for the minor axis is not well defined in literature; thus, isotropic parameters will be assumed. This difference in Young's modulus supports the validity of assuming and simulating the effects of creep and annealing only for the platinum resistive trace. The Sapphire substrate will also undergo some degree of creep and annealing, but at a much slower rate.

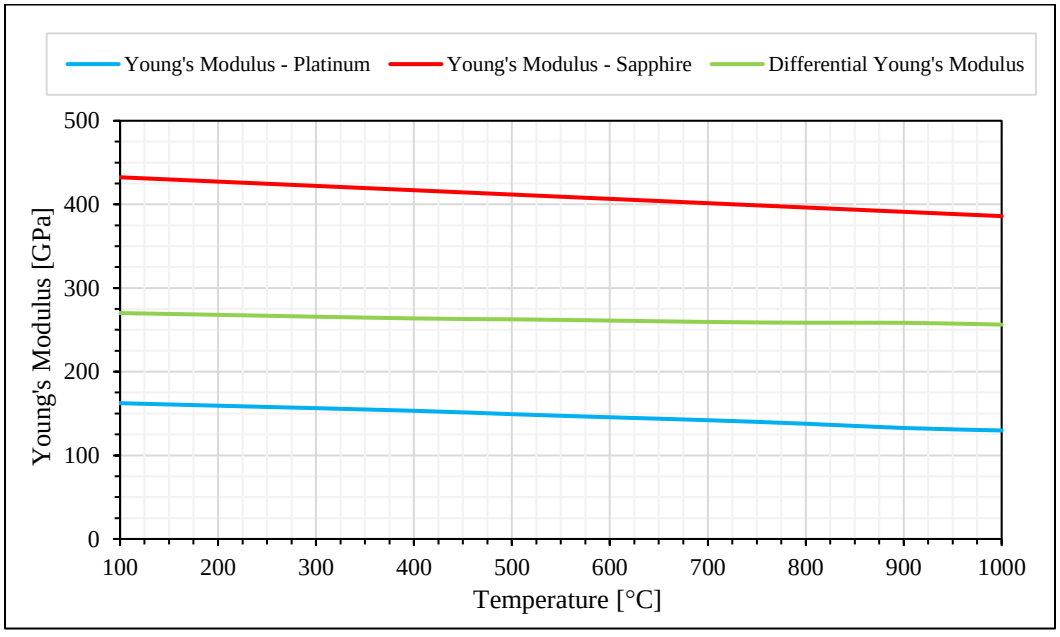

Figure 5-13: Temperature dependence of Young's modulus for platinum and sapphire [121] [122]

Determination of the temperature dependent creep rate for metals begins with the determination of the homologous temperature for platinum. As pure platinum has a melting point of 1,768 °C, and annealing or creep material transitions for bulk metals typically reach their full effect at around 40% of this temperature, the homologous temperature for pure platinum is approximately 707.2 °C.

From experimental data, it is known that platinum can exhibit annealing and creep at temperatures far below this value, as low as 200 °C, depending on the amount and magnitude of lattice defects in the material. An experimental characterization of creep for pure platinum is depicted in Figure 5-14, which supports this threshold temperature selection. Note that for materials with a high degree of work hardening, or a high amount of large lattice defects, the annealing temperature begins much lower, because the lattice bonds are already weakened, thus modifying them only requires a small amount of thermal energy. At the homologous temperature, all material samples exhibit annealing transitions, regardless of initial internal stress.

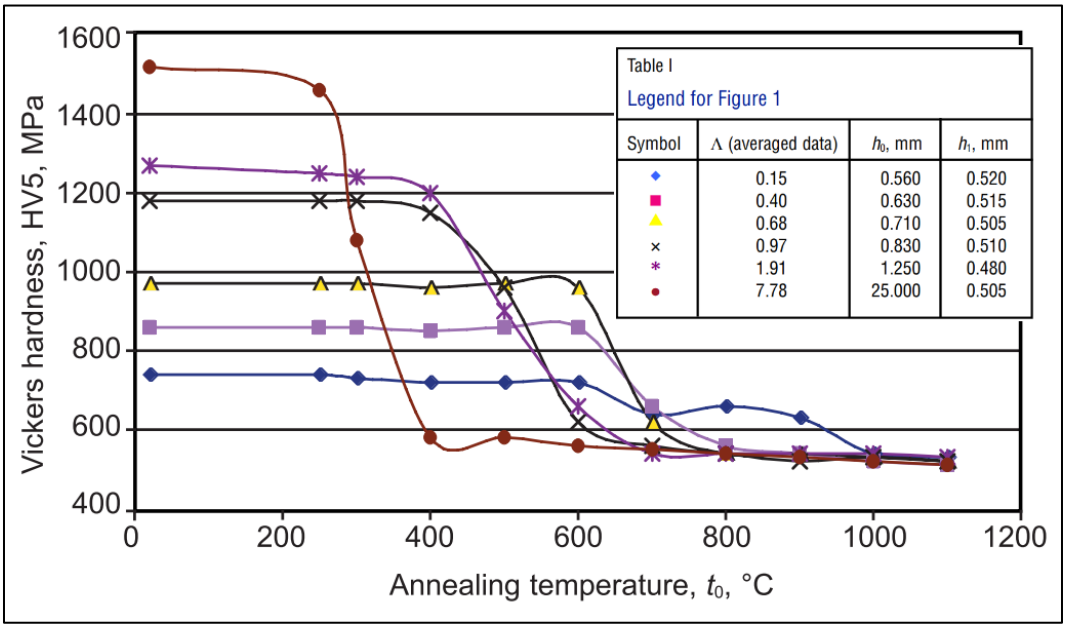

Figure 5-14: Annealing temperature onset as a function of Vickers hardness [125]

An investigation by NASA for optimization of fabrication processes for pure platinum thin film strain gauges [126] characterizes the change in temperature dependent resistance $(\Delta R(T), \Omega)$ due to annealing as a function of temperature $(T, °C)$, time (t, hr), film stress (σ_f, Pa), gauge factor (k), Young's modulus (E, Pa), and annealing rate (A, hr^{-1}) as defined in Equation 5-20. This relation is then linearized to produce Equation 5-21 and if intrinsic deposition film stress is assumed to be equal to $0.40(E/k)$, can be simplified to the relation defined in Equation 5-22.

$$\frac{\Delta R(T)}{R_0} = \frac{k}{E}\sigma_f e^{-A(T,\sigma_f)t} \qquad \text{Eq. 5-20}$$

$$A(T, \sigma_f) = 0.00580 hr^{-1}\left(\frac{k}{E}\sigma_f\right)(T - 172\,°C) \qquad \text{Eq. 5-21}$$

$$A(T) = 0.002321\ hr^{-1}(T - 172\,°C) \qquad \text{Eq. 5-22}$$

Assuming ideal conditions, annealing for six times the inverse of the time indicated by Equation 5-22 would result in resistivity returning to 0.1% of the un-stressed nominal value. The temperature dependent for both annealing rate and required annealing time are depicted in Figure 5-15.

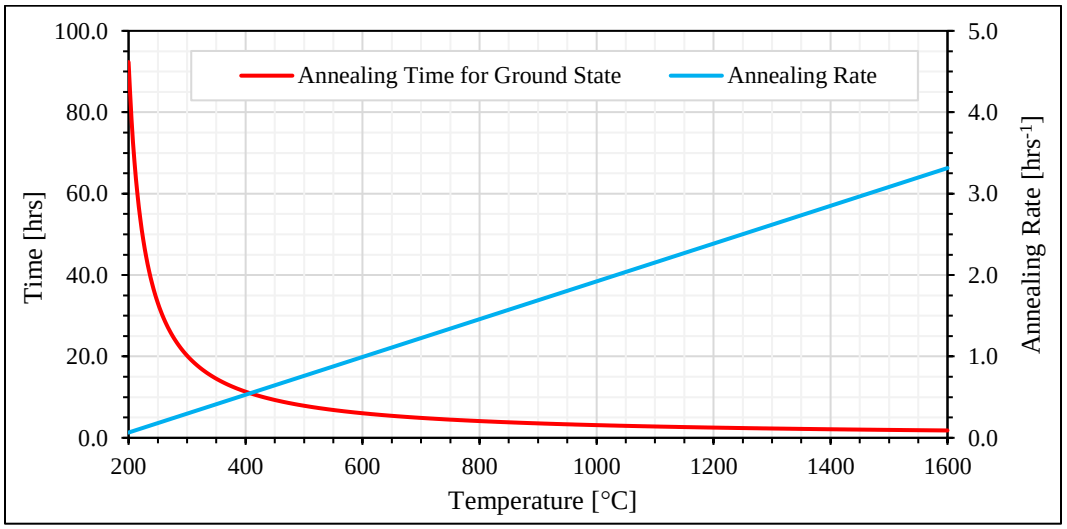

Figure 5-15: Annealing rate and annealing time required to return to 0.1% initial resistance [126]

This annealing rate characterization adequately approximates the decay rate of the piezoresistive portion of the resistance variation due to material strain, as well as the healing rate for minor lattice defects. Thus, it will be utilized to determine the time and temperature dependent error function for the proposed instrument in later sections.

5.2.5 Lattice Defect Formation and Decay Rate Model

As described in the previous chapter, lattice defects are described by four primary functional classes. These include vacancies, dislocations, grain formation and growth, and mechanical lattice deformations. The rate of simple vacancy formation and decay, as well as the rate of simple lattice dislocations are characterized explicitly in this section, which the rate of annealing and grain transition are characterized in the previous and next section, respectively, as these are functionally dissimilar enough to be more relevantly included with other processes.

The energy required for simple defects in the sapphire and platinum material lattices are 4.1 eV and 1.5 eV, respectively. These are defined as the simple defect energy (E_a, eV) and are related to the overall change in electrical resistance $(\Delta R/R_0)$ for a conductor as described in Equation 5-23 and Equation 5-24.

$$\Delta R/R_0 \approx 1200.0 exp(-E_a/kT) \quad \text{Eq. 5-23}$$

$$\tau = \tau_0 exp(E_a/kT) \quad \text{Eq. 5-24}$$

The rate at which simple lattice defects and vacancies are formed and annealed is characterized by Berry et al. [106] for equilibrium conditions at a range of temperatures. The vacancy density equilibrium is dependent on material temperature and decays according to an exponential function with half-life, tau, dependent on the activation energy for the defect. This temporal relation is defined in Equation 5-24, Where τ_0 is the time constant characteristic of the diffusion and equilibrium process, which ranges from milliseconds at 960 °C to hours at temperatures below 400 °C. This is very similar to the

annealing rate defined in the previous section, except this rate is for simple lattice defects, whereas the previous relation was for more complex, strain-induced lattice deformations.

This vacancy equilibrium effect on resistance is included in the temperature dependent resistivity relation developed for steady state analysis. The only situation in which it would need to be included again, as an additional term in the resistance calculation, is if the cooling rate was so rapid as to not allow the simple defects to anneal out of the material before they are 'frozen' in place at lower temperatures. As long as previously defined cooling rates are followed, this should not be of significant impact, even for temporal calculations, as other effects will dominate this effect in magnitude. Thus, this characterization is for information only and will not be included in performance analysis.

5.2.6 Grain Formation and Grain Growth Rate Model

The process by which atomic or molecular dislocations result in semi-permanent formations of groups of aligned atoms in a regular lattice is referred to as a grain transition. Similar to the previous section, these transitions occur when a lattice bond is broken by thermal energy and the atom changes location or orientation to become part of a new grain or leave a grain. Although this process can occur for either atoms or molecules, for simplicity, only references to atoms will be used henceforth.

Increases in thermal energy typically result in grain growth, typically from previously un-aligned atoms in the material lattice joining a nearby grain at the grain boundary. Once a large portion of unoriented atoms are aligned with a grain lattice, the grain formation rate slows, as any additional atoms must first be removed from an existing grain lattice before joining a new grain lattice. This transition has a higher threshold energy when compared to free atom transitions and does not result in a significant reduction in ground state energy. Thus, it occurs at a proportionally lower frequency for similar temperatures.

Although relatively rare, multiple atomic dislocations in a local area can result in the formation of an interstitial grain, or a new orientation which is not aligned with any other

nearby grain lattices. This process occurs more often at very high temperatures, when lattice dislocation rates are high and multiple adjacent lattice bonds break simultaneously, resulting in a high free atom density in a local area.

New grains can also be formed by contaminants in a material or by epitaxial shapes of adjacent material surfaces. In both of these cases, the external material lattice induces grain formation at a higher rate than for a pure material, causing preferential grain formation and growth at that location. An example of this is the preferential (111) orientation of platinum grains at the material boundary with alumina. The epitaxial structure of the alumina boundary preferentially forms this orientation of grain and the ratio of this specific orientation to other, random orientations in a material can provide a measure of thermal exposure of the material interface.

Stress on a material from thermal or mechanical interactions can cause grains to break apart into independent pieces, although materials will preferentially dislocate along grain boundaries, as the grain-to-grain material lattice bonds are significantly weaker when compared to the internal bonds within a grain. These effects are not considered for analysis, as they are not expected to occur in the normal operation of the proposed sensor.

Characterizing the rate of grain growth and decay is not trivial, as it depends on a wide range of factors, including material temperature, pressure, gain boundary orientation, the presence of impurities, and the epitaxial shape of the surrounding material interfaces. Although some Monte Carlo and molecular dynamics simulations have developed accurate estimations of the final grain configuration in platinum thin films [127], the estimates for the rate of grain growth aren't suitable for use in this temporal analysis due to the uncertainty range of the required input parameters.

The only significant resistance characterization dependent on grain size which has been developed for this investigation is the steady state thin film ground boundary scattering correction factor, which is only weakly impactful at the film thickness being considered.

Also, grain size after initial annealing is not expected to change significantly over the operating life of the sensor due to a maximum grain size being reached when the grain diameter is equal to the film thickness. Thus, due to a lack of accurate characterizations in literature, a temporal characterization of the grain size growth rate will not be included in the temporal analysis model. Grain size does significantly affect the mechanical properties of the platinum trace, specifically Young's modulus [128], but not to the extent that it would impact the overall validity of the evaluation being developed.

5.3 Estimate of Single Instrument Error

Critical to the evaluation of instrument performance and determination of applicability for replacement of contemporary instrumentation systems is the quantification of measurement error. Many factors influence the accuracy of thermal measurements and the most significant of these are described in this section and characterized as a function of environmental thermal exposure and measurement magnitude. The combination of these factors produces an integrated model for estimating measurement error over the expected operational lifetime of the instrument.

5.3.1 Joule Heating Error Mitigation

A common source of measurement error for resistance sensors is the self-heating, or joule heating, which occurs in the resistive trace of the instrument when a current is passed through it. Some amount of electrical power must be applied to the measurement circuit to determine the resistance of the element, which will always create some small amount of localized heating. The method of mitigation for this effect is specific to the type of instrument being utilized, but for thin film resistance instruments utilizing an AC or pulsed DC measurement sequence, a common methodology is defined by Pearce et al. as an algorithm of sequential measurement cycles.

Recalling Equation 4-2, the power dissipated via joule heating is equivalent to the square of the constant current $(i_{1,2}, mA)$ flowing through the resistance trace. If the excitation

current is varied across three separate measurements, with the magnitude of the excitation currents being apportioned in the ratio of 1:2:1, and the cycle time being apportioned in a ratio of 4:1:4, than the uncertainty in the extrapolation of the zero current resistance measurement (R_0, Ω) from the collected resistance measurements $\left(R_{1,2}, \Omega\right)$ without the effects of joule heating can be evaluated as defined in Equation 5-25.

$$R_0 = \frac{R_2 i_1^2 - R_1 i_2^2}{i_1^2 - i_2^2} \qquad \text{Eq. 5-24}$$

The nominal excitation current chosen for analysis is 10.0 mA, but this could be varied as 5 mA and 10 mA or 10 mA and 20 mA to achieve the benefit of joule heating error mitigation. This approach is valid for both the strain measurement and the RTD measurement utilized in the hybrid sensor proposed.

5.3.2 Evaluation of Steady State or Ground State Error

Contributions to measurement error which are not dependent on temporal material transition effects are those which will permanently shift the resistance-to-temperature calibration curve by alteration of the assumed ground state parameters of the device. This category would include variation in dimensional manufacturing parameters, uncertainty in the estimates for thin film resistivity multiplication factor, uncertainty in manufacturing annealing time and maximum grain size, and other types of uncertainty associated with the response of the sapphire substrate as a function of temperature, such as uncertainty in the temperature dependent response of the coefficient of thermal expansion.

Ultimately, steady state error should not pose an issue for characterizing the performance of the instrument, as all steady state error is essentially integrated into the initial calibration curve which is developed immediately after the fabrication process. Of course, this assumes the same measurement hardware used for calibration is then used for in-situ measurement, the calibration was performed with very slow thermal transitions and long soak times, and adequate annealing times are utilized following instrument fabrication.

Any fundamental variation in dimensional properties or uncertainty in material parameters will not change over time and will always contribute the same amount of differential resistance over the lifetime of the device.

The initial calibration curve for the purpose of analyzing the effects of temporal error for this investigation is assumed to be equivalent to the steady state performance depicted in Figure 5-12. This curve is assumed to have an initial uncertainty equivalent to the total uncertainty of the sensor, which is dependent on deployment configuration, as described in the next sections. Once the temporal error and geometric impact of resistance variation with temperature are accounted for, then the ground state error is adjusted to bring the corrected measurement of the RTD in line with the original calibration.

The realization of this ground state error adjustment is an offset of the entire calibration curve upwards by some fixed resistance, to account for the impact of non-temperature dependent effects which degrade the instrument over time. Over long exposure periods, the ground state error is expected to slowly grow due to the thermal diffusion of impurities or material transitions in the sapphire crystal lattice which produces a resistance change that is not temperature dependent.

The time-dependent ground state error $\left(E_g(t), \%\right)$ is defined by the relation of the time-dependent resistance offset $\left(R_{E-gs}(t), \Omega\right)$ to the initial resistance at the ground state $\left(R_g(t_0), \Omega\right)$, as described in Eq. 5-25. Note that the time dependence is in reference to a given thermal exposure profile, which is a function of temperature and time.

$$\frac{R_{E-gs}(t)}{R_g(t_0)} = E_g(t) \qquad \text{Eq. 5-25}$$

5.3.3 Evaluation of Temporal Error

The time-dependent temporal error $(E_t(t), \%)$ incurred as a result of a heating or cooling rate which exceeds the annealing rate, as defined in the analysis of temporal material

transition effects, is defined in Equation 5-26. This error can be expressed as a ratio of the geometric induced resistance change $\left(R_{geo-SG}(T), \Omega\right)$ and the piezoresistive induced resistance change $(R_{PZR}(\Delta T, t_a), \Omega)$ for a given thermal exposure profile.

$$\frac{R_{PZR}(\Delta T, t_a)}{R_{geo-SG}(T)} = E_t(t) \qquad \text{Eq. 5-26}$$

Note the difference between the time used for estimating the dissipation of temporal material transitions (t_a), such as the decay of piezoresistive effects, and the time which indicates the progression of the thermal exposure profile (t). The temporal error will fluctuate due to heating and cooling and will drop to zero over long time periods with no temperature transitions, whereas the ground state error will only increase over time.

The various temporal effects of material transitions which contribute to resistance errors can be superimposed, assuming they have only time related, temporary functional mechanisms. For example, the effects of lattice vacancies are considered temporal and can be summed with the effects of piezoresistive decay, as they will ultimately drive the resistance response of temperature transitions, and both are eventually annealed out without impacting the expected ground state resistance.

Temporal error cannot be generated with a permanent or steady state source of error, such as impurity concentration, even if it is propagated by a fundamentally time-dependent process, such as thermal diffusion. Although the driving mechanism of thermal diffusion may be characterized as a time-dependent function, the impact on resistance is permanent and must be evaluated separately. Ideally, this would be done by allowing the time-dependence of the propagation mechanism to decay to the point that the effect is no longer varying over time. At this point, a new ground state calibration curve should be developed by comparison of the strain temperature estimate and the RTD temperature estimate, which now accounts for the permanent change in resistance due to the presence of the contamination.

Note that this change only affects the RTD estimate and not the strain estimate because the strain estimate is a differential evaluation between two circuits with assumed identical environmental exposure, meaning that any material transition which affects the entire sensor is not observed. Because impurity migration via thermal diffusion is expected to be a constant term over the entire circuit, this would not impact the strain measurement accuracy, but may impact the stain measurement precision or error range if the resistance increase is significant, on the order of 10% of total resistance or more.

The rate of change for the magnitude of temporal error should be a logarithmic function of temperature and time and will be proportional to the difference between the annealing rate and the rate of heating or cooling, as evaluated at the measurement temperature. This error will be characterized for the heating rates of fuel pebbles in a pebble bed HTGR fuel recirculation system in the next chapter, as it is a direct indicator of the functional applicability of the proposed sensor to the target environment specified.

5.3.4 Complete Instrument Error Estimation Algorithm

The determination of instrument error is fundamentally based on the concept of starting with an accurate ground state calibration curve, which is established immediately after instrument fabrication and utilizes the exact same measurement hardware as will be used in the service of the instrument. This ground state calibration curve provides the temperature-dependent geometric $\left(R_{geo-RTD}(T), \Omega\right)$ and temperature-dependent resistivity $\left(R_{\rho}(T).\Omega\right)$ responses of the RTD resistance measurement $(R_{RTD}(T,t).\Omega)$ over the temperature range of the device $(\Delta T, °C)$, as defined in Equation 5-27. For this first calibration, the ground state error offset $\left(R_{E-gs}(t), \Omega\right)$ is equal to zero, because the thermal exposure since calibration is nearly zero $(t = 0)$.

$$R_{RTD}(T,t) = R_{\rho}(T) + R_{geo-RTD}(T) + R_{E-gs}(t) \qquad \text{Eq. 5-27}$$

Likewise, for the strain measurement, the initial strain gauge resistance measurement $(R_{SG}(T,t), \Omega)$ calibration curve is derived from the temperature-dependent geometric

$\left(R_{geo-SG}(T), \Omega\right)$ and annealing-time- and heating-rate-dependent piezoresistive responses $(R_{PZR}(\Delta T, t_a), \Omega)$ over the temperature range of the device, as defined in Equation 5-28. For the initial calibration, it is vital that the heating and cooling rate be slow enough to allow the piezoresistive portion of the resistance to decay to nearly zero for the measured temperature, as determined by the annealing rate at that temperature. Thus, this initial stain measurement becomes solely dependent on geometric variation between the traces parallel and perpendicular to the C-axis of the sapphire substrate, as described in Equation 5-29.

$$R_{SG}(T, t) = R_{geo-SG}(T) + R_{PZR}(\Delta T, t_a) \quad \text{Eq. 5-28}$$

$$R_{SG}(T) = R_{geo-SG}(T) \quad \text{Eq. 5-29}$$

As previously mentioned, note that the strain gauge response does not have a dependence on shifts of the ground state resistance curve due to it being a differential measurement rather than an absolute measurement.

At each measurement point, some amount of time has passed, thus the correction factor for the ground state resistance will start to increase by some unknown magnitude and must be evaluated. This is done by first recording the new values for RTD and strain gauge resistance, then estimating the response of the piezoresistive portion of the strain gauge measurement based on the differential temperature, differential time, the temperature-dependent Young's modulus for platinum, and the temperature-dependent differential coefficient of thermal expansion.

From these parameters, an evaluation of thermal film stress is made and is added to an isometric sum of film stress for each strain gauge trace. The temperature- and film-stress-dependent annealing rate is then estimated and the sum of film stress is reduced by the amount predicted. The residual film stress is then used to predict the piezoresistive portion of the strain gauge response. This is subtracted from the measured strain gauge resistance to create a strain gauge temperature measurement which is then analyzed to evaluate the temporal error of the measurement.

This ‘ground state’ strain gauge temperature measurement is only dependent on geometric variation and is proportional to the geometric portion of the RTD resistance response to temperature. The strain gauge geometric response is used to estimate the RTD geometric response, which is then combined with the temperature-dependent resistivity to evaluate the RTD ground state resistance for the measured temperature.

If the temporal error is very low (less than 0.1%) due to the film stress and piezoresistive portion of the strain gauge resistance being near zero, then a new ground state offset should be periodically determined. This is accomplished by simply comparing the ground state resistance at the time of measurement to the initial calibration ground state resistance. The difference in these values is then the new ground state offset, which accounts for permanent resistance increases in the element which will not anneal out over time. This offset is then used for every determination of RTD temperature after that point, returning the measured performance to the performance curve determined at calibration.

At this point an evaluation of the total error $(E_{total}(t), \%)$ can be made, which is simply the sum of the temporal and ground state error, as described in Equation 5-30.

$$E_{total}(t) = E_g(t) + E_t(t) \qquad \text{Eq. 5-30}$$

5.3.4.1 RTD and Strain Gauge Measurements: Accuracy vs Precision

The primary reason that the temperature-dependent strain response alone is not used to estimate the material temperature, and is instead used to correct the response of the RTD measurement, is that the strain response is extremely accurate but not precise. It is able to mitigate any effects which impact the overall resistance of the restive trace, but the differential measurement signal magnitude is very small, estimated to be an order of 1,000 times smaller than the magnitude of the RTD measurement. This means that it is prone to noise and external signal deterioration effects that would create large uncertainty in the final temperature measurement if it were used alone.

When used as a means of proportionally estimating the piezoresistive impact of an RTD resistance measurement, the strain gauge measurement is really being evaluated for changes in voltage or resistance over time, rather than the absolute measure of voltage or resistance, which helps to reduce the overall measurement uncertainty, and is essentially providing a range shift at every temperature step for expected temporal error. If this range is very accurate, it doesn't necessarily matter that it isn't precise, because the RTD measurement already has a high level of precision.

For example, if I know that the measurement is offset by some unknown magnitude for some period of time due to temporal error, it doesn't necessarily matter how large that offset is, as long as I have high certainty that the effect will be reduced to nearly zero after some known period of time.

The RTD measurement lacks some way of determining if the signal is drifting, which is why they are considered to have low accuracy at high temperatures. If the variance in the strain gauge measurement can indicate how much the curve may be drifting due to variation in sensor material stress or impurity migration, then RTD measurements can be both precise and accurate because they have excellent signal to noise ratios and now have a means of detecting whether the signal has drifted from its calibration point and if temporal effects are impacting the measurement.

Thus, using the combination of the two instruments is preferable to using only one of them, as they each support a different characteristic of the measurement quality via evaluation of fundamentally isolated processes; an absolute measurement of resistance with high precision and a relative measurement of resistance with high accuracy.

5.3.4.2 Required Assumptions for Error Estimation and Simulation

The determination of error is fundamentally linked to the thermal exposure profile and measurement rate. The shorter the period of time between measurements, the more accurate the sum of film stress becomes, this is especially true for rapid temperature

transitions. Over long periods of time at a stable temperature, the film stress and the temporal error will decay to zero as the material annealing rate slowly transfers the thermal stress into permanent material deformation, making the ground state measurement more accurate when compared to measurements taken during transition periods, as the variation in geometry is well characterized and repeatable; whereas the variation in thermal stress distribution will vary considerably for each temperature transition and is not repeatable.

Two fundamental assumptions of this calculation method are that the geometry changes immediately, but the residual film stress decays over time, and that the geometry transitions for heating and cooling obey the constant entropy variation of the 2nd law of thermodynamics, meaning they are perfectly reversible. These are both reasonable simplification assumptions, as in a real system some immediate elastic deformation will arise, based on the difference in Young's modulus between the film and the substrate and residual film stress, which will transition into plastic deformation over some time period. If the rate of heating or cooling is rapid, the difference between assuming immediate geometric change and actually calculating that geometric change as a function of the new temperature-dependent material properties with each step, will be slightly more significant.

If the initial and decay stress distributions are equivalent and the crystal lattice of the substrate does not undergo some kind of unexpected transition, then making these assumptions for a single heating cycle, such as that proposed for the use case of HTGR fuel monitoring, is likely an acceptable condition for validity of these assumptions, given the significant simplifications they enable for simulation of device performance.

5.4 Final Performance Simulation Model

In this section, the final performance model which integrates the steady state and temporal models previously developed is described and various initial tests results are provided. Physical design parameters and measurement ratios for the proposed device are investigated to determine if the analysis is useful for determining an optimal device design.

In the next chapter, this simulation model will be applied to the thermal exposure model for a pebble bed HTGR fuel element to evaluate the functional applicability of the proposed instrument as a thermal sensor for HTGR core environments.

5.4.1 Final Performance Simulation Algorithm

The final model which is used for determination of theoretical instrument performance is the integration of the previously defined steady state performance model with the temporal error estimation defined in the previous sections. The general order of the calculation follows the order described in the previous explanation of error estimation. This calculation algorithm results in a simulation framework in which a specified thermal exposure curve can be used as input and the expected steady state performance would predict the ground-state resistance of the device at that temperature, while the temporal error model would estimate an additional resistance term that is generated due to time-dependent material transition effects which have not fully decayed.

Note that the expected ground state error may not be evaluated accurately relative to the true physical system using this simulation, as the propagation mechanisms for permanent resistance modifiers, such as aluminum diffusion in platinum, are not well characterized. Thus, a constant impurity term will be added to simulate degradation of the instrument. This would be similar to the degradation process expected for low intensity radiation exposure which slowly dopes the platinum sensor by increasing impurity concentration.

The final performance simulation model actively tracks the dimensions and material parameters of the instrument over time, with the RTD and strain gauge output compared to determine the estimated error of the RTD measurement, as each of these devices produces a proportional measurement of temperature-dependent geometric variation of the resistive trace. The RTD output is primarily dependent on the trace length, width, film thickness, and material resistivity modified by the thin film correction parameter. The stain gauge output is driven by the two primary components which comprise the gauge factor, the steady state differential geometric and transient piezoresistive response to strain.

The algorithm used for instrument physics simulation is described by Table 5-3, using input parameters described by Table 4-2, with the various temperature dependent material parameters are defined as described by the polynomial curve fit developed for each of them in the previous investigations.

Table 5-3: Algorithm for Physical Simulation of Instrument Response

Step	Actions for Physical Simulation of Materials
P-1	Retrieve temperature from thermal exposure profile for current time
P-2	Update temperature dependent coefficient of thermal expansion (TEC): - For platinum: isotropic - For sapphire: parallel and perpendicular to C-axis
P-3	Update temperature dependent coefficient of resistivity (TCR) for platinum
P-4	Update temperature dependent Young's modulus for platinum and sapphire
P-5	Calculate change in trace dimensions par. and perp. to C-axis of substrate: - Length and width determined by CTE of sapphire - Film thickness determined by CTE of platinum - Determine excess thermal strain due to differential CTE - Expand film thickness to conserve volume of platinum
P-6	Calculate thermal film stress: - Calculate film stress from excess thermal strain for each sensor - Calculate thermal annealing rate for each sensor - Calculate residual thermal film stress for each sensor
P-7	Calculate strain gauge resistance: - Calculate geometric strain resistance change for each sensor - Calculate piezoresistive resistance change for each sensor - Calculate change in absolute resistance for each sensor
P-8	Calculate RTD resistance: - Use SG results, TCR, and trace geometry to determine RTD resistance - Add additional resistance to simulate impurity generation via radiation
P-9	Run measurement simulation algorithm and advance timestep

Table 5-4: Algorithm for Simulation of Instrument Operation

Step	Actions for Simulation of Instrument Operation
M-1	Apply constant excitation current (10 mA) to instrument
M-2	Collect RTD measurement: - Use circuit analysis to simplify WSB circuit to a single resistance - Use Ohm's law to determine the RTD voltage output
M-3	Collect strain gauge measurement: - Apply RTD excitation voltage - Determine SG voltage output based on WSB circuit analysis
M-4	Estimate the temporal error of the measurement: - Estimate the time derivative of the SG voltage measurement (slope) - Estimate the time derivative of the RTD voltage measurement (slope) - Estimate the apparent temporal error by comparing the two derivatives
M-5	If the temp. error is below the threshold (0.01%), est. the new G.S. offset: - Estimate the instrument temperature via SG voltage calibration curve - Estimate the RTD ground state voltage offset for the current temp.
M-6	Estimate the ground state error of the RTD measurement
M-7	Calculate the total error (sum of the temporal and ground state error)
M-8	Determine the final measured temperature and error range

The algorithm presented is broken up into two sections. The first section, presented in Table 5-3, represents the physical response of the materials and geometry of the sensor at each step of the thermal exposure profile. This is intended to be the true representation of the physical world. The second section, presented in Table 5-4, represents each step that would be taken by an operator to read the output of the sensor and to determine the error of the measurement and if a new ground state correction offset should be applied. This second, separate simulation is intended to provide only limited data so that the response of the instrument can be determined based only on the measurement algorithm presented in the previous section. The physical response portion of the simulation is run at every time step. The measurement portion of the simulation is run at every 10th time step as an initial

evaluation. This period between measurements can be varied, along with the physical design parameters of the instrument, to determine the sensitivity of each parameter on the overall performance of the instrument.

5.4.2 Final Performance Simulation Results

The output of the simulation for a demonstration thermal exposure cycle is presented in this section, to provide an example of the expected performance of the device and to identify unique performance characteristics for specific thermal conditions.

The input thermal exposure model used for simulation is presented in Figure 5-16. This model demonstrates two distinct heating rates over the course of 100 hours of exposure. The initial steady state temperature of the instrument is 500.0 °C, with no residual thermal stress present in the instrument. The initial heating period starts immediately, with instrument temperature increasing at a rate of 0.25 °C per minute for 2,800 minutes, until the instrument temperature reaches 1,200 °C. This heating period is then followed by a soak period of 1,700 minutes at a constant temperature of 1,200 °C. The second heating rate starts at 4,500 minutes and progresses for a period of 350 minutes, until a final temperature of 1,550 °C is reached. The final section is a soaking period at constant temperature, for 1,150 minutes at 1,550 °C.

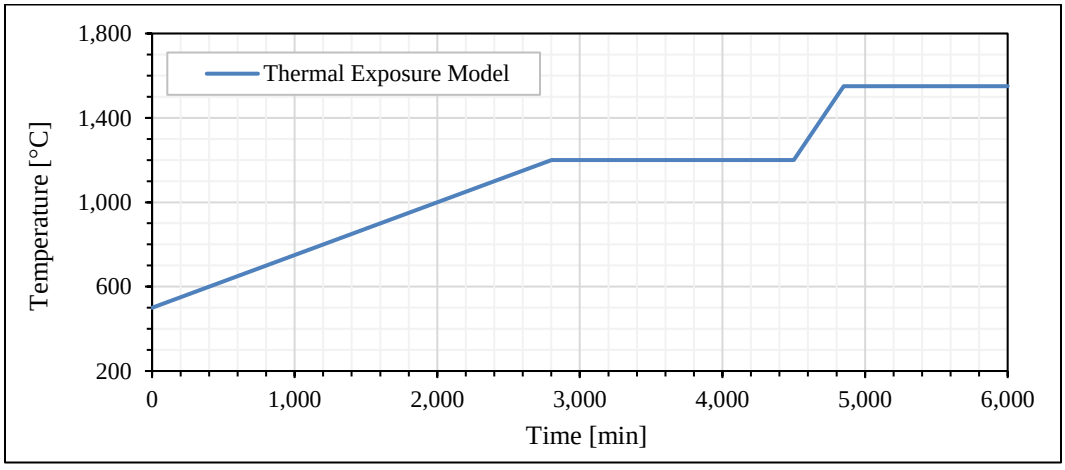

Figure 5-16: Demonstration thermal exposure model

During the heating periods, thermal stress is generated in the instrument traces due to differential thermal expansion between the platinum trace and the sapphire substrate. This occurs at a different rate for the traces parallel to the C-axis of the substrate and the traces perpendicular to the C-axis of the substrate, as depicted in Figure 5-17. The traces perpendicular to the C-axis have a larger thermal stress generation rate because the differential coefficient of thermal expansion is greater for platinum and the perpendicular axis of the sapphire than for platinum and the parallel axis of sapphire, as depicted in Figure 5-1. Thus, the amount of thermal stress created due to differential thermal expansion between these two materials is greater in the perpendicular direction than in the parallel direction; although the total elongation is greater for traces in the parallel direction.

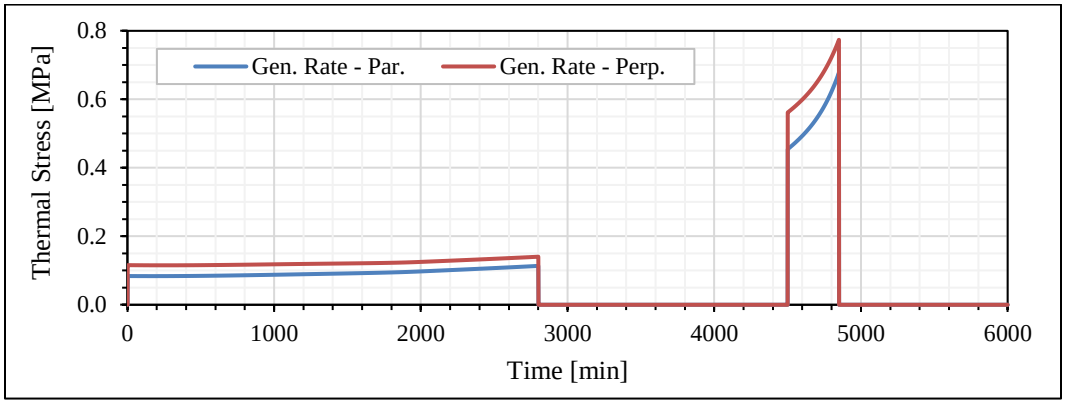

Figure 5-17: Thermal stress generation rate for parallel and perpendicular traces

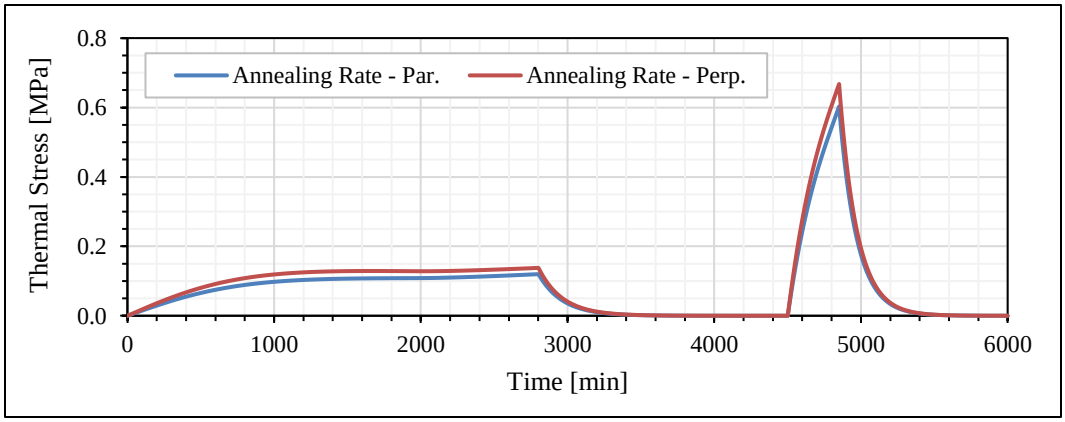

Figure 5-18: Thermal stress annealing rate for parallel and perpendicular traces

The rate of annealing, or thermal stress reduction is depicted in Figure 5-18 and is also different for traces in the parallel and perpendicular directions. This is because the annealing rate is dependent on temperature and residual stress in the trace material. As the total residual stress increases due to heating, the annealing rate increases as well, until the rates reach an equilibrium.

The total residual thermal stress for both parallel and perpendicular traces is depicted in Figure 5-19. Note that the perpendicular traces have a higher maximum residual stress, with both trace orientations reaching an equilibrium for the first heating period, but not for the second heating period. The residual stress decays to zero during the periods of constant temperature because no additional thermal stress is generated from differential thermal expansion, yet the annealing rate will continue to remove thermal stress as the trace material transitions from elastic to plastic deformation.

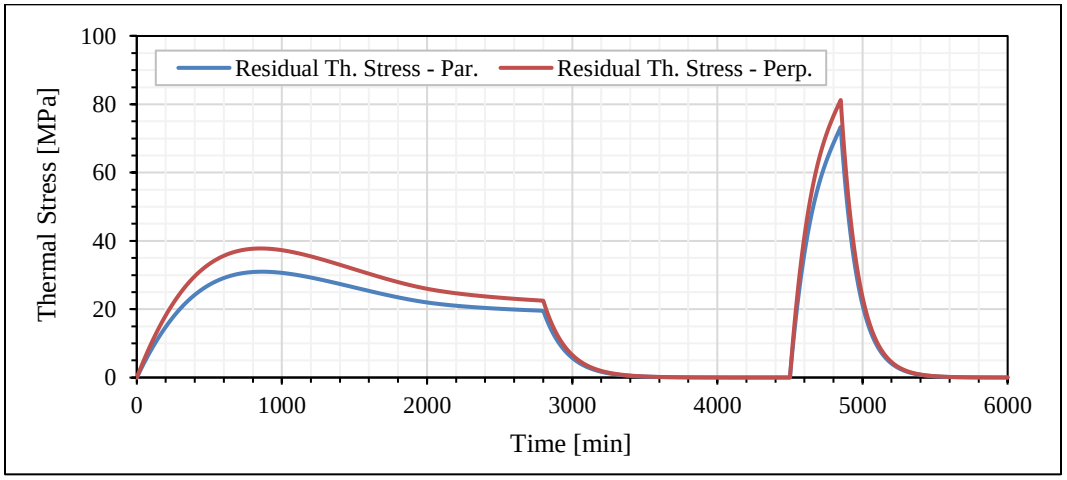

Figure 5-19: Residual thermal stress for parallel and perpendicular traces

The strain response of the instrument is depicted in Figure 5-20. This figure illustrates the change in resistance for both parallel and perpendicular traces, due to both geometric changes in trace length and cross-sectional area and piezoresistive changes due to film stress. Note that the piezoresistive response closely mirrors the residual thermal stress depicted in Figure 5-19, as it is essentially a product of the piezoresistive gauge factor,

Young's modulus, and the residual stress. The geometric strain response difference between the parallel and perpendicular traces grows with increasing temperature, with their difference being a measure of the current temperature of the instrument. Note that the parallel trace demonstrates a larger geometric response than the perpendicular trace, but the perpendicular trace demonstrates a larger piezoresistive response. This is because the CTE of sapphire is larger in the parallel direction, but the differential CTE between sapphire and platinum is greater in the perpendicular direction, as mentioned earlier. Thus, these responses oppose one another, with the piezoresistive response being much more apparent initially, but decaying away over time.

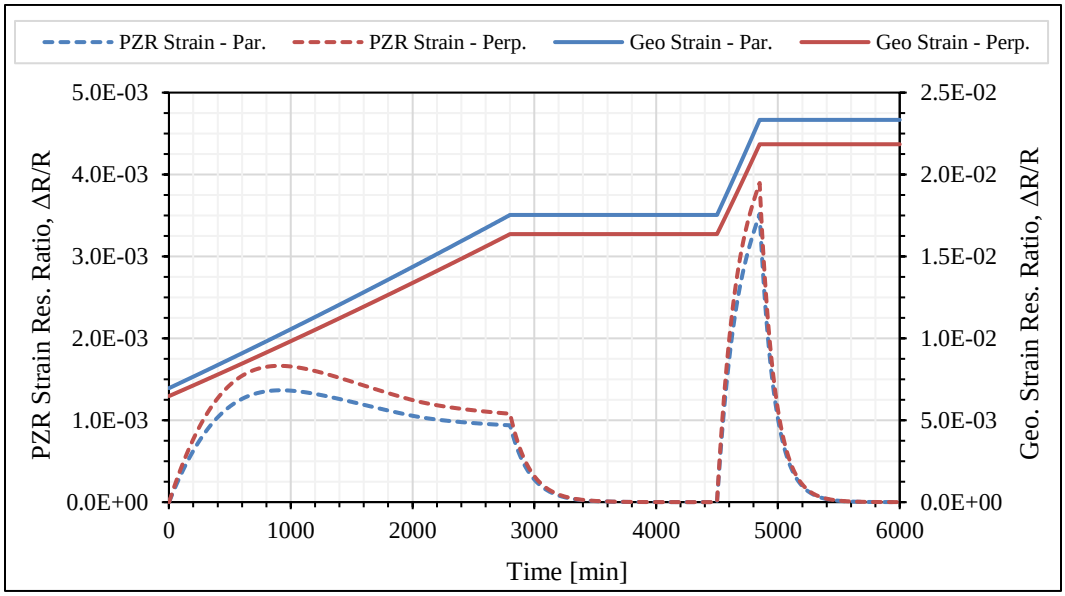

Figure 5-20: Strain response for geometric and piezoresistive effects

Integrating the strain response for both piezoresistive and geometric effects for both parallel and perpendicular traces creates the thermal exposure dependent response depicted in Figure 5-21. Note that the result of integration is that the response is dominated by the piezoresistive effects during temperature transitions, but these effects quickly decay once the instrument has reached a steady temperature. A WSB measurement circuit will compare the difference in the two curves depicted, doubling that difference for a full bridge

measurement, rather than measuring their absolute value. Thus, the differential measurement will decrease when piezoresistive effects dominate and grow larger as they decay, with the magnitude of the final difference over long periods at constant temperature being a proportional measurement of the instrument temperature, as determined by the magnitude of differential thermal expansion of the substrate C- and A-axis.

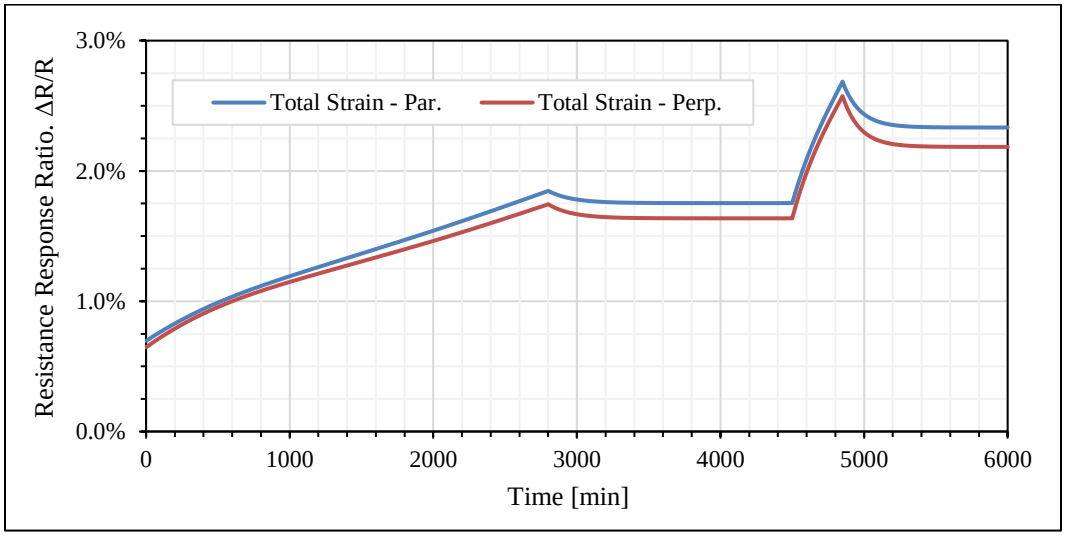

Figure 5-21: Combined geometric and piezoresistive response for par. and perp. traces

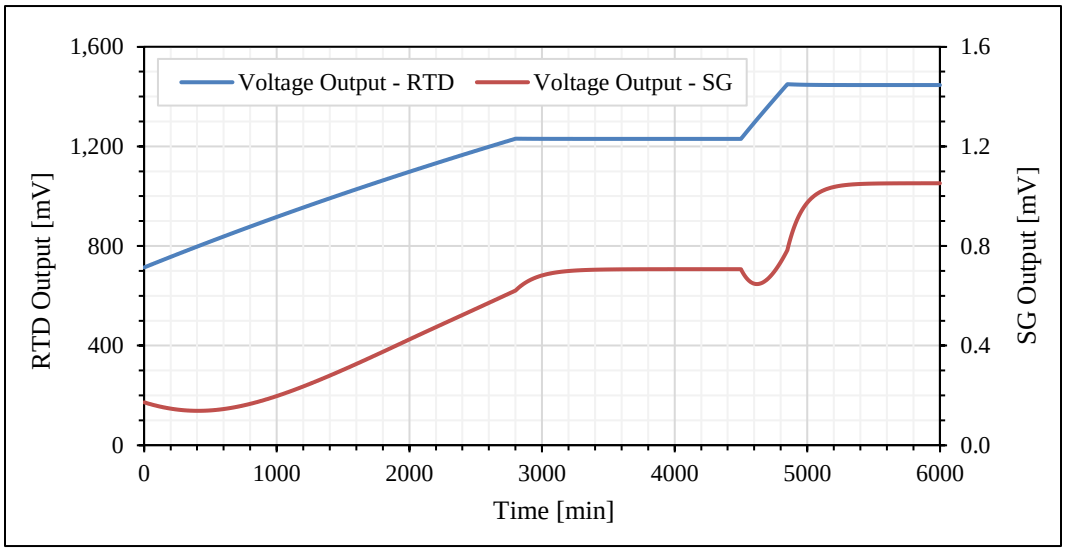

Figure 5-22: Voltage output for RTD and strain gauge measurements (at 10.0 mA)

If the RTD and strain gauge circuits are then coupled together with a constant excitation current of 10 mA, with two parallel and two perpendicular traces forming the four legs of a WSB measurement circuit, and the driving voltage of that circuit being equivalent to the RTD measurement voltage, the resulting voltage measured at the RTD and strain gauge voltage taps is depicted in Figure 5-22. Note that the RTD measurement only varies slightly from a linear response due to the effects of differential thermal expansion, while the strain gauge response is heavily influenced by the piezoresistive effects created by heating. The strain gauge response does eventually settle to a constant when the temperature is constant and the piezoresistive effects have annealed away. Note the drop in strain gauge output voltage for the final heating period, as predicted previously, due to the rapid increase in piezoresistive effects from an increase in residual film stress.

Another meaningful observation is the difference in output voltage scale for both of these instruments, with the RTD measurement having an output of approximately 1,420 mV at the end of the simulation, with the strain gauge response being only just above 1.0 mV. This difference contributes to the functional application of each of these instruments in the combined circuit, which was explored in the previous section when discussing the error and measurement correction algorithms used for operation of the instrument.

The coupling of the strain gauge and RTD circuits also creates a feedback mechanism due to the strain gauge excitation voltage being directly affected by the temperature of the instrument. This effectively increases the applied voltage to the strain gauge circuit as the instrument temperature rises. This non-uniformity isn't a problem, as this simply increases the magnitude of the strain response at higher temperatures compared to low temperatures, and would also be reflected in the initial calibration curve used to determine the coupling of the two instruments, but will cause the response to differ from the theoretical operation of a stand-alone strain gauge operating at a constant excitation voltage.

As depicted in Figure 5-23, the result of the piezoresistive response on the RTD measurement of the total resistance of the instrument is an increase in resistance due to

thermal stress in the instrument trace that will create some amount of measurement error until that stress is annealed away. Note that the RTD measurement reflects an increased temperature due to this effect, with the measured resistance converging with the zero-thermal-stress, or 'ground state', measurement as the film stress is reduced by holding the instrument at a constant temperature. This difference between the ground state measurement and the actual measurement is described as the temporal error and is proportional to the residual film stress in the instrument trace.

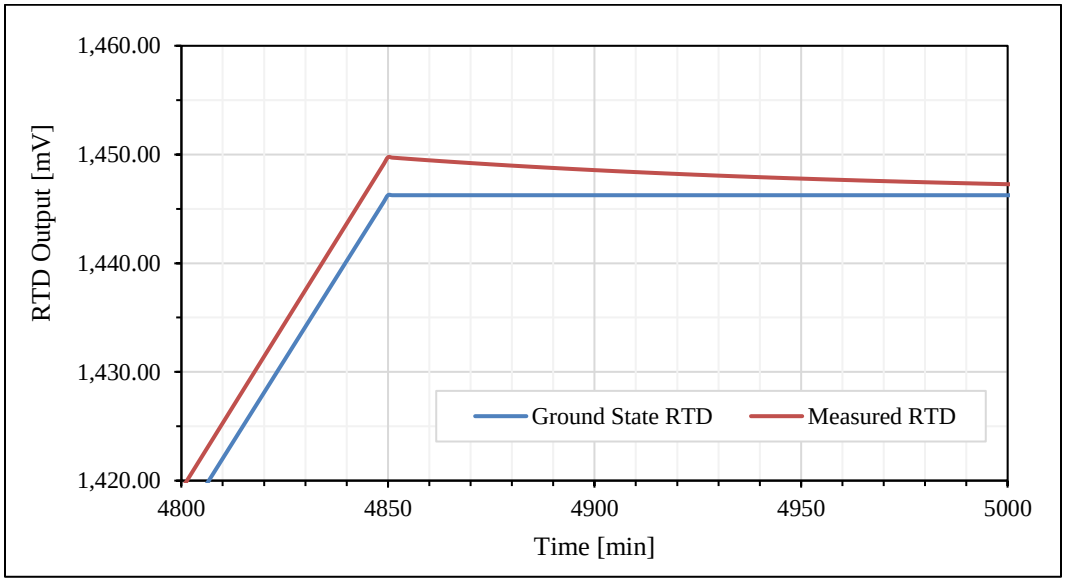

Figure 5-23: Ground state and measured RTD voltage output variance over time

A key challenge in the functional operation of the proposed HERTEL sensor is the estimation of this temporal error. If the temporal error can be verified as being near zero, then the strain measurement can be used as a temperature reference to adjust the RTD measurement and account for the addition of impurities or any other mechanism of instrument degradation that would increase the measurement resistance independent of temperature and thus cause the RTD calibration curve to drift. The challenge of using RTD instruments in harsh environments is that you don't know if this drift has occurred or how large the effect is. The only way to know these things is to compare RTD measurement to another independent temperature measurement and determine the offset.

When the instrument is deployed, the only data that is available for estimating the temporal error is the strain gauge voltage output and the RTD voltage output. If the absolute value of the percent rate of change of these two instruments is compared, the result is a reasonable estimation of the temporal error, which is fundamentally a function of the difference in the rate of change of the strain gauge compared to the rate of change of the RTD.

The difference between the estimated temporal error and the real temporal error for the example thermal exposure profile is depicted in Figure 5-24. Note that the estimate differs significantly from the real error when heating, but is relatively accurate during annealing periods. When both measurements are stable for long periods, the temporal error can safely be assumed to be very low, and an offset can be calculated from the initial calibration of the instrument which relates the ground state strain measurement to the ground state RTD measurement across a wide temperature range.

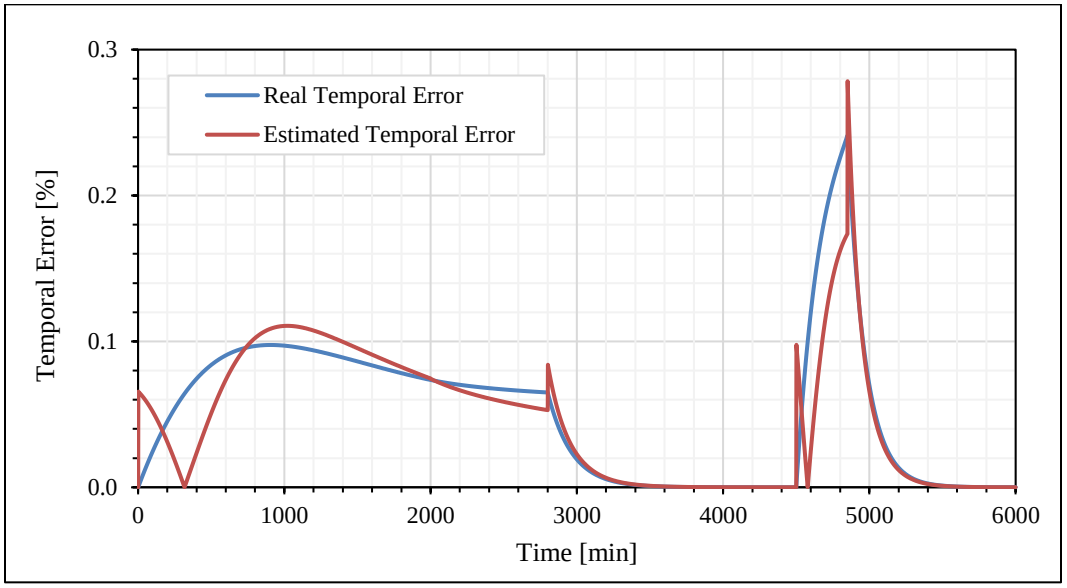

Figure 5-24: Real temporal error and estimated temporal error

Note that when the piezoresistive stress generation rate and the geometric stress generation rate are equal, this estimate function predicts zero temporal error, which is obviously not

accurate. This inaccuracy can be mitigated when using this estimate as a signal for generating a new offset if the signal is only generated when there are multiple estimates of zero temporal error in a short period, meaning the temporal error becomes very low and stays very low for a long period, which will only occur when the piezoresistive term has nearly completely decayed.

To test the functionality of the use of a ground state offset, a constant impurity term is added to the simulation, which simply adds some small amount of artificial resistance as a function of time. This term would be similar to the impurity generation rate for radiation exposure, for example, as it is not a function of temperature, but only of time. The RTD output with and without this impurity term is depicted in Figure 5-25. The overall effect of the impurity is not distinguishable from the normal output of the RTD at this scale, but the error created in the measurement is roughly equivalent in magnitude to the temporal error.

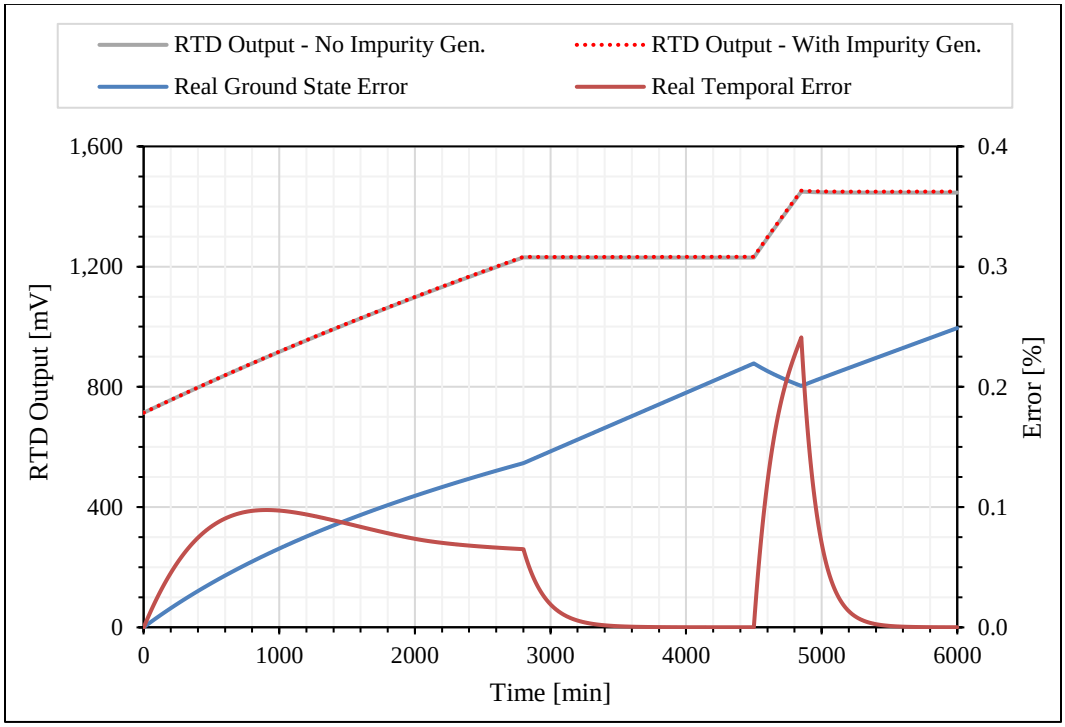

Figure 5-25: Effects of an additional impurity term on RTD output

Applying the previously described algorithm for generation of a ground state offset when the temporal error is very low, below 0.01% for three consecutive periods, the estimated ground state error can be compared to the real ground state error caused by the impurity to determine the ability of the HERTEL sensor to detect and offset calibration drift. The simulated performance is depicted in Figure 5-26.

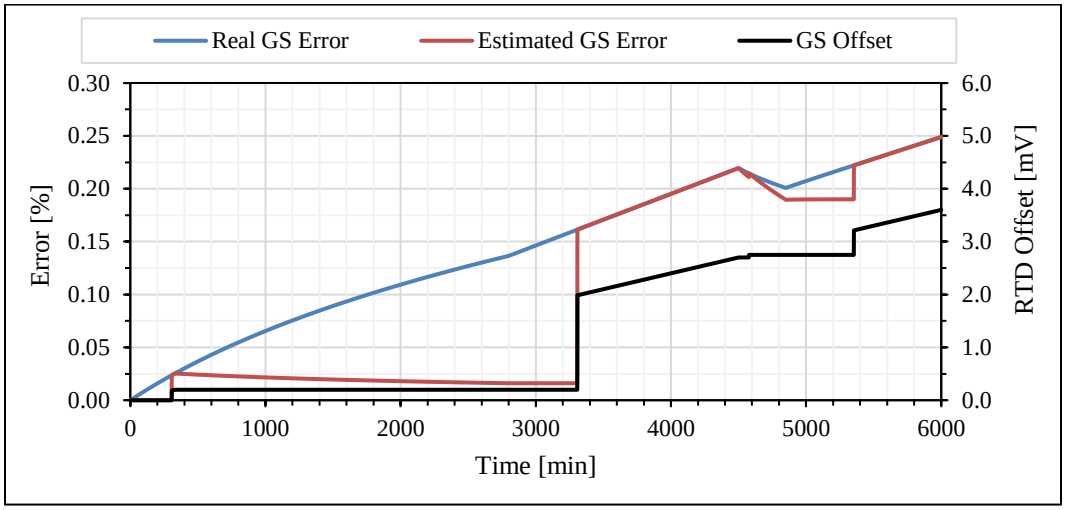

Figure 5-26: Real and estimated ground state error, with the generated ground state offset

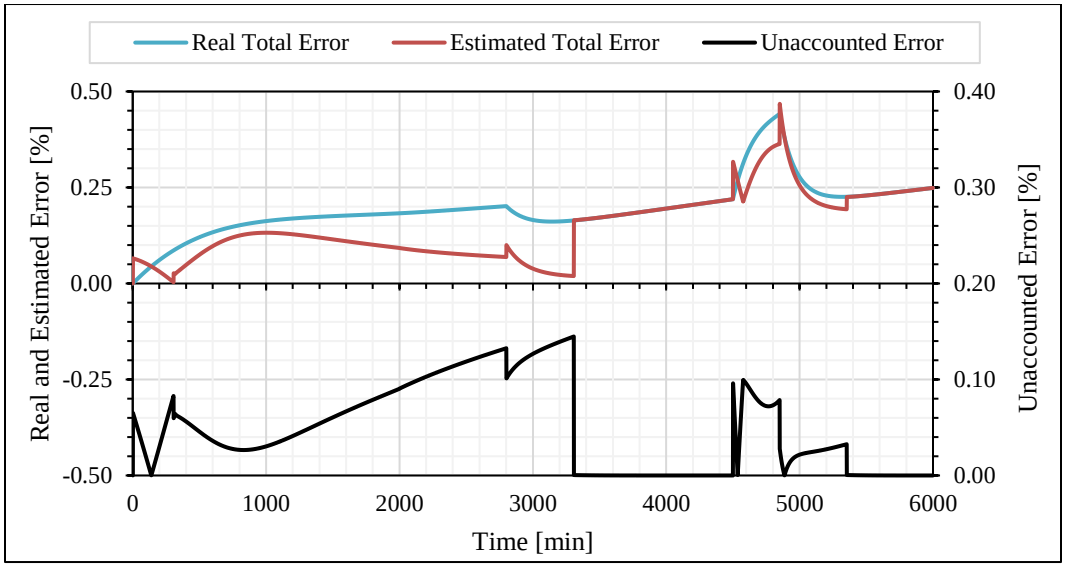

Figure 5-27: Comparison of real and estimated total error and determination of unaccounted error

To determine the overall performance of the HERTEL sensor, it is useful to compare the estimated total error and the real total error. Note that the estimated total error is only a function of what can be measured while the sensor is operating, the RTD and strain gauge voltage outputs, while the real error can be calculated from the physics of the simulation and accurately reflects the difference between measurement and the true physical state. Figure 5-27 depicts the real and estimated total error, which is the sum of temporal and ground state error, for the thermal exposure profile selected.

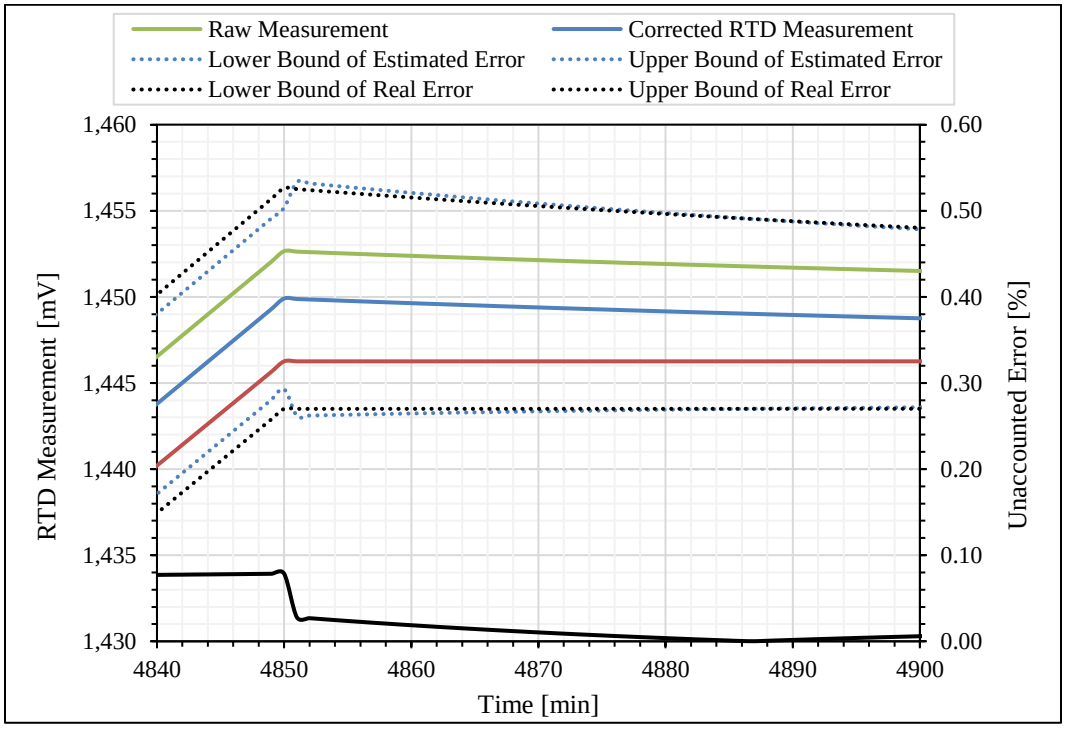

Figure 5-28: Effect of unaccounted error on error bounds for corrected measurements

The unaccounted error is a measurement of the difference between the real and estimated error of the HERTEL sensor and reflects the accuracy the error estimation algorithm. Note that the unaccounted error grows over long heating periods, because a new ground state offset cannot be calculated if the film stress and temporal error remains high. Once the temperature is stable, the unaccounted error drops to nearly zero, as a new ground state offset can continuously be calculated to account for the constant addition of impurities.

A closer inspection of the effects of this unaccounted error is depicted in Figure 5-28, which illustrates the variation in error bounds as the magnitude of unaccounted error changes over time. The raw measurement depicted is the measurement taken straight from the RTD voltage tap and reflects the additional resistance caused by impurities. The corrected measurement reflects the addition of the ground state offset, which mitigates a portion of the impurity resistance, but is still affected by the temporal error generated by the piezoresistive effects of differential thermal expansion. The ground state measurement is the true response of the instrument without temporal or ground state error.

Note the change in the error bounds placed on the corrected measurement as the unaccounted error drops to zero. The real error and estimated error converge as the unaccounted error is reduced. The true measurement is also within these bounds at all times, even when the unaccounted error is relatively high, indicating that the error estimation and correction algorithm is effective, at least for the conditions selected for instrument simulation.

The overall conclusions that can be drawn from this simulation is that the device can effectively maintain accurate operation in harsh conditions, even if the addition of an impurity is simulated. The RTD measurement provides a precise measure of the environmental temperature and the strain gauge measurement acts as a very accurate measure of the effects of temporal error and instrument drift. The ability of the differential strain gauge measurement to mitigate any effect which uniformly offsets the resistance of the device, such as temperature or impurity migration, means that comparing the measurements of both devices allows for the RTD to detect the onset and magnitude of drift mechanisms and correct for them, provided the instrument can operate at a stable temperature for long periods of time.

5.5 Determination of Design Parameter Sensitivity

The question of how much to vary design parameters to achieve a desired sensitivity is difficult to answer. The required variation can be estimated by utilizing the models described in the previous sections and targeting a range of performance, then varying the initial input parameters to determine the overall effect on the final instrument performance. This variation of error rate per percent change in the design variable is defined as the design sensitivity for that variable.

Due to the limited scope of this investigation, as well as the degree of uncertainty associated with predicting the material response to variation of temperature and thermal stress, it would not be beneficial to conduct a detailed investigation of design parameter sensitivity unless the initial results can be experimentally verified. Once the degree of precision in simulation is known, then a meaningful optimization of performance can be assessed through the determination of design parameter sensitivity.

As it stands, the presented device simulation is useful as a qualitative, theoretical assessment and verification of device performance, but lacks the precision and certainty to be useful as a quantitative tool for design optimization. Thus, this topic is outside the scope of this narrow theoretical investigation, as experimental verification and validation are similarly outside the scope. The tools and methods are developed and presented; they can be best utilized once experimental results provide a basic measure of simulation fidelity.

6 Evaluation of Functional Applicability

In this chapter, the functional applicability of the proposed hybrid-electrical-resistance-thermal (HERTEL) sensor is evaluated by applying the algorithm developed for performance analysis to the intended application of temperature measurement in HTGR core thermal environments to determine if meaningful improvements over contemporary instrumentation systems can be realized. If the HERTEL sensor demonstrates significantly improved accuracy, precision, durability, or flexibility in implementation, then the functional applicability will be confirmed and continued development of the proposed instrument system for the targeted application is warranted.

The process of demonstrating the described metrics begins with determining exact degree of performance which indicates an improvement over contemporary thermal instrumentation systems for pebble bed HTGR installations. The performance of a single HERTEL sensor is then compared to the performance of a single contemporary instrument, with the previously selected performance metrics being the primary determination of functional applicability.

6.1 Metrics for Evaluation of Functional Applicability

In this section, the design performance goals established in Chapter 4 are reviewed and compared to the expected performance of the thermal instrumentation utilized in the HTR-10 and HTR-PM process monitoring systems for the thermal exposure expected for deployment in the core region of the HTR-PM under steady state operating conditions.

The initial design goals were described as being primarily focused on measurement accuracy being equivalent or better than that which is established as the standard for K-type, class 1E thermocouples. These thermocouples have an expected accuracy of ± 1.5 °C or ± 0.4% of measured temperature, whichever is greater. Other goals included a response time of approximately 0.5 seconds and a durability which would enable the instrument to operate through a single pass of the reactor fuel circulation system.

Due to the extended time scales of the physical phenomena driving the operation of the HERTEL sensor, meeting the response time goal is not a straightforward determination. If a literal interpretation of response time is chosen, the goal may be possible to meet for steady state measurements if a measurement frequency of 2.0 Hz is used. Coupling this target with the error reduction strategy for alternating DC measurement cycles presented in the previous chapter, the 2.0 Hz measurement could be utilized as the fastest cycle of the three required measurements. Thus, the measurement cycle would be 5.0 mA excitation current for 2 seconds, 10.0 mA excitation current for 0.5 seconds, and 5.0 mA excitation current for 2 seconds. This sequence should result in the elimination of joule heating error and theoretically meeting the response time goal of 0.5 seconds.

However, this is a superficial interpretation of the response time, as it is commonly defined as measuring a given step-change in temperature of the surrounding environment within the specified time. While this might be possible, it would result in significant measurement error, as this is not the intended deployment operation mode. Thus, this goal can only be met, at best, superficially. The other two criteria, measurement accuracy and instrument durability, can be investigated more thoroughly.

In addition to this, a key advantage of the HERTEL sensor is the flexibility of deployment configuration. The sensor package is design to be a modular component which is compatible with passive sensing methods for eventual application of a wireless signal transmission deployment configuration. This will not be considered for evaluation of functional applicability specifically, as it is only a possible extension of the work presented here, rather than an immediately available capability.

6.2 Performance Comparison for HTR-PM Deployment

Determination of applicability is performed via comparison of instrument response in the target environment. Thus, two separate simulation frameworks are proposed. The performance of a K-type thermocouple is assumed to be a function of the accuracy bounds

established by the manufacturer for operation in the target environment and is directly evaluated using the provided parameters and thermal exposure model for the HTR-PM. The performance of the HERTEL sensor is simulated using the framework described in the previous chapter, with the HTR-PM thermal exposure model as the driving input.

6.2.1 HTR-PM Environmental Model

The environmental exposure model developed in Chapter 3, depicted in Figure 6-1, is used to evaluate instrument performance. The model provides thermal exposure profiles for fuel pebbles loaded at two specific locations, one at the core centerline and the other located 140 cm from the centerline, hear the periphery of the core. Note the time scale, as the expected traversal time is over 1000 days per the HTR-PM design specifications. These two thermal exposure profiles effectively illustrate the full range of expected thermal exposure, as all other radial locations would have an exposure profile bounded by these selected profiles.

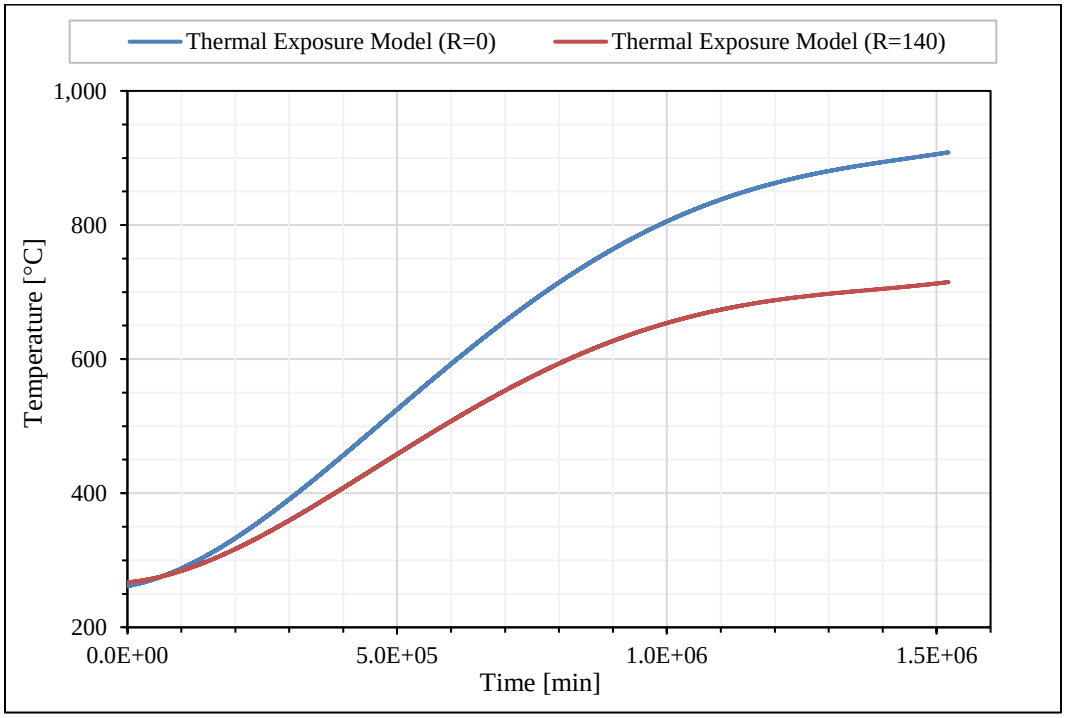

Figure 6-1: HTR-PM thermal exposure model for a single pebble fuel cycle

6.2.2 Simulation of Contemporary Instrument Performance

Application of the accuracy specifications for the class 1E, K-type thermocouple is relatively straightforward for the thermal exposure profiles provided. The true temperature, with upper and lower error bounds, is depicted in Figure 6-2 and Figure 6-3, which represent low and high temperature performance. At the low temperature, the standard error bound of ± 1.5 °C is used, while at the high temperature, the error bound of 0.4% of measured temperature is used.

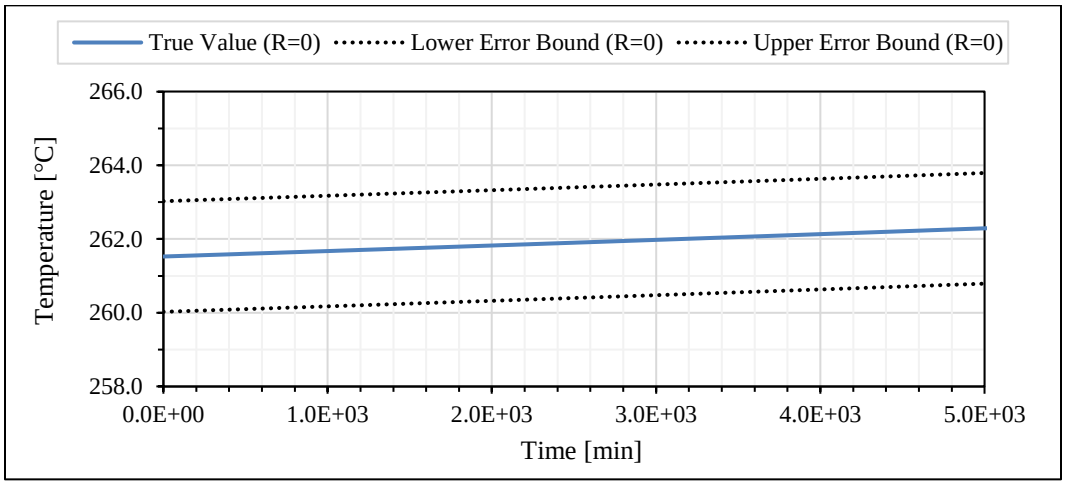

Figure 6-2: Thermocouple performance at low temperatures

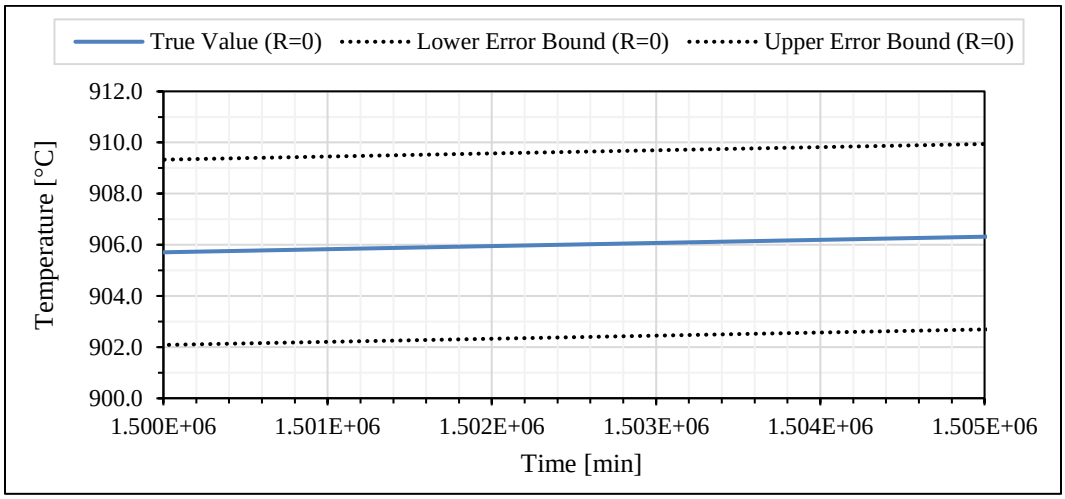

Figure 6-3: Thermocouple performance at high temperatures

6.2.3 Simulation of HERTEL Sensor Performance

Simulation of the performance of the HERTEL sensor is similar to the process used in the previous chapter. The thermal exposure model depicted in Figure 6-1 is used as the driving condition, with the resulting thermal stress generation and annealing rates depicted in Figure 6-4 and Figure 6-5, respectively.

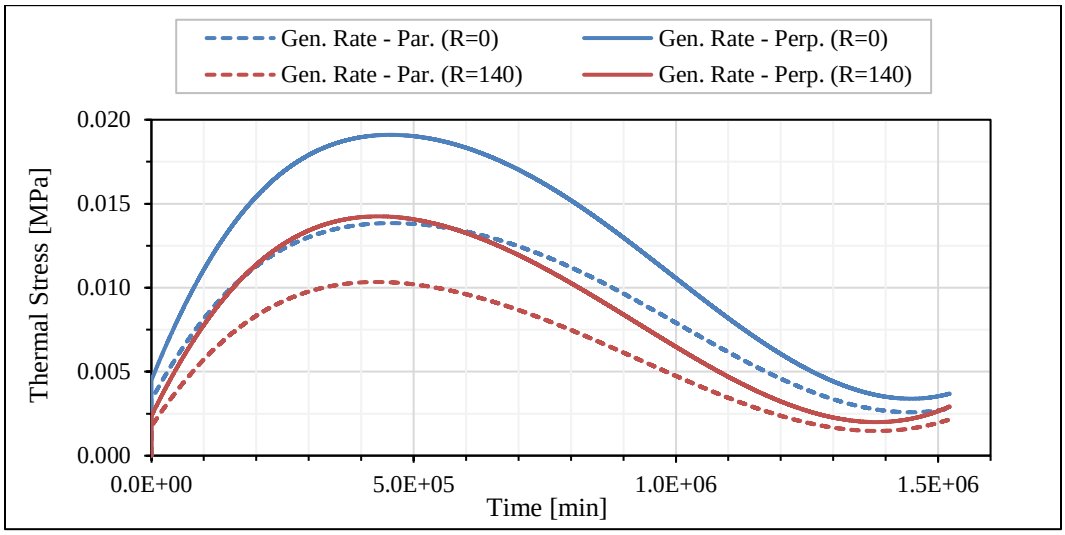

Figure 6-4: Thermal stress generation rate of the HERTEL sensor

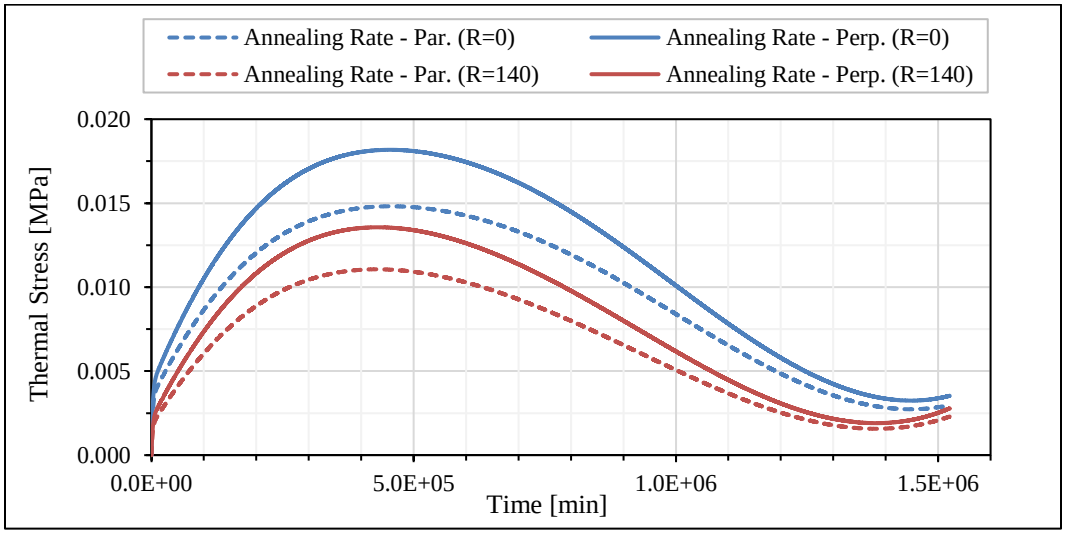

Figure 6-5: Thermal stress annealing rate of the HERTEL sensor

Close inspection of the thermal stress generation and annealing rates indicates that the two rates vary in similar ways. The maximum stress generation and annealing rate are achieved near the time of transition of the thermal exposure profile into a linear heating rate. After this point, both the stress generation and annealing rate decline as the temperature increases, with a slight increase near the end of the thermal exposure profile.

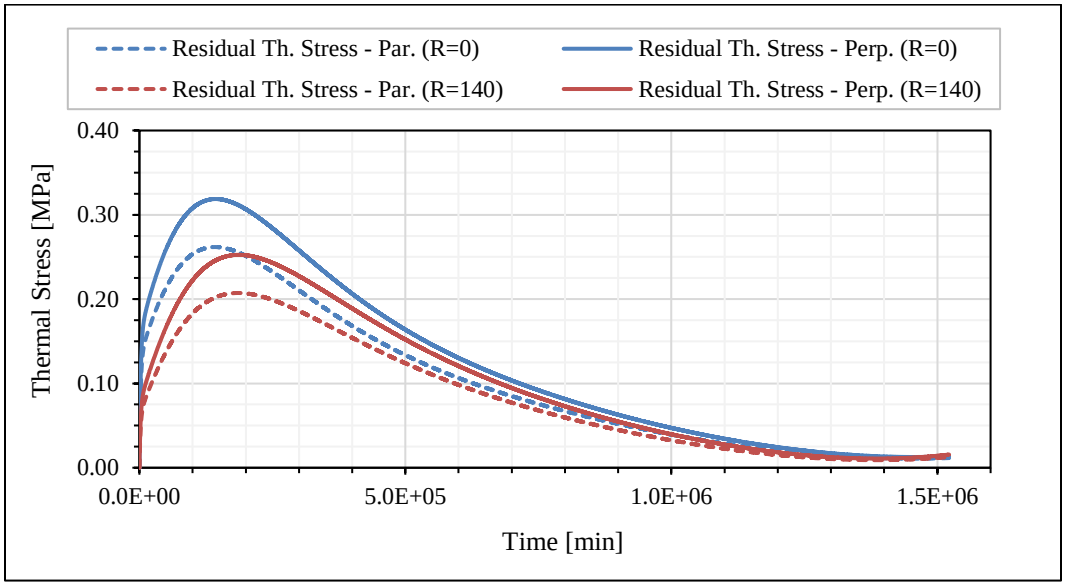

Figure 6-6: Residual film stress of the HERTEL sensor

As expected from the decline in thermal stress generation and annealing rates, the residual thermal stress in the instrument trace, depicted in Figure 6-6, peaks relatively early in the thermal exposure profile and then recedes via a decay relation. The early peak is likely primarily a result of the low temperature early in the exposure profile, which prohibits the annealing rate from proportionally increasing to match the stress generation rate. Thus, the residual thermal stress increases until the annealing rate reaches equilibrium and eventually overtakes the stress generation rate, slowly driving down the residual thermal stress with increasing temperature.

The response of the piezoresistive and geometric strain are depicted in Figure 6-7, with the piezoresistive response peaking at a similar time as the residual thermal stress and decaying

away to near zero as the temperature increases. The geometric response increases proportionally to the temperature increase for both the centerline and periphery locations.

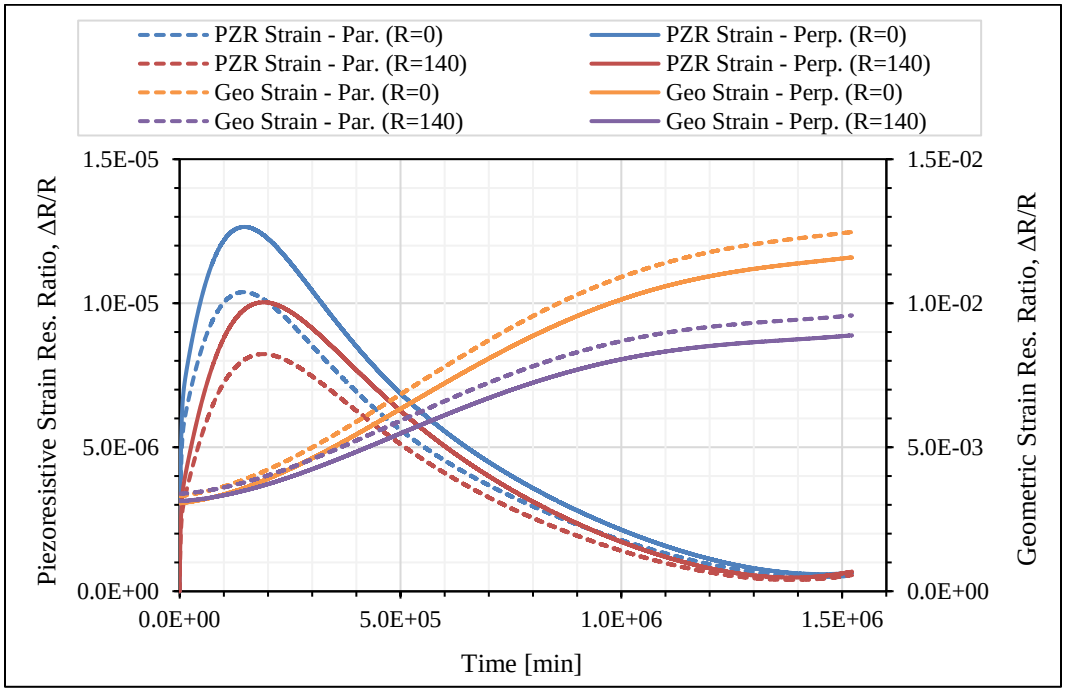

Figure 6-7: Piezoresistive and geometric strain response of the HERTEL sensor

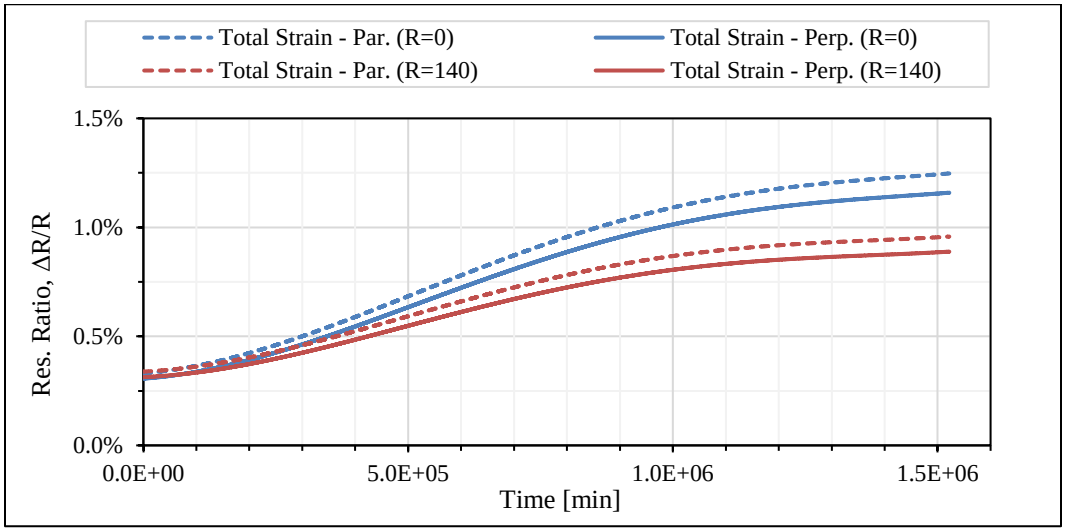

Figure 6-8: Total strain response of the HERTEL sensor

The piezoresistive and geometric strain response are combined to get the total strain response, depicted in Figure 6-8. The result of combination is a relative flattening of the response curve, as the piezoresistive portion of the response dominates at low temperatures and the geometric response dominates at high temperatures.

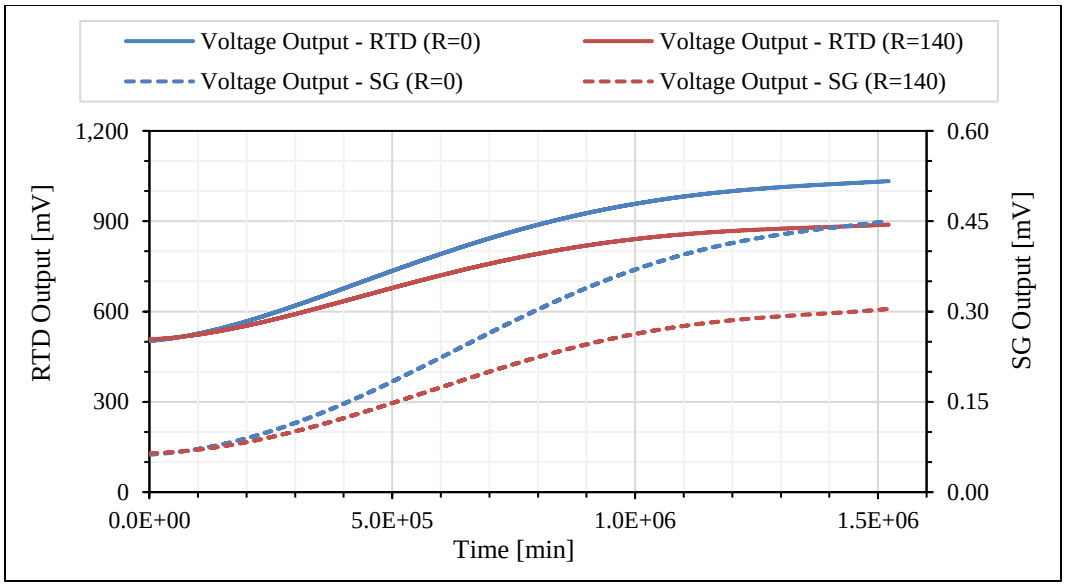

Figure 6-9: RTD and strain gauge voltage output of the HERTEL sensor

If an assumed 10.0 mA constant excitation current is applied to the instrument, the estimated voltage measurement at the RTD and strain gauge voltage taps is depicted in Figure 6-9. These response curves are generally proportional to the temperature increase depicted in the thermal exposure profile, as is expected from previous simulations.

The impact of temporal error variation on the RTD voltage measurement is depicted in Figure 6-10 and Figure 6-11, for high and low temperatures respectively. Temporal error results in a temperature measurement error of 0.00125 °C at the point of lowest piezoresistive impact and 0.004 °C at the point of highest piezoresistive impact. This aligns well with the depiction of real and estimated temporal error in Figure 6-12, which reaches a maximum of 7.54E-06 or 0.000754% at 147,420 minutes and 307.25 °C and a minimum of 3.53E-07 or 0.0000353% at 1,451,760 minutes and 900.15 degrees.

As is expected, the temporal error is highest at low temperatures and decays as the temperature increases. Note that the error estimation calculation, which is simply the absolute value of difference in slope of the strain gauge and RTD measurements, consistently predicts an error of approximately 10 times larger than the real error. This conservative estimate can be further refined by the addition of a multiplication constant, which would be derived specifically for the expected thermal exposure expected. In this case, this was not included.

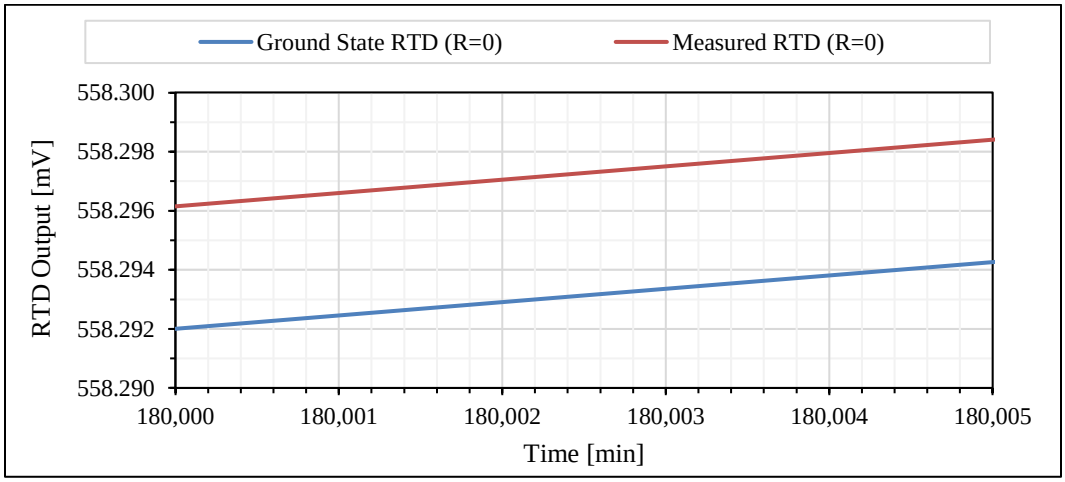

Figure 6-10: Measured and ground state RTD output with high temporal error

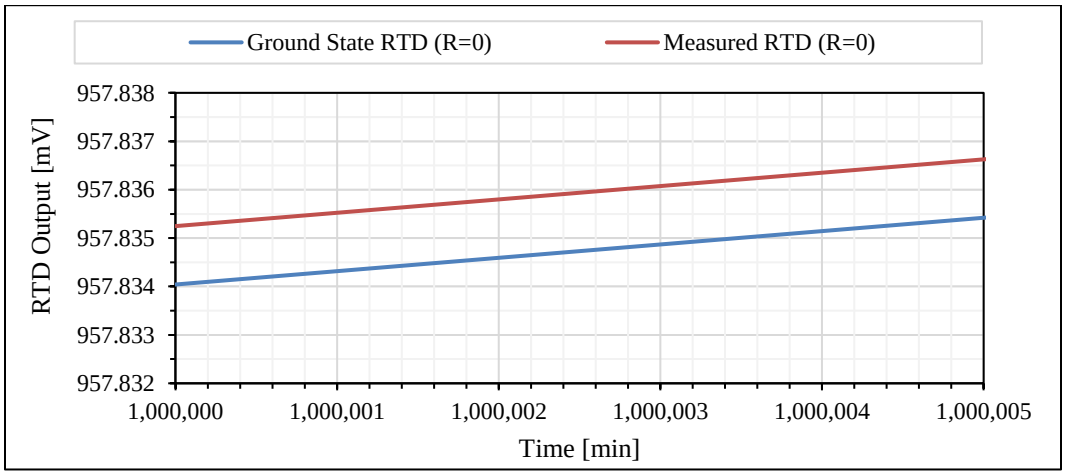

Figure 6-11: Measured and ground state RTD output with low temporal error

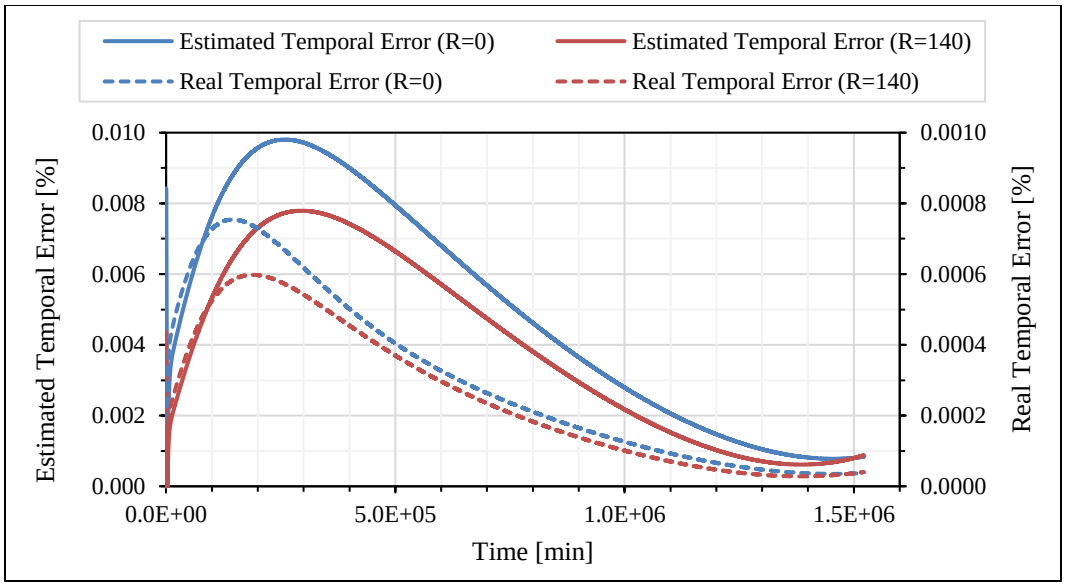

Figure 6-12: Real and estimated temporal error of the HERTEL sensor

The impact of impurity generation on the RTD voltage measurement is depicted for the two selected radial locations in Figure 6-13. The larger impact of impurity generation on the periphery location, as depicted by the larger ground state error, is a result of the same constant resistance being added for both locations. This ultimately amounts to a larger impact on the periphery location because it accounts for a larger percent of the total resistance of the instrument, which is lower due to the reduced temperature of the outer periphery compared to the core centerline.

The real and estimated ground state error arising from the detection and correction of ground state calibration drift is depicted in Figure 6-14, with good performance of the ground state correction algorithm indicated. This algorithm was adjusted from the previous simulation, as the estimate of temporal error was slightly different, being the difference of the slopes of the RTD and strain gauge measurements rather than the sum, and required only a single error estimation to be below 0.1%, rather than the three consecutive measurements threshold imposed on the previous simulation to reduce unintentional ground state offset calculations.

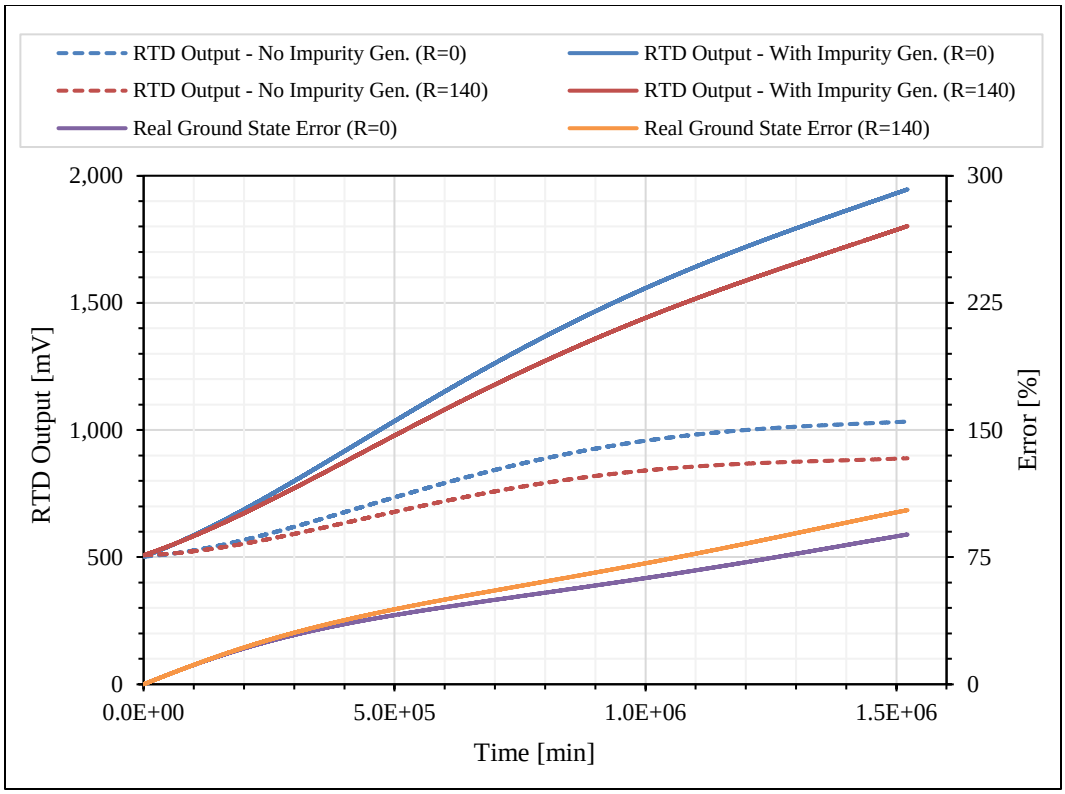

Figure 6-13: The effects of impurity generation on instrument output for the HERTEL sensor

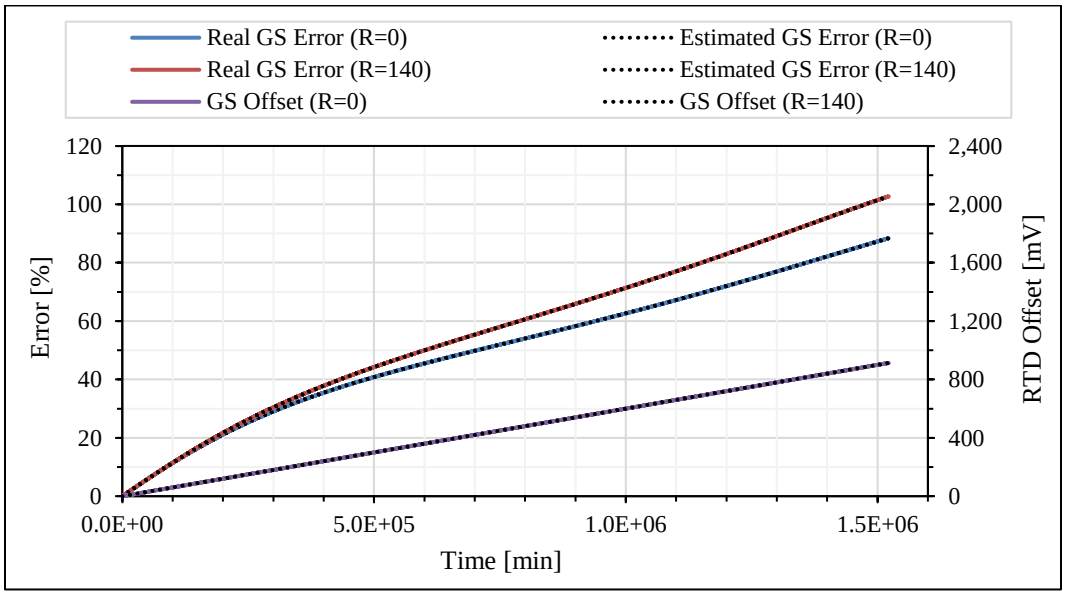

Figure 6-14: Real and estimated ground state error of the HERTEL sensor

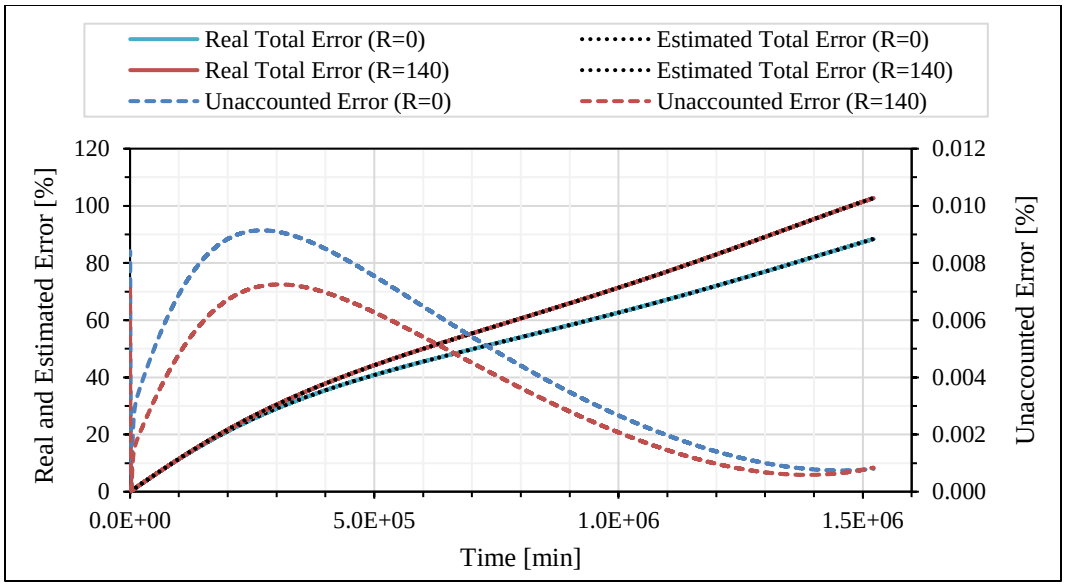

Figure 6-15: Real and estimated total error of the HERTEL sensor

The final indicator of HERTEL sensor performance is the real and estimated total error, depicted in Figure 6-15. The estimated total error is well aligned with the real total error, with a maximum unaccounted error of approximately 0.00914% for the centerline location at approximately 372.2 °C. This is almost entirely due to the overestimation of temporal error at low temperatures, with the ground state error contribution being minimized due to the temporal error remaining under the threshold of 0.01%, resulting in near constant calculation and application of a ground state correction offset. This overestimation of the temporal error could be reduced by the inclusion of a thermal-exposure-profile-specific scaling constant term to the error calculation, which was not included in this case.

6.3 Determination of Functional Applicability

At low temperatures, early in the specified thermal exposure profile, the thermocouple performance was predicted by the manufacturer's specification, with a variance of ± 1.5 °C of the measured value. At high temperatures, late in the thermal exposure profile, the thermocouple measurement variance becomes ± 0.4% of the measured value. The temperature at which these error estimations are equal is 375 °C.

At low temperatures, early in the thermal exposure profile, the HERTEL sensor has a relatively high amount of temporal error due to a low thermal annealing rate at low temperatures and a high amount of generated thermal stress from differential thermal expansion of the constituent materials. This results in the highest error of 9.14E-5 or 0.00914% occurring at around 372.2 °C if the unaccounted error is used, which is much higher than the maximum real temporal error of 7.54E-6 or 0.000754% which occurs at a temperature of 307.25 °C.

The total error of the measurement is not used in this case because the selection of impurity generation is arbitrary for this simulation. The ability of the HERTEL sensor to correct for the impact of impurity generation could be considered to be qualitatively validated, but not quantitatively validated, as the selection of total error for the comparison would be meaningless. In addition, the impact of impurity generation in the thermocouple is not characterized, and an equivalent comparison would require at least a basic characterization.

If functional applicability is determined by instrument accuracy alone, the HERTEL sensor has a theoretical maximum error range which is 500 times smaller than a class 1E, K-type thermocouple. This accuracy is not as high as a HTSPRT sensor, which has a maximum error of approximately half of the theoretical maximum error of the HERTEL sensor when used outside of a laboratory setting, but this performance metric for the HERTEL sensor is a significant improvement over contemporary thermal instrumentation for HTGR systems.

The theoretical durability of the HERTEL sensor is demonstrated in the ability to actively correct for impurity generation while in service. This capability is obviously not available for standard K-type thermocouples. In addition, if the stainless steel or Inconel sheath of the thermocouple is compared to the sapphire substrate which protects the HERTEL sensor, it is assumed that the HERTEL sensor would exhibit greatly improved durability as well.

Considering the increased accuracy and durability of the HERTEL sensor, it is clear that the instrument has a confirmed functional applicability for HTGR thermal systems.

7 Project Results, Conclusions, and Future Work

In this final chapter, the results of development efforts for the proposed **H**ybrid-**E**lectrical-**R**esistance-**T**h**E**rma**L** (HERTEL) sensor are presented in the form of an instrument design summary, including simplified drawings and a table of final design parameters, a summary of results of initial instrument performance simulation with integrated steady state and temporal operating conditions, a summary of applicability evaluation analysis, and a short summary of practical and philosophical conclusions drawn regarding insights from the overall instrument development project.

7.1 Instrument Design Summary

In this section, the instrument design process is summarized and presented in the form of a review of design motivations, a final design parameter table, a set of simplified engineering drawings of the instrument itself, and renders of the expected appearance of the final instrument in the proposed mounting configuration.

7.1.1 Instrument Design Basis

The process of instrument design began by investigation of the development status of HTGR systems, which have long been proposed as the ideal form of next generation reactor technology. A functionally unique HTGR design, the pebble bed variant of the core configuration, is identified as having a range of desirable characteristics as well as significant challenges for instrumentation, due to the dynamic structure of the core. The challenge of deploying thermal instrumentation in the harsh environment presented by HTGR systems is difficult, but adding the additional challenges of the pebble bed core configuration creates a situation where a novel approach is required.

Investigation of advanced instrumentation development at national labs and leading reactor testing sites shaped the general approach of utilizing a dual measurement system which is capable of detecting and correcting measurement drift. MEMS instrumentation was selected as the basis of development due to a range of favorable characteristics which

support high-density deployment configurations which require very little power to operate. MEMS fabrication processes produce extremely precise material and geometry parameters, can be scaled to high volume production very easily, and enable a class of physical operation which is simply not possible to realize with traditional manufacturing techniques.

The next component of the design basis utilized for instrument development was the selection of a target environment for operation. The Chinese HTR-PM demonstration plant was chosen due to it being the most advanced pebble bed reactor system being actively developed and constructed, with first criticality scheduled to occur in the next several years. Thermal hydraulic simulations utilized by the reactor developers were adapted and extended to create a three-dimensional temperature map of the steady state core during normal operation. Pebble migration studies were also analyzed to determine what thermal exposure is expected for a single fuel pebble as it traverses the reactor core via the fuel recirculation system. This thermal exposure model was then used as a thermal environment basis or reference for instrument design and evaluation of functional applicability.

Instrument design was fundamentally a process of selecting a system of materials which could effectively work together to provide stable, accurate operation in the thermal environment specified. RTD and strain gauge sensors were selected as the functional basis because they share similar operating characteristics, but measure electron mobility via fundamentally different mechanisms that can both be correlated to environmental temperature. The coupling of these two instruments into one integrated device, as presented, is novel and uniquely suited to both MEMS fabrication processes and the thermal processes which are targeted for HTGR thermal instrumentation.

The coupling of these two instruments is enabled by the unique characteristics of the constituent materials. Sapphire provides a very durable and stable foundation which also happens to exhibit an axially dependent coefficient of thermal expansion. Platinum provides a very chemically-stable thin film sensing material that provides linear response

across a wide temperature range and has a deep history of characterization literature and validation for prior use in both RTD and strain gauge measurement.

The final portion of the design process, the selection of instrument geometry, was shaped by investigation of platinum RTDs and strain gauges utilized by other similar industries as a starting point, then extending that design philosophy to couple the selected sensors and materials into one integrated device. The precise definition of geometry was relatively arbitrary, but necessary, in that it enables the operation of the device to be accurately simulated so that the functional applicability can be verified. The sensitivity of each design parameter can then be assessed and adjusted to produce a device that is targeted to deliver the best possible performance in the deployment configuration and environment selected.

7.1.2 Final Design Parameters

The final design parameters of the proposed HERTEL sensor are presented in Table 7-1.

Table 7-1: Final Instrument Design Parameters

Parameter	Unit	Value
Trace material / purity		Platinum (Pt) / 99.999% (5N)
Resistivity (TPW)	nΩ m	97.65
Film thickness	μm	4.0
Trace width	μm	40.0
Trace cross-sectional area	mm^2	1.6×10^{-4}
Trace length	mm	40.96
Resistance (TPW)	Ω	25.0
Axis parallel legs		18
Axial strain sensitivity ratio		5.54
Substrate material / purity		α-Alumina (Al_2O_3) / 99.999% (5N)
Substrate thickness	μm	725 ± 25
Crystal lattice orientation		A-Plane $(11\bar{2}0)$
Instrument package diameter	mm	10.0

7.1.3 Final Design Images and Drawings

Drawings reflecting the final selected design for the proposed HERTEL sensor are depicted in Figure 7-1, and Figure 7-2. Renders created from a CAD model used for instrument design are depicted in Figure 7-3 and Figure 7-5. Additional sensor engineering drawings and CAD model renders can be found in the appendix.

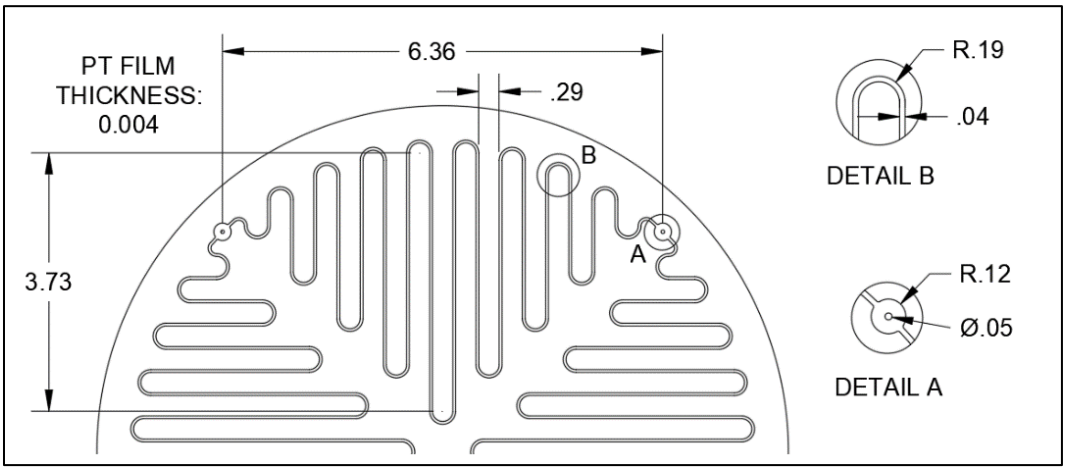

Figure 7-1: Final HERTEL sensor trace geometry (units: mm)

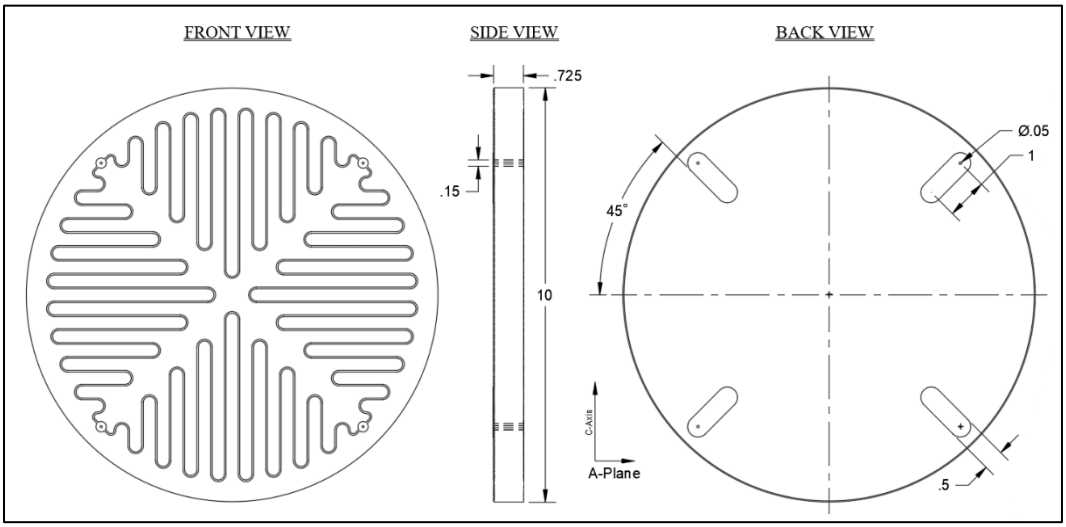

Figure 7-2: Final HERTEL sensor front, side, and back views (units: mm)

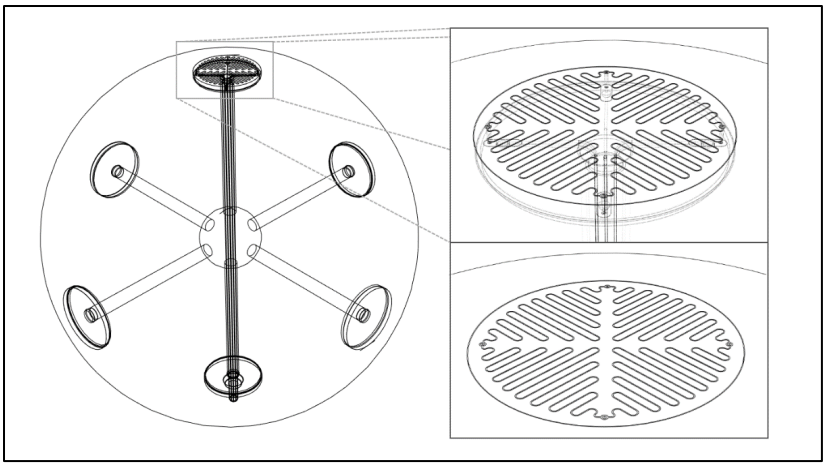

Figure 7-3: CAD model render of a single HERTEL sensor mounted on a fuel pebble

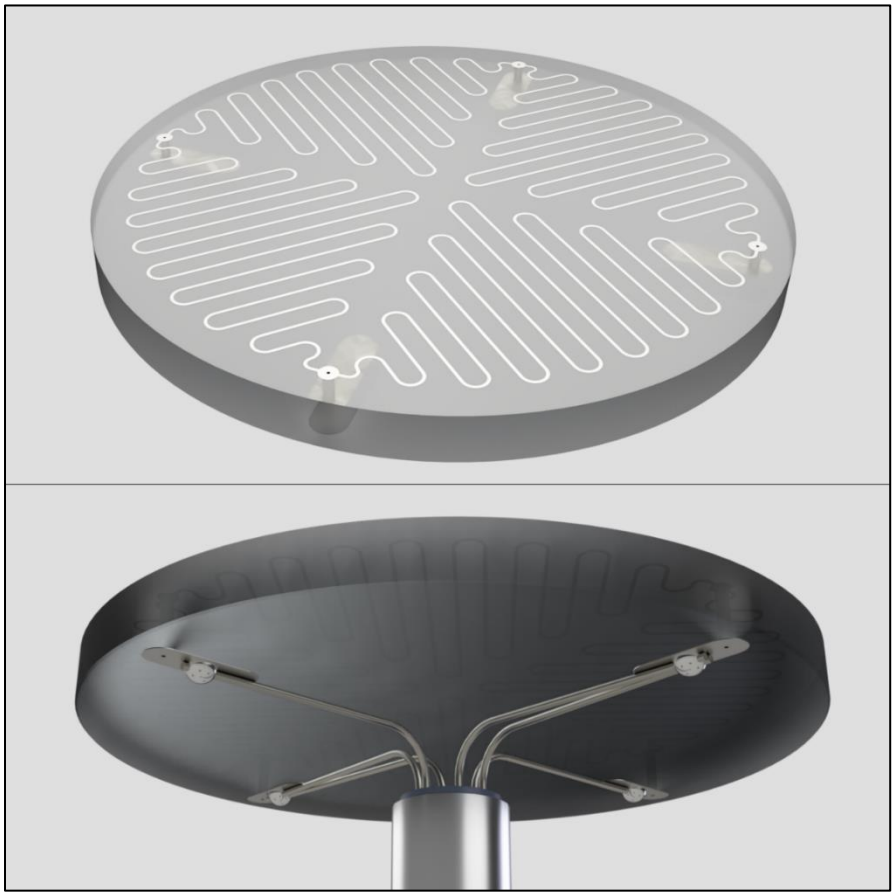

Figure 7-4: CAD model render of the proposed HERTEL sensor, top and bottom faces

7.2 Summary of Instrument Performance Analysis Results

Instrument performance was simulated under steady state and transient environmental conditions in Chapter 5, with the results summarized in the following sections. The fundamental operating premise is demonstrated in the linear response of the HERTEL sensor over a wide temperature range. The calibration drift mitigation capability of the HERTEL sensor is demonstrated in the results of integrated temporal and steady state performance analysis.

7.2.1 Steady State Performance Analysis

Steady state performance analysis predicts the voltage output depicted in Figure 7-5. Note that the RTD response is near linear across most of the operating temperature range and the strain gauge response is initially non-linear, but does transition into a linear response at high temperatures. Also note that the RTD response magnitude is approximately three orders of magnitude larger than the response magnitude of the strain gauge measurement.

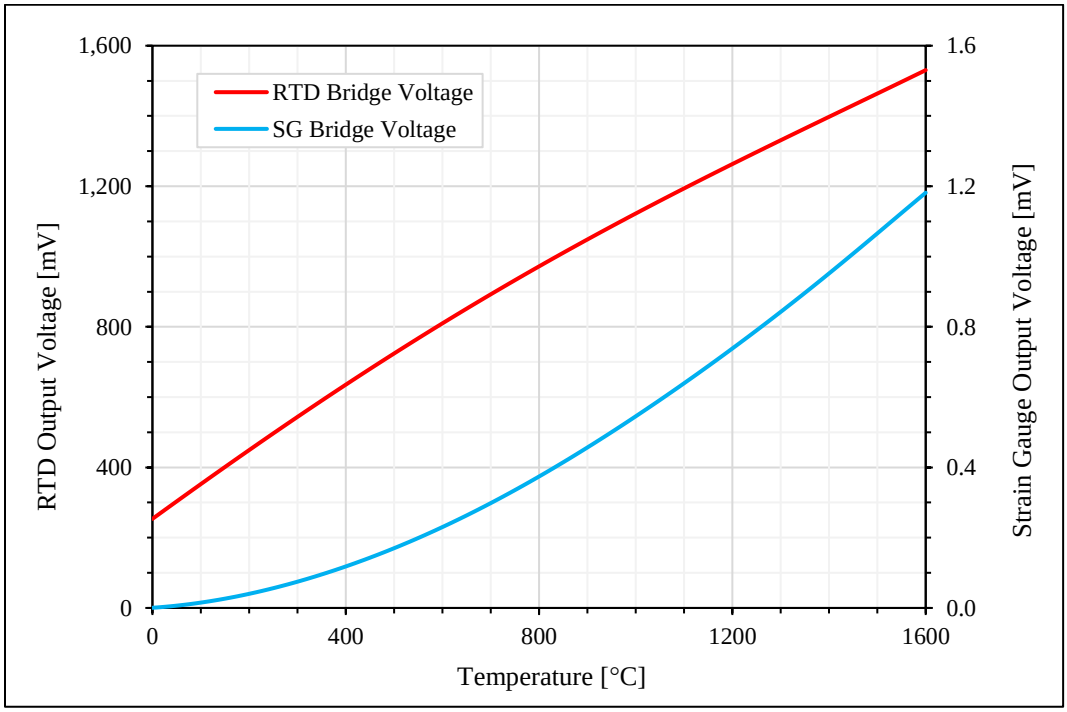

Figure 7-5: HERTEL sensor steady state performance with excitation current of 10.0 mA

7.2.2 Transient Performance Analysis

The performance of the HERTEL sensor was simulated for operation with the addition of transient material effects for a sample thermal exposure model, depicted in Figure 7-6, with instrument output depicted in Figure 7-7 and instrument error depicted in Figure 7-8.

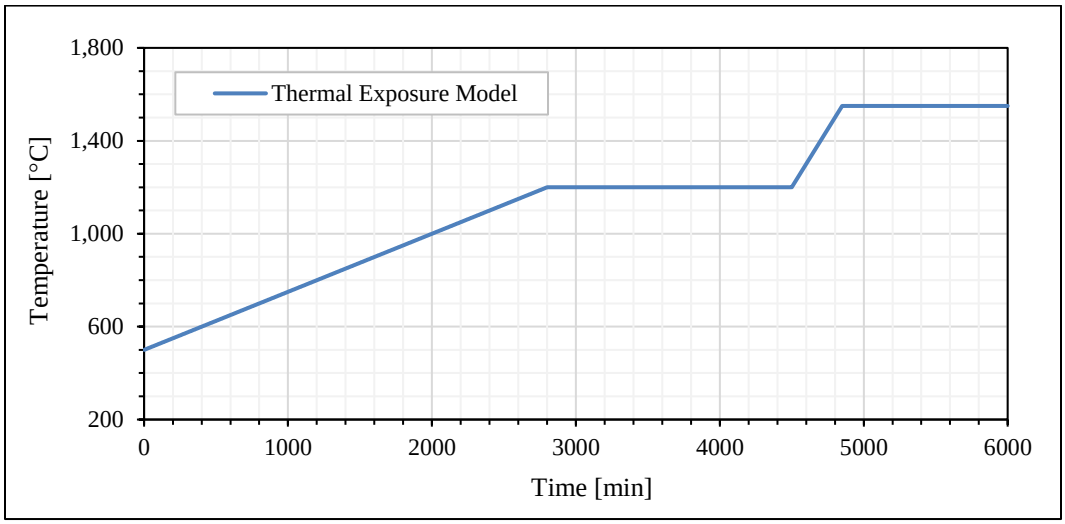

Figure 7-6: Simple transient thermal exposure model

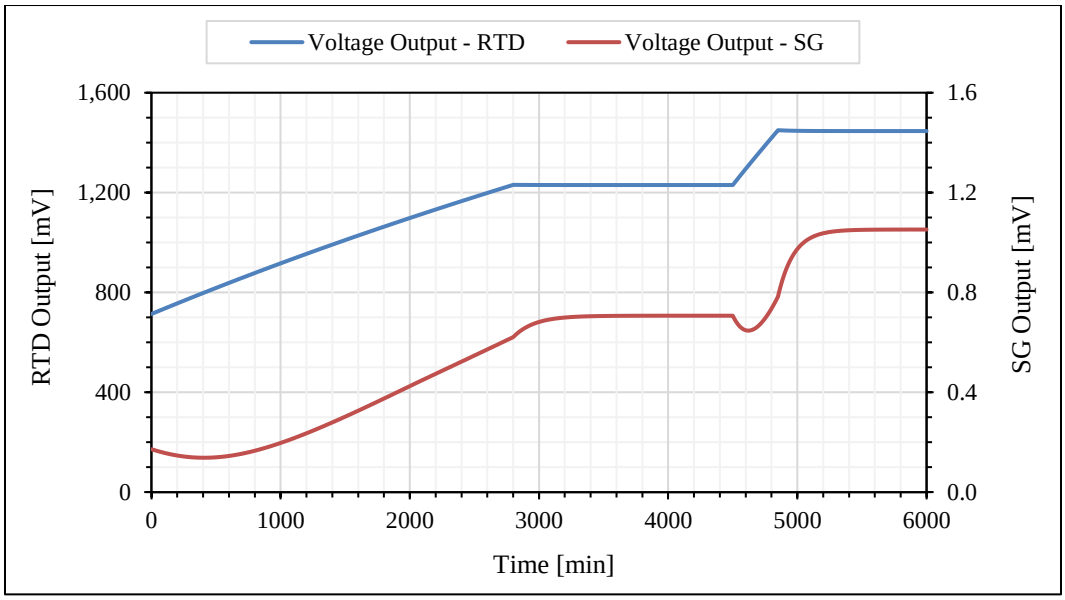

Figure 7-7: HERTEL sensor output for a transient thermal exposure profile

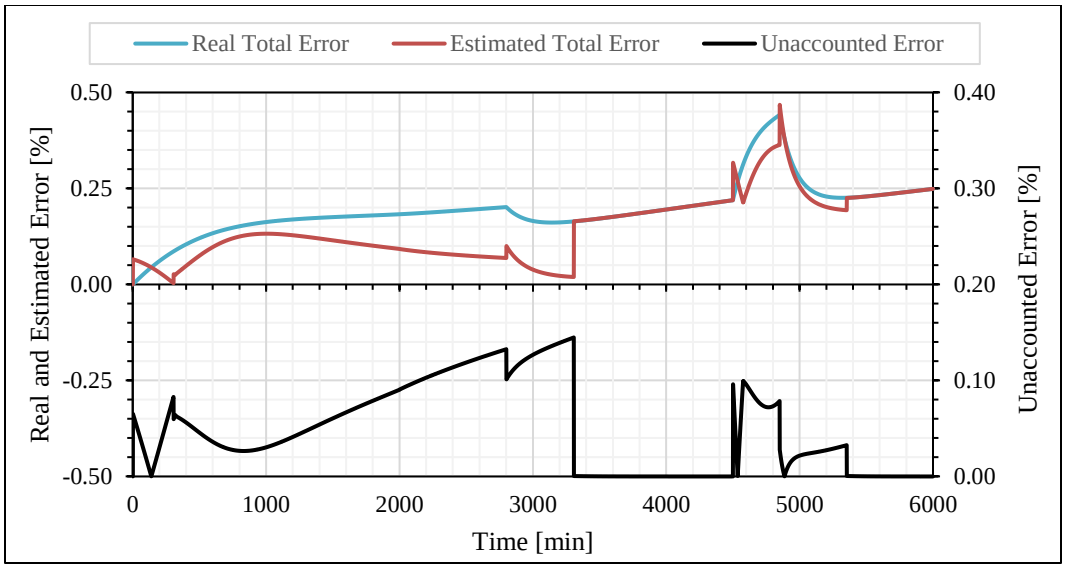

Figure 7-8: HERTEL sensor error estimation and real error comparison

Note that the transient simulation assumes an arbitrary rate of constant impurity generation in the sensor trace, which accounts for the nearly linear increase in error over time as the temperature of the thermal exposure input increases. The unaccounted error is a direct result of the algorithm used to estimate the magnitude of temporal error and trigger the calculation of a new ground state offset. In this case, a conservative estimate was used to prevent new ground state offsets from constantly being generated.

The steady state and transient models are also not directly comparable, because the simulation framework was refined and upgraded significantly in comparison to the fairly straightforward framework used for steady state simulation. See the supporting information in Chapter 5 for more information regarding the input parameters and differences in simulation algorithm for each case.

Overall, these results serve to theoretically validate the key operating mechanism of the HERTEL sensor; the ability to detect and mitigate mechanisms which ultimately result in calibration drift of the sensor in harsh environments. The results also make a key limitation of the device apparent, the requirement of long, stable periods for calibration correction.

7.3 Functional Applicability Evaluation Results

The functional applicability of the proposed HERTEL sensor was explored in an investigation of the performance improvements realized with the HERTEL sensor compared to contemporary HTGR thermal instrumentation at two radial locations in a pebble bed HTGR core thermal environment.

The HERTEL sensor demonstrated stable operation and significant improvement of theoretical measurement accuracy for a single sensor deployment configuration when compared to a K-type, class 1E thermocouple. The theoretical error range for the HERTEL sensor was up to 500 times smaller than the expected error range of a standard thermocouple in identical operating conditions. Utilizing a very simple algorithm for estimation of temporal error, a maximum of ± 0.00914% error was observed for the HERTEL sensor traversing the centerline thermal exposure profile of the HTR-PM. This is compared to the standard specification of ± 1.5% for a K-type, class 1E thermocouple, which is equivalent to the hardware which is proposed for deployment in the HTR-PM.

The HERTEL sensor sapphire substrate and capping layer should also have improved mechanical and chemical durability when compared to the stainless steel or Inconel sheathed thermocouples proposed for deployment in the HTR-PM. The response time of the HERTEL sensor was not determined to be an improvement over contemporary instrumentation; however, this is not a critical design parameter for the targeted deployment functionality. Due to the comparative advantages in both accuracy and durability, the HERTEL sensor is deemed to have a confirmed and valid functional applicability and further investigation and development effort is warranted.

The performance analysis which is utilized to reach this conclusion is similar to the transient analysis previously performed, except the thermal exposure model was derived from the operating conditions of the HTR-PM, as depicted in Figure 7-9, with an assumed mock-fuel-pebble deployment configuration, requiring over 1,000 days of accurate operation before being ejected from the core via the pebble bed fuel recirculation system.

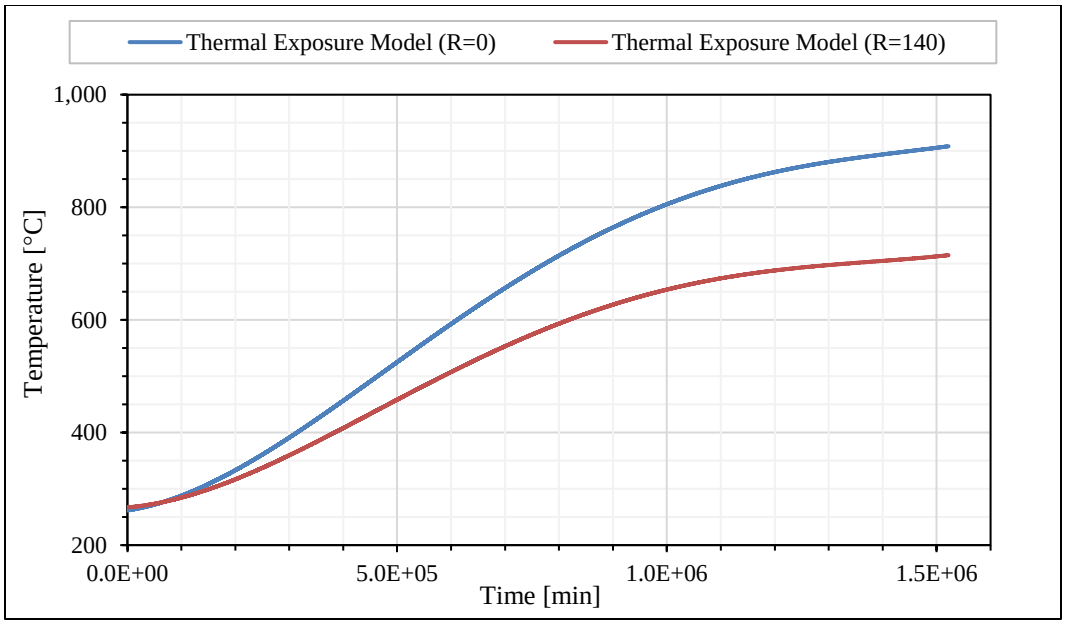

Figure 7-9: Derived HTR-PM thermal exposure model for two initial radial positions

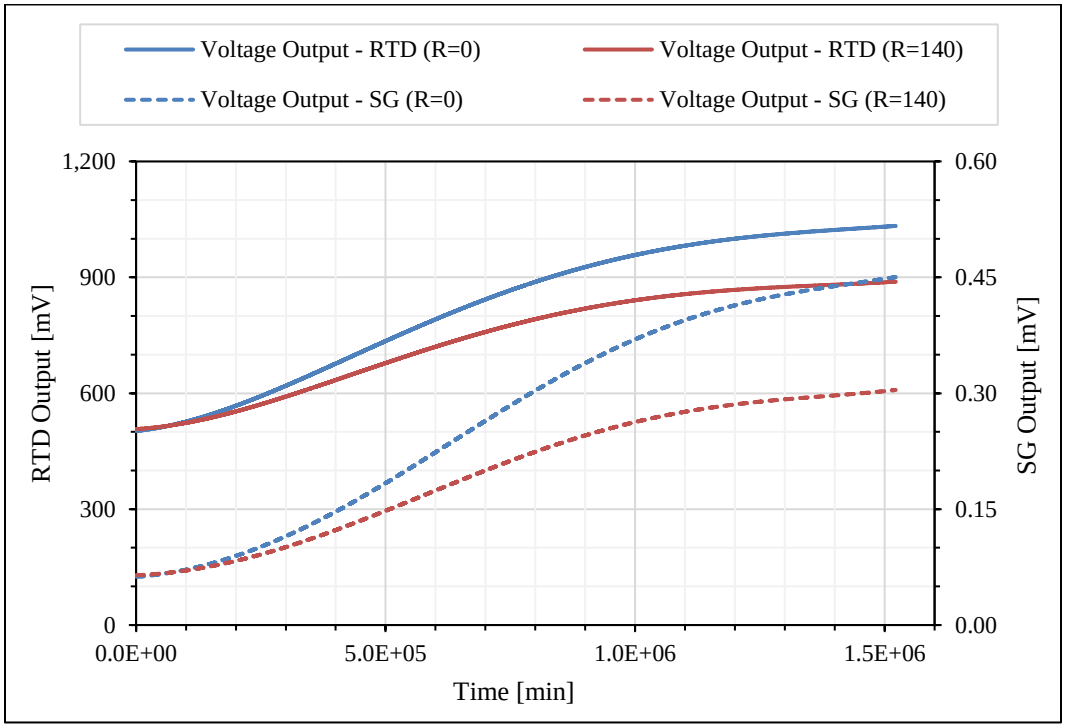

Figure 7-10: HERTEL sensor estimated performance for HTR-PM deployment

The estimated performance of the HERTEL sensor is depicted in Figure 7-10, with the real and compensated instrument output described by Figure 7-11 for a constant impurity generation rate over the lifetime of the sensor.

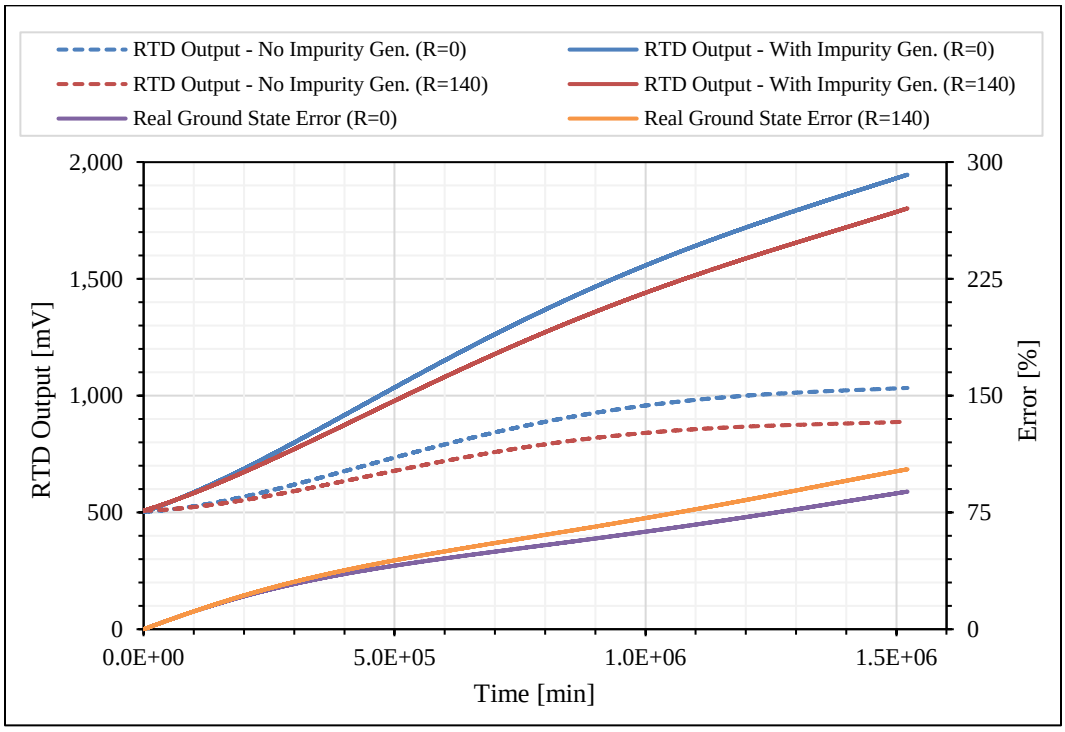

Figure 7-11: Raw and compensated output with estimated offset error for the HERTEL sensor

The real and estimated total error of the HERTEL sensor for the HTR-PM thermal exposure profile are depicted in Figure 7-12. Note that the unaccounted error drops very low at high temperatures and slow heating rates, this is the ideal situation for the HERTEL sensor drift correction algorithm, as it allows for temporal error to be very low due to a high annealing rate. Thus, ground state offsets can be calculated frequently, which constantly adjusts the output to account for the effects of impurities. Note that the real error nears 100% near the end of the instrument lifecycle, meaning that the effect of impurity migration is roughly equivalent to the effect which is being measured, as depicted in Figure 7-11. If the output were not corrected, the error of the raw measurement would be equivalent to this real error.

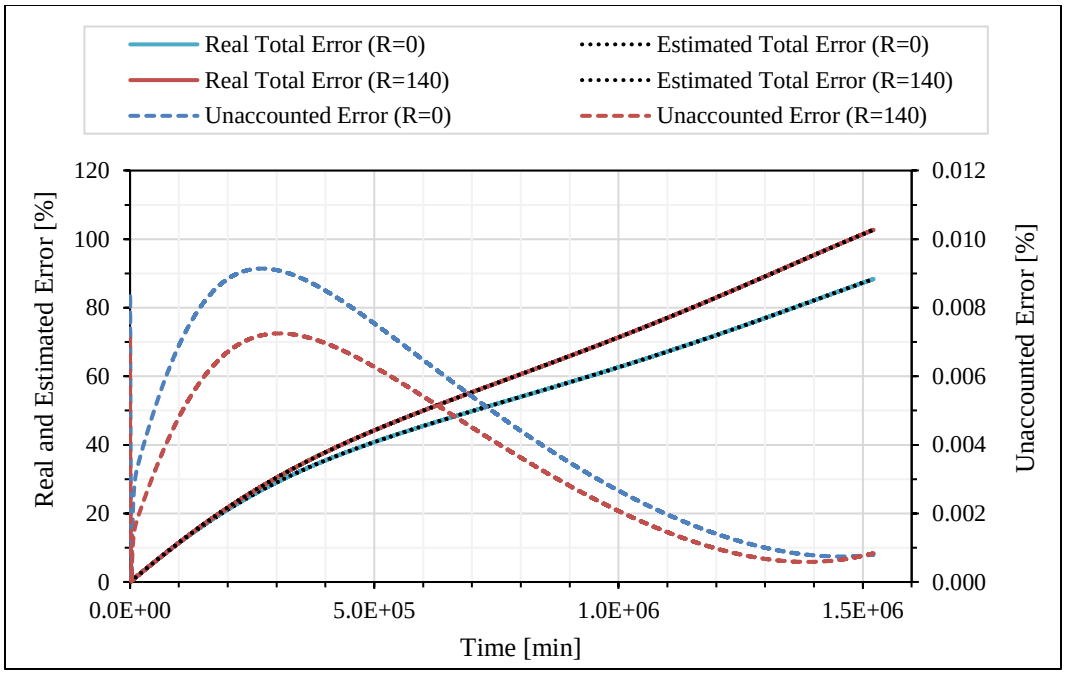

Figure 7-12: Real and estimated error for the HERTEL sensor for HTR-PM deployment

7.4 Overall Project Conclusions

The overall conclusions which can be drawn from this investigation can be divided into two distinct categories. These are a summary of results and development insights drawn from the presented investigation as well as a list of philosophical insights which are meaningful in the context of advanced thermal instrumentation development.

7.4.1 Summary of Results

The results developed over the course of this investigative endeavor are very encouraging. The proposed HERTEL sensor demonstrated a theoretical error bound up to 500 times smaller than the error bound of contemporary HTGR thermal instrumentation for identical thermal exposure in the core environment of the HTR-PM. This result; coupled with the inherent durability of the constituent materials, the self-calibrating capability demonstrated, the improvement of instrument accuracy over long measurement periods, and the flexibility which should eventually enable compatibility with wireless signal

transfer mechanisms, among many other functional advantages, promotes the idea that this approach to thermal instrumentation could be a breakthrough in design philosophy for very specific thermal instrumentation applications. The ability to detect and correct impurity generation effects further supports the target use case as radiation-tolerant reactor instrumentation, making for a potent argument for further development.

These apparent advantages should be considered cautiously, as the fundamental investigation here is qualitative as opposed to quantitative. The material properties utilized for performance simulation and assumptions made for simplification are not precise enough to guarantee the device performance will meet the results presented here, but great care was taken to always choose the conservative estimate when possible. The evaluation of functional applicability, even if experimentally demonstrated to be inaccurate by a factor of 100 or more, would still be compelling for durability improvements and functional extension possibilities alone.

At any rate, the work presented here is a relatively well-developed answer to the fundamental question that sparked this endeavor. How can measurements of the thermal environment of an HTGR core be collected? Furthermore; how can accurate, efficient, non-invasive, and frequent measurements the thermal environment of a dynamic, irregular, and unrestrained pebble bed HTGR core be collected? By aiming to answer the second question, a more definitive answer to the first question is also realized, and is presented here as a sequential manual of instructions for creating a device that may be an initial step toward a new generation of advanced reactor instrumentation.

7.4.2 Philosophical Instrumentation Development Insights

In summary, the investigation presented illustrates the relative power of micro-scale development capability and advances in thin film manufacturing. The instrument proposed would not have been possible to fabricate prior to the technological revolution that brought about MEMS fabrication techniques. The exploitation of micro-scale physics and high confidence in material parameters enables an approach to instrumentation which is

fundamentally different from traditional methods and although we have decades of progress in development and refinement of these techniques, the true capabilities and possible applications of this technology have only recently begun to be explored, much less deployed at a meaningful scale.

When this instrumentation development paradigm is applied to the fundamentally unique operational properties of the pebble bed reactor concept, the potential expansion of functionality is immediately apparent and extremely compelling. This investigation is proposed as a first step down the road toward integrated instrumentation and control mechanisms into autonomous reactivity and heat transfer optimization capability for pebble bed reactor cores. This could be further expanded into autonomous safety functions, bringing a new context to the concept of 'passively safe' reactor design. The results presented here stand on their own as being significant and progressive, but when viewed as an initial push toward the integration of advanced instrumentation with dynamic, unstructured reactor design concepts, the potential long-term outcomes of this preliminary research become more profound than otherwise considered.

7.4.3 Key Insights for Further Development

A number of fundamental insights have been derived from this investigation. The most significant of these are presented here, to summarize the progress and guide future work.

The most significant insight is that no single function instrument is capable of prolonged, accurate operation in a significantly harsh environment. The coupling of fundamentally isolated measurement functions is vital to ensuring that the various modes of measurement capability degradation are at the very least, apparent, if not compensated for. The combination of independent mechanisms to measure the same physical process, such as electron mobility, through the same material geometry ensures the complementary instruments are tightly coupled.

The exploitation of scale, particularly for mechanical interactions or coupling of volumetric material interactions, such as radiation exposure, constant thermal gradients, or isothermal boundary conditions, enables a range of assumptions that would not otherwise be possible. Extremely small-scale instruments can operate with an assumed uniformity in exposure, even in the presence of strong parameter gradients. Small scale mechanical devices, such a levers or membranes, often obey slightly different balances of physical forces when compared to their meso-scale counterparts. If this can be exploited, it can enable functionally unique applications which are not possible at larger scales.

Materials are absolutely critical for thin film and micro-scale devices. Interactions between materials, specifically at material interfaces, is vital to understanding and predicting how a micro-scale instrument will operate. A thorough material investigation should be the foundation of development using MEMS instrumentation and most of the key functional operability of the instrument should be a direct result of material interactions to exploit this inherent dependency of micro-scale interactions.

Long-term behavior is just as important as short-term response; especially when working in energetic (noisy) environments where measurement accuracy is critical. Long term resistance of a persistent force is futile. Long term adaption of the instrument to the surrounding environment is inevitable. The key functional advantage to the proposed HERTEL sensor is that the long-term behavior is well characterized and repeatable. Rather than try to precisely predict the short-term response, which is highly variable and dependent on a large number of parameters, a focus is placed on understanding and characterizing the persistent forces that will shape the long-term response. If you know where a particular transition will end, it doesn't really matter how it gets there, just that it eventually, inevitably, does arrive at that end.

7.5 Suggestions for Future Work

To continue development of the concepts proposed here, a range of topics for investigation are immediately apparent. In this section, each of these are identified and a general justification is provided.

7.5.1 Materials Investigation

As the performance of thin film instruments, and specifically MEMS instruments, are heavily dependent on material properties. Sapphire and platinum were chosen for this investigation because they are extremely stable across a wide temperature range and resist thermal and chemical corrosion, which greatly simplifies performance analysis and determination of functional applicability criteria, as the various effects which occur due to corrosion can simply be ignored. Adjusting the material selection criteria to prioritize device performance with an acceptable level of thermal or chemical corrosion may result in the consideration of materials not reviewed in this investigation.

Potential alternate materials for the platinum resistance trace include alloys of platinum and other platinum group metals. Rhenium, rhodium, iridium, molybdenum, tungsten, and zirconium alloys all offer significant improvements to various material parameters identified as being highly impactful to the accurate operation of the proposed sensor. Specifically, alloys which bring the resistance trace and substrate coefficients of thermal expansion into closer alignment, promote adhesion at the material boundary, or prevent thermal diffusion of impurities should be investigated, as these are the key mechanisms of signal drift.

Additional device sensitivity could be observed if a thermal diffusion material is used to allow for another means of instrument thermal exposure measurement. The mechanism by which this would be implemented is explored in the introductory chapters of this investigation and will not be reviewed again here.

Another possible functionality of an integrated thermal diffusion material could be the preferential reaction with the materials produced in a nuclear environment. If a material could be identified which is present in the platinum alloy and serves as sacrificial material to react with whatever materials are expected to be generated by nuclear reactions, then the high atomic mobility observed at high temperatures could serve to provide a means for the newly created molecule to travel out of the material lattice and avoid the calibration drift caused by impurities. This could provide a means of adapting the instrument design for use in nuclear, as well as thermal, environments.

Substrate material investigations should include other crystalline materials with directionally dependent thermal expansion coefficients. This should include a range of metal-oxide crystalline materials with hexagonal epitaxy, in which the metallic lattice bonds exhibit a larger linear expansion coefficient when compared to the oxygen lattice bonds. Doping of alumina is also a possibility and may offer various material parameter improvements.

Materials which do not exhibit directionally dependent thermal expansion could also be considered, if the sensor is constructed of two regions of different substrates bonded together. This would, of course, require a new approach to simulating the function of the device, as the differential thermal expansion at the material boundary could create additional stress which must be accounted for.

7.5.2 Prototypical Testing Program

The obvious objective after identifying any other potentially beneficial material combinations is the development of a robust testing program in which prototypical sensors can be fabricated and tested in a high temperature environment over long time periods. This testing program should verify and experimentally validate the calculated operation characteristics presented herein. Specifically, the expected durability of the device and the error reduction mechanisms should be qualified, as they are fundamental to the determination of applicability for the proposed target environment.

Performing a material variance study, in which a range of materials are investigated for utilization as resistance traces and substrates, would be beneficial in identifying potential material combinations which provide greater measurement stability and reduction of error. If various concentrations of alloyed materials can be tested, then a more precise characterization of the various degradation rates can be developed as a function of material composition.

Another fundamental testing objective should be to determine the effects of radiation exposure. This could be performed by operating the device in a test reactor sample port or by calibrating the instrument, exposing it to a well-defined radiation flux field, then repeating the calibration to determine the resistance offset of the calibration curve. Determination of the radiation tolerance is vital for further confirmation of instrument applicability for the proposed target deployment environment.

Once a baseline performance metric is established, then the evaluation of manufacturing sensitivity and design parameter sensitivity can also be performed. The slight variation which is expected to occur between sensor traces and between individual instruments can be extrapolated to sensitivity in the final instrument performance to determine the ultimate effects of manufacturing variance and establishment of dimensional tolerances. Once basic validation data is available, the simulation framework presented here can be improved and a geometric and material sensitivity study can be performed, as described at the end of Chapter 5, to ensure the final device delivers the best performance possible for a target thermal exposure profile.

7.5.3 Wireless Signal Transfer Investigation

A fundamental component of the applicability argument made for the proposed instrument is the expectation that the device will eventually utilize some form of wireless signal transfer. Once wired performance is established as a baseline metric, attempts at coupling

the sensor to an environmental energy harvesting and wireless signal transmission system can be developed and tested.

Various methods of passive signal transfer should be explored. A range of methods have been demonstrated in literature for MEMS devices in harsh environments, including LC coupling, RF backscatter, and passive high-frequency RF and laser resonators. All of these require that a signal generator sends out a burst of EM radiation, which is then attenuated and reflected by the wireless sensor, and collected by an antennae or optical sensor array.

All of these methods would require that a signal generator and collector be positioned in close proximity to the core volume, likely somewhere in the outer reflector. Placing these components in the vicinity of the harsh environment being monitored requires considerable engineering development to ensure these components can operate in this environment over long time periods without introducing additional error to the thermal measurement.

Other possible approaches to the implementation of wireless signal transmission include passive attenuation of the radiation emitted from the core. Scavenging energy and transmitting a signal by selective attenuation (forward scattering) of an already existing energy transfer mechanism, such as the gamma radiation profiles of the core as observed from a safe distance, is referred to as utilizing an "illuminator of opportunity". This approach offers considerable advantages, as it does not require an external excitation energy source and may allow for remote sensing of the transmission signal from a larger distance the previous methods.

In any case, the optimal deployment configuration requires the development of wireless signal transmission mechanism or adaption of an already existing technology for use in this instrumentation system. Although vital to the long-term deployment goals of the HERTEL sensor, the challenges presented are considerable and would require significant resources to investigate thoroughly.

7.5.4 Alternative Applicability, Deployment, and Functionality

Other applications for the proposed sensor should be investigated, particularly application to other thermal environments involving very high temperatures for very long time periods. These applications include temperature sensing in other high temperature reactor systems, in concentrated solar array heating assemblies, in refractory process monitoring, and in development and testing of propulsion systems for space and aircraft. It is likely that other applications exist in these areas and development funding may be easier to secure if the potential applicability is widened to include more technical sectors outside of nuclear instrumentation systems.

Alternative deployment configurations should also be evaluated, including static deployment in the outer reflector and core support structures, multi-instrument deployment in a single fuel pebble to determine if any cross-correlation of measurements can be used to further reduce the error bounds of the instruments, and deployment as a static device in prismatic block HTGR configurations. These should all present relatively straightforward improvements over the results presented here and might make a more concise and compelling funding request for further development.

Alternative functionality should be explored for the use of the sensors in DLOCA accident conditions. This is the primary design basis accident for pebble bed HTGRs and results in thermal transients which may create significant temporal measurement error for HERTEL sensors. However, the onset of such an accident may be detectable by the sudden temperature change, which should be accurately reflected as a temporal measurement, if not by a thermal measurement.

Another alternative functionality that should be investigated is an expansion of instrument monitoring capability. It is relatively well established that a critical assumption for accurate operation of the HERTEL sensor is that the thermal gradient is very flat across the sensor traces. A method for measuring this could be to use an eight-wire configuration instead of a six-wire configuration, allowing the RTD and strain measurements, as well as

the instrument power, to be switched between the two sets of inputs. Comparison of the two sets of measurements should allow for a determination of gradient impact, or perhaps overall instrument health, to be made. Both measurements should be equivalent if no significant gradient exists and the traces all have similar environmental exposure and material condition.

7.5.5 Integration into Fuel Pebble Manufacturing Processes

Finally, if the proposed device can be realized in a configuration which utilizes wireless signal transfer and exhibits good radiation resistance. An investigation into the possible sensor mounting locations for pebble bed fuel or equivalent unfueled graphite spheres should be investigated and opportunities to integrate the sensors into the manufacturing process for pebble bed fuel should be evaluated.

If a durable, accurate means of thermal monitoring and overall thermal exposure can be integrated into a small percentage of the fuel elements in a pebble bed reactor core, the possible increase in precision of reactor process monitoring would enable drastically improved confidence in characterization of the performance of the reactor. This could allow for dynamic annular fuel loading, increases in power density, better thermal distribution across the core, and the use of active flow control mechanisms with real-time feedback.

Ultimately, realizing the full potential of the pebble bed HTGR core concept requires the ability to monitor the thermal and radiation parameters of the core. If a means of indirect, remote sensing capability cannot be developed, then the integration of direct instrumentation into the pebble bed fuel spheres is a viable alternative for active monitoring of core conditions. The presented instrument is an ideal candidate for this type of deployment, if only a small initial step in a technical direction that will eventually enable this type of advanced instrumentation system.

Bibliography

[1] The U.S. Department of Energy, Office of Nuclear Energy, “Next Generation Nuclear Plant: A Report to Congress,” U.S. Department of Energy, Apr. 2010.

[2] Idaho National Laboratory, “NGNP Project 2011 Status and Path Forward,” Idaho National Laboratory, INL/EXT-11-23907, Dec. 2011.

[3] Y. Guan, F. Li, and M. Modarres, “A Method of Integrating Thermal-Hydraulic Analysis and Probabilistic Assessment for Safety Evaluation and Screening,” *Nucl. Technol.*, vol. 133, no. 3, pp. 290–309, Mar. 2001, doi: 10.13182/NT01-A3175.

[4] K. Kunitomi, S. Nakagawa, and S. Shiozawa, “Safety Evaluation of the HTTR,” *Nucl. Eng. Des.*, vol. 233, no. 1–3, pp. 235–249, Oct. 2004, doi: 10.1016/j.nucengdes.2004.08.028.

[5] Y. A. Hassan, “Large Eddy Simulation in Pebble Bed Gas Cooled Core Reactors,” *Nucl. Eng. Des.*, vol. 238, no. 3, pp. 530–537, Mar. 2008, doi: 10.1016/j.nucengdes.2007.02.041.

[6] Finis Southworth, “NGNP Industry Alliance and HTGR Deployment,” May 03, 2012.

[7] R. E. Walker, “Fort Saint Vrain Nuclear Power Station,” vol. 14, no. 163, pp. 1069–1073, 1969.

[8] James L. Everett III and Edward J. Kohler, “Peach Bottom Unit No. 1: A High Performance Helium Cooled Nuclear Power Plant,” *Ann. Nucl. Energy*, vol. 5, no. 8–10, pp. 321–335, 1978.

[9] Mabrouk Methnani, “High Temperature Gas-Cooled Reactors: Design Features, Potential, and Challenges,” in *Proceedings of the 2006 International Congress on Advances in Nuclear Power Plants (ICAPP 2006)*, Jun. 2006, pp. 160–165.

[10] D. Petti, “The Next Generation Nuclear Plant (NGNP).”

[11] Z. Wu, D. Lin, and D. Zhong, “The Design Features of the HTR-10,” *Nucl. Eng. Des.*, p. 8, 2002.

[12] S. Ball, “Sensitivity Studies of Modular High-Temperature Gas-Cooled Reactor Postulated Accidents,” *Nucl. Eng. Des.*, vol. 236, no. 5–6, pp. 454–462, Mar. 2006, doi: 10.1016/j.nucengdes.2005.10.029.

[13] Idaho National Laboratory, “HTGR Technology Course for the Nuclear Regulatory Commission - Module 5a: Prismatic HTGR Core Design Description,” May 24, 2010.

[14] Idaho National Laboratory, “HTGR Technology Course for the Nuclear Regulatory Commission - Module 6a: Pebble Bed HTGR Core Design Description,” May 24, 2010.

[15] Idaho National Laboratory, “HTGR Technology Course for the Nuclear Regulatory Commission - Module 6b: Pebble Bed HTGR Nuclear Design,” May 24, 2010.

[16] Idaho National Laboratory, “HTGR Technology Course for the Nuclear Regulatory Commission - Module 6c: Pebble Bed HTGR Thermal-Fluid Behavior,” May 24, 2010.

[17] William Beaver, *Nuclear Power Goes On-Line: A History of Shippingport*. Greenwood Press, 1990.

[18] J. H. Scobel, T. G. Theofanous, and S. W. Sorrell, “Application of the risk oriented accident analysis methodology (ROAAM) to severe accident management in the AP600 advanced light water reactor,” *Reliab. Eng. Syst. Saf.*, vol. 62, no. 1–2, pp. 51–58, Oct. 1998, doi: 10.1016/S0951-8320(97)00170-1.

[19] J. J. Janse van Rensburg and M. Kleingeld, “CFD Applications in the Pebble Bed Modular Reactor Project: A Decade of Progress,” *Nucl. Eng. Des.*, vol. 241, no. 9, pp. 3683–3696, Sep. 2011, doi: 10.1016/j.nucengdes.2011.05.018.

[20] C. G. du Toit, P. G. Rousseau, and T. L. Kgame, “Separate Effects Tests to Determine the Thermal Dispersion in Structured Pebble Beds in the PBMR HPTU Test Facility,” *Nucl. Eng. Des.*, vol. 271, pp. 437–443, May 2014, doi: 10.1016/j.nucengdes.2013.12.014.

[21] Y. A. Hassan and E. E. Dominguez-Ontiveros, “Flow Visualization in a Pebble Bed Reactor Experiment Using PIV and Refractive Index Matching Techniques,” *Nucl. Eng. Des.*, vol. 238, no. 11, pp. 3080–3085, Nov. 2008, doi: 10.1016/j.nucengdes.2008.01.027.

[22] H.-M. Prasser, “Novel Experimental Measuring Techniques Required to Provide Data for CFD Validation,” *Nucl. Eng. Des.*, vol. 238, no. 3, pp. 744–770, Mar. 2008, doi: 10.1016/j.nucengdes.2007.02.050.

[23] L. Wei and S. Zhong, “Design, Operation and Maintenance of Thermal Hydraulic Instrumentation System of HTR-10,” in *18th International Conference on Nuclear Engineering: Volume 1*, Xi’an, China, 2010, pp. 59–65, doi: 10.1115/ICONE18-29139.

[24] A. Tokuhiro and N. Kimura, “An Experimental Investigation on Thermal Striping Mixing Phenomena of a Vertical Non-Buoyant Jet with Two Adjacent Buoyant Jets as Measured by Ultrasound Doppler Delocimetry,” *Nucl. Eng. Des.*, p. 25, 1999.

[25] S. J. Ball, D. E. Holcomb, and M. S. Cetiner, “HTGR Measurements and Instrumentation Systems,” ORNL/TM-2012/107, 1040751, May 2012. doi: 10.2172/1040751.

[26] Mohamed Gad-el-Hak, *MEMS: Introduction and Fundamentals*, 2nd ed., vol. 1. CRC Press, 2005.

[27] S. Kim, T. Nam, and S. Park, “Measurement of Flow Direction and Velocity Using a Micromachined Flow Sensor,” *Sens. Actuators Phys.*, vol. 114, no. 2–3, pp. 312–318, Sep. 2004, doi: 10.1016/j.sna.2003.12.019.

[28] C. H. Ahn *et al.*, “Direct Fabrication of Thin Film Gold Resistance Temperature Detection Sensors on a Curved Surface Using a Flexible Dry Film Photoresist and Their Calibration Up to 450 °C,” *J. Micromechanics Microengineering*, vol. 23, no. 6, p. 065031, Jun. 2013, doi: 10.1088/0960-1317/23/6/065031.

[29] J. Sun, D. Cui, L. Zhang, X. Chen, H. Cai, and H. Li, “Fabrication and Characterization of a Double-Heater Based MEMS Thermal Flow Sensor,” *Sens. Actuators Phys.*, vol. 193, pp. 25–29, Apr. 2013, doi: 10.1016/j.sna.2013.01.010.

[30] M. Schwerter, T. Beutel, M. Leester-Schädel, S. Büttgenbach, and A. Dietzel, “Flexible Hot-Film Anemometer Arrays on Curved Structures for Active Flow Control on Airplane Wings,” *Microsyst. Technol.*, vol. 20, no. 4–5, pp. 821–829, Apr. 2014, doi: 10.1007/s00542-013-2054-y.

[31] N. Miyakawa, W. Legner, T. Ziemann, D. Telitschkin, H.-J. Fecht, and A. Friedberger, “MEMS-based microthruster with integrated platinum thin film

resistance temperature detector (RTD), heater meander and thermal insulation for operation up to 1,000°C," *Microsyst. Technol.*, vol. 18, no. 7–8, pp. 1077–1087, Aug. 2012, doi: 10.1007/s00542-012-1441-0.

[32] D. L. DeVoe, "Thermal issues in MEMS and microscale systems," *IEEE Trans. Compon. Packag. Technol.*, vol. 25, no. 4, pp. 576–583, Dec. 2002, doi: 10.1109/TCAPT.2003.809110.

[33] AREVA, "AREVA HTGR Information Kit."

[34] S. Shiozawa, S. Fujikawa, T. Iyoku, K. Kunitomi, and Y. Tachibana, "Overview of HTTR design features," *Nucl. Eng. Des.*, vol. 233, no. 1–3, pp. 11–21, Oct. 2004, doi: 10.1016/j.nucengdes.2004.07.016.

[35] A. Bredimas, "Status of the NGNP Industrial Alliance work and the business plan economics," p. 38.

[36] Z. Zhang and S. Yu, "Future HTGR developments in China after the criticality of the HTR-10," *Nucl. Eng. Des.*, p. 9, 2002.

[37] Z. Zhang *et al.*, "Current status and technical description of Chinese 2×250MWth HTR-PM demonstration plant," *Nucl. Eng. Des.*, vol. 239, no. 7, pp. 1212–1219, Jul. 2009, doi: 10.1016/j.nucengdes.2009.02.023.

[38] Y. Zheng, L. Shi, and Y. Dong, "Thermohydraulic Transient Studies of the Chinese 200MWe HTR-PM for Loss of Forced Cooling Accidents," *Ann. Nucl. Energy*, vol. 36, no. 6, pp. 742–751, Jun. 2009, doi: 10.1016/j.anucene.2009.02.007.

[39] Z. Zhang, Z. Wu, Y. Sun, and F. Li, "Design aspects of the Chinese modular high-temperature gas-cooled reactor HTR-PM," *Nucl. Eng. Des.*, vol. 236, no. 5–6, pp. 485–490, Mar. 2006, doi: 10.1016/j.nucengdes.2005.11.024.

[40] Z. Zhang, Z. Wu, Y. Xu, Y. Sun, and F. Li, "Design of Chinese Modular High-Temperature Gas-Cooled Reactor HTR-PM," in *Design of Chinese Modular High-Temperature Gas-Cooled Reactor HTR-PM*, Beijing, China, Sep. 2004, p. 8.

[41] G. Strydom and H. D. Gougar, "Preliminary reactor physics assessment of the HTR module with 14% enriched UCO fuel," *Nucl. Eng. Des.*, vol. 256, pp. 304–321, Mar. 2013, doi: 10.1016/j.nucengdes.2012.08.013.

[42] Z. Xiangwen *et al.*, “Preparation of spherical fuel elements for HTR-PM in INET,” *Nucl. Eng. Des.*, vol. 263, pp. 456–461, Oct. 2013, doi: 10.1016/j.nucengdes.2013.07.001.

[43] C. Fang, X. Bao, C. Yang, Y. Yang, and J. Cao, “The R&D of HTGR high temperature helium sampling loop: From HTR-10 to HTR-PM,” *Nucl. Eng. Des.*, vol. 306, pp. 192–197, Sep. 2016, doi: 10.1016/j.nucengdes.2016.03.012.

[44] World Nuclear News, “Moderator loading starts at Chinese demonstration HTGR,” *World Nuclear News*, Apr. 07, 2017. https://www.world-nuclear-news.org/NN-Fuel-loading-starts-at-Chinese-demonstration-HTGR-0704175.html (accessed Mar. 07, 2020).

[45] G. Zhao *et al.*, “Endurance test of full-scale mock-up helium circulator for HTR-PM,” *Nucl. Eng. Des.*, vol. 329, pp. 20–24, Apr. 2018, doi: 10.1016/j.nucengdes.2017.11.019.

[46] S. Knol *et al.*, “HTR-PM fuel pebble irradiation qualification in the high flux reactor in Petten,” *Nucl. Eng. Des.*, vol. 329, pp. 82–88, Apr. 2018, doi: 10.1016/j.nucengdes.2017.09.020.

[47] F. Gou, F. Chen, and Y. Dong, “Preliminary phenomena identification and ranking tables on the subject of the High Temperature Gas-cooled Reactor-Pebble Bed Module thermal fluids and accident analysis,” *Nucl. Eng. Des.*, vol. 332, pp. 11–21, Jun. 2018, doi: 10.1016/j.nucengdes.2018.03.022.

[48] J. Zhang, F. Li, and Y. Sun, “Physical Analysis of the Initial Core and Running-In Phase for Pebble-Bed Reactor HTR-PM,” *Sci. Technol. Nucl. Install.*, vol. 2017, pp. 1–6, 2017, doi: 10.1155/2017/8918424.

[49] AZO Sensors, “Thermocouple Types,” *azosensors*. https://www.azosensors.com/image.axd?src=%2fimages%2fArticle_Images%2fImageForArticle_787(9).jpg&ts=20170429033449&ri=503 (accessed Oct. 05, 2020).

[50] “Measure Temperature With RTD Sensors,” *DEWEsoft*. https://dewesoft.com/daq/measure-temperature-with-rtd-sensors (accessed Aug. 30, 2020).

[51] “TempCo RTD Technical Data,” *TempCo*. https://www.tempco.com/Tempco/Resources/Engineering-Data/RTD-Technical-Data.htm (accessed Aug. 30, 2020).

[52] D. A. Copinger, D. L. Moses, and L. R. Cupidon, “Fort Saint Vrain Gas Cooled Reactor Operational Experience,” NUREG/CR--6839, ORNL/TM--2003/223, 1495207, Jan. 2004. doi: 10.2172/1495207.

[53] S. J. Ball, M. S. Cetiner, and D. E. Holcomb, “TASK 1—INSTRUMENTATION IN VHTRS FOR PROCESS HEAT APPLICATIONS,” p. 63.

[54] H. L. Brey and C. Drive, “Initial Start-Up and Testing of the Fort St. Vrain HTGR – Lessons Learned which May Be Useful for the HTR-PM,” p. 8.

[55] K. Fan, F. Li, J. Guo, and X. Zhou, “Use readings of thermocouples to reconstruct the power distribution of HTR-PM,” *Ann. Nucl. Energy*, vol. 142, p. 107414, Jul. 2020, doi: 10.1016/j.anucene.2020.107414.

[56] F. Kai, L. Fu, Z. Xuhua, and G. Jiong, “Improved Harmonics Synthesis Method and its application in reconstructing power distribution of HTR-PM,” *Nucl. Eng. Des.*, vol. 355, p. 110351, Dec. 2019, doi: 10.1016/j.nucengdes.2019.110351.

[57] K. Korsah *et al.*, “Assessment of Sensor Technologies for Advanced Reactors,” ORNL/TM--2016/337, 1345781, Oct. 2016. doi: 10.2172/1345781.

[58] J. Yang, “A Silicon Carbide Wireless Temperature Sensing System for High Temperature Applications,” *Sensors*, vol. 13, no. 2, pp. 1884–1901, Feb. 2013, doi: 10.3390/s130201884.

[59] Y. Ji, Q. Tan, H. Wang, W. Lv, H. Dong, and J. Xiong, “A Novel Surface LC Wireless Passive Temperature Sensor Applied in Ultra-High Temperature Measurement,” *IEEE Sens. J.*, vol. 19, no. 1, pp. 105–112, Jan. 2019, doi: 10.1109/JSEN.2018.2872915.

[60] Y. Wang, Y. Jia, Q. Chen, and Y. Wang, “A Passive Wireless Temperature Sensor for Harsh Environment Applications,” *Sensors*, vol. 8, no. 12, pp. 7982–7995, Dec. 2008, doi: 10.3390/s8127982.

[61] T. T. Thai, H. Aubert, P. Pons, G. DeJean, M. M.Tentzeris, and R. Plana, “Novel Design of a Highly Sensitive RF Strain Transducer for Passive and Remote Sensing

in Two Dimensions," *IEEE Trans. Microw. Theory Tech.*, vol. 61, no. 3, pp. 1385–1396, Mar. 2013, doi: 10.1109/TMTT.2013.2243751.

[62] Q. Tan *et al.*, "Wireless Passive Temperature Sensor Realized on Multilayer HTCC Tapes for Harsh Environment," *J. Sens.*, vol. 2015, pp. 1–8, 2015, doi: 10.1155/2015/124058.

[63] L. M. Reindl, "Wireless Passive Sensors: Basic principles and performances," in *2008 IEEE Sensors*, Lecce, Italy, Oct. 2008, pp. 1607–1610, doi: 10.1109/ICSENS.2008.4716758.

[64] "Lift-off (microtechnology)," *Wikipedia*. https://en.wikipedia.org/wiki/Lift-off_(microtechnology) (accessed Oct. 06, 2020).

[65] S. Rao, G. Pangallo, and F. G. D. Corte, "An Experimental Study on the Performance of Two Temperature Sensors Based on 4H-SiC Diodes," *Procedia Eng.*, vol. 168, pp. 729–732, 2016, doi: 10.1016/j.proeng.2016.11.262.

[66] Lei, Man I., "Silicon Carbide High Temperature Thermoelectric Flow Sensor," Case Western Reserve University, 2011.

[67] J. K. Sim, J. Hyun, I. Doh, B. Ahn, and Y. T. Kim, "Thin-film resistance temperature detector array for the measurement of temperature distribution inside a phantom," *Metrologia*, vol. 55, no. 1, pp. L5–L11, Feb. 2018, doi: 10.1088/1681-7575/aa90bd.

[68] J. D. Wrbanek and G. C. Fralick, "Thin Film Physical Sensor Instrumentation Research and Development at NASA Glenn Research Center," presented at the ISA.

[69] J. Cui *et al.*, "Fabrication and characterization of nickel thin film as resistance temperature detector," *Vacuum*, vol. 176, p. 109288, Jun. 2020, doi: 10.1016/j.vacuum.2020.109288.

[70] A. K. Henning, N. Mourlas, S. Metz, and A. Zias, "A MEMS-based, high-sensitivity pressure sensor for ultraclean semiconductor applications," in *13th Annual IEEE/SEMI Advanced Semiconductor Manufacturing Conference. Advancing the Science and Technology of Semiconductor Manufacturing. ASMC 2002 (Cat. No.02CH37259)*, Boston, MA, USA, 2002, pp. 165–168, doi: 10.1109/ASMC.2002.1001596.

[71] X. C. Hao, Y. G. Jiang, H. Takao, K. Maenaka, T. Fujita, and K. Higuchi, “Zero temperature coefficient gas-sealed pressure sensor using mechanical temperature compensation,” in *2011 16th International Solid-State Sensors, Actuators and Microsystems Conference*, Beijing, China, Jun. 2011, pp. 116–119, doi: 10.1109/TRANSDUCERS.2011.5969152.

[72] S. Saremi, A. Alyari, D. Feili, and H. Seidel, “A MEMS-based hot-film thermal anemometer with wide dynamic measurement range,” in *IEEE SENSORS 2014 Proceedings*, Valencia, Spain, Nov. 2014, pp. 420–423, doi: 10.1109/ICSENS.2014.6985024.

[73] F. Mailly *et al.*, “Anemometer with hot platinum thin film,” p. 7, 2001.

[74] Z. Yang *et al.*, “Micro anemometer by a MEMS compatible lab-on-a-tube technology,” in *2015 Transducers - 2015 18th International Conference on Solid-State Sensors, Actuators and Microsystems (TRANSDUCERS)*, Anchorage, AK, USA, Jun. 2015, pp. 383–386, doi: 10.1109/TRANSDUCERS.2015.7180941.

[75] J. T. W. Kuo, L. Yu, and E. Meng, “Micromachined Thermal Flow Sensors—A Review,” *Micromachines*, vol. 3, no. 3, pp. 550–573, Jul. 2012, doi: 10.3390/mi3030550.

[76] S. Park, S. Kim, S. Kim, and Y. Kim, “A flow direction sensor fabricated using MEMS technology and its simple interface circuit,” *Sens. Actuators B Chem.*, vol. 91, no. 1–3, pp. 347–352, Jun. 2003, doi: 10.1016/S0925-4005(03)00109-6.

[77] S. Kim, S. Kim, Y. Kim, and S. Park, “A circular-type thermal flow direction sensor free from temperature compensation,” *Sens. Actuators Phys.*, vol. 108, no. 1–3, pp. 64–68, Nov. 2003, doi: 10.1016/S0924-4247(03)00268-1.

[78] R. Buchner, C. Sosna, M. Maiwald, W. Benecke, and W. Lang, “A high-temperature thermopile fabrication process for thermal flow sensors,” *Sens. Actuators Phys.*, vol. 130–131, pp. 262–266, Aug. 2006, doi: 10.1016/j.sna.2006.02.009.

[79] C. Lyons, A. Friedberger, W. Welser, G. Muller, G. Krotz, and R. Kassing, “A high-speed mass flow sensor with heated silicon carbide bridges,” in *Proceedings MEMS 98. IEEE. Eleventh Annual International Workshop on Micro Electro Mechanical Systems. An Investigation of Micro Structures, Sensors, Actuators,*

Machines and Systems (Cat. No.98CH36176), Heidelberg, Germany, 1998, pp. 356–360, doi: 10.1109/MEMSYS.1998.659782.

[80] M. T. Bensidhoum, M. Laghrouche, A. Sidi Said, L. Montes, and J. Boussey, "Fabrication flaws and reliability in MEMS thin film polycrystalline flow sensor," *Microsyst. Technol.*, vol. 20, no. 1, pp. 1–7, Jan. 2014, doi: 10.1007/s00542-013-1977-7.

[81] L. Kang *et al.*, "A flexible resistive temperature detector (RTD) based on in-situ growth of patterned Ag film on polyimide without lithography," *Microelectron. Eng.*, vol. 216, p. 111052, Aug. 2019, doi: 10.1016/j.mee.2019.111052.

[82] P. Liu, R. Zhu, and R. Que, "A Flexible Flow Sensor System and Its Characteristics for Fluid Mechanics Measurements," *Sensors*, vol. 9, no. 12, pp. 9533–9543, Nov. 2009, doi: 10.3390/s91209533.

[83] V. S. Turkani *et al.*, "Nickel Based Printed Resistance Temperature Detector on Flexible Polyimide Substrate," in *2018 IEEE SENSORS*, New Delhi, Oct. 2018, pp. 1–4, doi: 10.1109/ICSENS.2018.8589549.

[84] V. S. Turkani *et al.*, "Nickel Based RTD Fabricated via Additive Screen Printing Process for Flexible Electronics," *IEEE Access*, vol. 7, pp. 37518–37527, 2019, doi: 10.1109/ACCESS.2019.2904970.

[85] A. Shen, S. B. Kim, C. Bailey, A. W. K. Ma, and S. Dardona, "Direct Write Fabrication of Platinum-Based Thick-Film Resistive Temperature Detectors," *IEEE Sens. J.*, vol. 18, no. 22, pp. 9105–9111, Nov. 2018, doi: 10.1109/JSEN.2018.2869850.

[86] E. Sardini and M. Serpelloni, "Wireless Measurement Electronics for Passive Temperature Sensor," *IEEE Trans. Instrum. Meas.*, vol. 61, no. 9, pp. 2354–2361, Sep. 2012, doi: 10.1109/TIM.2012.2199189.

[87] J. M. English and M. G. Allen, "Wireless micromachined ceramic pressure sensors," in *Technical Digest. IEEE International MEMS 99 Conference. Twelfth IEEE International Conference on Micro Electro Mechanical Systems (Cat. No.99CH36291)*, Orlando, FL, USA, 1999, pp. 511–516, doi: 10.1109/MEMSYS.1999.746881.

[88] M. A. Fonseca, J. M. English, M. von Arx, and M. G. Allen, “Wireless micromachined ceramic pressure sensor for high-temperature applications,” *J. Microelectromechanical Syst.*, vol. 11, no. 4, pp. 337–343, Aug. 2002, doi: 10.1109/JMEMS.2002.800939.

[89] O. Chevalerias *et al.*, “Inductive Telemetry of Multiple Sensor Modules,” *IEEE Pervasive Comput.*, vol. 4, no. 1, pp. 46–52, Jan. 2005, doi: 10.1109/MPRV.2005.15.

[90] S. Mukherjee, “Chipless Radio Frequency Identification by Remote Measurement of Complex Impedance,” in *2007 European Conference on Wireless Technologies*, Munich, Germany, Oct. 2007, pp. 249–252, doi: 10.1109/ECWT.2007.4403993.

[91] “EPC C1G2 Compliant Passive Contact Temeprature Sensor - Datasheet.” Farsens.

[92] H. El Matbouly, S. Tedjini, K. Zannas, and Y. Duroc, “Chipless RFID Threshold Temperature Sensor Compliant with UHF and ISM Radio Frequency,” in *2018 2nd URSI Atlantic Radio Science Meeting (AT-RASC)*, Gran Canaria, May 2018, pp. 1–4, doi: 10.23919/URSI-AT-RASC.2018.8471585.

[93] H. El Matbouly, S. Tedjini, K. Zannas, and Y. Duroc, “Compact Multi Bit Slotted C-Scatterer for Threshold Sensitive Chipless Wireless Temperature Sensor,” *Technologies*, vol. 6, no. 3, p. 59, Jun. 2018, doi: 10.3390/technologies6030059.

[94] W. Miczulski, M. Krajewski, and S. Sienkowski, “A New Autocalibration Procedure in Intelligent Temperature Transducer,” *IEEE Trans. Instrum. Meas.*, vol. 68, no. 3, pp. 895–902, Mar. 2019, doi: 10.1109/TIM.2018.2857901.

[95] E. J. P. Santos and I. B. Vasconcelos, “RTD-based smart temperature sensor: Process development and circuit design,” in *2008 26th International Conference on Microelectronics*, Nis, Serbia and Montenegro, May 2008, pp. 333–336, doi: 10.1109/ICMEL.2008.4559289.

[96] Jiang Chengyu, “Advanced Flow Measurement and Active Flow Control of Aircraft with MEMS.”

[97] X. Sun *et al.*, “CFD investigation of bypass flow in HTR-PM,” *Nucl. Eng. Des.*, vol. 329, pp. 147–155, Apr. 2018, doi: 10.1016/j.nucengdes.2017.12.009.

[98] S. J. Ball *et al.*, “Next Generation Nuclear Plant Phenomena Identification and Ranking Tables (PIRTs) Volume 2: Accident and Thermal Fluids Analysis PIRTs,” ORNL/TM-2007/147, 1001274, Mar. 2008. doi: 10.2172/1001274.

[99] Y. Zheng, J. Lapins, E. Laurien, L. Shi, and Z. Zhang, “Thermal hydraulic analysis of a pebble-bed modular high temperature gas-cooled reactor with ATTICA3D and THERMIX codes,” *Nucl. Eng. Des.*, vol. 246, pp. 286–297, May 2012, doi: 10.1016/j.nucengdes.2012.02.014.

[100] C. Zhipeng, W. Yan, and Z. Yanhua, “Discussion on the accident behavior and accident management of the HTGR,” *Nucl. Eng. Des.*, vol. 360, p. 110497, Apr. 2020, doi: 10.1016/j.nucengdes.2019.110497.

[101] N. Gui, X. Huang, X. Yang, J. Tu, and S. Jiang, “HTR-PM-based 3D pebble flow simulation on the effects of base angle, recirculation mode and coefficient of friction,” *Ann. Nucl. Energy*, vol. 143, p. 107442, Aug. 2020, doi: 10.1016/j.anucene.2020.107442.

[102] Y. Li, N. Gui, X. Yang, J. Tu, and S. Jiang, “Effect of friction on pebble flow pattern in pebble bed reactor,” *Ann. Nucl. Energy*, vol. 94, pp. 32–43, Aug. 2016, doi: 10.1016/j.anucene.2016.02.022.

[103] P. A. Cundall and O. D. L. Strack, “Discussion: A discrete numerical model for granular assemblies,” *Géotechnique*, vol. 30, no. 3, pp. 331–336, Sep. 1980, doi: 10.1680/geot.1980.30.3.331.

[104] IAEA, “Status Report 96 - High Temperature Gas Cooled Reactor - Pebble-Bed Module (HTR-PM),” IAEA.

[105] H. M. Hashemian and J. Jiang, “Nuclear plant temperature instrumentation,” *Nucl. Eng. Des.*, vol. 239, no. 12, pp. 3132–3141, Dec. 2009, doi: 10.1016/j.nucengdes.2009.08.030.

[106] A. I. Pokhodun *et al.*, “Platinum Resistance Thermometry,” p. 56.

[107] L. Wang *et al.*, “Laser machined ultrathin microscale platinum thermometers on transparent oxide substrates,” *Sens. Actuators Phys.*, vol. 300, p. 111657, Dec. 2019, doi: 10.1016/j.sna.2019.111657.

[108] “Sapphire Orientation Definitions & Drawing.” Rayotek.

[109] S. T. Kompan, “Thermal Expansion of Solids - Recent Research and Standard Materials,” *Sci. Proc. XIII Int. Congr. Mach. Technol. Mater.*, 2016.

[110] Vishay Precision Group, “Measurement of Thermal Expansion Coefficient Using Strain Gages.” Micro-Measurements, Nov. 01, 2010, Accessed: Sep. 10, 2020. [Online].

[111] J. Han *et al.*, “MEMS-based Pt film temperature sensor on an alumina substrate,” *Mater. Lett.*, vol. 125, pp. 224–226, Jun. 2014, doi: 10.1016/j.matlet.2014.03.170.

[112] “Single Crystal Sapphire.” Kyocera.

[113] T. Dinh, H.-P. Phan, A. Qamar, P. Woodfield, N.-T. Nguyen, and D. V. Dao, “Thermoresistive Effect for Advanced Thermal Sensors: Fundamentals, Design Considerations, and Applications,” *J. Microelectromechanical Syst.*, vol. 26, no. 5, pp. 966–986, Oct. 2017, doi: 10.1109/JMEMS.2017.2710354.

[114] H. S. Bal, “Characterization of Sapphire: for its material properties at High Temperatures,” p. 56.

[115] X. Lin *et al.*, “The impact of thermal annealing on the temperature dependent resistance behavior of Pt thin films sputtered on Si and Al2O3 substrates,” *Thin Solid Films*, vol. 685, pp. 372–378, Sep. 2019, doi: 10.1016/j.tsf.2019.06.036.

[116] J. Guo, L. Tong, and L. Chen, “Platinum Alloy Strain Gauge Materials,” p. 9.

[117] K. A. Marino and E. A. Carter, “The effect of platinum on Al diffusion kinetics in β-NiAl: Implications for thermal barrier coating lifetime,” *Acta Mater.*, vol. 58, no. 7, pp. 2726–2737, Apr. 2010, doi: 10.1016/j.actamat.2010.01.008.

[118] F. Yi, W. Osborn, J. Betz, and D. A. LaVan, “Interactions of Adhesion Materials and Annealing Environment on Resistance and Stability of MEMS Platinum Heaters and Temperature Sensors,” *J. Microelectromechanical Syst.*, vol. 24, no. 4, pp. 1185–1192, Aug. 2015, doi: 10.1109/JMEMS.2015.2394483.

[119] R. K. Kirby, “Platinum - Thermal Expansion Reference Material,” p. 7.

[120] T. Schössler, F. Schön, C. Lemier, and G. Urban, “Effect of high temperature annealing on resistivity and temperature coefficient of resistance of sputtered platinum thin films of SiO2/Pt/SiOx interfaces,” *Thin Solid Films*, vol. 698, p. 137877, Mar. 2020, doi: 10.1016/j.tsf.2020.137877.

[121] R. Weiland, D. F. Lupton, B. Fischer, J. Merker, C. Scheckenbach, and J. Witte, "High-Temperature Mechanical Properties of the Platinum Group Metals," *Platin. Met. Rev.*, vol. 50, no. 4, pp. 158–170, Oct. 2006, doi: 10.1595/147106706X154198.

[122] E. R. Dobrovinskaya, L. A. Lytvynov, and V. Pishchik, "Properties of Sapphire," in *Sapphire*, Boston, MA: Springer US, 2009, pp. 55–176.

[123] D. R. White, M. Ballico, and V. Chimenti, "Uncertainties in the Realization of the SPRT Subranges of the ITS-90." Aug. 2019.

[124] G. Bernhardt, C. Silvestre, N. LeCursi, S. C. Moulzolf, D. J. Frankel, and R. J. Lad, "Performance of Zr and Ti adhesion layers for bonding of platinum metallization to sapphire substrates," *Sens. Actuators B Chem.*, vol. 77, no. 1–2, pp. 368–374, Jun. 2001, doi: 10.1016/S0925-4005(01)00756-0.

[125] B. Yu. N. Loginov, A. V. Yermakov, L. G. Grohovskaya, and G. I. Studenok, "Annealing Characteristics and Strain Resistance of 99.93 wt.% Platinum," *Platin. Met. Rev.*, vol. 51, no. 4, pp. 178–184, Oct. 2007, doi: 10.1595/147106707X237708.

[126] J. D. Wrbanek, K. L. H. Laster, A. Corporation, and B. Park, "Preparation and Analysis of Platinum Thin Films for High Temperature Sensor Applications," p. 26, 2005.

[127] V. Yadav and N. Moelans, "Analysis of grain topology and volumetric growth rate relation in three-dimensional normal grain growth," *Acta Mater.*, vol. 156, pp. 275–286, Sep. 2018, doi: 10.1016/j.actamat.2018.04.056.

[128] J. Li *et al.*, "Molecular dynamics simulation of mechanical properties of nanocrystalline platinum: Grain-size and temperature effects," *Phys. Lett. A*, vol. 383, no. 16, pp. 1922–1928, Jun. 2019, doi: 10.1016/j.physleta.2018.10.053.

Appendix: Instrument Drawings & Renders

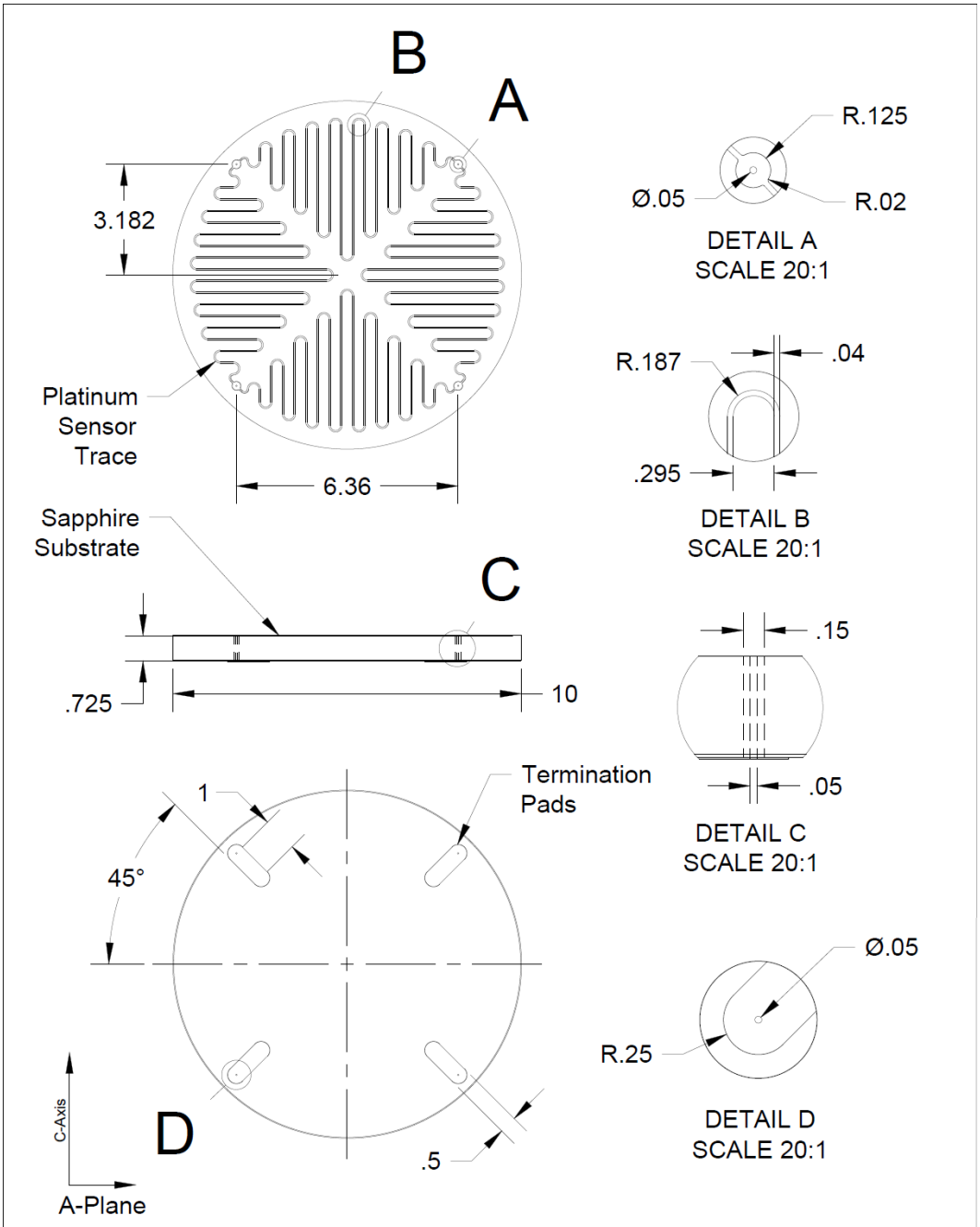

SUBSTRATE PROPERTIES	TRACE PROPERTIES	NAME
Material: Sapphire (Alpha-Alumina) Lattice Orientation: A-Plane Unit Size: 10.0 mm x 725 um (0.725 mm)	Material: Pure Platinum (99.999%) Trace Film Thickness: 4.0 um (0.004 mm) Terminal Film Thickness: 10.0 um (0.01 mm)	HERTEL Sensor Array Double-Sided, No Capping Layer

DRAWN: Matthew A. Hertel - 9/26/2020	UNITS: mm	SIZE: A	SCALE: 5 to 1	REV: A	SHEET: 1 of 1

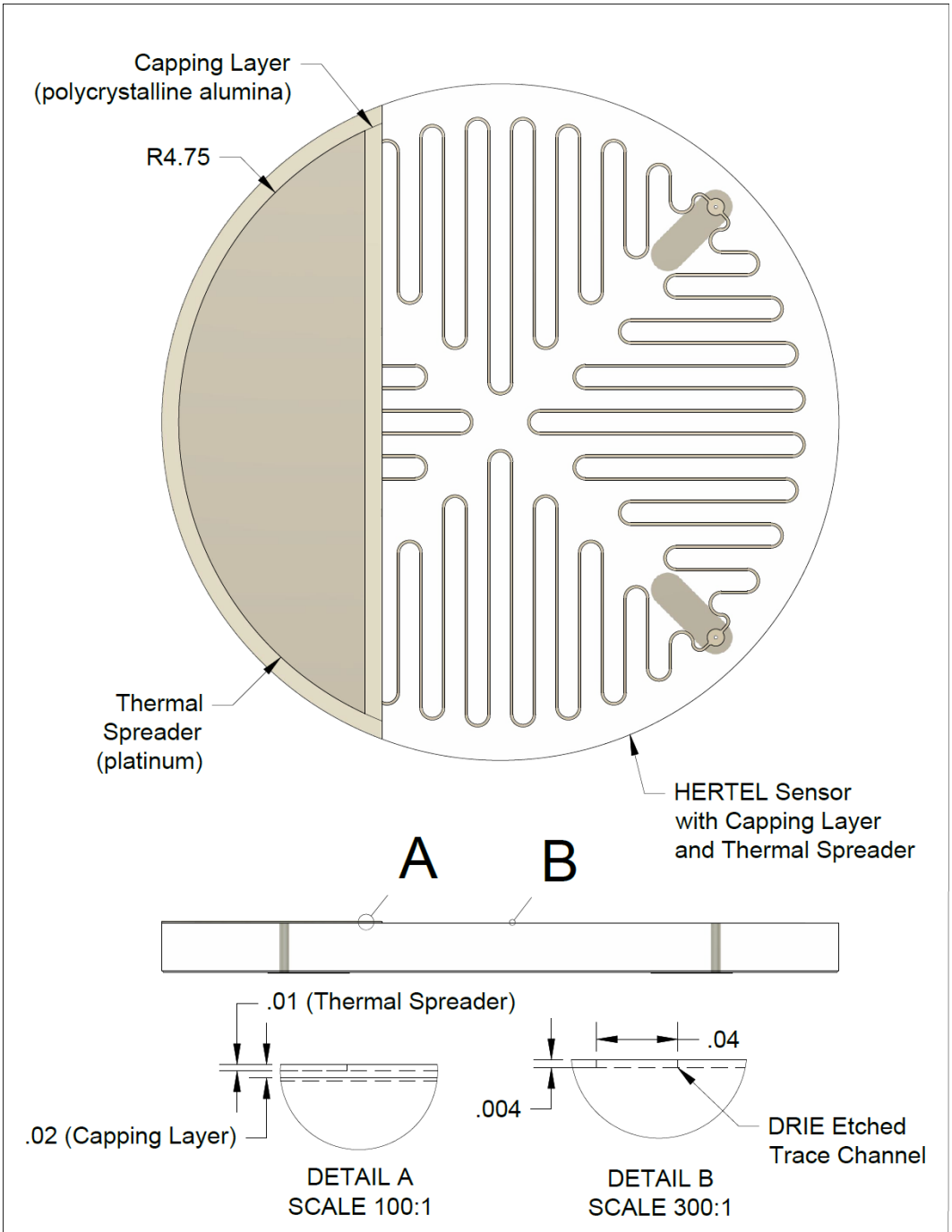

SUBSTRATE PROPERTIES	TRACE PROPERTIES	NAME
Material: Sapphire (Alpha-Alumina) Lattice Orientation: A-Plane Unit Size: 10.0 mm x 725 um (0.725 mm)	Material: Pure Platinum (99.999%) Trace Film Thickness: 4.0 um (0.004 mm) Terminal Film Thickness: 10.0 um (0.01 mm)	HERTEL Sensor Array Double Sided, DRIE Trace Channel, with Capping Layer and Heat Speader

DRAWN: Matthew A. Hertel - 9/26/2020	UNITS: mm	SIZE: A	SCALE:10 to 1	REV: A	SHEET: 1 of 1

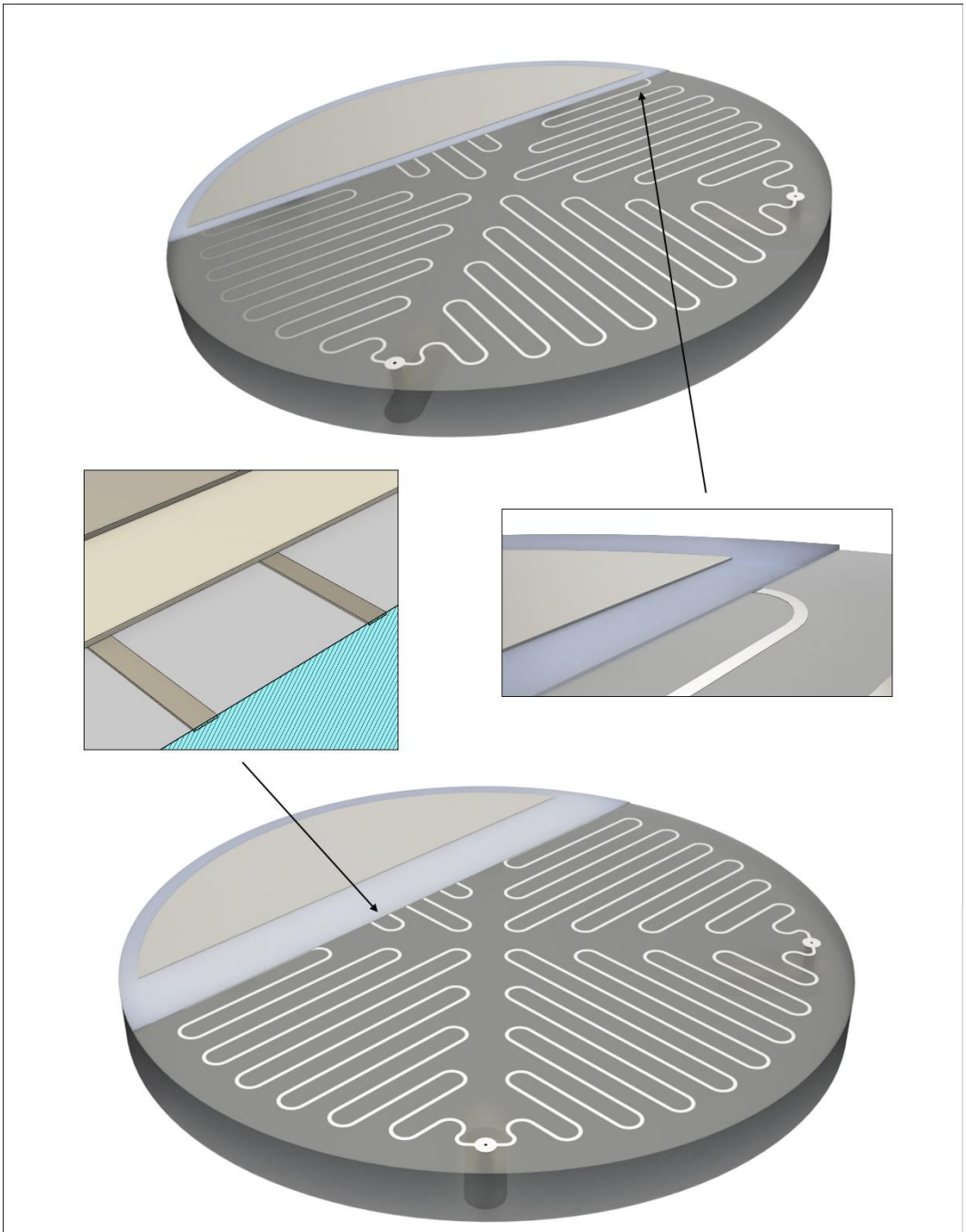

SUBSTRATE PROPERTIES	TRACE PROPERTIES	NAME
Material: Sapphire (Alpha-Alumina) Lattice Orientation: A-Plane Unit Size: 10.0 mm x 725 um (0.725 mm)	Material: Pure Platinum (99.999%) Trace Film Thickness: 4.0 um (0.004 mm) Terminal Film Thickness: 10.0 um (0.01 mm)	HERTEL Sensor Array Renders w/ Capping Layer and Thermal Spreader

DRAWN: Matthew A. Hertel - 9/26/2020	UNITS: mm	SIZE: A	SCALE:	REV: A	SHEET: 1 of 1